UiT
THE ARCTIC
UNIVERSITY
OF NORWAY

FACULTY OF SCIENCE AND TECHNOLOGY
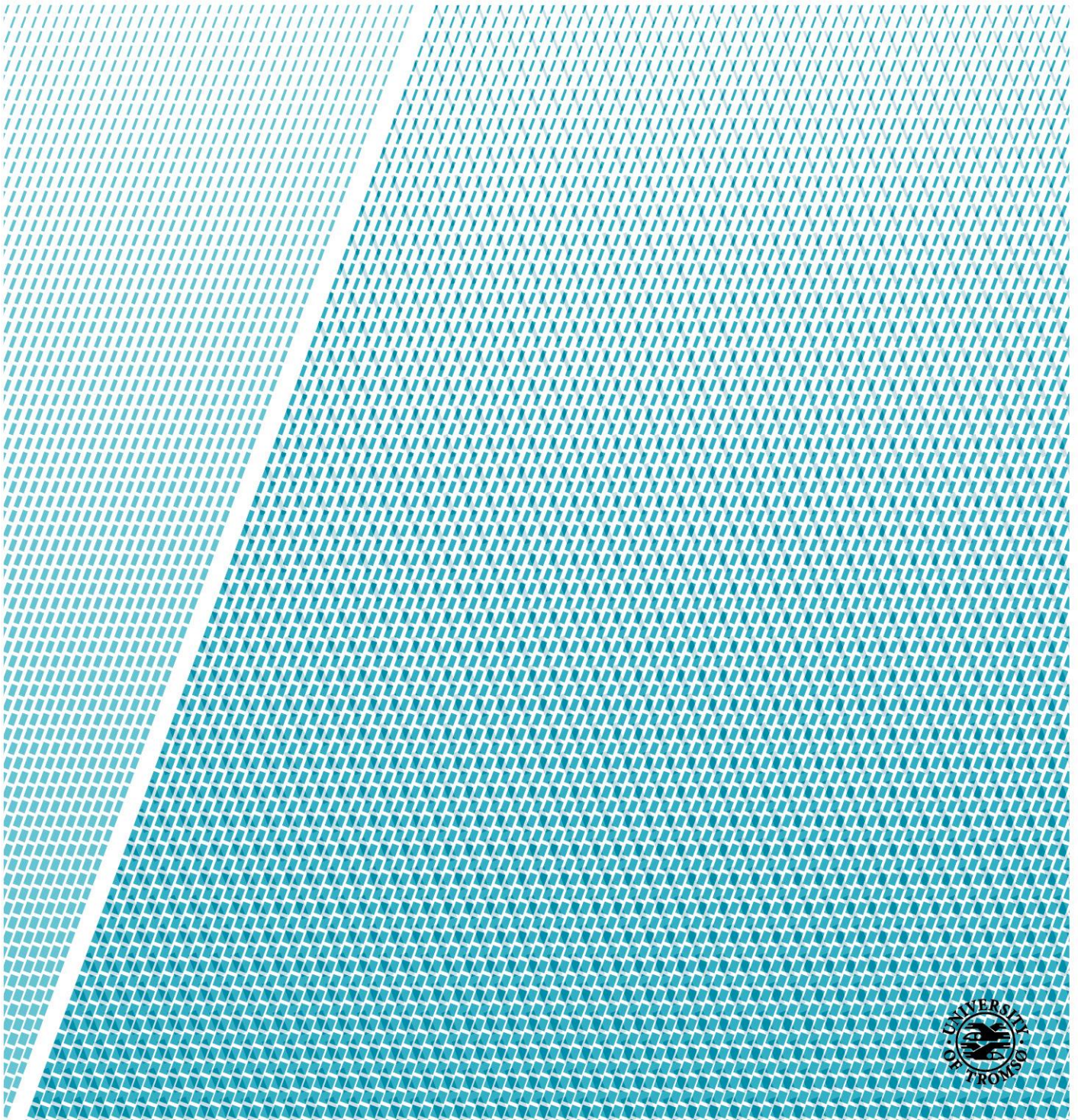DEPARTMENT OF GEOLOGY

Ice sheet dynamics in the Brunt Basin, Weddell Sea, Antarctica, since the last glacial period

Simon Helle Sørli
GEO-3900 Master's Thesis in Geology   *November 2016*

Abstract

High-resolution swath bathymetry, TOPAS sub-bottom profiles and four gravity cores from the Brunt Basin, southeastern Weddell Sea in Antarctica, were analysed with the purpose of reconstructing the ice sheet dynamics since the last glacial. Data collection was carried out by the British Antarctic Survey (BAS) and data analyses were carried out in a collaboration between the Department of Geosciences at UiT the Arctic University of Norway in Tromsø and BAS.

The swath bathymetry and TOPAS sub-bottom profiles were analysed to investigate the seafloor morphology and sub-bottom acoustic information, in order to identify glacial landforms indicative of ice sheet extent, basal regime and dynamics during the last extensive ice advance and its subsequent retreat. Multi-proxy analyses of the gravity cores were performed to determine depositional environments. This included physical properties, e.g. wet-bulk density, shear strength and magnetic susceptibility, the acquisition and interpretation of X-radiographs and line-scan images, qualitative element-geochemical analyses using an Avaatech XRF core scanner, analyses of the bulk granulometry and, in particular, of the sand fraction, as well as smear-slide investigations. Three radiocarbon dates were obtained from calcareous material, and one radiocarbon date was obtained from the acid insolvable organic fraction of the sediments.

The swath bathymetry displays a widespread distribution of glacial landforms providing evidence of past ice sheet activity within the study area. This includes subglacial landforms indicative of fast flowing ice, such as mega-scale glacial lineations, glacial lineation. Lateral shear-moraines, formed subglacial at the transition between fast and slow flowing ice. Additionally, ice-contact features such as grounding zone-wedges and recessional moraines, provide information about extent and dynamics during the deglaciation. Locally abundant iceberg scouring has eradicated any evidence of past ice sheet extent that might have formed during full glaciations within the outermost 24 km of the continental shelf of the Brunt Basin.

The TOPAS sub-bottom profiles and the gravity cores provide additional information about the glacial regime and ice-sheet dynamics within the study area. Acoustically transparent layers, corresponding to soft deformation till recovered in the gravity cores, indicate widespread deformation sliding at the base of a fast flowing ice stream in the middle and outer basin. In the northern part of the inner basin ice flow occurred as localized basal sliding, whereas slow flowing ice occupied the southern part of the inner basin and the shallower bank.

One radiocarbon date obtained from glaciomarine sediments 20 cm above the transition from the subglacial sediments, yields an age of ~8.5 calibrated kilo years before the present (cal. ka BP), indicating that the subglacial sediments and landforms were formed during the last glaciation. Assuming constant sedimentation rates after grounding line retreat, deglaciation of the inner part of the Brunt Basin occurred ~11.9 cal. ka BP.

Low to absent biogenic contents within the sediments deposited after the deglaciation, indicate that extensive ice shelves or perennial sea ice cover were located above the core locations prior to ~2.8 cal. ka BP, when the onset of seasonal open marine environment occurred. The latter resulted in increased productivity in the water masses. However, the biogenic content remained relatively low and sediment deposition occurred mainly from iceberg rafting.

Acknowledgments

I can't believe I made it! Finally ready to submit my master thesis. However, I couldn't have done this alone. There are a lot of people who have helped me along the way, and I would especially like to express my gratitude to the following people:

- First and foremost, Matthias Forwick! For great counseling, feedback and always making time for me. Without him, this would never have looked like a master thesis.
- Clause-Dieter Hillenbrand, Rob Larter, James Smith and Kelly Hogan for all the help I have gotten during my master thesis, and for making my stay at Cambridge excellent. Special thanks goes out to CD, for all the time he has invested in my thesis. This would never have worked out without him.
- The Brithish Antarctic Survey for making the data available for this project.
- Jan Sverre Laberg for his positive contributions to this master thesis and inspiring lectures.
- The ladies at the lab at UiT, Trine Dahl, Ingvild Hald and Karina Monsen, who always have been helpful and positive.
- My family for always supporting me and believing in me. You are great!
- My office partner Paul Velsand, for spell checking my master thesis.
- Marte Festøy for always being there for me and taking care of me through this intense period of my life. I am forever grateful and I would never have made it without her.

Table of Contents

Abbreviations:

AABW = Antarctic Bottom Water

AAIW = Antarctic Intermediate Water

ACC = Antarctic Circumpolar Current

AMS = Accelerator mass spectrometry

APIS = Antarctic Peninsula Ice Sheet

ATL = Acoustic transparent layer

ATR = Acoustic transparent ridge

BAS = British Antarctic Survey

cal. ka BP = Calibrated kiloyears before present

cal. yr BP = Calibrated years before present

CDW = Circumpolar Deep Water

CTD = Conductivity, Temperature and Depth

EAIS = East Antarctic Ice Sheet

ETH = Eidgenössische Technische Hochschule

GZW= Grounding zone wedge

HSSW = Sigh Salinity Shelf Water

IBCSO = The International Bathymetric Chart of the Southern Ocean

ISW = Ice Shelf Water

LCDW = Lower Circumpolar Deep Water

LGM = Last Glacial Maximum (~19-23 ka)

Ma = Million years ago

MS = Magnetic susceptibility

MICADAS = MIni radioCarbon Dating System

MSCL = Multi-Sensor Core Logger

MSGL = Mega-scale glacial lineation

NADW = North Atlantic Deep Water

Sv= Sverdrup ($10^6 m^3/s$)

UCDW = Upper Circumpolar Deep Water

WAIS = West Antarctic Ice Sheet

WSBW = Weddell Sea Bottom Water

WSDW = Weddell Sea Deep Water

x

1 Introduction

1.1 Objectives

The main objectives of this thesis are analyses of swath bathymetry, high-resolution seismic and multi-proxy analysis of sediment cores with the purpose of:

- Determining the timing and extent of the last advance of the Antarctic Ice sheet on to the Weddell Sea Shelf in the region of the Brunt Basin, and the subsequent retreat.
- Identifying the ice flow regime, fast-flow vs. slow-flow; warm-based vs. cold-based
- Reconstruction the dynamics of ice retreat
- Reconstructing the environmental conditions after the deglaciation

1.2 Motivation

Antarctica contains the biggest ice sheet on the earth, the Antarctic Ice Sheet, which is storing 26.5-26.9 million km^3 of ice, equal to a potential global sea level rise of 58.3 m (Fretwell et al., 2013). The Antarctic Ice Sheet is divided into three sub-ice sheets (Fig. 1.1); The East Antarctic Ice Sheet (EAIS), the West Antarctic Ice sheet (WAIS), and the Antarctic Peninsula Ice Sheet (APIS). The ice sheets are located inland and are drained by fast flowing outlet glaciers and ice streams, which transports ice from the interior of the Antarctic continent to the coast (Rignot et al., 2011). Ice shelves occur as seawards extensions of the ice sheet in several regions (Fig. 1.1), which provides backstress, buttressing the ice sheet by reducing velocity and loss of mass trough outlet glaciers and ice streams (Van der Veen, 1997; Benn and Evans, 2010; Matsuoka et al., 2015).

Recent studies have shown that the regions of the APIS and WAIS have lost a lot of volume recently. Driven by ongoing and past acceleration of marine-terminating outlet glaciers, mainly caused by upwelling of relative warm Circumpolar Deep Water (CDW) causing sub-ice shelf melt, manifested in the collapse of ice shelves on the Antarctic peninsula (e.g. Vaughan and Doake, 1996; Scambos et al., 2003; 2004; Rignot et al., 2004; 2008; Cook et al., 2005). Whereas the EAIS seems to gain volume, due to increased snow accumulation (Davis et al., 2005; Rignot et al., 2008; Shepherd et al., 2012).

Especially the WAIS has gotten a lot of attention lately. Large parts of the ice sheet are grounded below the sea surface with multiple seafloor slopes inclined towards the interior of Antarctica (Bamber et al., 2009; Fretwell et al., 2013), making it prone to rapid retreat, detachment and collapse (e.g. Mercer, 1978; Oppenheimer, 1998; Vaughan, 2008; Hellmer et al., 2012).The current observed negative mass balance, which accounts for about 10 % of the present global sea level rise (Meier et al., 2007), together

with rapid retreat of the grounding lines (e.g. Joughin et al., 2010; Tinto and Bell, 2011; Shepherd et al., 2012; Rignot et al., 2014), are raising concerns that a large-scale collapse could occur within human timescale (Katz and Worster, 2010; Gladstone et al., 2012; Favier et al., 2014; Joughin et al., 2014). Such a collapse would potentially lead to a global sea level rise of 3.4 m (Bamber et al., 2009; Fretwell et al., 2013).

To understand and predict potential collapses and/or contribution to further sea level rise, it is necessary to understand the behavior of the Antarctic Ice Sheet in the past (Smith et al., 2011). Knowledge about i.e., the extent and dynamic during the last glacial, and the subsequent deglaciation can be obtained by analyses of swath bathymetry, high-resolution seismic and sediment cores (e.g. Evans and Pudsey, 2002; Ó Cofaigh et al., 2002; Evans et al., 2005; Hillenbrand et al., 2012; Larter et al., 2012; Livingstone et al., 2012; Stolldorf et al., 2012).

The Weddell Sea is a key region for investigating the Antarctic Ice Sheet behavior, as more than 22% of the ice from the WAIS, the EAIS and the APIS are currently drained in to the Weddell Sea (e.g. Joughin et al., 2006). Reconstructions of the last glacial cycle in the Weddell Sea may provide important information about the Antarctic Ice Sheet extent and dynamics, and can be used to test and improve numerical ice sheet models, to better predict future ice sheet response to rising sea level and global temperatures (e.g. Hillenbrand et al., 2014). However, the glacial history in the Weddell Sea during the LGM is still being debated (e.g. Hein et al., 2011, 2014; Hillenbrand et al., 2012; 2014; Larter et al., 2012; Stolldorf et al., 2012). Very limited data provides difficulties in constraining the last extend of grounded ice in the eastern Weddell Sea (e.g. Anderson and Andrews, 1999; Kristoffersen et al., 2000b; Stolldorf et al., 2012; Gales et al., 2014). Existing data suggest two alternative scenarios reconstructions of the LGM (Hillenbrand et al., 2014; section 1.3.1), and additional data is urgently needed to reconstruct the ice sheet history in the Weddell Sea with some certainty (Hillenbrand et al., 2014).

1.3 Glacial history of Antarctica

The onset of the Antarctic Ice Sheet is linked to enrichment in deep-water marine $\delta^{18}O$ values ~34 Ma (million years ago), and the continental margin of Antarctica has been occupied by grounded ice on and off since then (e.g., Zachos et al., 1996; Coxall et al., 2005; Bohaty et al., 2012).

The extent, configuration and dynamics of the Antarctic Ice Sheet during the last glacial/interglacial cycle, and the timing and style of retreat has been the subject of several studies through the last decades (e.g. Denton and Hughes, 1981; Bentley, 1999; Anderson et al., 2002; Wright et al., 2008; Livingstone et al., 2012). Recently, Bentley et al. (2014) synthesized the growing number of geological data regarding the Antarctic ice sheet history during the last glacial/interglacial cycle, where detailed reviews were divided into six sectors (Fig. 1.1): East Antarctica (Mackintosh et al., 2014), Weddell Sea (Hillenbrand et al., 2014), Ross Sea (Anderson et al., 2014a), Amundsen-Bellingshausen Sea (Larter et al., 2014), Antarctic Peninsula (Ó Cofaigh et al., 2014), and sub-Antarctic Islands (Hodgson et al., 2014).
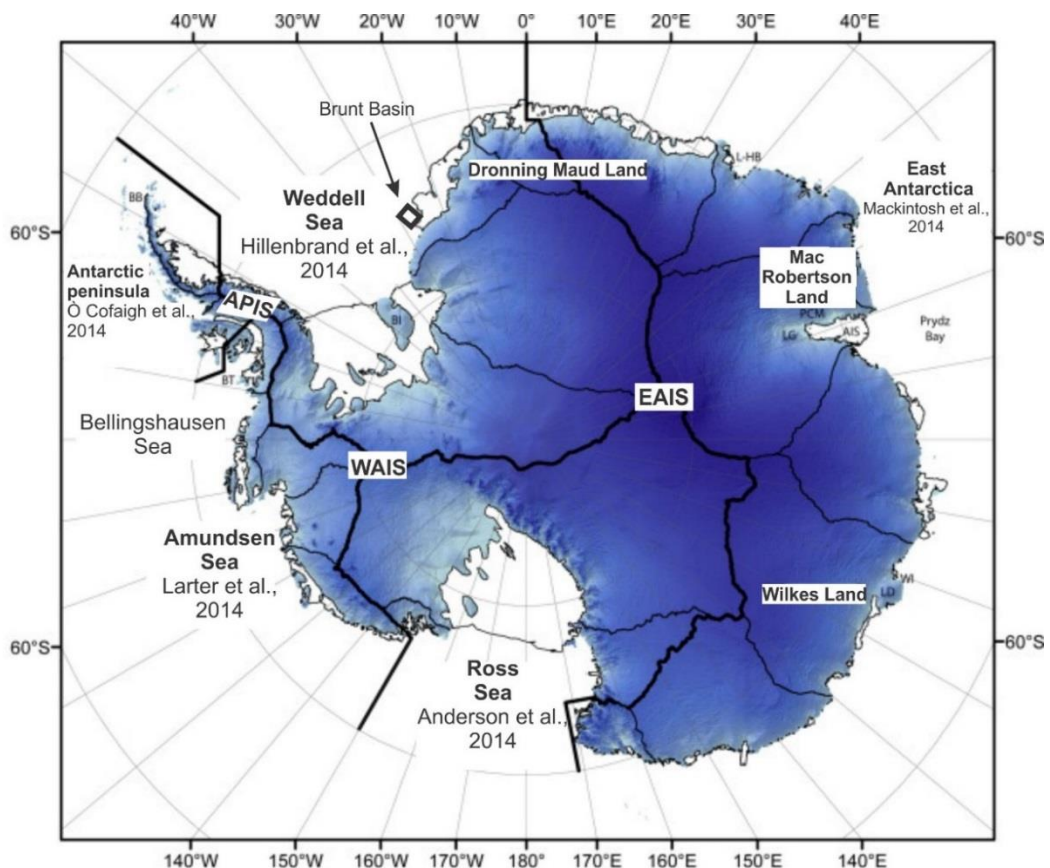
Fig. 1.1. Map of Antarctica with the location of the APIS, WAIS, and EAIS. The Antarctic Ice Sheet is marked with blue shading that indicates the ice sheet elevation, ice shelves are in white. The black thick solid lines show the boundaries for the reviewed sectors. The black box shows the location of the Brunt Basin and the study area. The thin black lines show the ice divides according to Zwally et al. (2012). Modified from Bentley et al. (2014).

During the LGM, fjords and troughs acted as pathways for channelized fast-flowing ice streams draining ice from the interior of the Antarctic Ice Sheet, similarly to the present day configuration, but much more extensive (Rignot et al., 2011; Livingstone et al., 2012). Slower and less dynamical areas of ice separated the ice streams, and beyond the grounding line as a seawards extension of the Antarctic Ice Sheet, areas of ice shelves covered parts of the ocean, feed by both fast and slow flowing ice. However, recent studies argue that grounded ice did not reach the continental shelf edge everywhere around the Antarctic margin, and that the maximum extent and the subsequent retreat was not synchronous for the Antarctic Ice sheet during the last glaciation (e.g. Anderson et al., 2002; Bentley et al., 2014).

Data from parts of the East Antarctic margin indicates large differences in the timing of retreat (Fig. 1.2), where the onset of retreat in some regions began at ~18 kiloyears before present (ka BP), and the grounding line had retreated close to its present position by ~12 ka BP, whereas other regions started retreating at ~12 ka BP (cf. Mackintosh et al., 2014). In other sectors, such as in the western Ross Sea (Fig. 1.1), grounded ice did not reach the shelf edge and the onset of retreat occurred mainly after ~13 ka BP (Licht et al., 1996; Anderson et al., 2014a). Whereas in the Bellingshausen Sea, grounded ice advanced to, or close to the continental shelf, and the onset of deglaciation began as early as 25.5 ka BP (Hillenbrand et al., 2010; Larter et al., 2014).
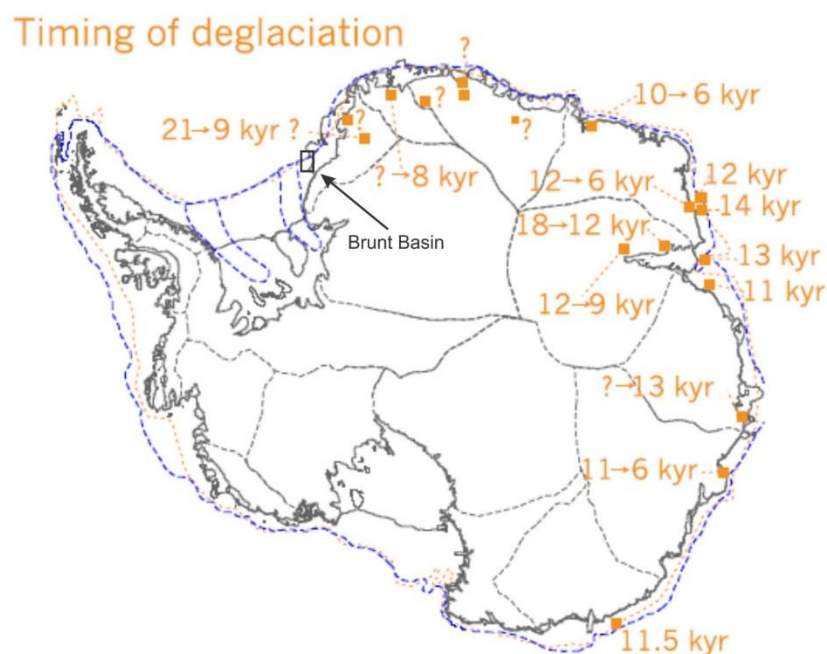
Fig. 1.2. The timing of deglaciation at different sites from East Antarctica, both marine and terrestrial dates are shown, where the ages are rounded to nearest thousand years. Numbers separated by arrows indicates the onset and complete deglaciation. Single numbers on the continental shelf show the onset of marine sedimentation. The black box shows the location of the Brunt Basin. The estimated LGM grounding zone positions with orange line is from Anderson et al. (2002) and blue line is from Livingstone et al. (2012). Kyr – kiloyears. Modified from Mackintosh et al. (2014).

1.3.1 The Weddell Sea

The Weddell Sea region (Fig. 1.3) provides an ideal area of investigating the asynchronous behavior of the Antarctic Ice Sheet, as it receives ice form APIS, WAIS, and EAIS. Reconstruction of the Antarctic Ice Sheet during the last glacial/interglacial cycle in the Weddell Sea sector has been the target of multiple studies for the last decades (e.g. Anderson et al., 1980; Elverhøi, 1981; Anderson et al., 1991; Melles and Kuhn, 1993; Bentley and Anderson, 1998; Anderson and Andrews, 1999; Bentley et al., 2010; Hein et al., 2011; Hillenbrand et al., 2012; Larter et al., 2012; Stolldorf et al., 2012). Conflicting data from terrestrial studies (e.g. Fogwill et al., 2004; Bentley et al., 2010; Hein et al., 2011; Hodgson et al., 2012), ice core studies (EPICA Community Members, 2006; Mulvaney et al., 2007) and marine studies (e.g. Elverhøi, 1981; Melles and Kuhn, 1993; Bentley and Anderson, 1998; Anderson and Andrews, 1999; Kristoffersen et al., 2000a; 2000b; Hillenbrand et al., 2012; Larter et al., 2012; Stolldorf et al., 2012), provides difficulties in an overall consensus regarding the ice extent in the Weddell Sea sector (Hillenbrand et al., 2014).

Terrestrial data suggest no thickening in the eastern section (Shackleton Range cf. Fogwill et al., 2004; Hein et al., 2011, 2014), and minor thickening of the western section (Ellsworth Mountains, cf. Bentley et al., 2010), of the drainage basins in the Weddell Sea (Fig. 1.3). The ice core data suggest a limited ice thickening in central Dronning Maud land (EPICA Community Members, 2006), and that Berkner Island (Fig. 1.3) acted as an independent ice center and was not overridden by inland ice during the LGM (Mulvaney et al., 2007). Contrasting, marine data suggest both a restricted advance (Anderson and Andrews, 1999; Stolldorf et al., 2012) and a more extensive advance (Elverhøi, 1981; Bentley and Anderson, 1998; Hillenbrand et al., 2012; Larter et al., 2012).

Additionally, spares amounts of calcareous material to date, reworking of sediment due to current winnowing and iceberg scouring, which leads to inverted ^{14}C ages, provides difficulties in getting constrains on the glacial history in the Weddell Sea (Hillenbrand et al., 2012; Stolldorf et al., 2012; Hillenbrand et al., 2014).

Hillenbrand et al. (2014) proposed two alternative scenarios of the LGM and its subsequent retreat, based on different interpretations of the glacial and geological datasets from the Weddell Sea sector. Scenario A suggests a more restricted advance during LGM, whereas scenario B suggest a more extensive advance (Fig. 1.4-Fig. 1.8).

Scenario A (Fig. 1.5-Fig. 1.8) is consistent with terrestrial data and uses the oldest marine dates as minimum ages for grounding line retreat (Anderson and Andrews, 1999; Stolldorf et al., 2012). Most of the subglacial landforms indicating a grounding event were assumed to be of pre-LGM age, and

grounding line positions are mainly based on glaciological modelling to fit the terrestrial geological data (Bentley et al., 2010; Le Brocq et al., 2011; for details see Whitehouse et al., 2012).

According to scenario A, maximum advance of grounded ice occurred ~20 ka BP and was mainly focused on the shelf between the Roone and Flichner troughs (Fig. 1.5), reaching close to the shelf edge in the Hughes Trough. The Roone and Flichner troughs experienced no or minor advances of grounded
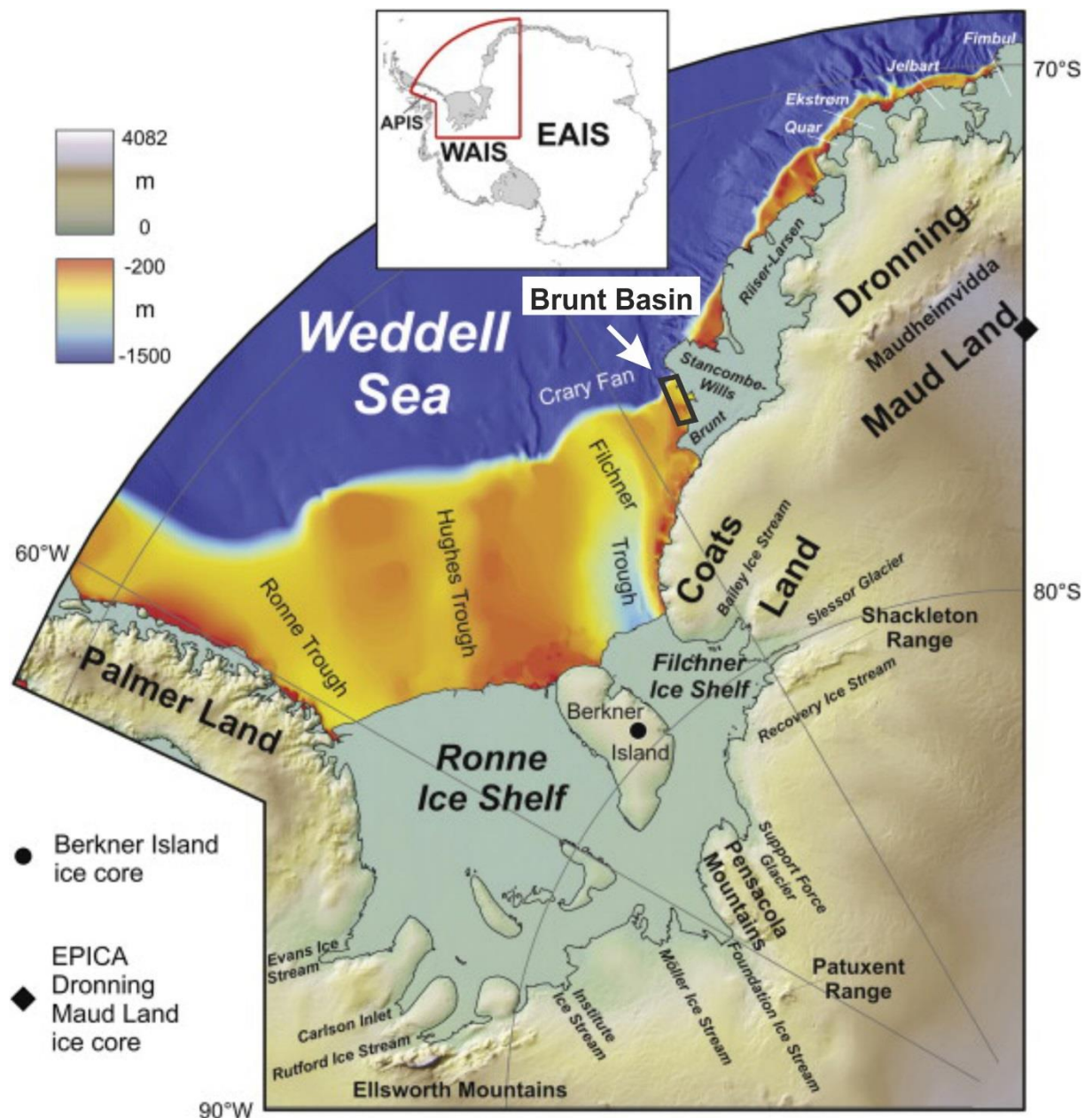
Fig. 1.3. Overview map of the Weddell Sea according to Bedmap2 (Fretwell et al., 2013), with shelf bathymetry and ice sheet elevation (in meters above sea level), with ice-shelves displayed in light blue shading. Inset map shows Antarctica, with the sub-ice sheets, where ice shelfs are displayed with gray shading, and the location of the Weddell Sea sector outlined by the red line (APIS- Antarctic Peninsula Ice Sheet, EAIS- East Antarctic Ice Sheet, WAIS- West Antarctic Ice Sheet). Modified from Hillenbrand et al. (2014).

ice, but extensive ice shelves or light-grounded ice are expected to have occurred in the two troughs (Hillenbrand et al., 2014). In the eastern part of the Weddell Sea, the grounding line advanced to the mid-shelf, and no ice was occupying the study area, north of the Brunt Ice shelf (Fig. 1.5).

Scenario B (Fig. 1.4-Fig. 1.8) uses the dates from the marine sediment cores as a mixture between minimum and maximum ages for the ice sheet retreat, assuming that the older dates were obtained by reworked microfossils that originally were deposited before the LGM (Hillenbrand et al., 2014). A hiatus between ~31.0 and ~21.5 cal. ka BP in the marine dates, observed north of the Flichner-Ronne and Riiser-Larsen ice shelves is suggested to represent advance of grounded ice and the termination of the hiatus is assumed to correspond closely to grounding line retreat (Hillenbrand et al., 2014).

Fig. 1.4. Grounded ice sheet extent according to Scenario B in the Weddell Sea sector at 25 ka. The different certainty levels given for the grounding line (GL) are indicated. The black circles show different core locations used for reconstructing the grounding line. The location of core 3-7-1 is indicated with the arrow. The location of the Brunt Basin is indicated with the black box. Note that in Scenario A, the maximum extent was not reached before ~20 ka, and is therefore not included in the 25 ka reconstruction. Modified from Hillenbrand et al. (2014).

Grounding line positions for scenario B are a mixture of, subglacial landforms of unknown age, sediment cores that recovered subglacial or over-consolidated sediments with no or limited ages available, or inferred grounding line position (Hillenbrand et al., 2014).

Scenario B then suggests that the grounded ice was at the shelf edge or close to the shelf edge at most locations at ~25 cal. ka BP. Except north of the Quar Ice Shelf and Brunt Ice Shelf, including the study area (Fig. 1.4), where grounded ice had retreated before ~28 and ~33 cal. ka BP, respectively (Anderson et al., 2002; Stolldorf et al., 2012; Hillenbrand et al., 2014).

Fig. 1.5. Grounded ice sheet extent according to Scenario A and B in the Weddell Sea sector at 20 ka. The different certainty levels given for the grounding line (GL) are indicated. The black circles show different core locations used for reconstructing the grounding line, and the red circles indicate ice sheet elevation at different locations. The location of core 3-7-1 is indicated with the arrow. The location of the Brunt Basin is indicated with the black box. Modified from Hillenbrand et al. (2014).

Three scenarios have been proposed explaining ice advancing to the shelf edge, and the limited thickening of the ice sheet indicated by terrestrial data (Larter et al., 2012). (i) An ice plain extending from the modern grounding line all the way to the shelf break (Le Brocq et al., 2011; Hillenbrand et al., 2012). (ii) Ice shelf thickening and touchdown of the Ice Shelf onto the seafloor (Hillenbrand et al., 2012). (iii) Change in drainage pattern of ice into the Flichner Trough so that the ice was source from the Pensacola Mountains and not the Shackleton Range (Fig. 1.3), which would be consistent with interpretation by Hein et al. (2011), as there was no ice thickening in the Shackleton Range.
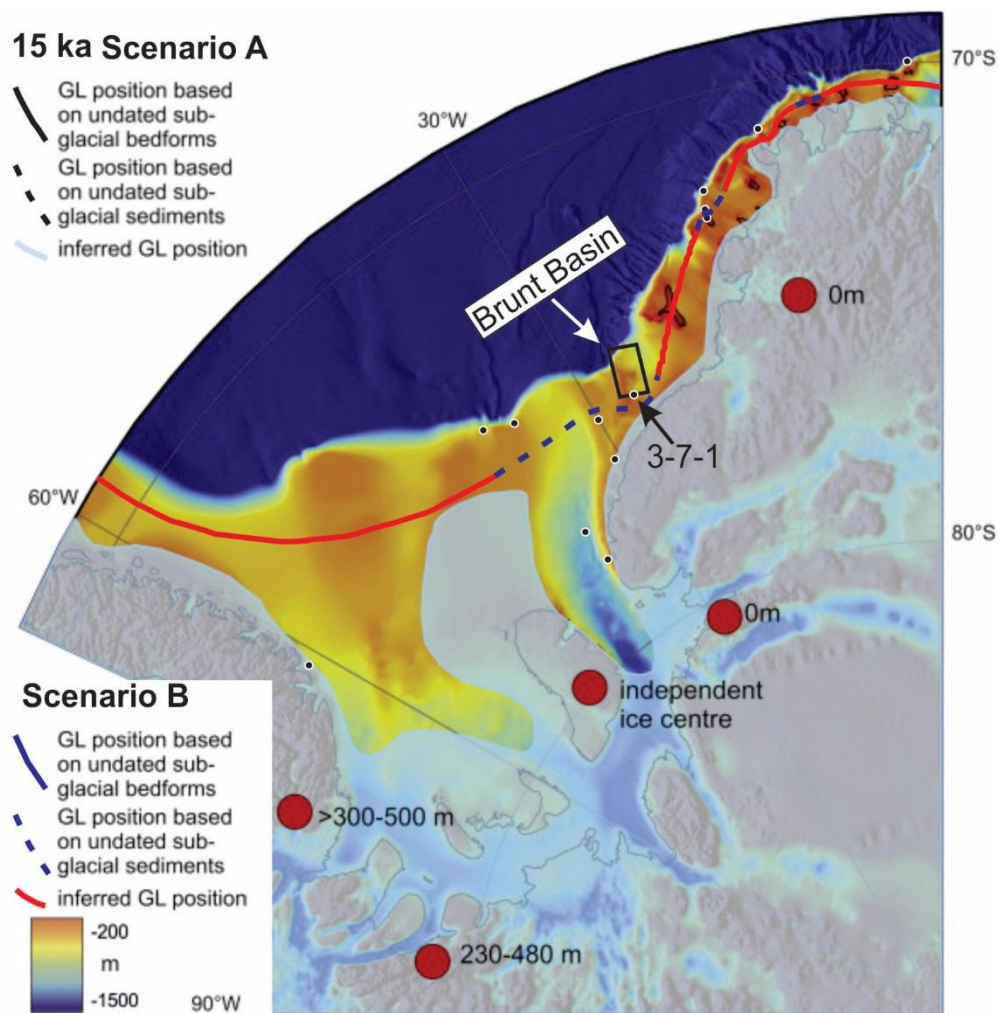
Fig. 1.6. Grounded ice sheet extent according to Scenario A and B in the Weddell Sea sector at 15 ka. The different certainty levels given for the grounding line (GL) are indicated. The black circles show different core locations used for reconstructing the grounding line, and the red circles indicate ice sheet elevation at different locations. The location of core 3-7-1 is indicated with the arrow. The location of the Brunt Basin is indicated with the black box. Modified from Hillenbrand et al. (2014).

The deglaciation history has also been assessed in the two scenarios, where deglaciation started around ~20 and ~25 cal. ka BP for scenario A and B, respectively (Hillenbrand et al., 2014). The retreat rate is much faster for scenario A than for B. The grounding line had reached close to its present grounding line position on the eastern Weddell Sea at ~15 cal. ka BP in scenario A. Scenario B suggest a minor re-advance or pause in the retreat at ~15 cal. ka BP, based on a grounding zone wedge (GZW) in the outer most part of the Flichner Trough (Fig. 1.3), reported by Larter et al. (2012). Grounded ice was located at the outer or mid shelf at most locations.
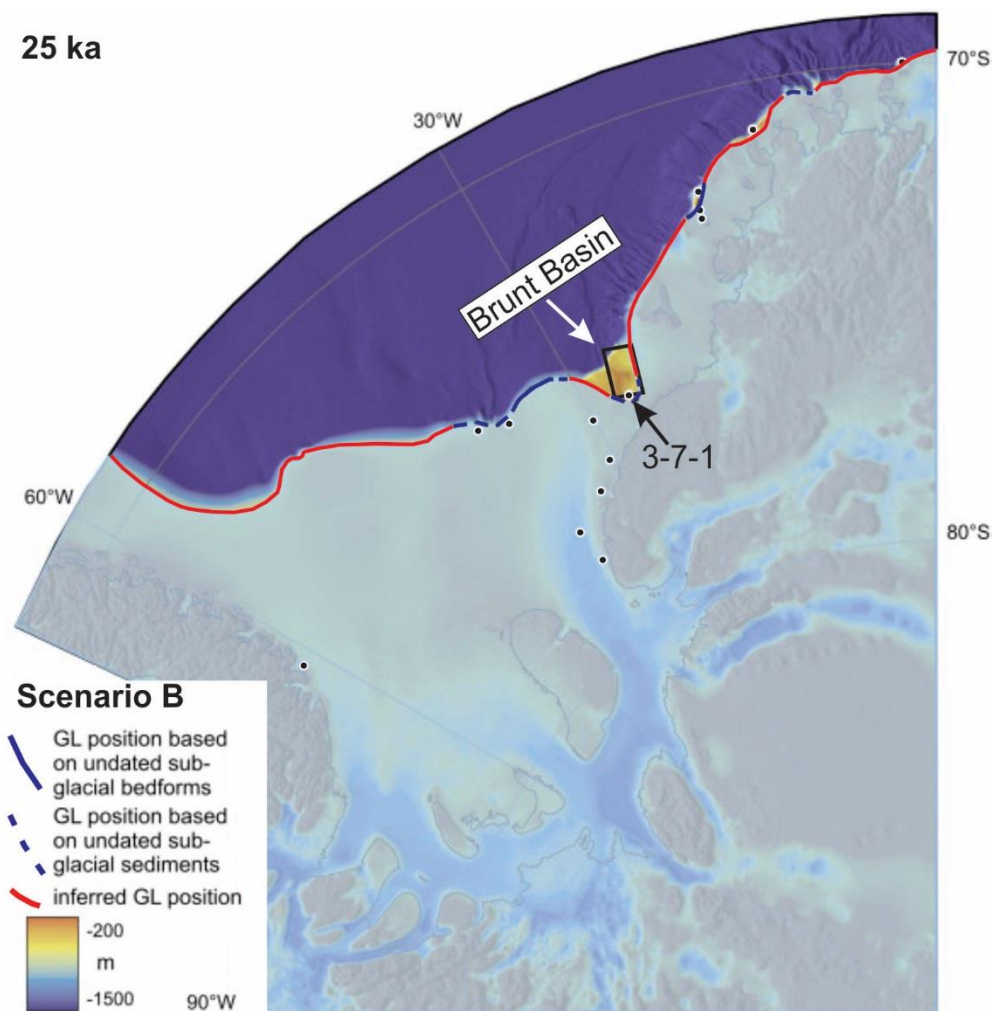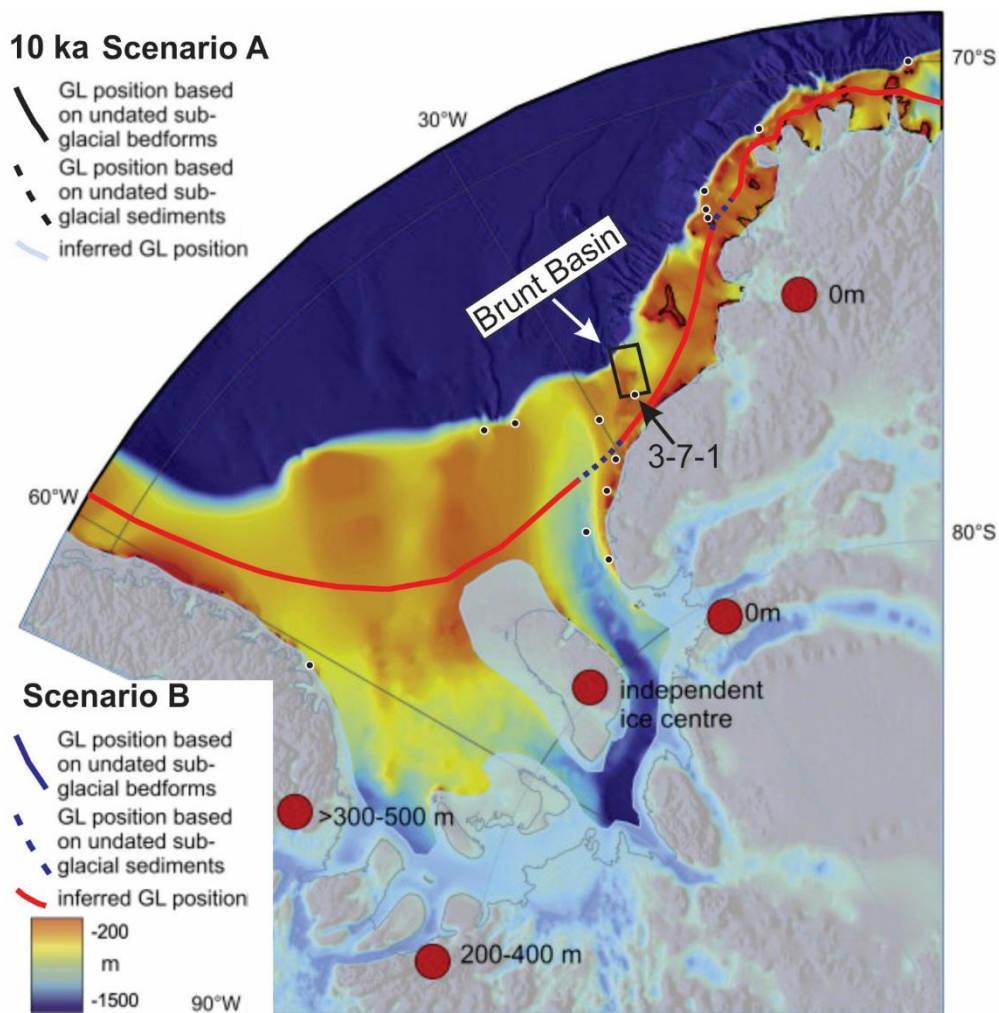

Fig. 1. 7. Grounded ice sheet extent according to Scenario A and B in the Weddell Sea sector at 10 ka. The different certainty levels given for the grounding line (GL) are indicated. The black circles show different core locations used for reconstructing the grounding line, and the red circles indicates ice sheet elevation at different locations. The location of core 3-7-1 is indicated with the arrow. The location of the Brunt Basin is indicated with the black box. Modified from Hillenbrand et al. (2014).

At ~10 cal. ka BP, the grounding line in scenario A had retreated to the inner shelf everywhere, except immediately north of the Berkner Island (Fig. 1. 7). In scenario B the grounding line had retreated from the outer shelf in all locations (Hillenbrand et al., 2014).

At ~5 ka the grounding line had retreated close to or at its present-day grounding line for scenario A, whereas the grounding line for scenario B reached out to the present day calving line of Flichner –Ronne Ice shelf (Fig. 1.3; Fig. 1.8; Hillenbrand et al., 2014).
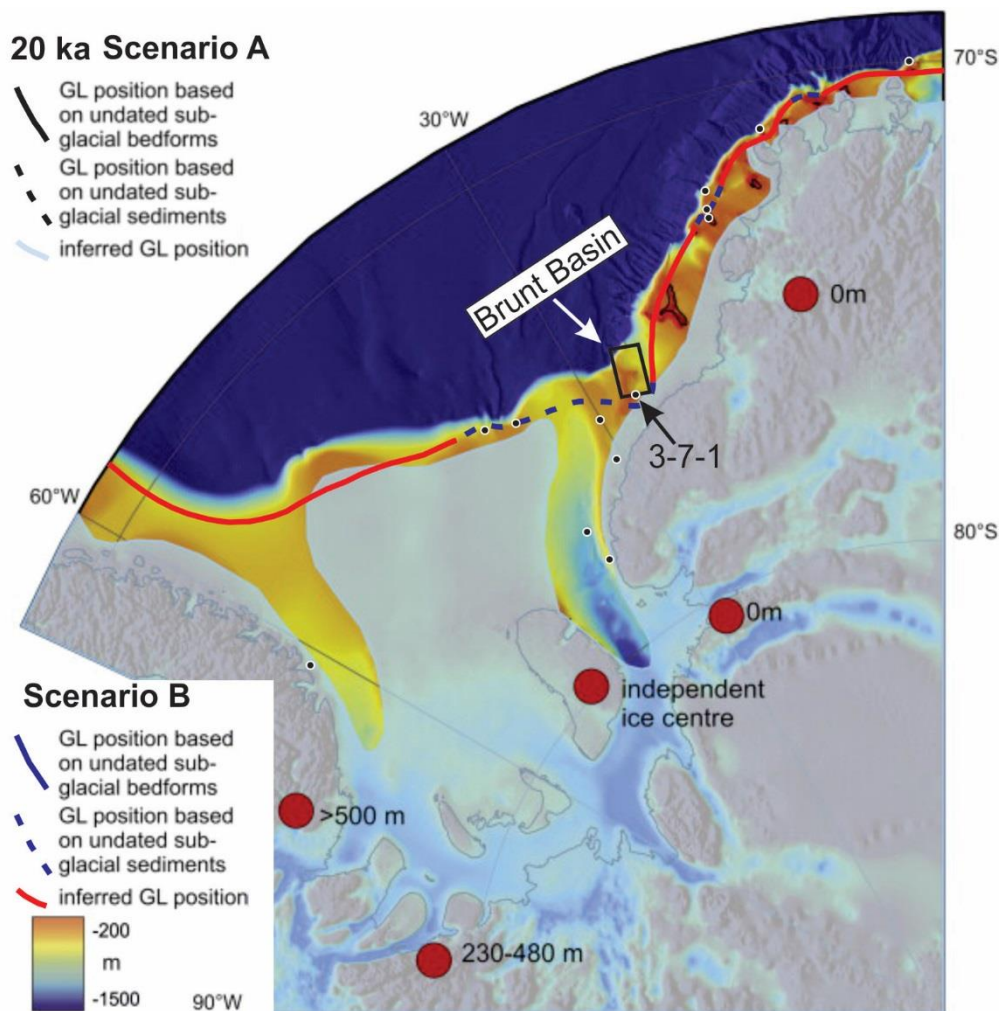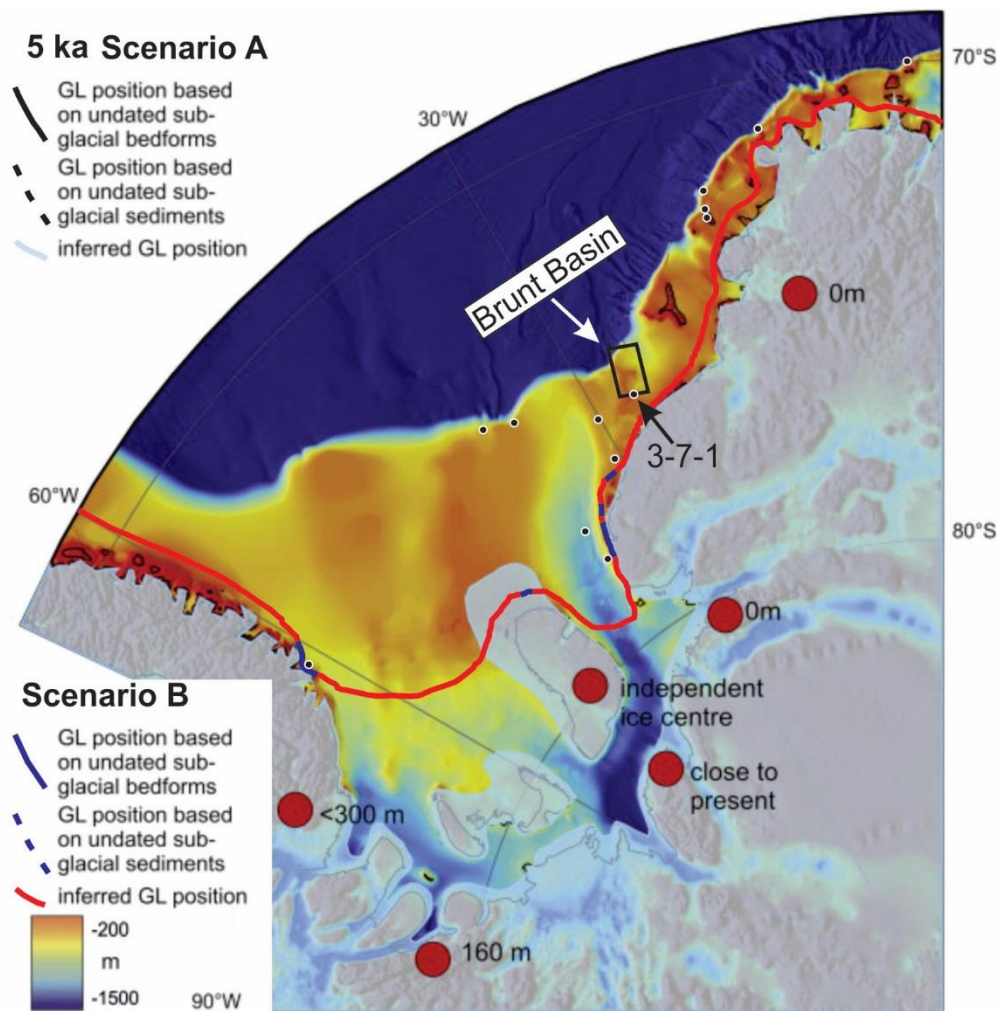

Fig. 1.8. Grounded ice sheet extent according to Scenario A and B in the Weddell Sea sector at 5 ka. The different certainty levels given for the grounding line (GL) are indicated. The black circles show different core locations used for reconstructing the grounding line, and the red circles indicates ice sheet elevation at different locations. The location of core 3-7-1 is indicated with the arrow. The location of the Brunt Basin is indicated with the black box. Modified from Hillenbrand et al. (2014).

1.3.2 Brunt Basin

In the scenarios suggested by Hillenbrand et al. (2014), ice did not advance onto the shelf at the location of the Brunt Basin in scenario A, or had retreated before ~25 cal. ka BP in scenario B. This was based on ^{14}C ages obtained from core 3-7-1, on the bank west of the Brunt Basin (e.g. Fig. 1.4), originally presented by Anderson et al. (1980). The core 3-7-1 was originally interpreted to be composed of glaciomarine sediments. ^{14}C ages from benthic foraminifera provided inverse down-core ages (Table 1.1), of 26.666 and 13.640 uncorrected ^{14}C years (Smith and Licht, 2000), which were incorrectly reported in an correct stratigraphic order by Bentley and Anderson (1998) and Anderson and Andrews (1999).

Stolldorf et al. (2012) re-examined core 3-7-1, using detailed grain-size analyses and obtaining several more ^{14}C ages (Table 1.1). This lead to a reinterpretation of the sediments at the base of core 3-7-1, to be subglacial till. The ^{14}C ages obtained by Stolldorf et al. (2012) were also not in chronological order (Table 1.1), indicating that the sediments were reworked either by iceberg scouring or current winnowing (Hillenbrand et al., 2014). However, the authors suggest that grounded ice had retreated from the eastern shelf of the Weddell Sea, which includes the Brunt Basin before ~33 calibrated years before present (cal. yr BP), based on non-pronounced hiatus in the ^{14}C ages (Stolldorf et al., 2012).

According to the scenarios suggested by Hillenbrand et al. (2014), no major thickening occurred in the EAIS (Fig. 1.5), which is the source area of the Brunt Ice Shelf System (Fig. 1.1; Fig. 2.1; Hulbe et al., 2005). This was based on geomorphic mapping (Hättestrand and Johansen, 2005), ^{14}C ages obtained from mumiyo samples (Thor and Low, 2011) and surface exposure dating (Hein et al., 2011).

Table 1.1.
Uncorrected ^{14}C ages from core 3-7-1 recovered close to the study area. References : a) Stolldorf et al., 2012, b) Anderson and Andrews, 1999, c) Smith and Licht, 2000.

Core	Laboratory code	Water depth (m)	Sample interval (cm)	Material dated	^{14}C yr BP.	References
3-7-1	87463	235	70-70	Echinoid	>52.800	a
3-7-1	AA-27756	235	200-200	Benthic	26.660	b, c
3-7-1	95860	235	223-227	Benthic	28.930	a
3-7-1	96164	235	223-227	Benthic	30.740	a
3-7-1	96250	235	223-227	Benthic	29.490	a
3-7-1	95861	235	304-308	Benthic	17.980	a
3-7-1	96165	235	304-308	Benthic	13.315	a
3-7-1	96251	235	304-308	Benthic	15.330	a
3-7-1	96262	235	304-308	Benthic	14.655	a
3-7-1	96263	235	304-308	Benthic	14.970	a
3-7-1	95862	235	348-352	Benthic	16.610	a
3-7-1	96166	235	348-352	Benthic	18.820	a
3-7-1	96252	235	348-352	Benthic	19.400	a
3-7-1	AA-27757	235	400-400	Benthic	13.640	b, c

2 Study area

2.1 Physiographical Setting

The Antarctic continent is the southernmost continent on the Earth, located over the South Pole. Most of the continent is located south of the Antarctic Circle (66º 34' S), except the northernmost part of the Antarctic Peninsula. It covers an area larger than 14 million km^2, making it the fifth largest continent, with a coastline of ~17,968 km, surrounded by Southern Ocean (Anderson, 1999). The Antarctic continent can be divided into three major areas, the Antarctic Peninsula, the West Antarctica and the East Antarctica, each area covered by "its own" ice sheet (Fig. 1.1).

The Brunt Basin (~26ºW, ~75ºS) is located in the southeastern Weddell Sea, seawards of the Coats Land (Fig. 1.3 and Fig. 2.1). It is a depression in the seafloor north of the Brunt Ice shelf and west of the Stancombe-Wills Ice Tongue, which are ice shelves situated seawards from the Caird Coast. To the west of the Brunt Basin, a shallower unnamed bank separates the Brunt Bain from the Halley Through (Gales et al., 2014). The Lyddan Island and the Risser-Larsen Ice Shelf is located northeast of the Brunt Basin. The British Antarctic Survey (BAS) research station Halley VI (Fig. 2.1) is located on the Brunt Ice Shelf (Anderson et al., 2014b).

2.2 Brunt Ice Shelf System

The Brunt Ice Shelf and the Stancombe-Wills Ice Tongue occupies the ocean south and east of the study area, in the Brunt Basin (Fig. 2.1), also referred to as the Brunt Ice Shelf System, but there is large variation within the literature regarding the names (e.g. Thomas, 1973; Wuite and Jezek, 2009; Anderson et al., 2014b). Together they form a continues body of floating ice, which contains three different moving units (e.g. Thomas, 1973; Anderson et al., 2014b).

The eastern sector is occupied by the fast moving Stancombe-Wills Ice Tongue (Fig. 2.3), extending more than 225 km beyond its grounding line (Wuite and Jezek, 2009). It is fed by the fast flowing Stancombe-Wills Glacier (Fig. 2.2) that drains the area of Heimfrontfjella (Thomas, 1973; Hulbe et al., 2005) , the westernmost part of the Maudheimvidda (Fig. 1.3). The Lyddan Island and the Risser-Larsen Ice Shelf confine the eastern margin of the Stancombe-Wills Ice Tongue (Hulbe et al., 2005). However, within the literature the name of the ice feeding the Stancomb-Wills Ice Tongue, differ between Stancomb-Wills Glacier (Rignot, 2002; Hulbe et al., 2005; Wuite and Jezek, 2009), and Stancomb-Wills Ice Stream (Simmons and Rouse, 1984; Humbert et al., 2009; Khazendar et al., 2009).

The slower moving Brunt Ice Shelf (Fig. 2.2) occupies the western region, and is fed by slow flowing ice from the Caird Coast. Wedges of calved meteoric ice in a mélange of marine ice are located near the

grounding line, where the space between the calved blocks are later filled with wind-blown snow as the ice flows northward (Hulbe et al., 2005). Where the Brunt Ice Shelf terminates in the north, a zone of the ice shelf is grounded on several pining points, called the McDonald Ice Rumples (Fig. 2.1), which provides backstress to this region and produces compression ridges in the ice shelf (Thomas, 1973;
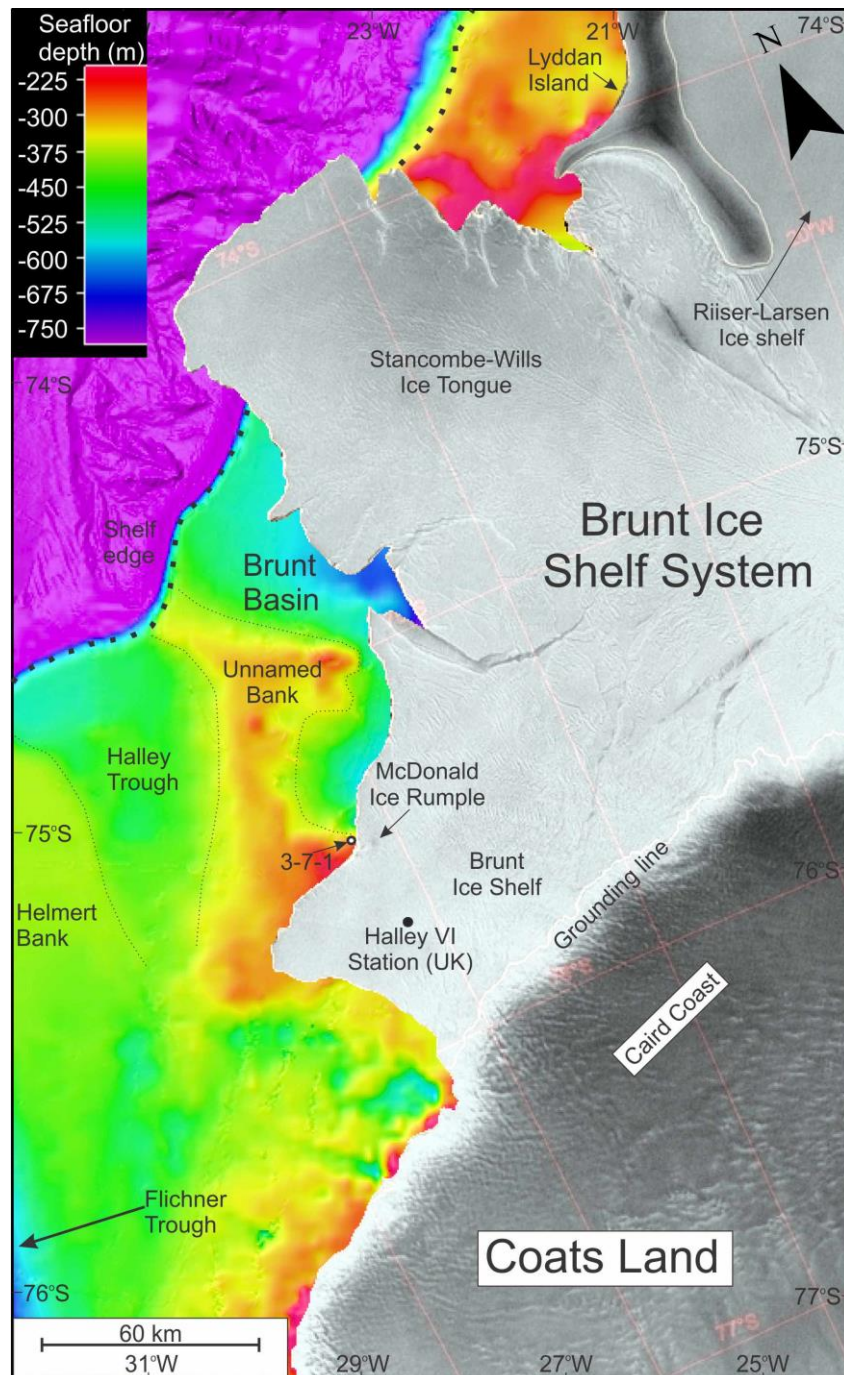
Fig. 2.1. Overview map of the Brunt Basin region with the shelf bathymetry according to the IBCSO Version 1.0 (Arndt et al., 2013) with an Envisat synthetic aperture radar image of the Brunt Ice Shelf System from 4th March 2011. The dark areas in the Envisat synthetic aperture radar marks the position of grounded ice. Also note the location of core 3-7-1. The location this figure is indicated in e.g. Fig. 1.3

Anderson et al., 2014b). In the middle, between the Stancomb-Wills Ice Tongue and Brunt Ice Shelf (Fig. 2.2), there is a shear zone of large ice rafts in a mélange of marine ice covered with snow (Hulbe et al., 2005; Wuite and Jezek, 2009).

Both the Brunt Ice Shelf and the Stancomb-Wills Ice Tongue have a slightly positive mass balance (King et al., 1996; Rignot, 2002), dominated by basal freeze-on of ice (Rignot, 2002), and the mass loss is predominantly caused by calving ice (Depoorter et al., 2013).

Anderson et al. (2014b) suggested that both the Brunt Ice Shelf and the Stancomb-Wills Ice Tongue have gone through significant calving events in recent time, based on historical records of the ice-front position. With the last known large scale calving event occurring in 1971 (Thomas, 1973). Due to location of the BAS research station Halley, large cracks and rifts in the ice shelves are continuously being monitored, and in the same study Anderson et al. (2014b) argued that the Stancomb-Wills Ice Tongue will experience a large scale calving event within 2020.
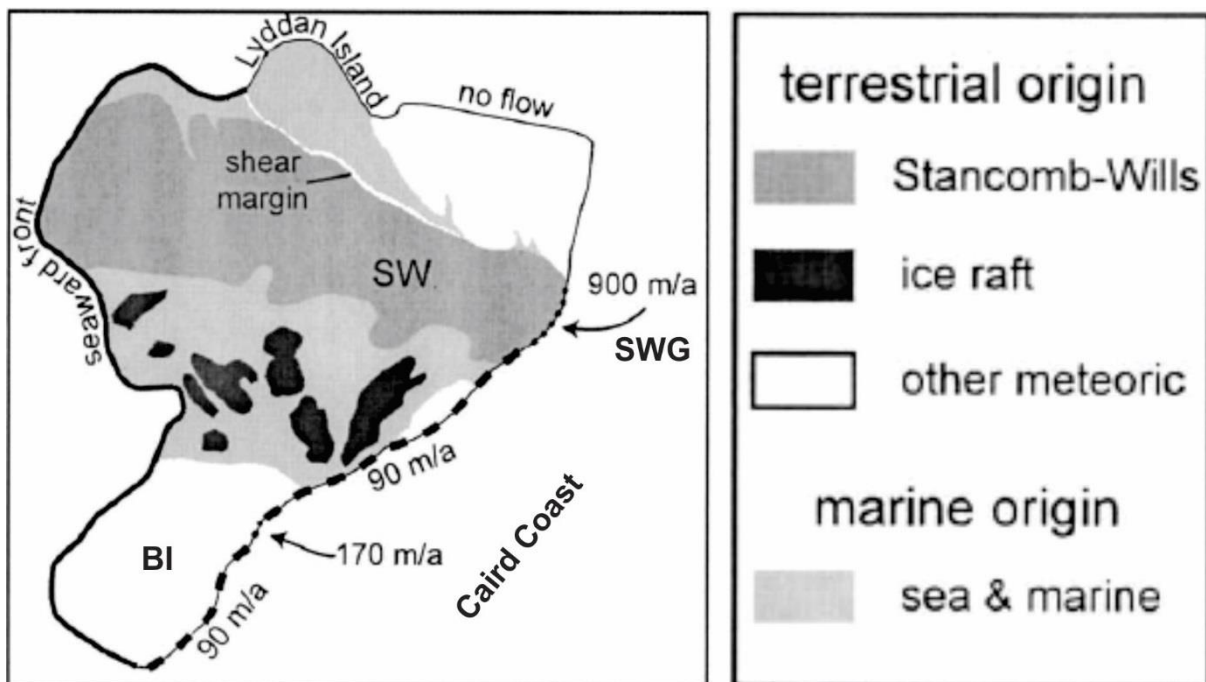
Fig. 2.2. Classified ice type of the Brunt Ice Shelf System, from Hulbe et al. (2005), with the inflow velocity of ice feeding the ice shelf. The dotted line marks the grounding line. The legend at the right describes the classified types of ice, where terrestrial ice is derived from land, and marine ice is formed at or near the sea surface. SW-Stancombe-Wills Ice Tongue, BI-Brunt Ice Shelf, SWG- Stancombe-Wills Glacier.
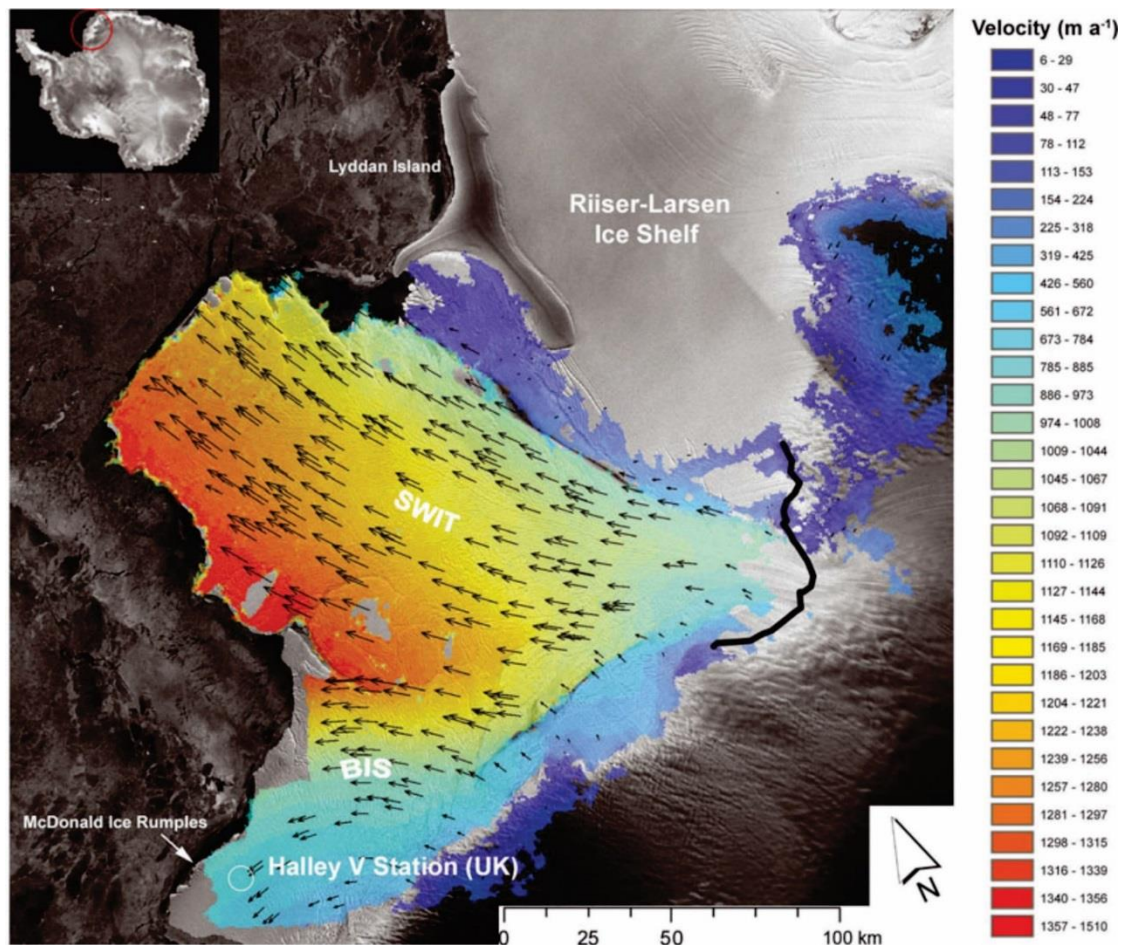
Fig. 2.3. Ice-flow velocity on the Brunt Ice Shelf System. The velocity field is derived from feature tracking, on RADARSAT-1 images from 1997 to 2000, representing a 3 years average. The arrows show the direction of flow, and the colors indicate the velocity of the flow. The black solid line indicates the approximate grounding line position. Note that the Stancombe-Wills Ice Tongue (SWIT) reaches up to 1350 meter per year in velocity, whereas the Brunt Ice Shelf (BIS) has much slower velocity. From Wuite and Jezek (2009).

2.3 Sea Ice

The Antarctic sea ice conditions differ from the sea ice conditions in the Arctic in several ways (Turner and Overland, 2009). The main difference is that sea ice in the Arctic is semi-enclosed by surrounding land, whereas Antarctic sea ice has no boundary to the north and is free to float northwards to warmer waters (Fig. 2.4). This leads to large seasonal variation in the Antarctic sea ice extent. With extensive sea ice growth during winter (September), with an average extent of 18.5 million km^2, which almost completely melts away during summer (February), with an average extent of 3.1 million km^2 (Parkinson and Cavalieri, 2012; Li et al., 2016).

In contrast to Arctic sea ice, the Antarctic sea ice is currently showing an overall increasing trend with a record extent in 2014 exceeding 20 million km^2 (National Snow and Ice Data Center, 2014). The reason for this overall increase in sea ice extent is still unclear (Sigmond and Fyfe, 2010), but can at least partly be explained by two processes. Freshening of the ocean surface by increased precipitation and basal

melt of ice shelves (Zhang, 2007; Bintanja et al., 2013) and decreasing levels of ozone in the stratosphere, which leads to stratospheric cooling and increasing winds (Gillett and Thompson, 2003; Shindell and Schmidt, 2004; Turner et al., 2009). However, the ozone concentration above Antarctica are expected to recover within the next 100 years, and if the concentration of greenhouse gas continues to increase with similar rates as today, temperatures on the Antarctic continent are projected to increase by serval degrees, which will lead to a reduction of the sea ice extent to about one third of the present extent (Turner et al., 2014).
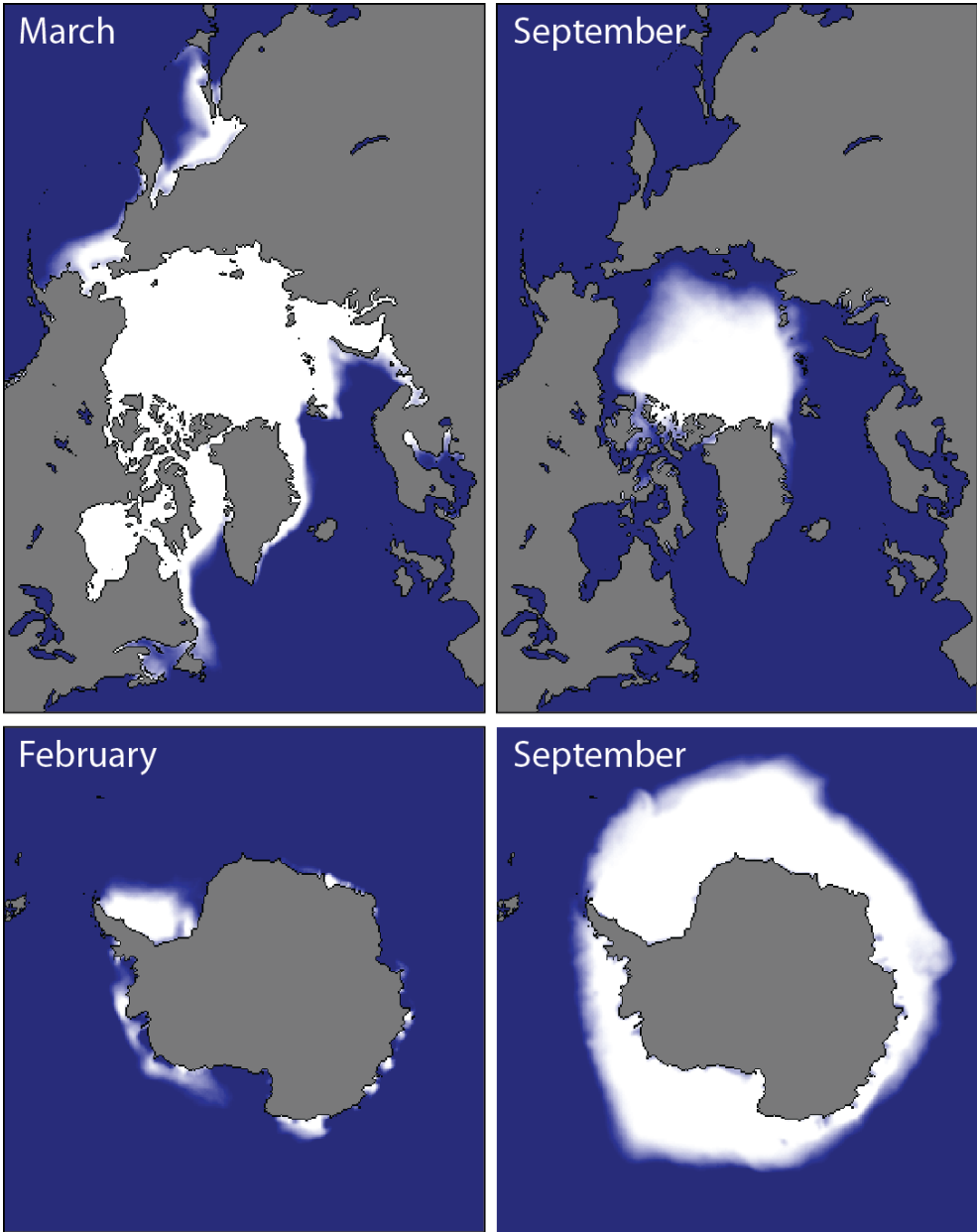
Fig. 2.4. Arctic (Above) and Antarctic (below) average sea ice extent from 1981-2010, at the approximate seasonal maximum and minimum extent. From National Snow and Ice Data Center, 2016.

2.4 Geomorphology of glaciated continental shelves

High latitude continental shelves modified by successive glaciations have a characteristic morphology (Fig. 2.5). This includes large scale morphological features such as banks and troughs, and smaller scale features such as moraines, glacial lineations and iceberg scours, reflecting glacial processes during the last glaciation and the deglaciation (Vorren, 2003). During glaciations, troughs have been eroded and acted as pathways for fast flowing ice stream, draining the interior of the ice sheets (e.g. Vorren and Laberg, 1997; Anderson, 1999; Ó Cofaigh et al., 2002; Livingstone et al., 2012). These palaeo-ice streams can leave distinct imprints on the seafloor, such as mega-scale glacial lineations (MSGL) (Clark, 1993). Grounding zone wedges (GZW) and marginal-moraines marking the position of grounded ice commonly occur in the troughs (Ship et al., 1999; Dowdeswell et al., 2008; Larter et al., 2012; Rydningen et al., 2013; Batchelor and Dowdeswell, 2015). The shallower banks are often characterized by iceberg scours and marginal moraines, but typically lack glacial landforms indicative of fast flowing ice, indicating slower flowing ice (e.g. Ottesen and Dowdeswell, 2009; Klages et al., 2013; Rydningen et al., 2013).

The Antarctic continental shelf is an end member of the high latitude continental shelves, with deeper troughs and a general inclined slope towards the continent (Anderson, 1999), which differ from other high latitude continental shelves, which generally slopes towards the shelf edge. This difference is
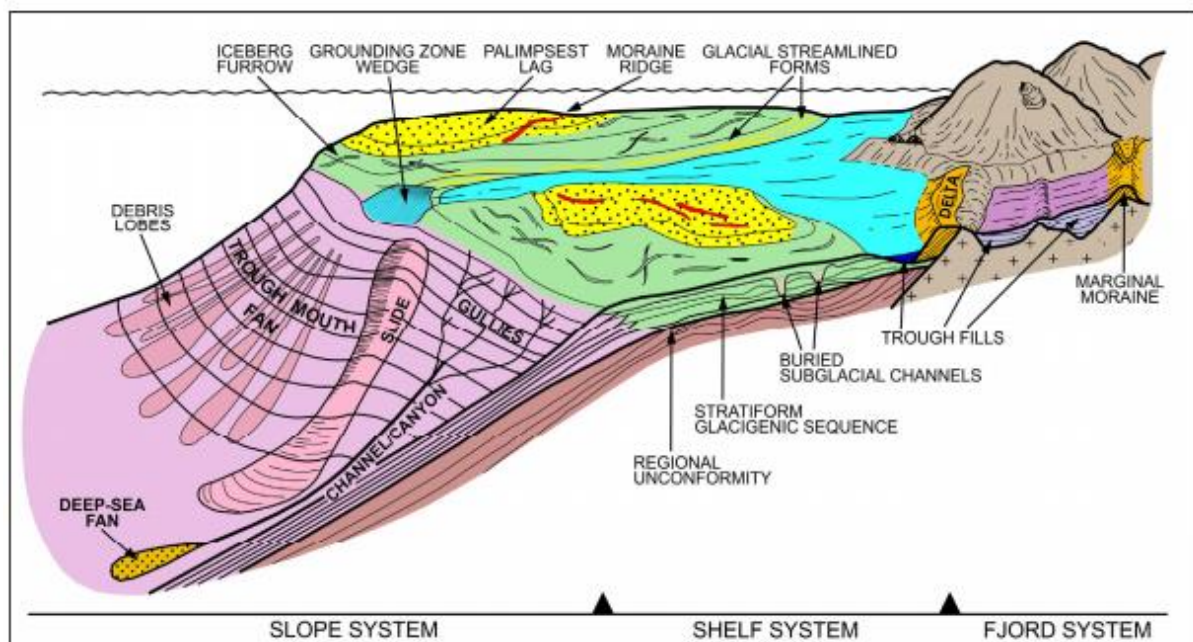
Fig. 2.5. Model showing the main glacigenic morphological elements and lithofacies of a passive glaciated continental margin, exemplified by the margin off northern Norway. Modified by Rydningen (2014), from Vorren (2003).

presumably because the Antarctic continental shelf has been glaciated since 34 Ma and exhibit a more mature glacial morphology (Ten Brink et al., 1995; Uri and Schneider, 1995; Zachos et al., 1996; Bohaty et al., 2012).

2.4.1 Morphology in the Weddell Sea

The continental shelf in the southern Weddell Sea north of the Ronne and Flichner ice shelves (Fig. 1.3) is ~450 km wide and is generally ~400-500 m deep (Arndt et al., 2013). In eastern part of the Weddell Sea (~25ºW to 0ºW) the distance between the shelf edge and the ice-shelf varies between 0-80 km and the water depths are generally between 300 and 400m (Hillenbrand et al., 2014). Three major troughs extend from the Ronne and Flichner ice shelves to the shelf edge, the Flichner Trough, Hughes Trough and Ronne Trough, with water depths up to 1200 m near the ice front in the Flichner Trough (Fig. 1.3; Stolldorf et al., 2012; Larter et al., 2012). Subglacial topography shows that the three troughs are northward extensions of subglacial troughs that get deeper towards the interior beneath the WAIS and EAIS (see Fig. 1.8; Ross et al., 2012; Fretwell et al., 2013; Hillenbrand et al., 2014).
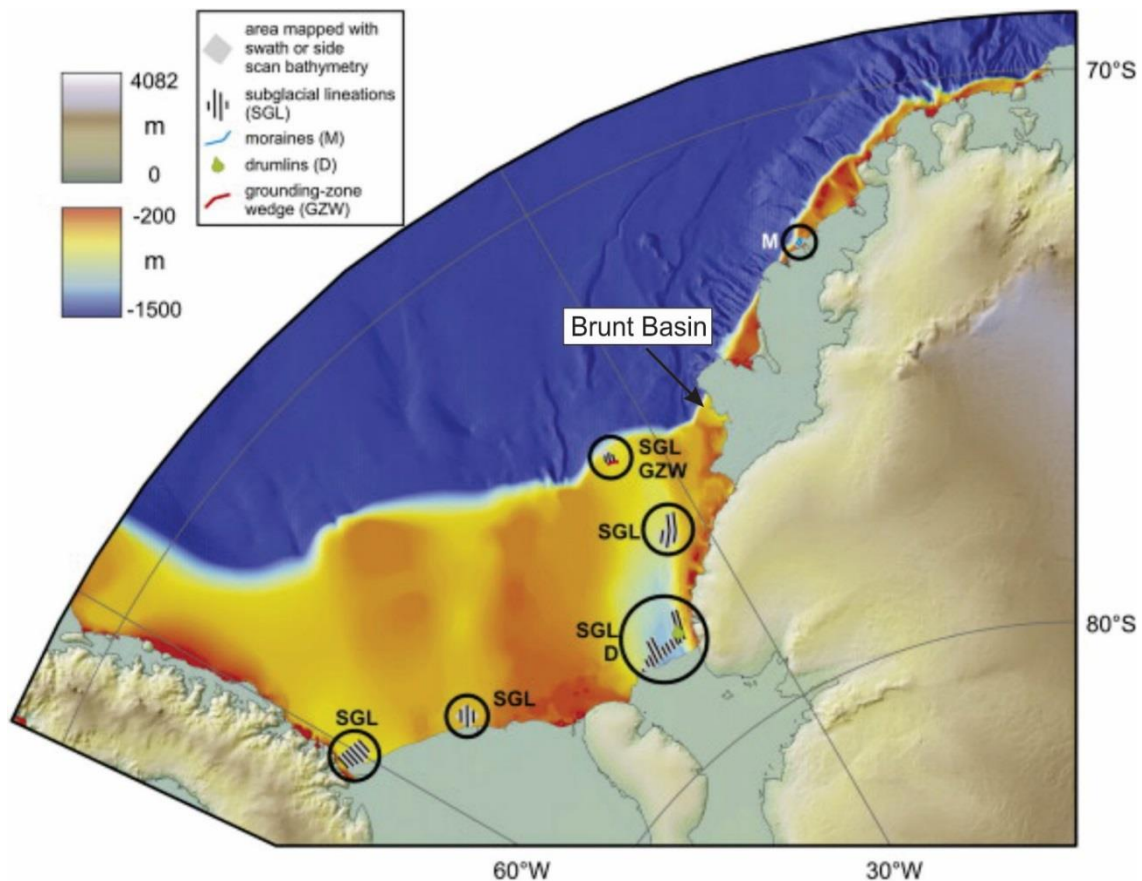
Fig. 2.6. Location of subglacial landforms in the Weddell Sea sector mapped by high-resolution bathymetry. The location of the Brunt Basin is indicated by the arrow and the circles highlight the areas for which data have been published by Kristoffersen et al. (2000b), Larter et al. (2012) and Stolldorf et al. (2012). Modified from Hillenbrand et al. (2014).

Glacial lineations are reported from all the three troughs mentioned above, and a GZW has been reported from close to the shelf edge in the Flichner Trough (Fig. 2.6; Larter et al., 2012; Stolldorf et al., 2012). The only glacial landforms reported from the eastern Weddell Sea are two moraines parallel to the shelf edge, outside the Risser-Larsen Ice Shelf (Fig. 2.6; Kristoffersen et al., 2000b).

2.5 Sediment sequence on glaciated continental shelves

Sediments deposited on glaciated continental shelves differ from sediments deposited on low latitude, non-glaciated shelves (Zecchin et al., 2015). Glacial processes influence the depositional environment and are recorded in the sediment sequences (Vorren et al., 1983a; Anderson, 1999). Analyses of the sedimentary sequences and the related facies can be used to reconstruct the depositional environments and changes through time, e.g. glacial -interglacial cycles (e.g. Butt et al., 2000; Fielding et al., 2000; Hillenbrand and Fütterer, 2001; McKay et al., 2009).

A sedimentary sequence on high latitude shelves that represent the transition from the LGM to the Holocene includes all or some of the following in the successive order: (i) Ice contact sediments overlain by (ii) glaciomarine sediments, proximal to (iii) ice distal sediments, which again is overlain by (iv) paraglacial sediments and (v) post glacial sediments (Syvitski, 1991).

(i)   Ice contact sediments

Ice-contact sediments record the present of grounded ice, and sediment deposited by the ice can be till sheets, (mega-scale) glacial lineations, terminal-, lateral,- recessional moraines, GZW, subaquatic till deltas and glacigenic debris flow deposits which are mainly derived from subglacial sediments (Vorren et al., 1983a; Syvitski, 1991; Anderson, 1999; Hillenbrand et al., 2005; Zecchin et al., 2015). Ice contact sediments will generally have no to poor sorting, no stratification except for glaciofluvial deposits such as eskers (Boltunov, 1970). Sediments that have been ice-loaded are sediments that have been deposited prior to the overriding of grounded ice, and can obtain a abundant microfossil assemblage and structures such as stratification and lamination, dependent on the original deposition environment (Elverhøi, 1981; Syvitski, 1991; Elverhøi and Roaldset, 1983; Melles and Kuhn, 1993; Hillenbrand et al., 2012).

(ii)   Glaciomarine proximal sediments

Glaciomarine proximal sediments are deposited close to the grounding line. The proximity to the grounding line controls the influence of marine and glacial environment on the sediments. With less influence of marine environment closer to the grounding line, and vice versa (Domack et al., 1999; Licht et al., 1999; Hillenbrand et al., 2012; Smith et al., 2014). The glacial detritus may be deposited directly

from the ice front, or indirectly from the ice front by gravity flows, meltwater plumes, currents, sub-ice shelf melt-out and ice rafting, and are typically composed of coarse grained sediments, with alternations of stratification and lamination (e.g. Syvitski, 1991; Elverhøi et al., 1983; Domack et al., 1999). Glaciomarine sediments may be deposited between 0-100s km from the grounding line, depending on the size, dynamics and basal debris of the ice system (Licht et al., 1999; Syvitski, 1991).

(iii)   Glaciomarine distal sediments

Glaciomarine distal sediments have stronger influence of marine environment and less of the glacial environment (Syvitski, 1991). The sediments typically contain mud, which originates from suspended material from meltwater plumes, ocean currents and eolian transport, together with ice-rafted debris where the amounts are dependent on calving rate and the debris incorporated in the ice (e.g. Mackiewicz et al., 1984; Dowdeswell and Dowdeswell, 1989; Dowdeswell and Scourse, 1990). The ice distal sediments may include being close to the grounding line, if the ice is relative debris free, with no glacial melt water discharge, or hundreds of km from the ice front, if the ice is highly active and sediment rich (Syvitski, 1991).

(iv)   Paraglacial coastal sediments

Paraglacial coastal sediments are marine sediments deposited close to the coast with glaciofluvial origin and are deposited after the ice sheet has retreated to a terrestrial position. High ablation rates, leads to erosion by fluvial processes of glacial and proglacial deposits , and vast amount of sediments are transport from the terrestrial ice sheet to the coast (Syvitski, 1991).

(v)   Post glacial sediments

Post-glacial sediments are deposited without the influence of a distant ice sheet, and deposition is primarily from non-glacial processes, such as hemipelagic and current related sedimentation (Elverhøi, 1981; Camerlenghi et al., 2001; Zecchin et al., 2015; Rebesco et al., 2016). They typically have high amounts of organic content and microfossils, and can occur as mud in the deeper part of the shelf, or as sand and gravel lags in the shallower waters (Vorren et al., 1983a; 1989; Syvitski, 1991).

The troughs usually contain the thickest sedimentary sequences on the glaciated shelves which provides higher resolution for reconstructing palaeo-environment changes (Vorren et al., 1983a). The sediments in the troughs are also less vulnerable for reworking from current winnowing and iceberg scouring, but can be affected mass movement from the trough slopes (Vorren et al., 1983a; 1984). The sedimentary

sequences on the banks are thinner, due to cold based ice depositing thinner layers of till and stronger currents, which transports sediments from the banks to the deeper regions of the shelves (Vorren et al., 1984; Zecchin et al., 2015). Due to the shallow depth of most banks, they are prone to reworking by iceberg scouring and current winnowing, which makes the banks a poor target for investigating palaeo-environment changes (Vorren et al., 1984).

The Antarctic continental shelf is an end member concerning the other glaciated shelves and glacial marine environments, due to its vast amount of ice shelves, ice flow by internal creep, and polar climate which limits the melt water production (Syvitski, 1991; Elverhøi, 1984).

Cores retrieved from the Antarctic continental shelf generally show a three-folded stratigraphy, with bioturbated to massive, diatom-, or foraminifera bearing muds (open marine environment) at the top. Stratified to massive, sandy to gravelly sediments (sub-ice shelf/perennial sea ice cover environment) in the middle, and massive diamictons (subglacial environment) at the base (e.g. Domack et al., 1999; Dowdeswell et al., 2004; Evans et al., 2005; Hillenbrand et al., 2005; 2009; Smith et al., 2011; 2014). Subglacial till recovered from palaeo-ice stream troughs on the Antarctic continental shelf typically have low shear strength (e.g. Evans et al., 2005; Ó Cofaigh et al., 2005b; Reinardy et al., 2011a). However, iceberg turbated sediments, gravity-flow deposits, and ice-rafted sediments can also produce massive diamictons with low shear strength (e.g. Hillenbrand et al., 2005; 2009; 2010; Smith et al., 2011; 2014). This provides difficulties in separating between subglacial and glaciomarine sediments based on sedimentological parameters alone, and previous studies have emphasized that detailed swath bathymetry and sub-bottom profiles might be helpful in the interpretation of the depositional environments of the sediment (e.g. Domack and Harris, 1998; Anderson, 1999; Licht et al., 1999; Hillenbrand et al., 2005). This subglacial till with low shear strength, are commonly associated with subglacial deformation of soft sediments beneath ice streams (e.g. Evans et al., 2005; King et al., 2009; Reinardy et al., 2011a), and the name used within the literature varies (e.g. Anderson, 1999; Evans et al., 2005; Ó Cofaigh et al., 2005b; Hillenbrand et al., 2010; 2012). In this study soft deformation till will be used (cf. Hillenbrand et al., 2012).

2.5.1 Sediments in the Weddell Sea

The Weddell Sea is dominated by terrigenous sediments, predominantly deposited in subglacial and glaciomarine environments, with spars amounts of biogenic content (Hillenbrand et al., 2012). Anderson (1972) provided the first evidence of grounded ice on the Weddell Sea shelf, from sediment cores recovering subglacial tills. Glaciomarine sediments of various character and thickness typically overlie the subglacial tills (e.g. Anderson et al., 1980; Elverhøi, 1981; Elverhøi and Roaldset, 1983; Hillenbrand et al., 2012). Recently, Hillenbrand et al. (2012) re-investigated several sediment cores recovered in the

southern Weddell Sea. Based on the sedimentological properties of the sediments, the authors assigned a deposition environment for the different types of sediments recovered in the cores from the southern Weddell Sea shelf (Table 2.1).

3.5 kHz sub-bottom acoustic profiles for the southern Weddell Sea in the Flichner Trough and the Ronne Trough shows thick acoustically transparent layers (Fig. 2.7), originally interpreted as glaciomarine sediments (Haase, 1986; Fütterer and Melles, 1990; Melles and Kuhn, 1993). Hillenbrand et al. (2012) suggested that the acoustically transparent layers could be soft deformation till deposited at the base of an ice stream (e.g. Ship et al., 1999; Evans et al., 2005; Ó Cofaigh et al., 2005a, , 2005b, , 2007; Reinardy et al., 2011a, , 2011b), based on the similarities to soft deformation till layers reported from other areas on the Antarctic shelf. The glaciomarine sediments overlain the subglacial tills in eastern Weddell Sea shelf, east of the Flichner Trough (Fig. 1.3) are composed of coarse-grained sediments, dominated by iceberg rafted sediments (Anderson et al., 1980; Elverhøi and Roaldset, 1983; Elverhøi, 1984). Sponge spicules and bryozoan dominates the biogenic deposition (Elverhøi and Roaldset, 1983; Elverhøi, 1984). Seismic profile lines from the eastern Weddell Sea extending from the Brunt Ice Shelf to the Riiser-Larsen show a thin sediment drape above an unconformity, which is suggested to indicate repeated cycles of glacial advances across the continental shelf during the Quaternary (Elverhøi, 1984).

Table 2.1.
Facies interpretation of the different sediment types recovered in cores from the southern Weddell Sea shelf. From Hillenbrand et al. (2012).

Lithology	Sedimentary structures	Key sedimentological properties	Additional comments	Facies interpretation
Muddy to sandy sediment, variable gravel content	Massive, slightly to strongly bioturbated, slightly to moderately stratified or laminated	Medium to high water content and porosity, low shear strength and density, medium to high microfossil content, moderately to well sorted, moderate to high variability of parameters		Glaciomarine deposition (GM) under seasonal sea-ice coverage (si)
Muddy to sandy sediment, low to moderate gravel content	Massive, slightly to well stratified or laminated, slightly to moderately bioturbated	Medium to high water content and porosity, low to medium shear strength and density, low microfossil content, moderately to well sorted, low to moderate variability of parameters		Glaciomarine deposition (GM) under permanent sea-ice coverage or in a distal sub-ice shelf setting (pi)
Muddy to sandy diamicton, high gravel content	Massive, slightly stratified or laminated	Highly compacted, low to medium water content and porosity, high shear strength and density, low to moderate microfossil content, poorly to moderately sorted, low variability of parameters	Previously classified as "paratill"	Iceberg turbate (IT)
Muddy to sandy diamicton, moderate to high gravel content	Massive, slightly to moderately stratified or laminated, variable degree of bioturbation	Low to medium water content and porosity, variable density, low to moderate microfossil content, poorly to moderately sorted	Previously classified as "paratill"	Calving-line sediment (CLS)
Muddy to sandy sediment, muddy to sandy diamicton, moderate to high gravel content	Massive, slightly to well stratified or laminated, slightly bioturbated	Low to medium water content and porosity, variable shear strength, medium to high density, low microfossil content, poorly to moderately sorted, low to medium variability of parameters	Previously classified as "paratill"	Proximal sub-ice shelf sediment (SIS)
Muddy to sandy diamicton, moderate to high gravel content	Massive, slightly bioturbated (only at the top)	Highly compacted, low water content and porosity, high shear strength and density, absence or very low content of microfossils, poorly sorted, low variability of parameters	Previously classified as "orthotill"	Subglacial till (ST)
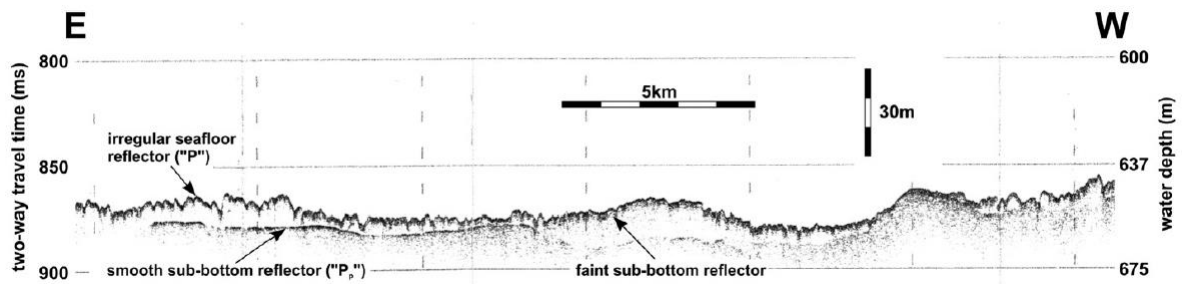
Fig. 2.7. 3.5 kHz sub-bottom acoustic profile from Ronne Trough (for location of the line see Fig.1 in Hillenbrand et al. (2012)). Two-way travel times are converted into water depths using seawater sound velocity of 1500 m/s. From Hillenbrand et al. (2012).

2.6 Oceanography

2.6.1 The southern Ocean

The Southern Ocean (Fig. 2.8) encircles the Antarctic continent and extends to c. 60° south. The 60° boundary was placed by the International Hydrographic Organization in year 2000, but both the boundary and the existence of the Southern Ocean is being debated by geographers (Rosenberg, 2016). Some argue that the waters around Antarctica only are an extension of the Atlantic, Indian and Pacific Ocean, whereas oceanographers argue that, the waters around Antarctica are a distinct body of water and differ from its bordering seas and puts the boarder at the northern limit of the Sub-Antarctic front (Fig. 2.9). In this thesis, the water masses around Antarctica are referred to as the Southern Ocean.
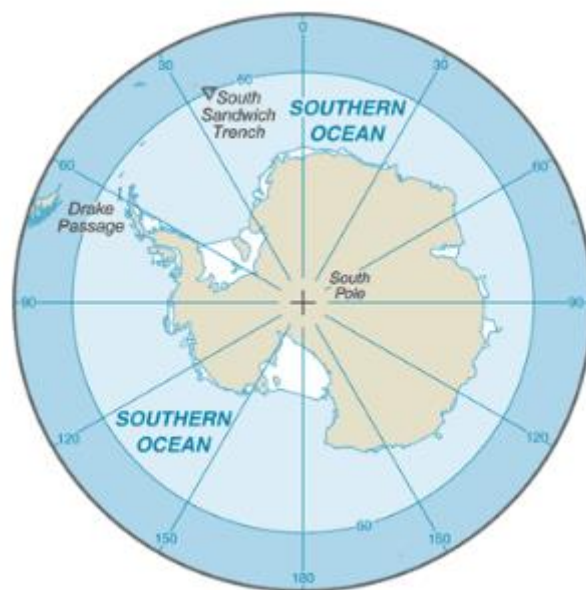
Fig. 2.8. The Southern Ocean. From The World Factbook (2014)

The main feature of the Southern Ocean in terms of circulation is the Antarctic Circumpolar Current (ACC), formed after the opening and deepening of the Drake Passage (Fig. 2.8) and the Tasman-Antarctic gateway, located south of Tasmania (Fig. 2.9). The onset of the ACC in terms of age is not clear, but it has previously been linked to the formation of full development of Antarctic continental glaciation at the start of Eocene –Oligocene boundary, ~34 Ma (e.g. Kennett, 1977; Lawver et al., 1992). However, other studies argue that the ACC as we know it today, initiated long after the Eocene-Obligocene boundary (Barker and Thomas, 2004; Barker et al., 2007). Pfuhl and McCave (2005), puts the onset of ACC at the boundary of Oligocene-Miocene (~23.95 Ma), and links it to the Miocene-1 glacial event.

The Southern Ocean circulation plays a key role in the global thermohaline circulation (Rahmstorf, 2002), and any changes in the Southern Ocean circulation pattern can alter the global ocean circulation and climate (Carter et al., 2009). Interaction between the water masses in the ACC and Antarctic Ice Sheet produces the densest (> 28.27 kg/m3) and coldest water masses (-1.7oC) involved in the global thermohaline circulation, the Antarctic Bottom Water (AABW)(Orsi et al., 1999). Subpolar Gyres (Fig. 2.9) south of the ACC are the regions where production of AABW occurs (e.g. Weddell Sea, Ross Sea and Wilkes Land). The Weddell Sea region is a major source of AABW, and contributes to 50-70% of AABW formation (Nicholls et al., 2009a) and, hence, is crucial for the global thermohaline circulation (Rahmstorf, 2002).

2.6.2 The Antarctic Circumpolar Current (ACC)

The ACC is a wind-driven current, which flows clockwise around the Antarctic continent, and connects the Pacific, the Atlantic, the Indian and the Southern Oceans (Fig. 2.9). The ACC extends vertically all the way to the ocean floor in most places (Barker and Thomas, 2004), and has a total length of 24,000 km (Olbers et al., 2004). Cunningham et al. (2003) measured the absolute average yearlong transport through the Drake Passage (Fig. 2.8) of the ACC to be 134 ± 11.2 Sv (Sverdrup, 1×10^6m^3/s), which makes it the largest current in terms of volume transport.

The ACC is mostly composed of Circumpolar Deep Water (CDW) volumetrically (Nicholls et al., 2009a), which is composed of a mixture of water masses from all the oceans the ACC encounter and the southern extent of North Atlantic Deep Water (NADW) (Orsi et al., 1999). The can be further subdivided in to Upper Circumpolar Deep Water (UCDW) and Lower Circumpolar Deep Water (LCDW) (Fig. 2.10;Orsi et al., 1995). The UCDW is recognized by its low oxygen levels, whereas the LCDW has a higher salinity content, inherited from the input of NADW (Orsi et al., 1995; Whitworth et al., 1998). Antarctic Intermediate Water (AAIW) lies above the CDW (Fig. 2.10 Nicholls et al., 2009a).

The formation of AABW occurs generally due to upwelling of LCDW at the continental slope in subpolar gyres, like the Weddell Sea Gyre (Fig. 2.9), where it mixes with super-cold shelf water (Orsi et al., 1999). The AABW then sinks downslope through passages on the continental shelf edge (Fig. 2.10) and on to the abyssal basins surrounding the Antarctic margin (Orsi et al., 1999). The AABW is then transported northward in the bordering oceans following the bathymetry, and reaches as far as ~5° south in the Atlantic Ocean (Nicholls et al., 2009a), where it meets the NADW in the Atlantic Ocean.
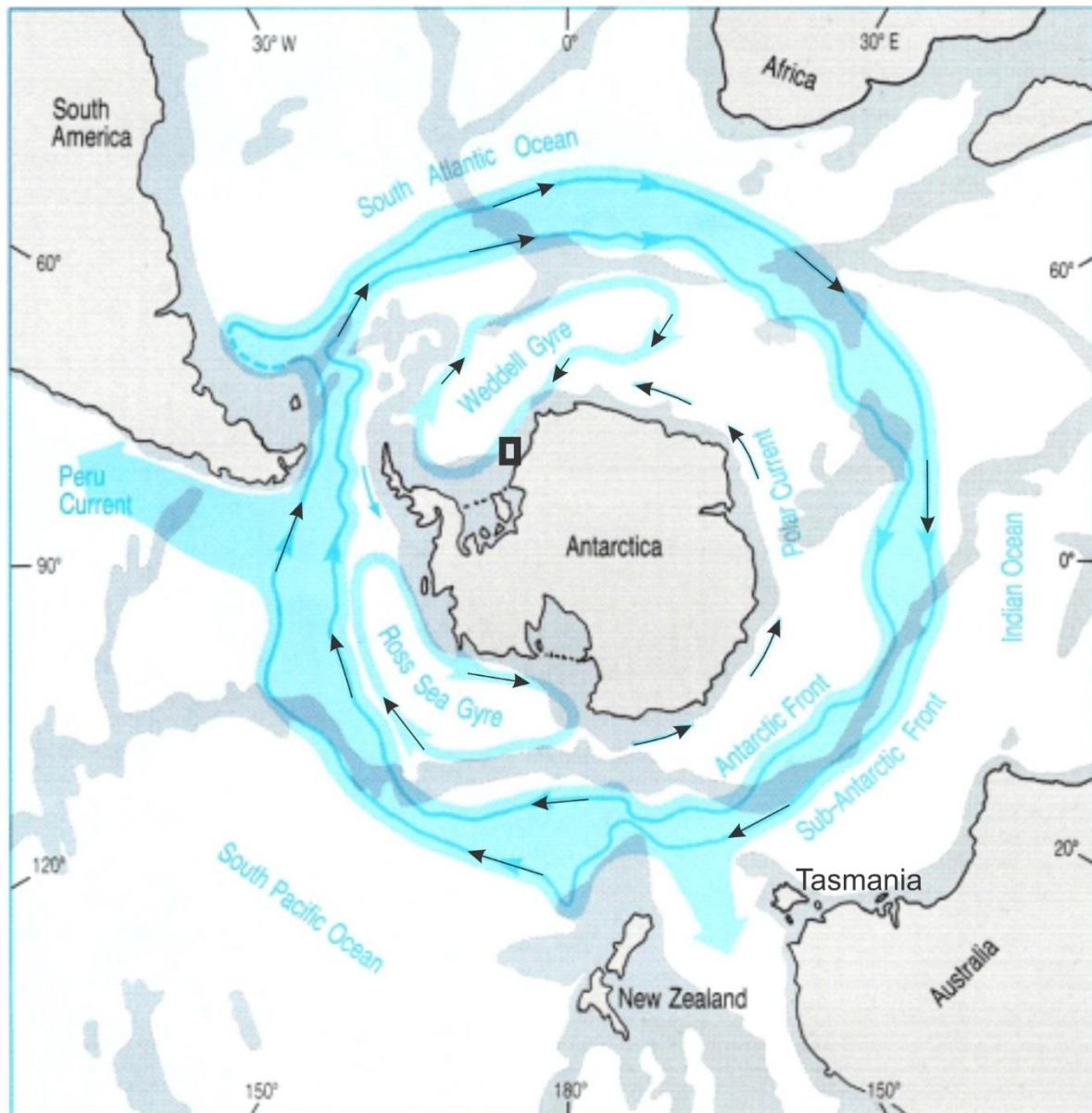
Fig. 2.9. Schematic map showing the mean path of the Antarctic Circumpolar Current (light blue tone; the solid slightly darker blue lines represent the average positions of the Antarctic Front and the Sub-Antarctic Front). The approximal position of the Weddell Sea Gyre and the Ross Sea Gyre are indicated, as is the path of the Polar Current. The Antarctic Divergence is between the Polar Current and the Antarctic Circumpolar Current. Gray shading indicates water depth less than 3000m, light gray shading indicates land. The approximate location of the Brunt Basin is indicated with the black box. Slightly modified from The Open University, 2002.

Some of the deep water masses mixes, and the NADW continues to flow southwards on top of the AABW, due to its lower density and connects with the ACC (Orsi et al., 1999).

The ACC contains four front (Fig. 2.10; Carter et al., 2008), these are listed form south to north; the Antarctic Southern Front, the Southern front, the Polar Front and the Subantarctica Front. North of the ACC we find the Subtropical Front (Orsi et al., 1995). The Meridional gradients in the surface properties of the water masses generally slopes downwards away from the Antarctic continent and define the observed fronts (Fig. 2.10; Orsi et al., 1995; Carter et al., 2008).

2.6.3 Weddell Sea

Multiple water masses occur in the Weddell Sea, and the largest feature is the Weddell Sea Gyre (Fig. 2.9), which branches off from the ACC and flows westwards along the Antarctic continent (Ryan et al., 2016). Warm saline waters are injected from the ACC at its northeastern boundary (~30º E) (Ryan et al., 2016). As the water masses makes its way to the southern Weddell Sea, cooling and brine rejection in polynyas (Fig. 2.11), transforms a large part of the water masses into High Salinity Shelf Water (HSSW) (Foldvik et al., 2004; Nicholls et al., 2009a). Some of the newly formed HSSW mixes with the water masses to form Weddell Sea Bottom Water (WSBW) or eventually Weddell Sea Deep Water (WSDW)(Nicholls et al., 2009a; Ryan et al., 2016). Some of the HSSW flows landwards under the
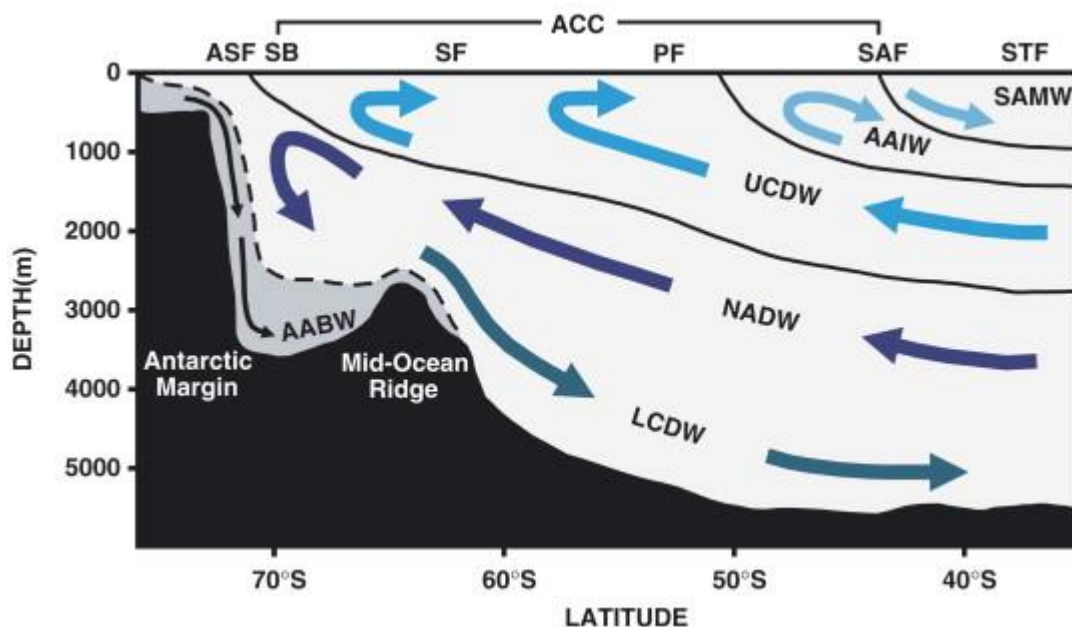
Fig. 2.10.Schematic section of the main water masses and frontal systems located around the Antarctic margin. The flow of Antarctic Circumpolar Current (ACC) is towards the reader. AABW- Antarctic Bottom Water, LCDW- Lower Circumpolar Deep Water, NADW- North Atlantic Deep Water, UCDW-Upper Circumpolar Deep Water, AAIW- Antarctic Intermediate Water. SAMW- Subantarctic Mode Water, ASF- Antarctic Slope Front, SB- Southern Boundary of the ACC, SF- Southern Front, PF- Polar Front / Antarctic Convergence, SAF, Subantarctic Front, STF-Subtropical Front. From Carter et al. (2008).

ice-shelf, where it gets super-cooled in sub shelf cavities, due to interaction with the base of the ice shelf (Fig. 2.11; Nicholls et al., 2009a), and are modified into Ice Shelf Water (ISW) (Foldvik et al., 1985; 2004; Nicholls et al., 2003). ISW is cooled below the surface freezing point (~-1.9°C), and it can have temperatures as low as -2.3°C, due to the pressure below the ice shelves (Nicholls et al., 2009a). As the ISW escapes from its sub-ice shelf position and rises towards the surface, it can become in situ supercooled (Foldvik and Kvinge, 1974) and produce ice crystals, which can contribute to freezing on of marine ice below the ice shelf (Foldvik et al., 2004). This results in convection and mixing of the water masses and formation of WSBE (Foldvik et al., 2004). This is the major processes forming WSDW and WSBW, which are major contributors for the formation of AABW (Orsi et al., 1993; Nicholls et al., 2009a).

2.6.4 Brunt Basin

Close to the Brunt Basin the Weddell Sea Gyre branches of to the south, and flows around the Brunt Ice Shelf without directly interacting with the ice shelf (Fig. 2.12; Nicholls et al., 2009a). Southwest of the Brunt Ice Shelf it interacts with the coastal current, which most likely is composed of water that has followed the eastern Weddell Sea ice shelves front and distinct ISW characteristics has been observed in deeper part of the water column (Nicholls et al., 2009a).
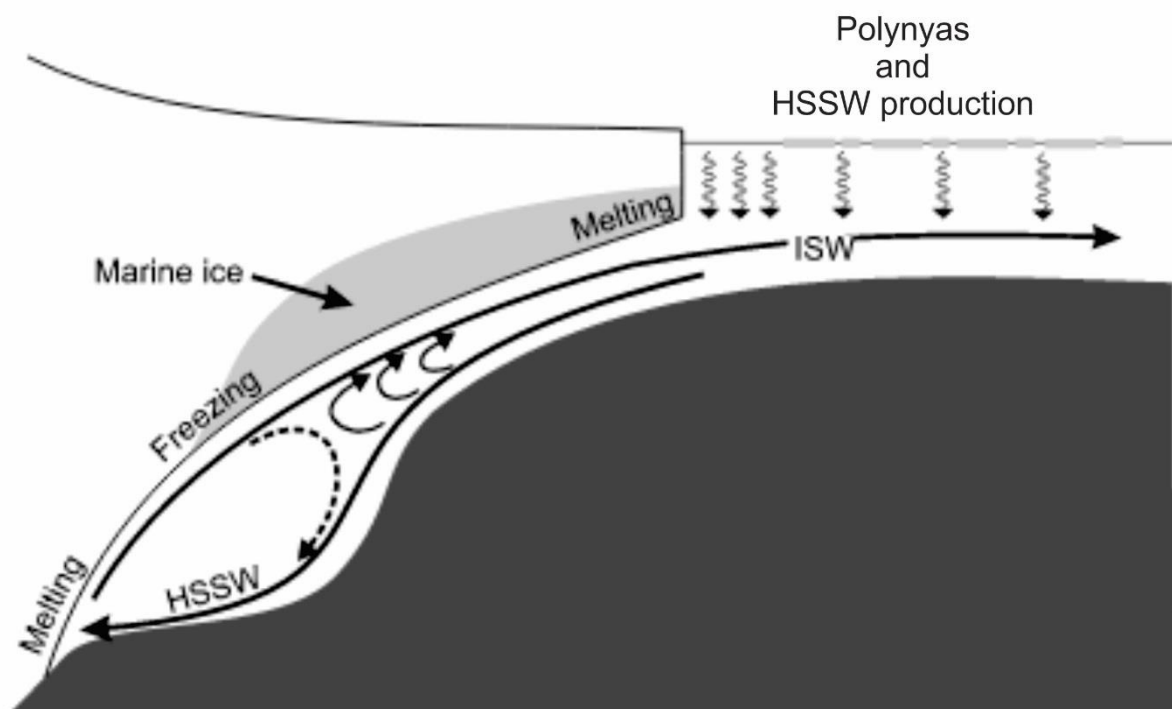
Fig. 2.11. Two-dimensional schematic model of formation of High Salinity Shelf Water (HSSW) and Ice Shelf Water (ISW). Slightly modified from Nicholls et al. (2009a).

Anderson (1993), presented evidence of two recurring coastal winter polynyas off the Brunt Ice shelf, linked to katabatic winds off the ice shelf, which should allow formation of HSSW, with similar processes as in the southern Weddell Sea (Nicholls et al., 2009a). In contrast, Fahrbach et al. (1994) concluded that no bottom water was formed in the southeastern Weddell Sea, in the Brunt Ice Shelf region.
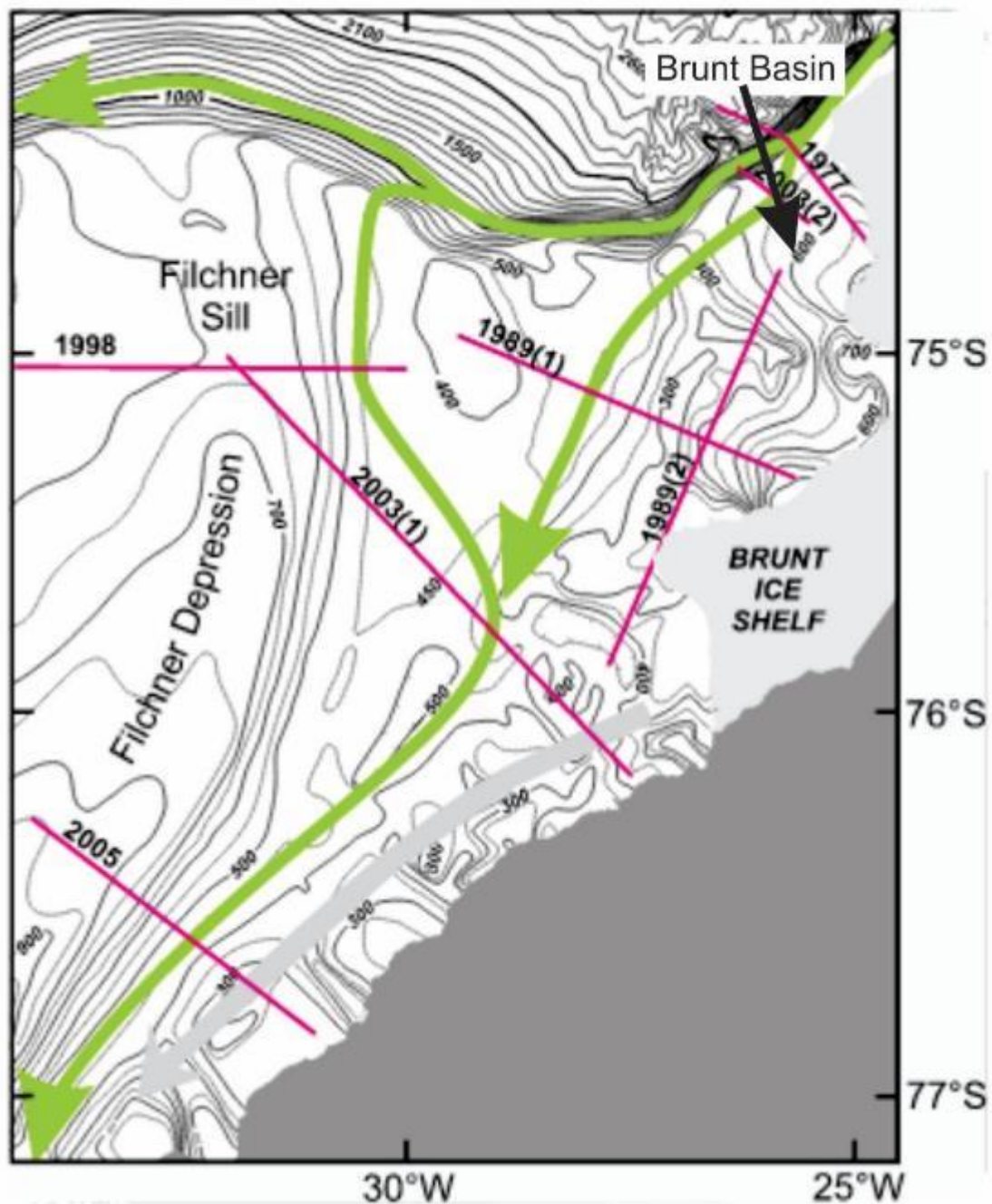
Fig. 2.12. Map showing the inflow pathways onto the southern Weddell Sea shelf. The green arrows represent flows of water from the Weddell Sea Gyre, The gray arrow represent the coastal current. Red lines indicate survey lines. The location of the Brunt Basin is indicated with a black arrow. Modified from Nicholls et al. (2009a).

Fer et al. (2012), observed the presence of ISW masses related to the Brunt Ice Shelf (Fig. 2.13c) and in situ super-cooled water. Where they observed ascending ice crystals towards the surface, which where suggested to cause convection and increased dissipation rates of the water masses. Fer et al. (2012) suggested further that the outflow of ISW from the base of the Brunt Ice Shelf might connect with the southwards branching current of the Weddell Sea Gyre (Fig. 2.12). The upper 80 m of the water masses consisted of relatively fresh, warmer waters (Fig. 2.13) and the mean current velocity along the Brunt Ice Shelf was measured to be 2-5 cm s^{-1} (Fer et al., 2012).
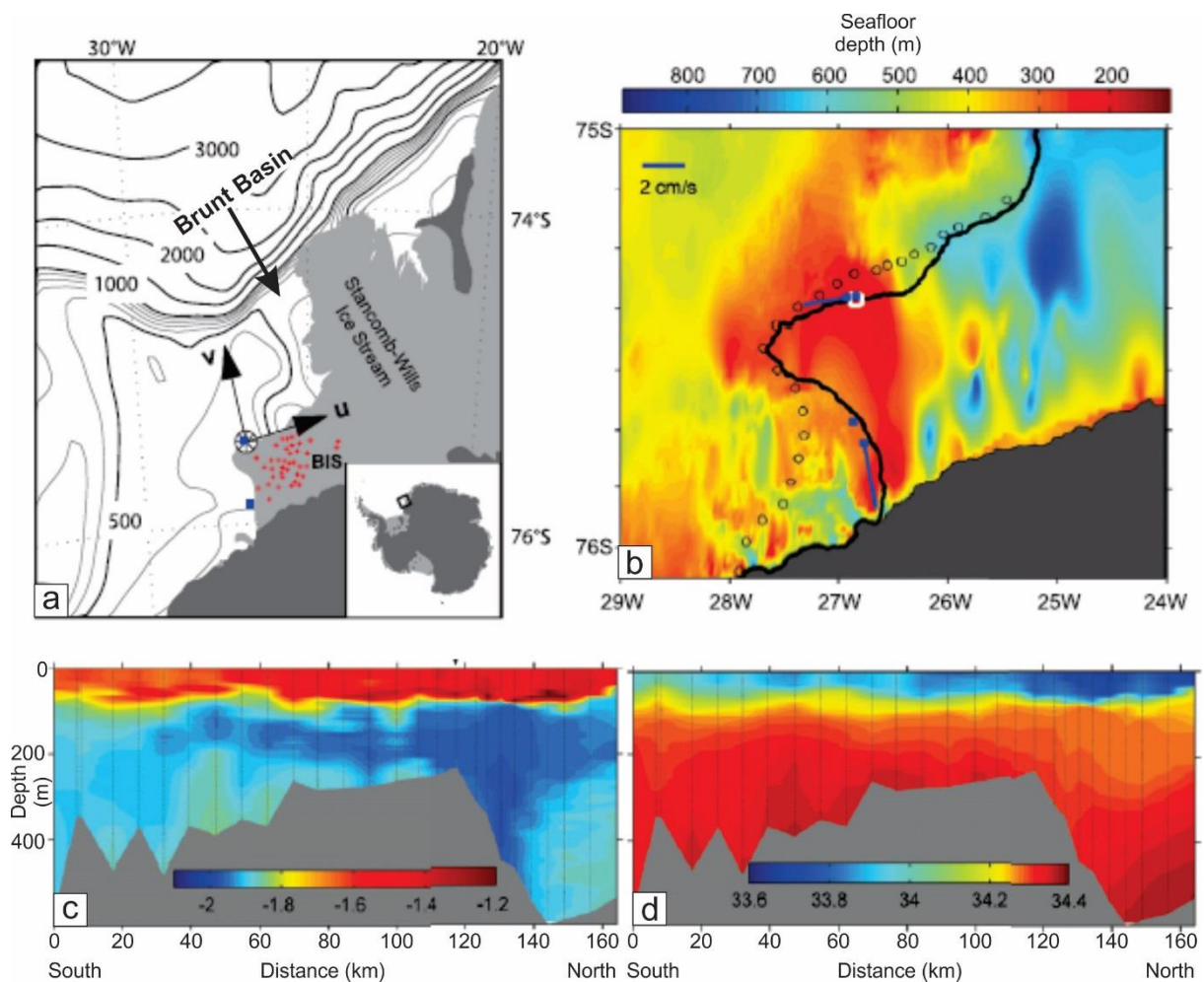
Fig. 2.13. (a) Location of the Brunt Ice Shelf (BIS) and the Brunt Basin (b) Seafloor bathymetry below and beyond Brunt Ice Shelf. Black solid line indicated the front of Brunt Ice Shelf. Circles indicates the position of conductivity, temperature and depth (CTD) stations. Blue squares show the position of moorings location, both moorings was displaced by icebergs, and both the deployment and recovery location are shown. (c) Temperatures and (d) salinity along the CTD section on Fig. b. Note the cold water (< 2°C) ascending the shallower areas in the northern part of the CTD section. Slightly modified from Fer et al. (2012).

3 Material and Methods

This study uses high-resolution swath bathymetry, TOPAS sub-bottom profiles, and multi-proxy analysis of four sediment cores. All the material was collected by the British Antarctic Survey (BAS), most of it during cruise JR244 on board RRS James Clark Ross between the 3rd and 5th of march, 2011. Additional swath bathymetry lines that intersected the study area was added to the data set (Fig. 3.1), which was collected during the cruises JR97 (in 2005) and JR259 (in 2012).
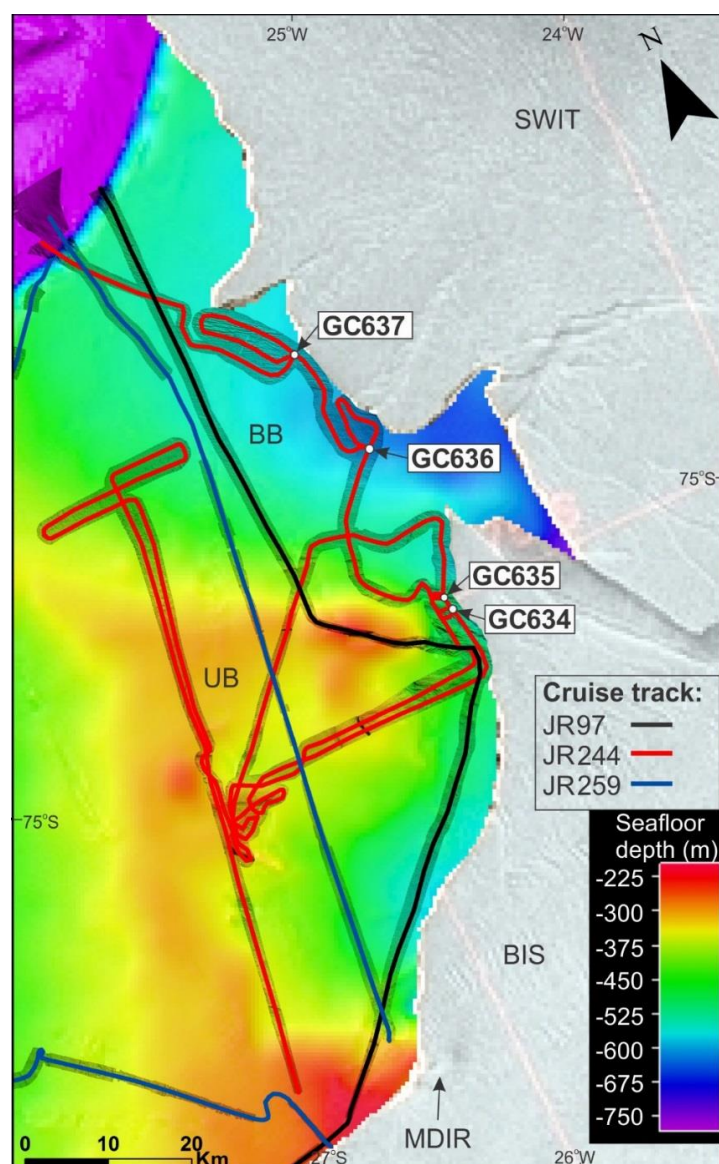
Fig. 3.1. Bathymetrical map according to IBCSO (Arndt et al., 2013) overlain by the high resolution swath bathymetry used in this study, with an Envisat synthetic aperture radar image of the Brunt Ice Shelf System, taken the 4th March 2011. The different cruise tracks are illustrated with different colors and the location of the recovered gravity cores (GC) are shown. SWIT-Stancomb-Wills Ice Tongue, BIS- Brunt Ice Shelf, MDIR- McDonald Ice Rumples, BB- Brunt Basin, UB, Unnamed bank.

3.1 Swath Bathymetry

Swath bathymetry is collected by using multibeam echosounder systems that sends out series of high frequency multiple beams (soundings) in a wide fan-like swath towards the seafloor (Fig. 3.2). The beams are then reflected at the seafloor and recorded as the travel back to the ship (Denbigh, 1989). The width of the swath fan is increasing with increasing water depths, but can also be adjusted, by adjusting the angles of the emitted beams (Denbigh, 1989). Each beam that is recorded consists of two coordinates (e.g. latitude and longitude position) and a depth value, which are used to produce bathymetrical maps, by gridding the recorded beams in a software (e.g. Fledermaus). The water depth on bathymetrical maps are typically plotted as color-codes, but can also be shown as plots of soundings, or as contours (Fig. 3.2; Carter, 2006).
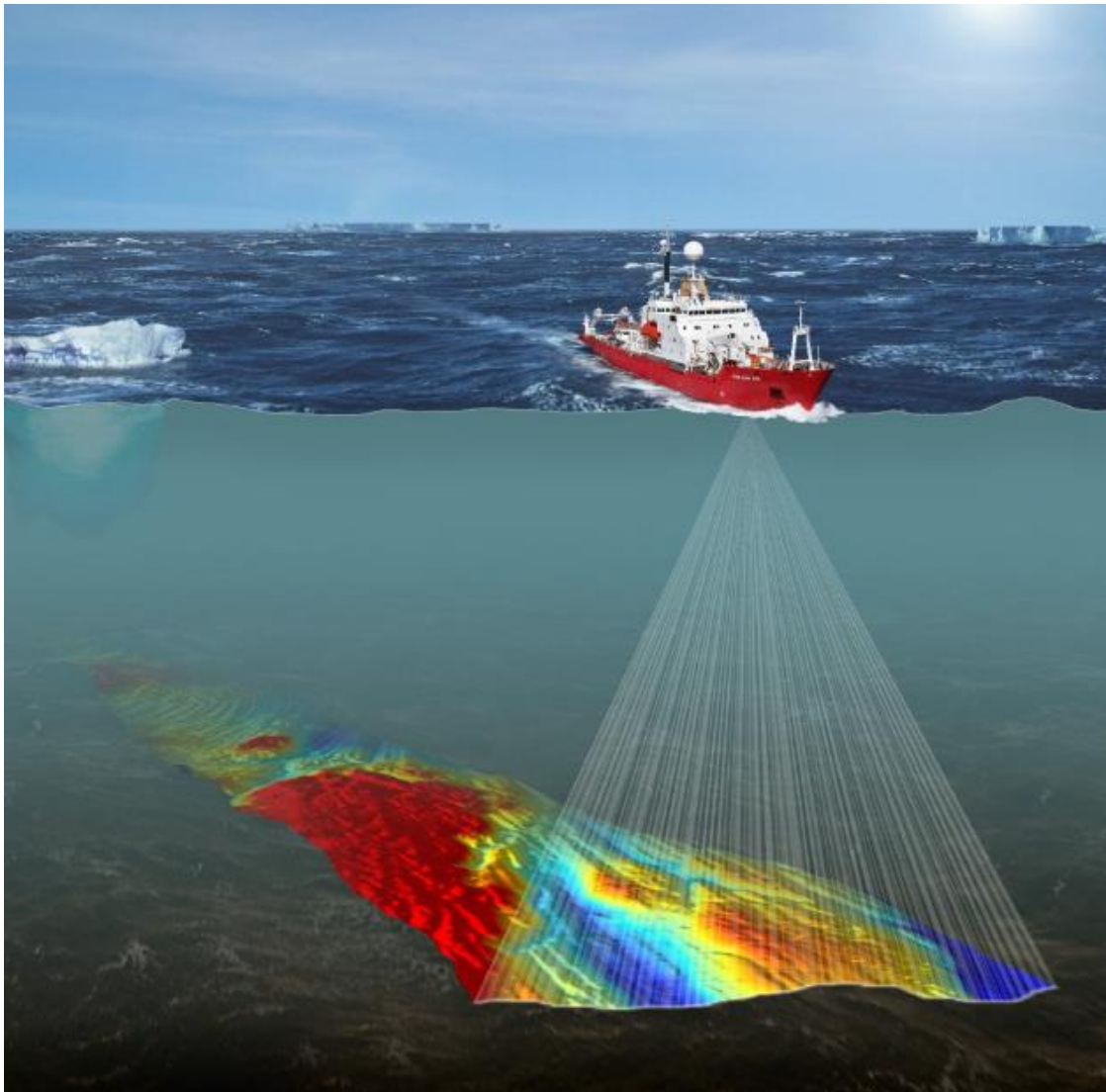
Fig. 3.2. Illustration of the JRR James Clark Ross using the multibeam echosounder system mapping out the seafloor. The beams are reflected at the seafloor, and returns to the ship where the beams are recorded. A swath bathymetrical map illustrates the seafloor morphology from the recorded beams. From British Antarctic Survey.

The swath bathymetry data used in this study were acquired with a hull-mounted Kongsberg-Simrad EM 120 (JR97 and JR244) and EM 122 (JR259) multibeam echo sounder onboard the RRS James Clark Ross. Both the EM 120 and EM 122 systems consist of 191 beams, each 1º x 1º and in the frequency range of 11.25-12.75 kHz (e.g. Larter et al., 2012; Gales et al., 2014). The maximum swath width coverage is 132º, i.e. up to 5.5 times the water depth for the EM120 system, and 134º, up to 6 times the water depth for the EM122 system. The operating water depths for both systems range from 20 to 11.000 m (Kongsberg Maritime, 2005; Kongsberg Maritime, 2013; Gales et al., 2014).

The Seatex Seapath 200 motion sensor unit, provided the system with corrections for vessel roll, pitch and yaw using real-time electronic beam steering. The sound velocity profile (SVP) used to calculate the beam raypaths and the sea floor depth in near-real-time, was based on a conductivity-temperature-depth (CTD) measurement taken prior to data collection in the study area for the JR224, and the SVP casts used for the JR97 and JR259 are unknown.
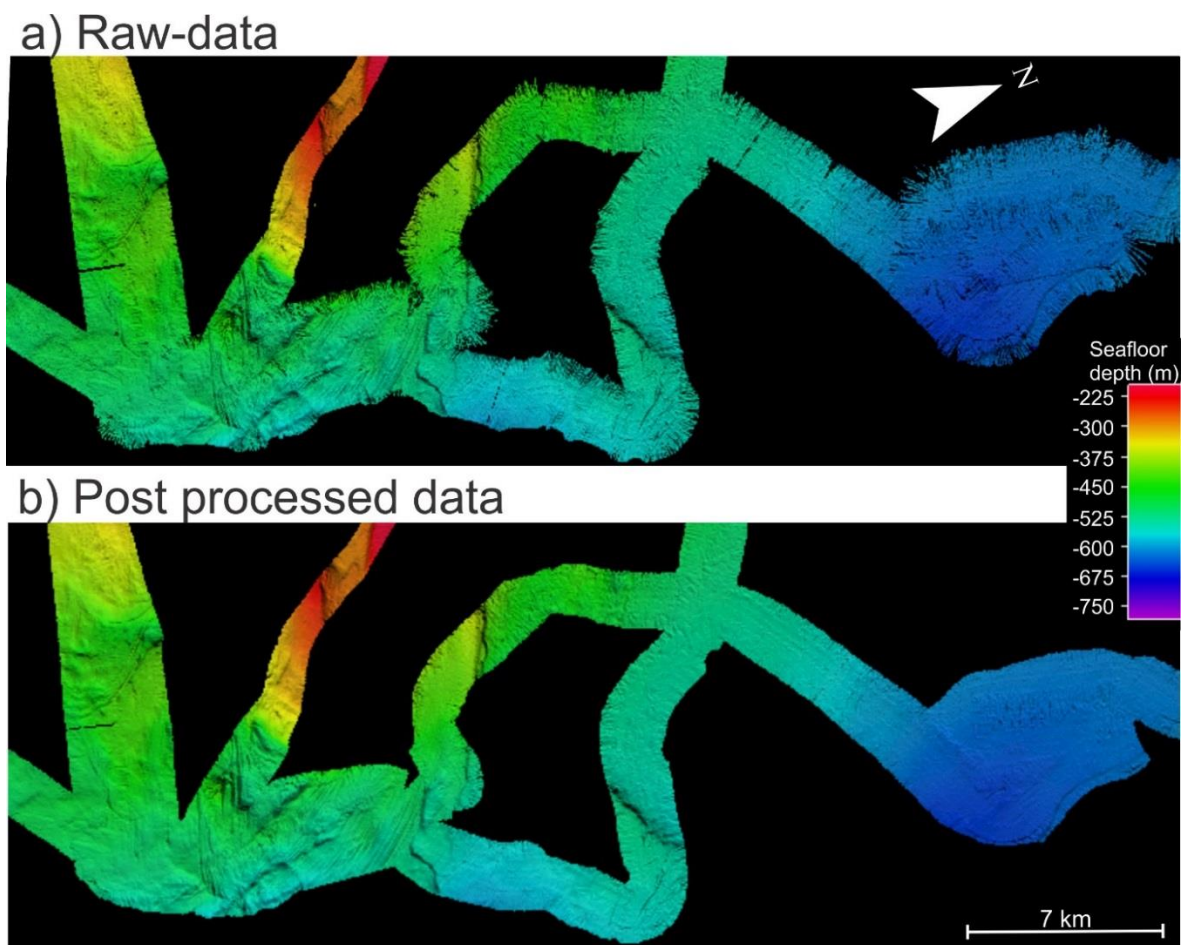
Fig. 3.3. Bathymetrical data (a) before processing and cleaning, and (b) after processing. Both images are projected on WGS84 UTM 26S, grid cell size 20 m and illuminated with a 116.3º azimuth and 6.3º sun angel.

The three swath bathymetry data sets were processed using Fledermause 7.5.x 3D editor, in order to anomalous depths and artifacts (Fig. 3.3). DMagic was used to grid the data. Most of the data were gridded to a cell size of 20 m, but some areas were gridded to a cell size of 15 m where the quality of the data allowed for it. All the data was processed by the author of this thesis. Fledermause7.5.x 3D was used for visualization, interpretation and exporting the bathymetry into ARCmap 10.3. The maps were created in ARCmap 10.3. and polished in CorelDRAW X6.

3.2 Sub-bottom profiler (TOPAS)

Sub-bottom profilers use soundwaves to map out the sub-seafloor (Gutowski et al., 2002; Sounding, 2003). The soundwaves reflect back at interfaces in the sub-surface if there is a sufficient acoustic impedance contrast. The impedance contrast is the product of density and the sound velocity differences above and below an interface. Hence, sub-bottom profiles do not only show the stratification of the sediments, but can also show structures, unconformities, fluids etc. As the soundwave encounters an interface of sufficient acoustic impedance contrast, some of the soundwave energy is reflected back towards the surface, whereas some of the energy is transmitted further downwards to the next interface. The strength of the returning signal is dependent on the acoustic impedance contrast. A large contrast in impedance gives a strong signal. Positive or negative signals are dependent on the reflection coefficient, if the soundwave is reflected at an interface where the layer below have lower acoustic impedance, the returning signal will be negative, and vice versa.

Topographic Parametric Sonar (TOPAS) is a sub-bottom profiler system that uses a parametric acoustic array (Foote et al., 2010; Kongsberg Maritime, 2012). It transmits two high frequency signals at the same time, and due to the nonlinear propagation in the water column, the signal interferes and generates a virtual endfire array, comprising new acoustic signals at the difference and sum frequencies (Fig. 3.4; Foote et al., 2010). However, it is only the low frequency waves (the sum of the transmitted frequencies), that are used for sub-bottom profiling (Foote et al., 2010). The low frequency signals generated have a relatively high frequency bandwidth (~ 80%) that are tens to hundred ms long, which gives relatively deep penetration, low signal-to-noise ratios and high vertical resolution compared to traditional chirp sub-bottom profilers. The narrow beam width generated by the virtual endfire array diminishes the side lobe effect (smaller Fresnel zone) and gives great spatial resolution (Fig. 3.4; Kongsberg Maritime, 2012). Resolution of 15 cm or better has been achieved at water depths of more than 3.8 km, with penetration down to more than 200 m below the seafloor. The performance is dependent on sediment type, transmitted signal, noise level and water depth, etc. (Kongsberg Maritime, 2012).
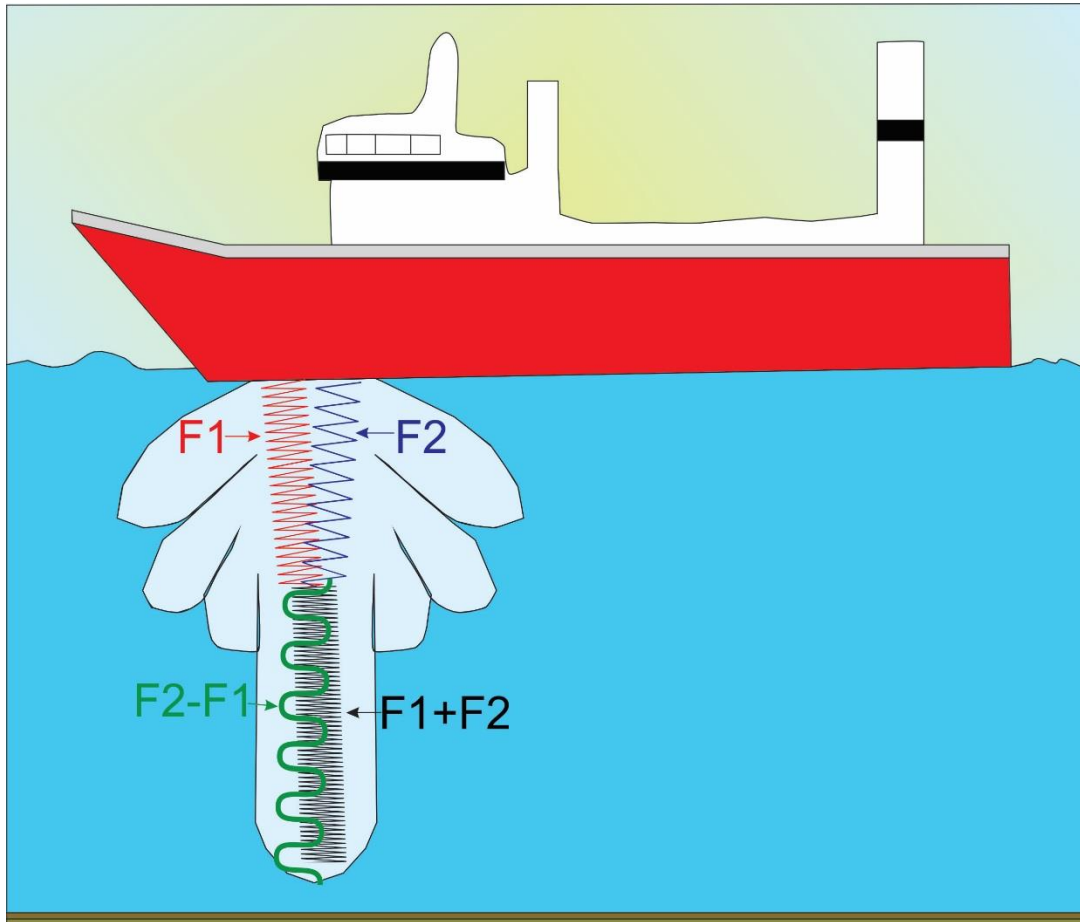
Fig. 3.4. Simplified sketch of the TOPAS system. The two signals transmitted (F1 and F2), interfere, causing a virtual endfire array and introducing two new signals. The frequency of the new signals are the sum (F1+F2) and the difference (F2-F1) of the two original frequency signals. The signal that is recorded and used for investigating the sub-bottom is the sum frequency (F1+F2).

The sub-bottom profiles used in this thesis were acquired with a hull-mounted Kongsberg TOPAS PS 18 system, transmitting two primary frequencies at around 18kHz, which due to the parametric effect generated a 10 to 15 ms-long secondary chirp pulse, ranging from 1300 to 5000Hz, with a beam width of 5°x5°. By using this configuration of the TOPAS system, a penetration depth of more than 50 m in fine-grained unconsolidated sediments can be achieved, with a vertical resolution ~1 m (e.g. Larter et al., 2012; Gales et al., 2014). The data were recorded at a sample rate of 20 kHz and instantaneous amplitude records were displayed as variable density traces, after cross-correlating the received signals with the secondary transmission pulse signature (Larter et al., 2012). A Seatex GPS receiver was used to acquire navigation data.

The raw files where processed using a TOPAS software from Kongsberg, by using match filter, time-variable gain, attribute processing, and gain, in that order, before exporting them as SEG-Y format files. The SEG-Y files were then imported into Petrel (2014), for better visualization and interpretation. All the data was processed by the author of this thesis.

3.3 Sediment Cores

Four gravity cores from the Brunt Basin were recovered during the JR244 cruise in March 2011 (GC634, GC635, GC636, and GC637), location and information about the cores are shown in Table 3.1 (see also Fig. 3.1).

Table 3.1.
Core station location and information on the cores used in this study.

Core ID	Date	Time (UTC)	Location	Latitude (S) Longitude(W)	Water Depth (m)	Penetration (m)	Recovery (m)
GC634	04.03.11	18:08	Brunt Basin Inner basin	75º00'.42 25º26'.96	500	1	0.15
GC635	04.03.11	19:57	Brunt Basin Inner basin	74º59'.50 25º27'.81	494	1.5	1.165
GC636	04.03.11	23:48	Brunt Basin Middle basin	74º48'.71 25º28'.53	626	3	1.765
GC637	05.03.11	03:06	Brunt Basin Outer basin	74º41'.03 25º34'.90	606	3	2.695

The gravity corer was built by P. Smit, in the Netherlands in 2010. It consisted of a 3 m long aluminum framework, core bucket, steel barrels, liner, core catcher and a bomb weight on top, as a regular gravity corer. The liners used inside the barrels were 2.70 m long. The steel barrels and plastic liners have diameters of 130 mm and 110mm, respectively. The core GC637 over-penetrated, but due to lack of time the site was not resampled with a longer core configuration.

The cores were split into smaller sections onboard the ship, then investigated with Multi-Sensor Core Logger (MSCL, which will be described more in details below in section 3.4.1), then they were stored at 4ºC, at the BAS facilities in Cambridge, until they were opened in February 2016.

3.4 Laboratory work

The laboratory work was done both at the BAS facilities in Cambridge in February and March, 2016, and at the Department of Geology at the University of Tromsø (UiT) between April and September, 2016. Visual core descriptions, logging, shear strength measurements, sampling, and production of smear slides were performed at BAS. MSCL was done at the British Ocean Sediment Core Research Facility (BOSCORF), in Southampton. The remaining analyses were carried out at UIT. A detailed description of the analyses will follow below.

3.4.1 Multi-sensor core logger (MSCL)

The cores were logged prior to opening with a GEOTEK MSCL Standard (Fig. 3.6), at BOSCROF, in Southampton, to determine some of the physical properties of the sediments in a non-destructive way, such as, Magnetic susceptibility (MS), P-wave velocity and wet-bulk density. Temperature measurements and core diameter were also measured during logging. After opening the cores were logged with a GEOTEK MSCL-S at the UIT, with a magnetic susceptibility point sensor, except for GC636, because of repeated instrumental failure.

Prior to logging the different sensors needs to be calibrated, and the cores need to be at room temperature, as changes in temperature can influence the physical parameters during the measurements (Weber et al., 1997). The cores are placed on the belt of the MSCL and are moved by a core pusher, driven by the belt, and as the core moves past the different sensors, the physical parameter are measured. A laser beam together with a positioning sensor, identifies at which depth the measurements are taken in the core (GEOTEK, 2000). The measuring- increment and -time can be in different intervals, and the measuring- increment and –time was set to 1 cm and 10 seconds for the point sensor. The measuring increment at BOSCROF was also 1 cm.
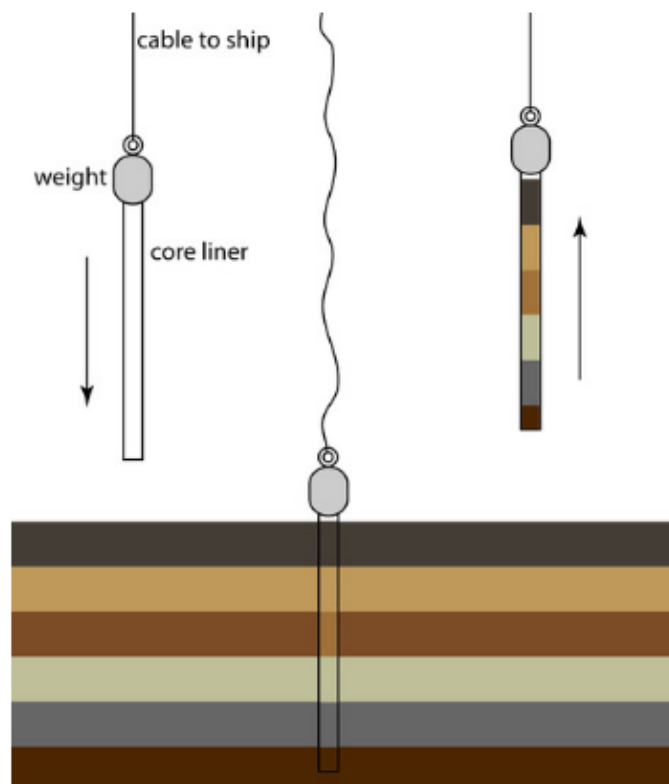
Fig. 3.5. Simplified illustration of a gravity corer in operation. The core weight is sufficient to penetrate into the sediments, a core catcher is placed at the bottom of the core allowing sediments to enter the core, but keeps the sediments within the core when it is hauled back to the ship. From http://chem.libretexts.org/.
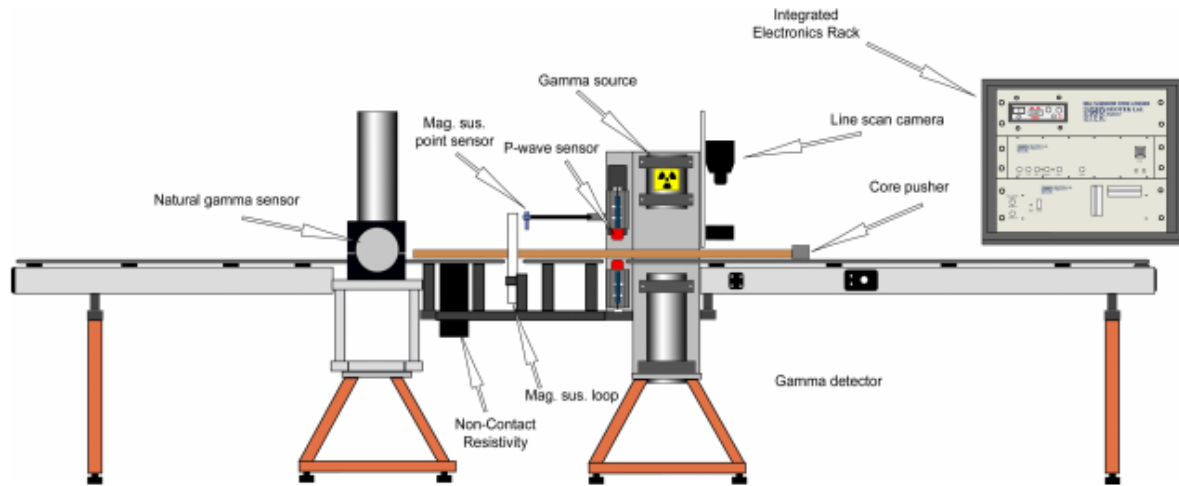
Fig. 3.6. Illustration of the GEOTEK Multi Sensor Core Logger, with its main features. From GEOTEK (2000).

3.4.1.1 Magnetic susceptibility (MS)

Magnetic susceptibility (MS) is a dimensionless parameter, which measures the material ability to become magnetic in response to an applied magnetic field (Dearing, 1999). In the MS sensor, an oscillator circuit generates a low intensity, non-saturated, alternating magnetic field. If the sensor is influenced by material with magnetic susceptibility, this will cause changes in the oscillator frequencies (Bartington, 2002). Material with high MS (e.g. magnetite) will strengthen the magnetic field, whereas material with low MS (e.g. calcite) will weaken the magnetic field (GEOTEK, 2014). The recorded changes in frequencies are converted into magnetic susceptibility values, which are displayed as basic mass or volume specific unit of either SI or CGS (Bartington, 2002). Gunn and Best (1998) found the typical values to be between -10×10^{-5} and 900×10^{-5} (SI) for marine sediments. The MS values used in this study are displayed in (10^{-5}) SI units.

MS can be of great use in reconstructing palaeo climate (Dearing, 1999), where it can be used to: e.g. correlate changes in depositional environment, correlation between cores and correlation to marine oxygen isotope records (e.g. An et al., 1991; Anderson, 1993; Bloemendal et al., 1995; Mosola and Anderson, 2006; Jessen et al., 2010). However, the MS values in different cores should not be compared, but patterns of stronger and weaker MS can certainly be compared over larger areas.

The whole cores were measured with a BARINGTON MS2C loop sensor. A BARTINGTON MS2E point sensor was used on the archive halves of the cores to obtain higher resolution of the MS, and correct for unrepresentative MS values, produced by e.g. single pebbles or cobbles in the sediment. Fig. 3.7, illustrate the two different ways of measuring.

According to Gunn and Best (1998) the loop sensor takes an average reading over 14 cm on each side of the sensor, whereas as Weber et al. (1997) states an average reading of 10 cm on each side of the sensor. Thus, even if it takes an average reading, the sediment closest to the loop sensor will have the highest influence on the values. The loop sensor is sensitive to slumping and irregularities inside the core, such as pebbles and cobbles, which will affect the MS values and can give anomalous values, whereas slumped regions where there are less sediments will typically produce anomalous low values (Gunn and Best, 1998). At both top and bottom of the core sections, air measurments influence the results leading to lower values.
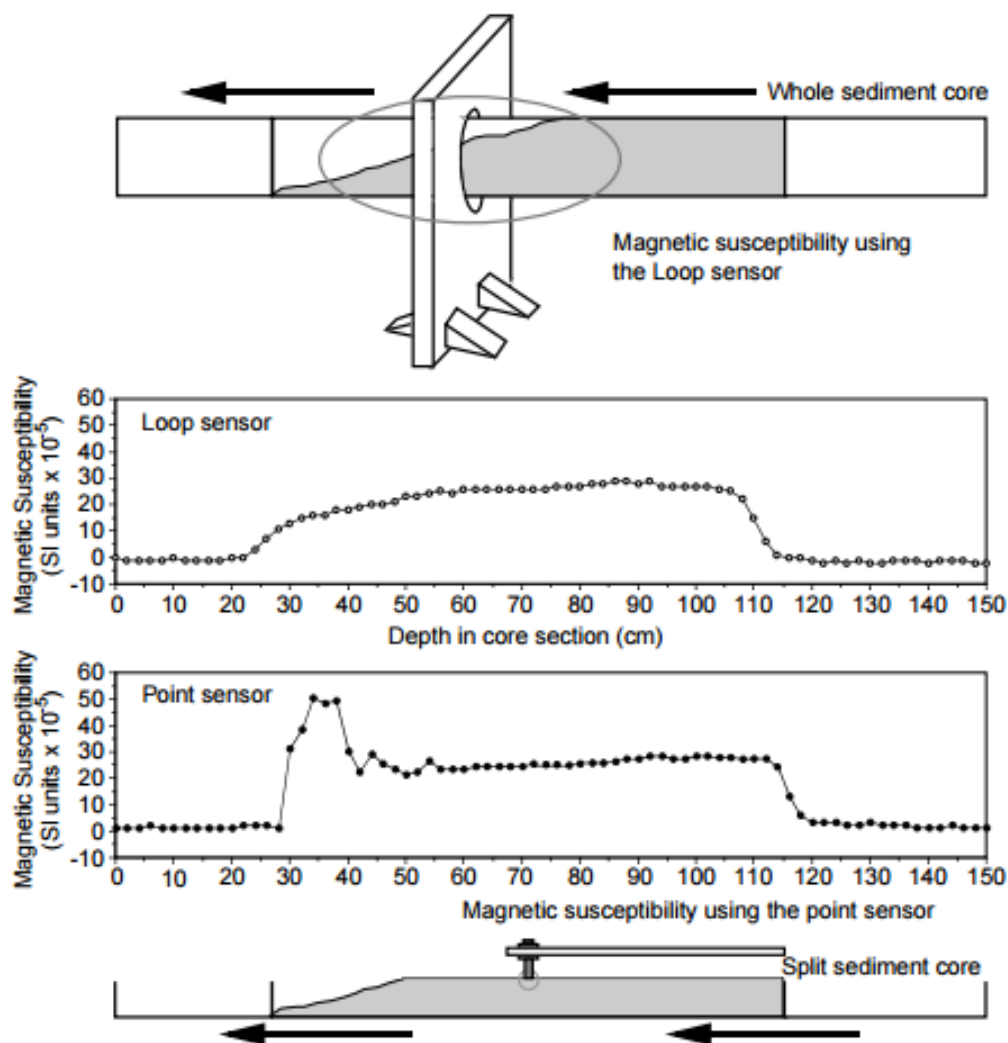
Fig. 3.7. Illustrates the differences between loop and point sensor measurements on a whole and a split core affected by slumping. The dark grey illustrates sediments with equal MS inside the core, and the light grey circle illustrates the area that is influencing the sensor. The loop sensor readings show anomalously low values in the slumped region, due to less volume of sediment, which also affect the measurement from the undisturbed sediments region, due to averaging over a large area of the core. The point sensor show constant values from the undisturbed sediment region, which are not affected by the slumped region, since the measurements are influence by a smaller area. However, the point sensor also show anomalously values in the slumped region, which are most likely caused by poor contact with irregular sediment surface. The loop sensor also show anomalously low values at the bottom of the core, as it's averaging outside of the core.

In comparison, the point sensor is only affected by sediments within a diameter of 2 cm, and receives 50% of it's signal from the upper 3 mm of the sediment, which gives a much better resolution than the loop sensor (Gunn and Best, 1998). The point sensor is also less affected by irregularities and slumping, as it can avoid to measure on top of single pebbles and cobbles, and is not as volume dependent as the loop sensor.

3.4.1.2 Wet-bulk density

The wet-bulk density is simply a measurement of the mass (wet-weight) divided on the wet-volume of the particles in a material, where mineral composition and compaction of the sediments are important factors of the bulk density (GEOTEK, 2014).

$$\text{Wet-bulk density} = \frac{Mass}{Volume}$$

The wet-bulk density is obtained by sending a narrow beam of parallel photons (gamma ray) from a [137]Cs (cesium) source through the sediment core, and recording the unattenuated photons that pass through the core with a detector on the opposite side of the core (Gunn and Best, 1998; GEOTEK, 2014). The incident photons are attenuated by Compton scattering, which means that they are scattered by electrons in the core and loses parts of its energy (Evans, 1965; Weber et al., 1997). Since the density of the sediment is directly related to the density of electrons in the core, the wet-bulk density of the core can be calculated from the received unattenuated photons (Evans, 1965; GEOTEK, 2014). A dense sediment will have a dense composition of electrons, and less unattenuated photons will be received, and vice versa. The thickness of the core, which is necessary for calculating the wet-bulk density, is measured by displacement of transducers, as explained in section 3.4.1.6.

3.4.1.3 P-wave velocity

P-waves (primary waves) are compressional waves which propagate through a medium by alternation of compression and extension in the medium, in the direction of the propagation (GEOTEK, 2014). The P-wave velocity is dependent on the density, modulus of incompressibility and modulus of rigidity of the sediment, and hence, P-wave velocity and changes in the P-wave velocity can give important information of sediment and its characteristics (e.g. Hamilton, 1971; Burger, 1992; Klages et al., 2013).

The p-wave velocity is measured by sending a short p-wave pulse from a transducer through the core, which is received at a transducer on the other side of the core. Both the traveling time and the traveling distance (core diameter) are recorded with a resolution of 50 ns and 0,1 mm, respectively (GEOTEK, 2014). The P-wave velocity are then calculated:

$$V_P = \frac{d}{t}$$

Where (d) is the traveling distance, (t) the traveling time and (V_p) is the P-wave velocity.

3.4.1.4 P-wave amplitude

The P-wave amplitude is measuring the intensity of the p-wave signal and is primary a used to obtain information about the sediments and the core liner contact. The contact between the core liner and the sediments, will affect both the p-wave velocity and the p-wave amplitude, and if the P-wave amplitudes is low, the P-wave velocity measurement may not be accurate, (M. Forwick, personal communication). The P-wave amplitude can also be used for porosity calculations, where high values may reflect a lower porosity of the sediments (GEOTEK, 2000).

The P-wave amplitude was used to correct for anomalous values in the P-wave velocity. At depths where the P-wave amplitudes were lower than 89, the P-wave velocity results were excluded. This gave a rather patchy result for the P-wave velocity, and it was therefore left out of the result part.

3.4.1.5 Temperature measurements

To measure the temperature, a platinum resistance thermometer probe is used. This is important as the MS, P-wave, wet-bulk density measurements are affected by the temperature, which needs to be accounted for (Weber et al., 1997).

3.4.1.6 Thickness measurements

Two rectilinear displacement transducers are mounted on the P-wave transducers and can measure the thickness of the core to a precision of 0.1 mm (Gunn and Best, 1998 206). The core thickness is measured as the deviation from a reference thickness, derived from a reference core with similar thickness as the measured core (GEOTEK, 2014). The thickness measurements are then used to calculate the wet-bulk density and P-wave velocity.

3.4.2 Core splitting

Before splitting the cores, the MSCL data was investigated to identify possible areas were there could be difficulties in the core splitting process. Two circular saws were used to cut the liners of the cores, a utility knife was used to cut the caps on the section ends, and a cheese wire was used to cut the sediments into two halves. The cutting procedure was always from bottom to top of the core sections to prevent contamination from younger sediments from being dragged into older sediments, which can lead to a wrong chronology of the sediments when they are dated. One half of the cores was chosen as a working half, where destructive analysis were made, whereas the other half was chosen as an archive half, and was only used for non-destructive measurements.

3.4.3 Visual description

The sediment surface of the half of archive the cores was cleaned and systematically investigated. Visible observations of lithological boundaries, changes in grain-size, sedimentary structures and texture, clast-content, organic matter and color variation was described and general remarks were noted. The color were determined and named according to the *Munsell Soil Color Charts* (Munsell). These observations together with the observations done from the X-radiographs and grain-size data are the results of the lithological logs presented in chapter 6, page 91.

3.4.4 Shear strength

Shear strength measurements provide information of the stiffness of sediments, which are usually related to grain-size, water content, and processes during and after deposition of the sediments. The shear strength can therefore be used to infer the depositional environment or the post depositional environment of the sediments, and can help to distinguish between subglacial and proglacial depositional environments of diamictons (e.g. Vorren et al., 1983b; Elverhøi, 1984; Hillenbrand et al., 2005; Forwick and Vorren, 2009; Smith et al., 2011). Subglacial diamictons deposited by a slow flowing grounded ice (lodgment till), have high shear strength (> 50 kPa), which can be used to separate it from diamictons deposited below fast flowing ice streams (soft deformation till) and diamictons deposited in proglacial environments (glaciomarine), which have lower shear strength (e.g. Elverhøi, 1984; Evans et al., 2005; Ó Cofaigh et al., 2005b; Forwick and Vorren, 2009; Reinardy et al., 2011b).

The shear strength measurements were preformed every 5-10 cm, using a hand-held shear vane in the working half of the cores. The shear vane was pushed vertically into the sediment, and was rotated slowly until the sediment gave in to the rotation stress applied. This way of measuring assumes that the shear vane is uniformly shearing a cylinder of sediment around the axis of the vane, and fails in a cylinder around the shear vane when the maximum shear strength is reached (Kuhlmann, 2013).

One of the core section had de-watered in one half, meaning that most of the water had left one half of the section, and entered the other. Shear strength measurements was obtain from both the working half and the archive half of this section, and the values plotted in the results (e.g. Fig. 6.11; page 102) are average measurements.

3.4.5 X-radiographs

X- radiographs is a valuable method, using electromagnetic radiation to image the sediments in the core, which makes it possible to recognize features such as shells or fine-scaled sedimentary structures, which are not visible at the sediment surface (Lofi and Weber, 2001). As the X-rays travel through the sediment core, they are attenuated by the sediments in the core. More X-ray are attenuated in material of high

density (e.g. gravel-cobble rich and compacted sediment), whereas less is attenuated in low density material (e.g. fine-grained, soft and bioturbated sediment) (Van Geet et al., 2000; Ketcham and Carlson, 2001). The level of attenuation through the cores is commonly displayed as a greyscale image, where the grey values are proportional to the attenuation, which again is related to the density (Van Geet et al., 2000). Hence, the grey scale intensity reflects spatial differences in the sediment density, and it should be noted that the radiographs are not "true visualizations" of the density differences (Van Geet et al., 2000).

X-radiographs were taken both of the working half and the archive half sections of the cores, using a GEOTEK MSCL-XCT, with a voltage of ~120 kV, and a current of ~225μA, taking images every 2 cm. The working half was photographed for investigation of calcareous material that could be dated, whereas the archive photos was used for investigating structures, clast distribution, and for calcareous material. The contrast was adjusted to make the features on the X- radiographs as clearly as possible. X-radiographs images were re-taken with 1cm and 0.5 cm spacing in one core section to investigate possible artifact, this is described more in details in section 6.1.6 page 95.

3.4.6 XRF scanning

X-ray fluorescent (XRF) core scanning, is a non-destructive method, which is measuring bulk sediment element composition directly at the surface of split sediment cores (e.g. Jansen et al., 1998; Richter et al., 2006; Tjallingii et al., 2007). It uses X-rays from rhodium (Rh) to excite the material on the surface of the core, which then generates and emits secondary, fluorescent X-rays (Richter et al., 2006).

The X-rays emitted from the X-ray tube are generated by electrons transmitted from a cathode, which collides with an anode. The amount of electrons emitted are dependent on the current in the cathode and the acceleration of the electrons are dependent on the voltage between the cathode and the anode. If the incoming X-rays have enough energy, they eject an electron from an inner shell of the atom, making the atom unstable (Jansen et al., 1998; Richter et al., 2006). To create a more stable electronic configuration, an electron from an outer orbital will fall back into the inner orbital, and the energy difference between the orbitals is emitted as a secondary fluorescent X-ray (Fig. 3.8; Jansen et al., 1998; Richter et al., 2006; Tjallingii et al., 2007). The fluorescent X-rays are measured by a detector of the XRF scanner, processed and analysed for the geochemical composition of the surface of the sediment core (Brouwer, 2006).

Since each element produces a characteristic X-ray- energy and –wavelength, the amplitude peaks in the XRF spectrum will be proportional to the concentration of elements in the core surface (Richter et al., 2006).

The whole system measures through a flushed helium chamber to improve the detection of lighter elements (e.g. Mg and Al), and to prevent absorption of emitted soft radiation through air (Richter et al., 2006). The current detection limit for the Avaatech XRF core scanner is ranging from Mg to U in the periodic table (Avaatech). Since the range of energy required to excite the different elements is too large to collect the data in one run, the measurements are normally acquired during several runs, with different current and voltage intensity's. Additional filters can be applied to attenuate some of the hard radiation from the X-ray tube and improve detection of the elements of interest (Richter et al., 2006).

Before scanning, the cores were adjusted to room temperature to avoid condensation and formation of water film between the foil and the sediment surface to prevent reduction of the lighter elements XRF signal (Tjallingii et al., 2007). After reaching room temperature, the sediment surface was smoothened, covered with a 4µm Ultralene foil to prevent contamination and excess air trapped between the film and sediments were removed. The measured area was 10 mm in down-core direction and 12 mm in cross-core direction. The cores were scanned every 10 mm as long as the surface of the core allowed it. Counting time was 10 sec. The measurements were conducted in two runs, with the different settings listed in Table 3.2.
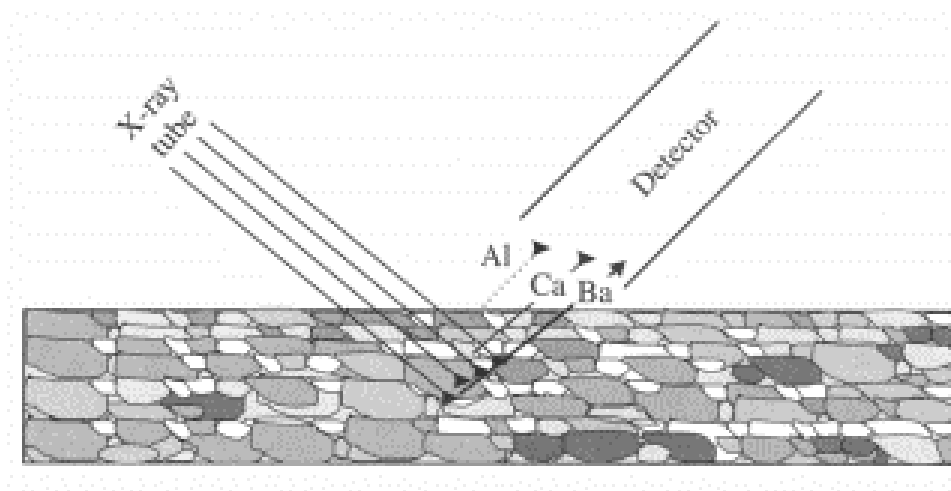
Fig. 3.8.Simplified diagram showing the principle of XRF logging on spilt sediment cores and response of selected elements to incoming X-ray. From Richter et al. (2006).

Table 3.2.
The two different settings used together with the elements, which were analysed in the different settings.

Setting	Voltage	Current	Filter	Elements analysed
1	10 kV	1000µA	non	Al, Si, S, K, Ca, Ti, Mn, Fe,
2	30 kV	2000µA	Pd thick	Rb, Sr, Zr

When interpreting and presenting the XRF data, the data should be plotted as element ratios, e.g. Fe/Al, or as Fe/Sum of several abundant elements, instead of presenting results of single elements (Weltje and Tjallingii, 2008). By using the element ratio, matrix effects related to dilution of secondary radiation are reduced, which can be caused by; uneven/rough surface, porosity differences in the sediment, water film and/or air bubbles between the sediment surface and the 4µm Ultralene foil (Weltje and Tjallingii, 2008). This is because all the elements in the area that is affected by dilution will have lower values and their ratios will still be similar, even if the light elements will be more affected. Whereas by plotting them as single elements, they will have artificially low values.

3.4.7 Color imaging

Color images were taken of the core shortly after opening at the BAS facilities in Cambridge. Prior to taking the photos, the sediment surface of the core was cleaned using plastic card, and the images were taken using a SLR camera.

The cores were also photographed in Tromsø, about two months later, using a Jai L-1070CC 3 CCD RGB Line Scan Camera, which has a resolution of 70 µm. The sediment surface was cleaned and were exposed to air for some time to let water at the sediment surface evaporate, as it can cause reflections and poorer quality of the images.

3.4.8 Water content

Individual sub-samples, 1 cm thick slices of the sediments were taken at intervals of 5-20 cm down core and on either side of lithological boundaries. The samples were then weighed, freeze dried, and weighed again to obtain the sediment water content. About 2 g from each sample was stored as archive samples, the remaining sample was weighed again to be prepared for further analysis. One of the core sections had de-watered, meaning that most of the water had left one half of the core. The water content measurements were obtained from the half that had gotten most of the water.

3.4.9 Grain size distribution

Selected samples used for water content analysis were chosen for further grain-size distribution analyses. The samples were choses so the analysis would show a representative grain size distribution throughout the core, and help identifying lithological boundaries. The samples were wet-sieved using a 63 µm sieve, and a 2mm sieve. The first 250 ml of water and mud was collected and stored. The fraction was then dried in a heat oven at 50°C. The samples were then weighted, and the weight percent (wt. %) of each fraction was calculated. The classification of grain-size used is based in the Udden-Wentworth grain-size scale for clastic sediments, where mud is less than 63 µm, sand is between 63 µm-2 mm, and gravel are above 2 mm. (Fig. 3.9; Nichols, 2009b).

Fig. 3.9. The Udden-Wentworth grain-size scale for clastic sediments. The clast diameter in millimeters is used to define the different sizes of the scale Based on Udden (1914) and Wentworth (1922). Slightly modified from Nichols (2009b).

3.4.10   Smear-slide analysis

Smear slides can be used to make quantitative estimates on the biogenic content in the mud fraction (< 63 µm), and investigate biogenic assemblages in the mud fraction such as diatoms and siliconflagellates, which are typically too small from the sand fraction, and making (e.g. Dahlgren and Vorren, 2003; Hillenbrand et al., 2010; Smith et al., 2014). Thus, also morphology grains and mineral assemblage can be investigated with smear slides.

Most of the smear slides were prepared at the BAS facilities in Cambridge, while few were prepared at UiT. The smear slides at BAS were prepared following the standard procedure at BAS. The procedures are; (1) A small amount of a mud sample is placed on a thin glass slide, water is added to the mud, and the mud sample is smeared out on the thin glass slide. (2) The sample is left to dry. (3) When the sediments has dried completely, 2-3 drops of optical cement (Norland Optical Adhesive) is added to the sample and a cover slide is placed on top of the sample and the optical cement. (4) The smear slides is then placed under ultraviolet light for 30 min. Smear slide preparation at UiT did not following these procedures. Instead of the optical cement, glue was used and the samples were not placed in ultraviolet light. However, the samples turned out to be good.

The smear slides were investigated using a light microscope, where the biogenic content and assemblages in the mud fraction were estimated.

3.4.11 Analysis of sand fraction

Analyses of the grain composition in sediments can be used to infer the source area of the sediments, and changes in the depositional environment where sediments from a different source area are introduces to the environment(e.g. Hobbs, 1998; Diekmann and Kuhn, 1999; Domack et al., 1999; Forwick and Vorren, 2009; Baeten et al., 2010).

The sand grain fraction of the samples used for water content and grain size analyses was used for analysing the sand fraction. The sand fraction samples were split using a sample splitter to make the volume of the samples appropriate for counting the grains.

At least 300 grains were counted under a microscope. The grains were distinguished between: Terrigenous, authigenic, and biogenic components (Table 3.3). The terrigenous components were further distinguished on behalf of their mineralogical composition, and when a grained contained more than on mineral it was defined as a lithoclasts (e.g. one sand grain containing mafic and quartz mineral). The authigenic and biogenic component was also distinguished between different specimens, which are all listed in Table 3.3. The sand fraction content of the different compounds could then be calculated in percentages.

Table 3.3.
The different components of the sand fraction that were distinguished when counting the grains in the sand fraction.

Terrigenous	Authigenic	Biogenic
Quartz and feldspar	Micro manganese nodule	Planktic foraminifera
Lithoclast	Pyrite	Benthic calcareous foraminifera
Mafic	Glauconite	Benthic agglutinated foraminifera
Mica		Radiolaria
Volcanic glass		Diatoms
Other terrigenous		Sponge spicules
		Other biogenic

3.4.12 Scanning electron microscope (SEM)

Scanning electron microscope (SEM) can be used to obtain high-resolution images of microscopic specimens, and element composition of the specimen (Todokoro and Ezumi, 1999; Hitachi, 2011). The SEM uses focused beams of high energy electrons that interact with atoms on the surface of the investigated specimens. This produces emission of secondary electrons, which are used to produce the SEM images. The beams of high energy electrons also excites the atoms in a similar manner as the XRF scanning (section 3.4.6), producing XRF emission, and as each element produces a characteristic signal, the element composition can be estimated (Kanemaru et al., 2009).

A SEM Tabletop TM3030 Hitachi was used to investigate the element composition and the structures of 19 grains from the sand fraction, to verify what type of grains they were. One of the SEM images are displayed in Fig. 6.4 (*p.* 94).

3.4.13 Radiocarbon dating

Four radiocarbon dates were obtained, using the Accelerator Mass Spectrometry (AMS). Two calcareous radiocarbon dates were obtained from GC634. One from the planktonic foraminifera *Neogloboquadrina pachyderma sinistral* (N. Pachyderma sin.) and one date from a benthic foraminifera *Cibicides specimen* (Cibicides sp.). Additionally, one acid-insoluble organic (AIO) fraction radiocarbon date was obtained from the same core at the same depth. One calcareous date was obtained in GC635

from one shell valve (Table 3.4). The calcareous and the AIO material was sampled from 1 cm thick slides of sediments (e.g. 12.5-13.5 and 49.5-50.5 sample interval).

Due to low calcareous content in the sample interval, the samples was analysed at the Eidgenössische Technische Hochschule (ETH) laboratory in Zurich, which can date calcareous matter down to 0.6 mg, by using the new MIni radioCarbon Dating System (MICADAS). For more details about the MICADAS see Synal et al. (2007), Wacker et al. (2010); ETH (2013).

Table 3.4.
The calcareous microfossils and shell collected for radiocarbon dating. Mg- milligram, g-gram.

LAB REFERENCE	CORE	SAMPLING DEPTH (CM)	SPECIES	WEIGHT OF SAMPLE
69711.1.1	GC634	12	N. Pachyderma sin.	1.1 mg
69710.1.1	GC634	12	Cibicides sp.	1.2 mg
70776.1.1	GC634	12	AIO	26.4 g
69709.1.1	GC635	50	One shell valve	2.7 mg

3.4.13.1 Principle of radiocarbon dating

^{14}C is a radioactive carbon isotope that is formed in the upper part of atmosphere, when nitrogen (^{14}N) and neutrons from cosmic rays collides (Bowman, 1990). The ^{14}C is then rapidly combined with oxygen molecules and forms chains of carbon dioxide (CO_2). The CO_2 is then mixed throughout the atmosphere and enters the oceans, where it via photosynthesis processes enters plant material and can become part of calcareous ($CaCO_3$) marine organisms. In this way, the ^{14}C is included into the carbon cycles, where the organisms are continuously taking up "newly formed" ^{14}C. When organisms die, they stop being part of this exchange, and the radioactive ^{14}C isotope starts decaying with a half-life of 5730 years (Bowman, 1990).

3.4.13.2 Calibration and marine reservoir effect

The formation of ^{14}C production trough time has varied due to variations in different factors such as, sunspot activity and the earth's magnetic field (Bowman, 1990; Hughen et al., 2004). This leads to a non-constant concentration of ^{14}C in the atmosphere and in living organisms trough time, and the radiocarbon ages obtained from calcareous or organic matter needs to be calibrated in order to be presented in calendar years (Bowman, 1990).

At the ocean-atmosphere interface, ^{14}C is mixed into the ocean water, resulting in input of ^{14}C that compensates for the reduction of ^{14}C in the surface waters, and a more or less similar concentration of ^{14}C in the surface water and the atmosphere. However, when water masses sink downwards, the input of ^{14}C to the water masses stops. Due to the decay of ^{14}C, the water masses get diluted in ^{14}C. Consequently, the apparent age of the water masses increases due to the lower content of ^{14}C. The apparent age of the water masses is dependent on, (i) how long the waters have been subdued from the surface, (ii) income of "fresh" water and ^{14}C from surface layers and, (iii) income of "older" waters diluted in ^{14}C (Bowman, 1990). Due to mixing and currents, "older" water masses are injected into the surface water masses, which causes a difference in the concentration of ^{14}C in atmosphere and the surface water in the ocean, known as the marine reservoir effect (Bowman, 1990). The reservoir effect can vary locally over short distances, depending on the factor mentioned above. These factors need to be corrected for when marine organisms are dated. Because they will have an apparent age that are older than their real age, since they incorporate carbon (C) from older water masses that are diluted in ^{14}C (Bowman, 1990).

The CALIB 7.1 software (Stuvier and Reimer, 1993; Reimer et al., 2013) was used to calibrate the radiocarbon ages. The program uses the Marine13 calibration curve with an average marine reservoir age of 405 years (Reimer et al., 2013). However, the Marine13 only corrects for the average marine reservoir effect and local marine reservoir effect needs to be corrected for. In this thesis, correction for the marine reservoir effect used is 1300 ± 70 years, as suggested by Berkman and Forman (1996), and also applied by Hillenbrand et al. (2014) for marine dates obtained from the Weddell Sea. As the pre-fixed correction for the marine reservoir effect for Marin13 is 405, the local reservoir effect used was 895 ± 70. The calibrated ages are based on the mean 1σ range (Table 6.1, page 94)

The calibrated dates presented in this study are shown in calibrated years before present (cal. years BP) or calibrated kiloyears before present (cal. ka BP). The BP (before present) refers to before 1950 in modern calendars, which is regarded as the zero point in the radiocarbon timescale (Bowman, 1990). This year has been chosen due to the impact that nuclear weapon testing from 1945 and the increasing fossil fuel burning have on the ^{14}C concentration in the atmosphere and thus also in the oceans (Bowman, 1990).

3.4.13.3 AIO dating

Due to spars amounts of calcareous material in marine sediments from the Antarctic shelf, it is sometimes necessary to date the AIO fraction of the sediments (e.g. Licht et al., 1996; Domack et al., 1999; Smith et al., 2011). A bulk sample is taken from the targeted depth, and the sample is treated with acid to remove any carbonate in the sample (Kihl, 1975; Andrews et al., 1999). One problem with the

AIO dating is that it is subjected to contamination from old organic matter eroded from the Antarctic continent or reworked from older sediments, which can lead to significant "apparent" older ages for the sediments (e.g. Licht et al., 1996; Domack et al., 1999; Smith et al., 2011). The age difference between the apparent age and the real age of the sediments are often called local contamination offset (e.g. Smith et al., 2011). One way to correct for the local contamination offset is if you have ^{14}C ages from calcareous microfossils at the same depth. However, AIO dating is typically used due to lack of calcareous matter. Another way to correct for the local contamination offset is by obtaining the local contamination offset from the seafloor surface at the position of the core, and applying that for the sediment down core. However, changes in depositional environment and source area can possibly change the local contamination offset due to changes in the input of "older" organic matter (e.g. Heroy and Anderson, 2007; Smith et al., 2011; Hillenbrand et al., 2010).

4 Swath Bathymetry

The available swath bathymetrical data from offshore the Brunt Ice Shelf System reveals a variety of geomorphological landforms indicative of former grounded ice within the study area. These landforms have been identified, described and interpreted more in details bellow and based on these observations, a map has been produced of the landforms observed (Fig. 4.2).

4.1 Large-scale morphology

The swath bathymetrical data was draped on top the IBCSO data set (Arndt et al., 2013) in order to investigate the large-scale morphology of the study area (Fig. 4.1). The water depths within the swath bathymetrical data set, vary between ~202-640 m, which are relatively shallow compared to the southern Weddell Sea (Fig. 1.3; Arndt et al., 2013; Fretwell et al., 2013). In the southwestern-western part of the study area, a shallower curving bank is separating the Brunt Basin and the Halley trough (Fig. 4.1; Gales et al., 2014). The shallower bank is oriented in an oblique angle (~45°) to the shelf edge and has a varying topography with large ridges and depressions. The slope between the bank and the Brunt Basin is irregular and varies between ~3,5° to less than 1°.

The Brunt Basin is located in the northeastern-eastern part of the data set, and is a depression on the seafloor in front of the Brunt Ice Shelf System. The Brunt Basin has a landward dipping geometry, which is similar to troughs eroded by Antarctic palaeo-ice streams, with an over-deepened inner basin, mainly the result of subglacial erosion during repeated glacial cycles (e.g. Ten Brink et al., 1995; Anderson, 1999; Livingstone et al., 2012; Fretwell et al., 2013). The Brunt Basin is divided into three sub-basins: the inner, middle, and outer basin (Fig. 4.1). The area defined as the inner basin is shallower than the other parts of the basin, with seafloor depths between ~420-500 m. From the inner part of the basin, the seafloor slopes gently towards a depression in the middle of the basin, with seafloor depths down to ~640 m. In the outer part of the basin, towards the shelf edge, the seafloor has a gentle slope, dipping southward, away from the shelf edge, where the seafloor depth reaches between 490-500 m at the shelf edge (Fig. 4.1).
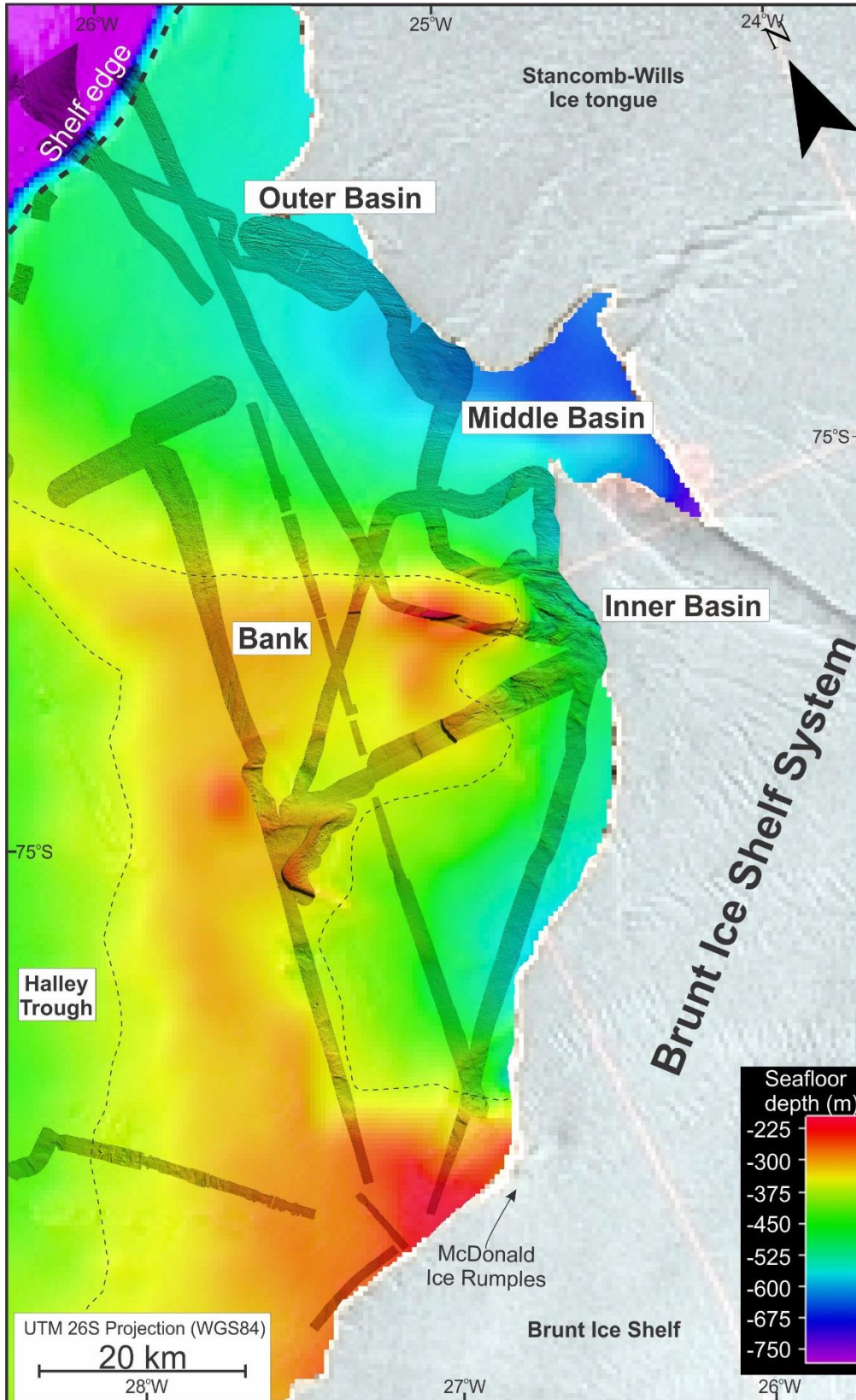
Fig. 4.1. Large-scale bathymetry with the location of the bank, basins and the shelf edge. The swath bathymetrical data is draped on top the IBCSO bathymetry (Arndt et al., 2013), with an Envisat synthetic aperture radar image of the Brunt Ice Shelf System, taken the 4th March 2011. The bathymetry is illuminated with an azimuth of 57°, and a sun angle of 6,5°.
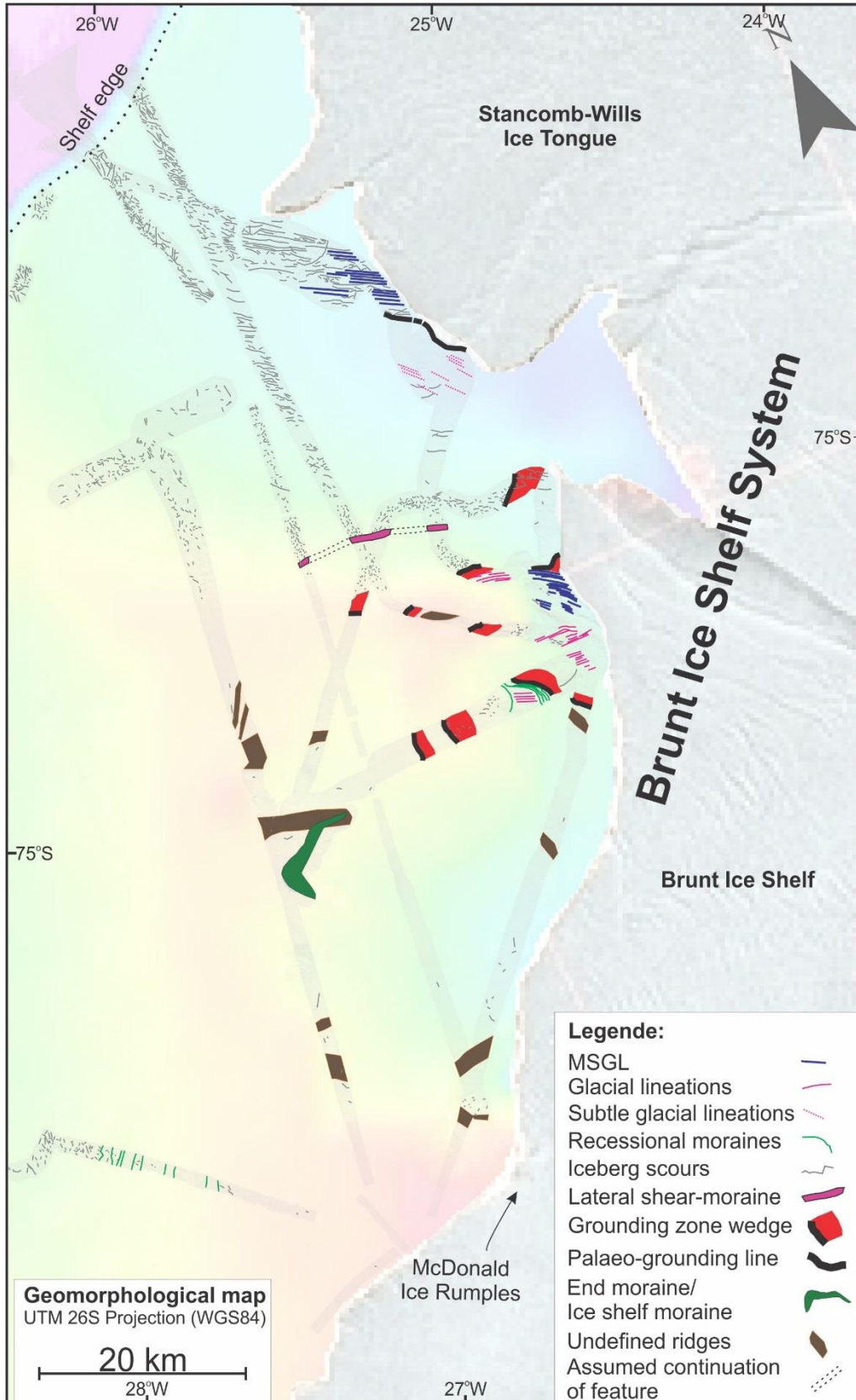
Fig. 4.2. Geomorphological map of the study area, including a transparent version of the swath bathymetry data overlain the IBCSO (Arndt et al., 2013), and a Envisat synthetic aperture radar image of the Brunt Ice Shelf System from 4th of March 2011.

4.2 Elongated linear features:
Mega-scale glacial lineations (MSGL) and glacial lineations

4.2.1 Description

Several sets of linear to curvilinear elongated linear features are observed in the basin. They are generally symmetrical in cross profile and can be subdivided into four different types based on their morphology.

Type-I lineations consist of two sets of lineations that occur as prominent parallel ridges and troughs (Fig. 4.3). These lineations are between 0.7-6 km long, but they are presumably longer as they seem to extend beyond the limits of the bathymetrical data set and some appear to be overprinted by iceberg scours (described in section 4.3; Fig. 4.3d and e). The width and height of these ridges are between 100-300 m and 2-10 m, respectively. The elongation ratio (length: width) varies between 6:1 and 40:1 and the wavelength between the crest of the ridges varies between ~250-200m. Bifurcation of a few Type-I lineations are observed, which are shown in Fig. 4.3b.

Type-II lineations consist of three sets of lineations that are less pronounced than the Type I lineations and occur as smaller and narrow ridges aligned parallel (Fig. 4.4). These lineations are between 0.5-1.4 km long, and their widths and heights vary between 80-150 m and 2-5 m, respectively. Their length-to-width ratios vary between 5:1 and 8:1. Some of the Type-II lineations are located on top of a GZW (Fig. 4.4a; described in section 4.8, page 75), and the two sets of Type-II lineations in Fig. 4.4d, have a GZW and recessional moraines (described in section 4.5, page 67) located between them.

Type-III lineations consist of a complex pattern of linear to curvilinear ridges, located in the inner part of the basin in front of the slope towards the bank (Fig. 4.5). The ridges are between ~0.4-3.2 km long, with a various height and width of ~1-6 m and ~60-200 m, respectively. Some of the ridges are highly linear, whereas others show less linearity which creates the complex pattern (Fig. 4.5c). The ridges that are less linear are located on a topographical high, where they appear to bifurcate or bend, and on the western side of this topographical high, there is a cluster of arch-shaped ridges (Fig. 4.5c and d; arch-shaped ridges- iceberg scours, see section 4.3). The ridges are generally symmetrical in cross-profile (Fig. 4.5e), but have a slightly steeper slope than the Type-I lineations.

Type-IV lineations consist of one set of very subtle lineations (Fig. 4.6) that occur on an almost featureless sub-horizontal seafloor, at depths between ~600-640 m. These lineations are 0.7-2.2 km long, a width of ~60-100 m and a general height less than 1.5 m. Due to their subtle appearance, it is difficult to measure the exact width and length, and therefore their elongation ratio was not measured. From Fig.

4.6b, we can see that these subtle lineations are not generally parallel or transverse to the cruise track suggesting that they are real features, rather than artifacts.
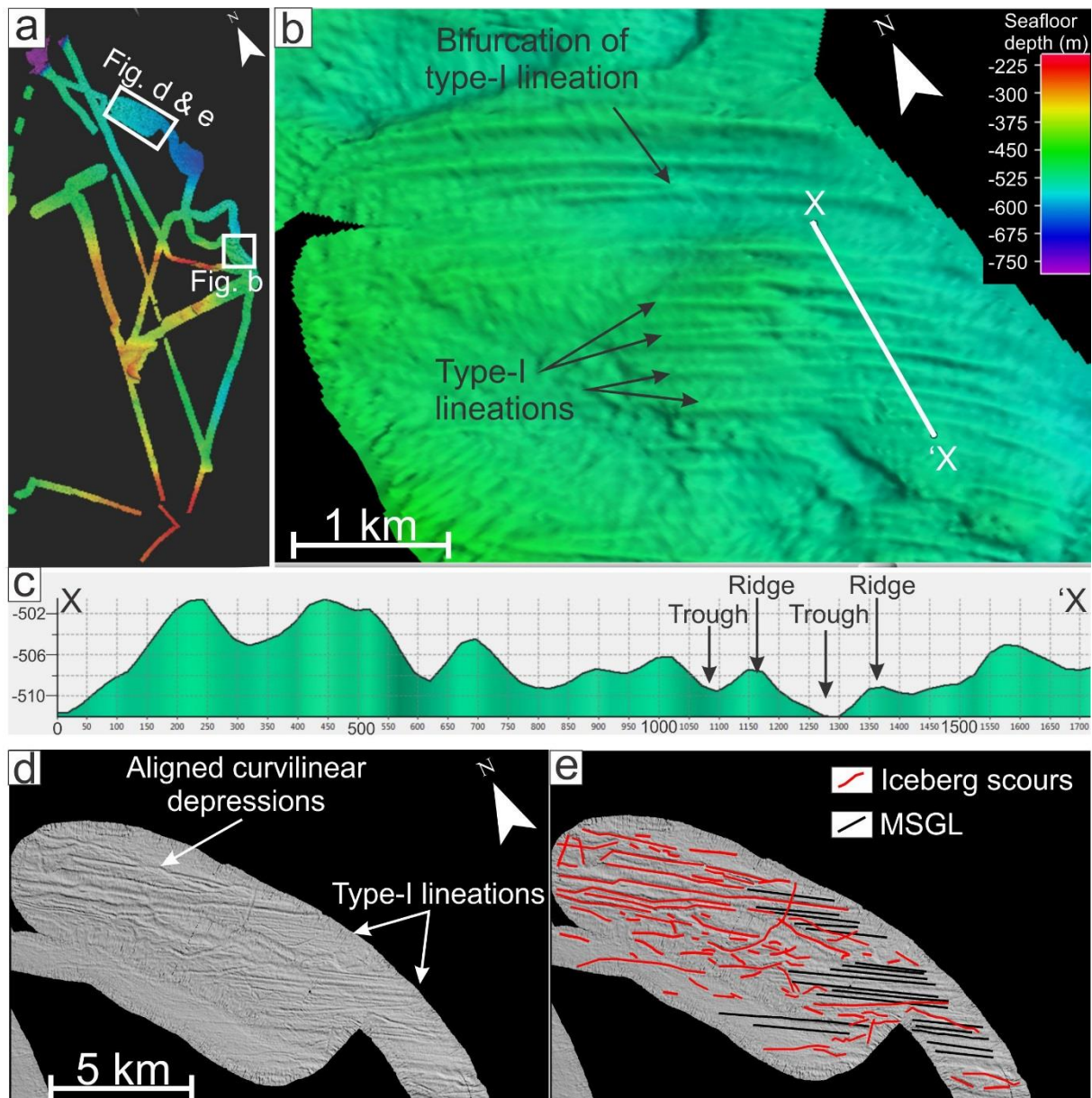
Fig. 4.3. Type-I lineations: Mega-scale glacial lineations (MSGL). (a) The white box indicates the location of Fig. b. (b) Type-I lineations in the inner part of the shelf, note the bifurcation if the lineation in the northern part of the figure. The white line indicates the profile line in Fig. c. (c) Cross-sectional profile line through the Type-I lineations, with ridges and troughs. (d) Grayscale image of the outer basin with Type-I lineations and cross-cutting curvilinear depressions. (e) Interpretaion of Fig. d. All images are illuminated with an azimuth of 57°, and a sun angle of 6.5°
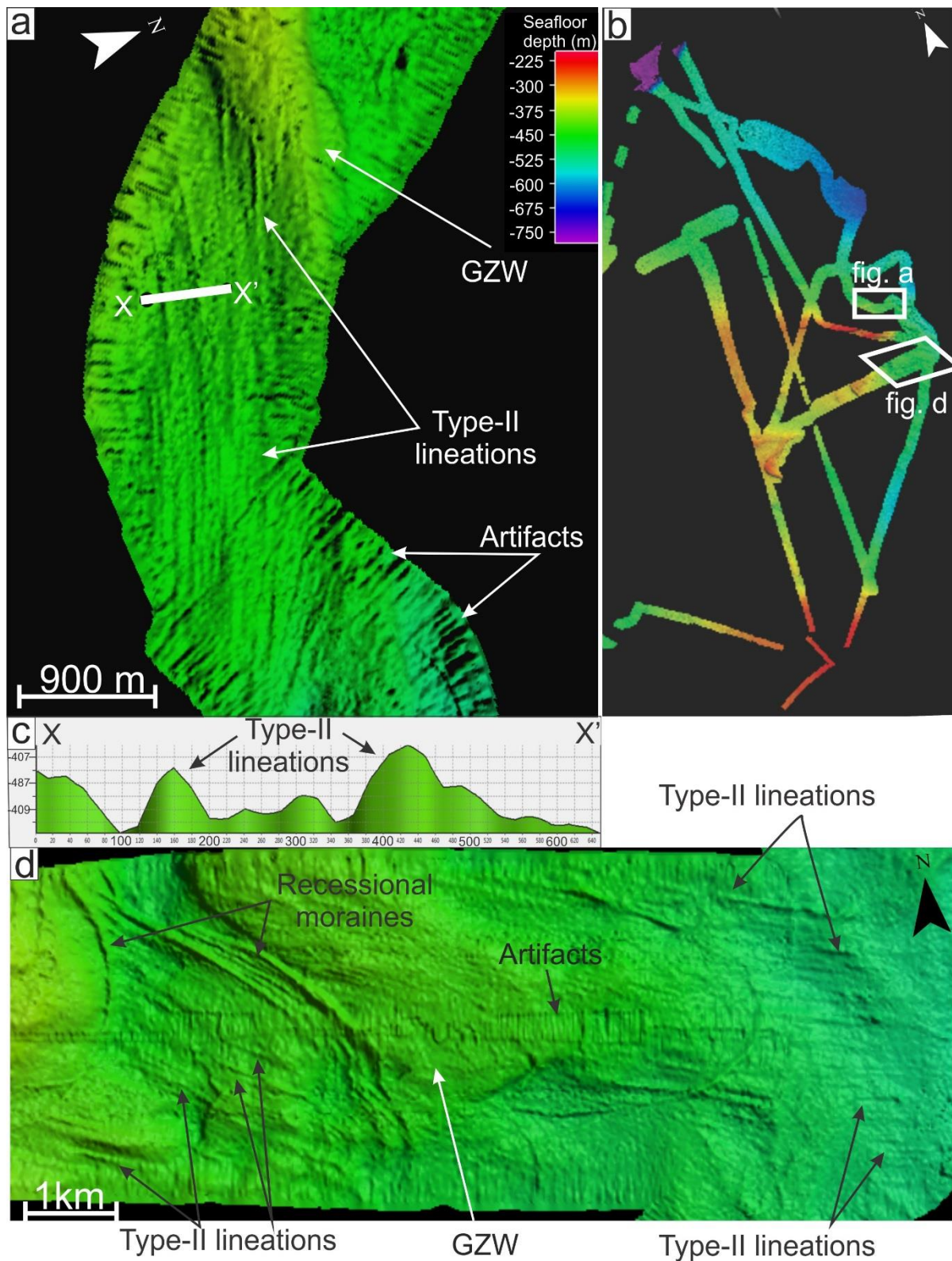
Fig. 4.4. Type-II lineations: Glacial lineations. (a) Type-II lineations that are slightly curving towards the south, some of the lineations are located on top a grounding zone wedge (GZW). The white line shows the location of the profile line in Fig. c (c) Profile line through Type-II lineations. (d) Two sets of Type-II lineations with slightly different directions. All images are illuminated with an azimuth of 38º, and a sun angle of 4.9º, except the image in Fig. b.
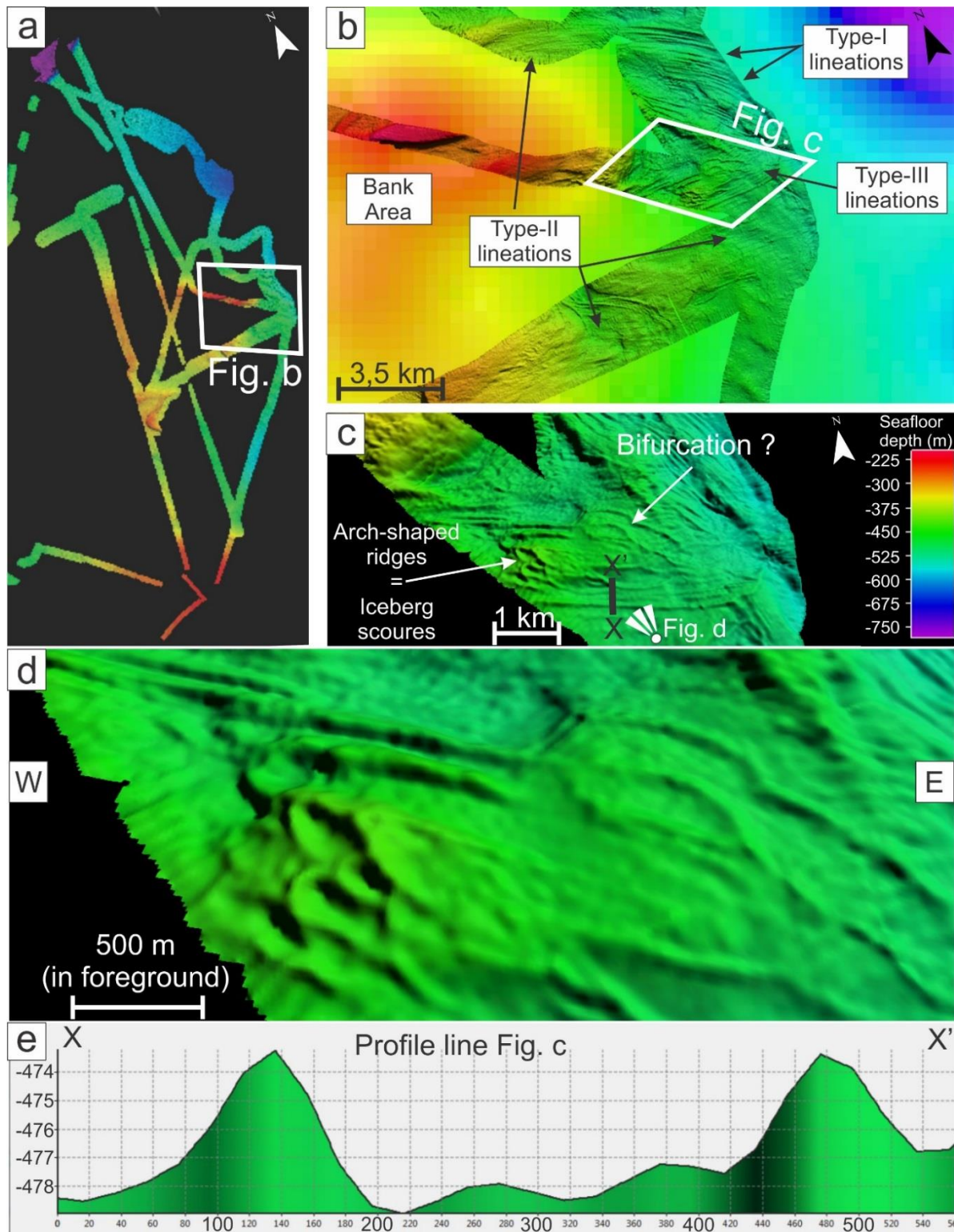
Fig. 4.5. Type-III lineations: Glacial lineations. (a) Inset map indicating the location of Fig. b. (b) Location of the Type-I, Type-II, and Type-III lineations in the inner basin. The with box indicates the location of Fig. c. (c) The Type-III lineations with a complex pattern of bifurcation and arch-shaped ridges (iceberg scours). The black line show the location of Fig. e (d) 3D-veiws of the Type-III lineations, with the bifurcation and the arch-shaped ridges visualized in an oblique angle. View angle is indicated in Fig. d. (e) Profile line through the Type-III lineations. All images are illuminated with an azimuth of 42°, and a sun angle of 6.5°, except the image in Fig.b. Vertical exaggeration of Fig. d is 6.
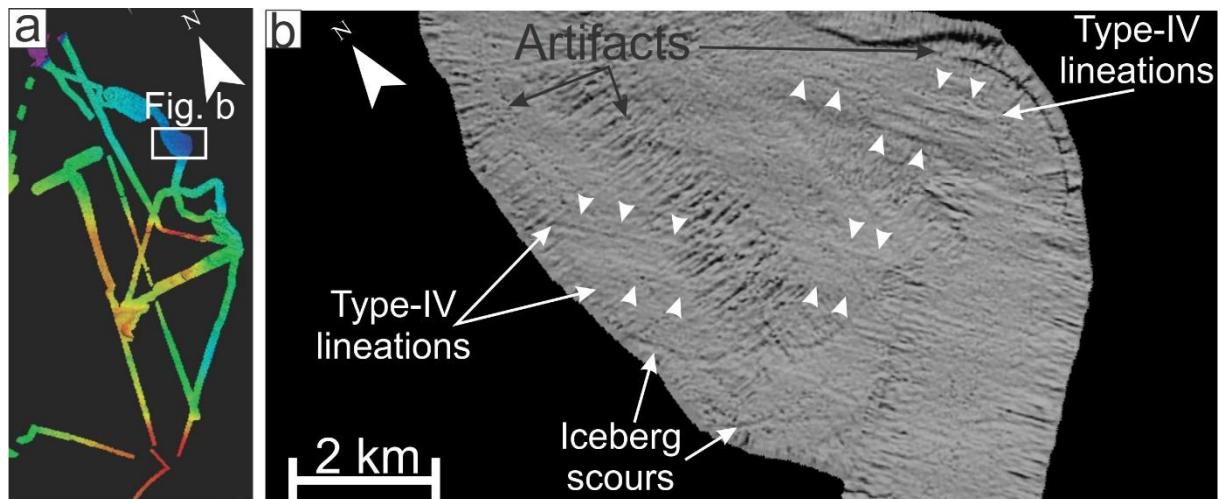
Fig. 4.6 Type-IV lineations: Glacial lineations. (a) Inset map indicating the location of Fig. b. (b) Grayscale image of the Type-IV lineations (the very subtle lineations) located in the middle basin. The short white arrows points towards some of the Type-IV lineations. The image in Fig. b is illuminated with an azimuth of 15,5°, and a sun angle of 3.6°.

4.2.2 Interpretation

The elongated linear features describe above are interpreted to be glacial lineations, which have been formed at the base of grounded ice in the Brunt Basin, where they reflect the direction of ice flow during their formation (Clark, 1993; Stokes and Clark, 2002b; Ottesen et al., 2005a; King et al., 2009).

The Type-I lineations (Fig. 4.3) are of similar morphology as MSGL reported from a number formerly ice-stream filled troughs on the Norwegian, Svalbard, Greenland and Antarctic continental margin (e.g. Ó Cofaigh et al., 2002; 2005a; Evans et al., 2004; 2005; Ottesen et al., 2005a; 2007; Dowdeswell et al., 2014). MSGL have for a long time been suggested to be forming parallel to the ice flow in a soft deforming till layer at the bed of fast flowing ice streams (e.g. Clark, 1993; Dowdeswell et al., 2004), which was confirmed by observations done by King et al (2009) from a radio-echo survey of MSGL forming bellow the Rutford Ice Stream. They are hence inferred to be MSGL, formed parallel to the former ice flow direction. Bifurcation of MSGL has also previously been reported from the continental shelf on Svalbard and Antarctica (Ó Cofaigh et al., 2005b; Dowdeswell et al., 2010; Hogan et al., 2010a).

The Type-II lineations (Fig. 4.4) are smaller in dimension and not as clearly defined as the Type-I lineations or MSGL typically found in high-latitude troughs, and are therefore believed to reflect different dynamics, with a more slow flowing ice during their formation (e.g. Stokes and Clark, 2002b; Ottesen and Dowdeswell, 2009). However, processes after their deposition can have affected their preservation, and hence their morphology, such as high post-sedimentation rates or grounded ice retreating over and modifying the lineations, making them more subtle. An indication of this could be deposition of recessional moraines or GZW in near vicinity of the lineations (Dowdeswell et al., 2008), which are in fact located near the Type-II lineations in Fig. 4.4d (see also Fig. 4.11d, page 69). However,

it is not possible to say from the currently available data, wheatear the morphology of the lineations have been modified after their formation, as there is no clear cross-cutting relationship between the two landforms resolvable in the bathymetrical data. The Type-II lineations are therefore only tentatively interpreted as glacial lineations at this point.

The set of Type-III lineations observed in Fig. 4.5, has also been considered to be recessional moraines, crevasse squeeze ridges or being a produced of iceberg scouring due to their bifurcation/bending and their lesser linearity. However, due to their symmetrical shape in cross-profile and that their orientation is similar to the other glacial lineations in the inner basin, they have also been interpreted as glacial lineations. Their complex pattern has most likely been created by later iceberg scouring (section 4.3), which has created the arch-shaped ridges and the bending/bifurcation of the ridges in Fig. 4.5c. The bifurcation observed could also have been formed as a result of topographical variation in the part of the inner basin and/or the steep slope towards the bank located in front of the bifurcated lineations. This could have affected the basal conditions and the dynamics of the ice, and as shown in Fig. 4.5a, the bifurcation of these lineations has occurred over a topographical high. This topographical high could have acted as a sticky spot where ice diverged around it, and/or the steep slope towards the bank could have made the ice flow diverge (e.g. Stokes et al., 2007; see also Fig. 4 therein).

The Type-IV lineations (Fig. 4.6) are even smaller and more subtle than the Type-II lineations. As the ridges are located in the deepest part of the basin, the subtle appearance of the ridges are inferred to have been be caused by a thin ice, which were lightly or episodically grounded in the areas of the subtle lineations. Evans et al. (2005) observed similar subtle lineations in the Prince Gustav Channel and the Robertson Trough, and suggested a similar formation of the subtle lineations.

There is an on-going debate regarding the origin of MSGL, if they are product from deposition, erosion or a combination of both (Clark, 1993; Clark et al., 2003a; Ó Cofaigh et al., 2005b; Spagnolo et al., 2014). Furthermore, bifurcation of MSGL do not support the groove ploughing theory (Clark et al., 2003a), and the exact formation of the various types of glacial lineations remains difficult to infer.

4.2.3 Distribution and direction

The different sets of glacial lineation sare distributed from the outer basin to the inner basin (Fig. 4.2), and their orientation varies between the different sets. One set of MSGL (Type-I lineations) is located in the outer part of the basin, and one set is located in the inner part of the basin (Fig. 4.3 and Fig. 4.5a). In the outer part of the basin, MSGL are observed 24 km from the shelf break, where they are situated on a relatively flat surface, oriented in a northwesterly direction (Fig. 4.3). The MSGL located in the

inner basin, are located in an area of uneven topography and are slightly curving, with a general direction towards the west-northwest, where they appear to curve around the bank towards the west.

The glacial lineations (Type-II lineations) located in the inner part of the basin (Fig. 4.2 and Fig. 4.4), have slightly different directions. The glacial lineations in Fig. 4.4a have a similar direction as the MSGL in the inner basin and have the same curving trend. The two sets of glacial lineations (Type-II and Type III) furthest to the southeast have a direction towards the west (Fig. 4.5), and the glacial lineations (Type-II) furthest towards the southwest have a more west-northwestern direction. The subtle lineations located in the middle of the basin have a direction is towards the northwest (Fig. 4.6).

4.3 Curvilinear depressions and rimmed semi-circular depressions: Iceberg scours

4.3.1 Description

Large parts of the study area consist of both linear to curvilinear depressions on the seafloor with a cross-cutting pattern (Fig. 4.7 and Fig. 4.8). They are commonly U-shaped in cross profile, but some are V-shaped or have a flat bottom. Most of the features have berms on the along their sides and some of these features have arch-shaped ridges and/or semi-circular depression at their termination (Fig. 4.7). The depths of the depressions vary between 7 m and less than 1 m, and the length varies between a couple of hundred meters to 11 km. Profile lines along the center axis of some of these depressions show corrugated ridges along the center of the depressions (Fig. 4.8d). The longest curvilinear depressions are located in the outer part of the basin, whereas on the gentler slope towards the bank, the curvilinear depressions are shorter with a complex pattern of arc-shaped ridges and rimmed semi-circular depressions (Fig. 4.7a and d). On the steeper slopes, such as the slope between the basin and the bank or the slope at the shelf edge, a complex pattern with semi-circular depressions and ridges occur (Fig. 4.7d). The curvilinear depressions commonly occur with random orientations, but in the outer basin, there are several aligned curvilinear depressions (Fig. 4.8), that are linear to semi-linear with a semi-parallel orientation towards the northwest. These are cross-cutting some of the MSGL (Fig. 4.3d and e), but are cross-cut by randomly oriented curvilinear depressions (Fig. 4.8).
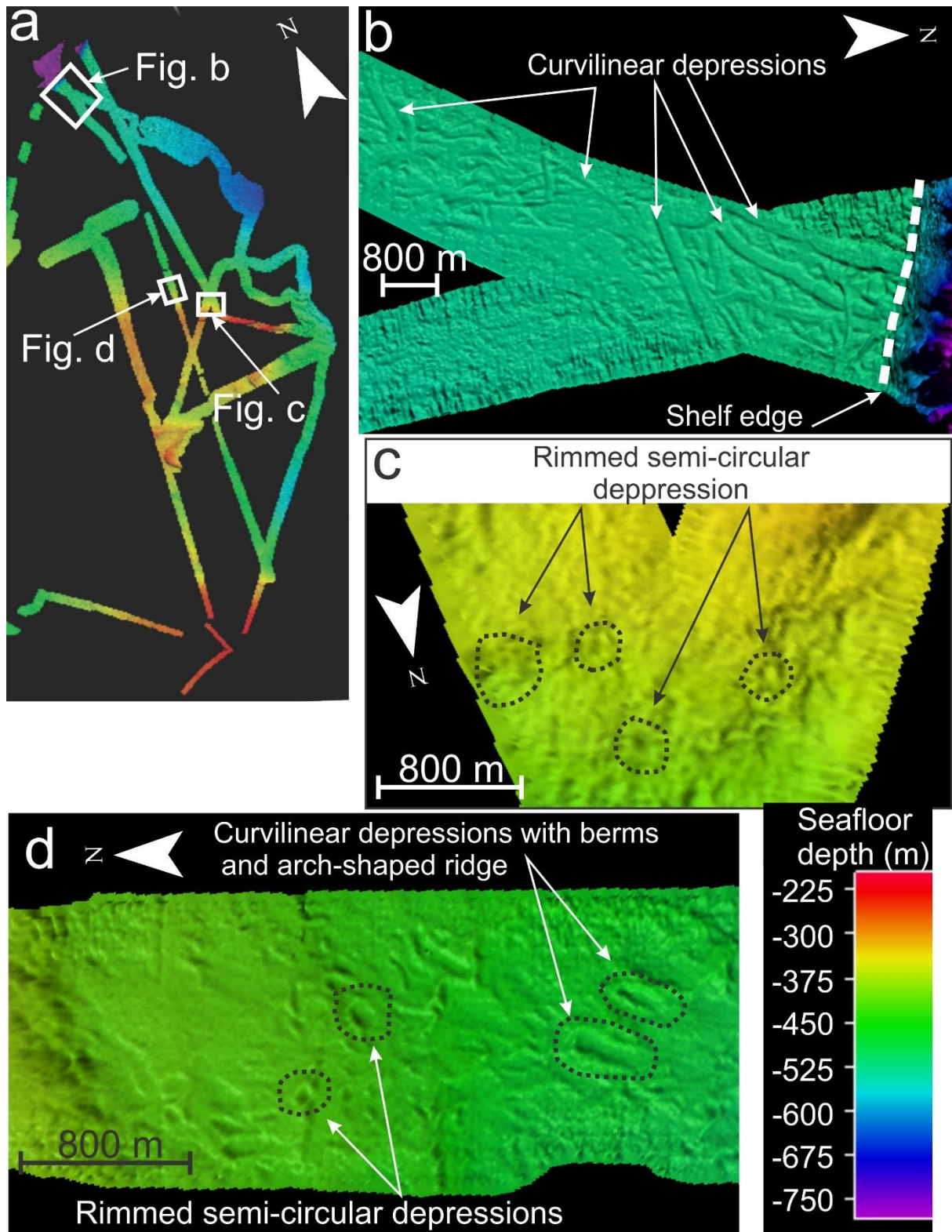
Fig. 4.7. Curvilinear depressions, arch-shaped ridges and rimmed semi-circular depressions: Iceberg scours. (a) Inset map indicating the location of Fig. b, c and d. (b) Curvilinear depressions at the shelf edge (c) Chaotic pattern of rimed semi-circular depression on the steeper bank basin slope. (d) Curvilinear depressions with berms on the side, with arch-shaped ridges at their termination, and rimmed semi-circular depressions. Fig. b is illuminated with an azimuth of 38º, and a sun angle of 4,9º, Fig. c is illuminated with an azimuth of 89,4º, and a sun angle of 4,9º, and Fig. d is illuminated with an azimuth of 123,7º and a sun angle of 12,1º.
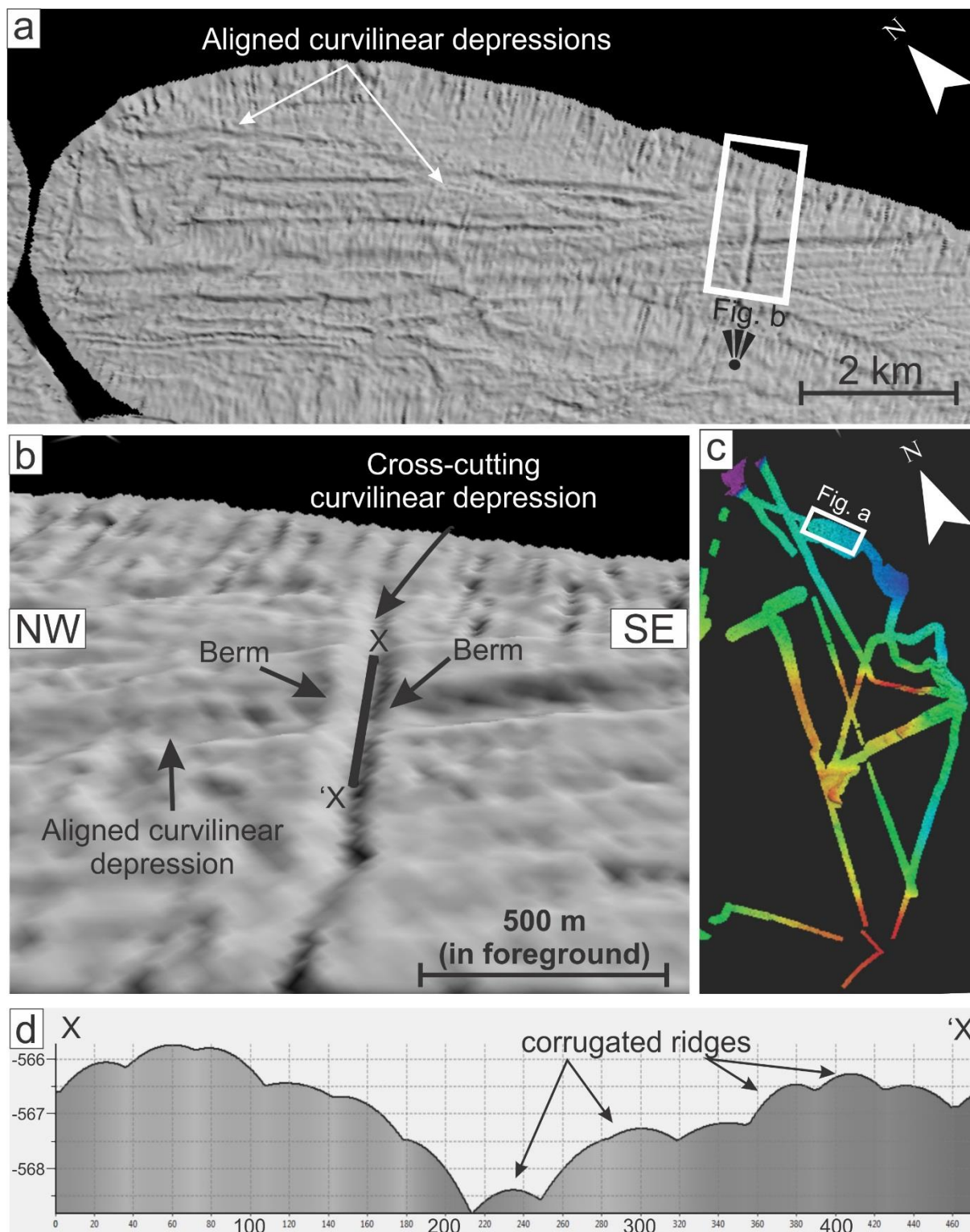
Fig. 4.8. (a) Grayscale image of aligned curvilinear depressions in the outer basin and random oriented curvilinear depressions (See also Fig. 4.3 where the curvilinear depression has been mapped out). Note the artifacts at the side of the bathymetrical lines, and in the overlapping parts. (b) 3D view of a random oriented curvilinear depression superimposed on the aligned curvilinear depression. Black line shows the profile line in Fig. d. View direction and location are indicated in Fig. a. (c) Indicating the location of Fig. a. (d) Profile line along the axis of the curvilinear depression showing corrugated ridges. Fig. a and b are illuminated with an azimuth of 98,1° and a sun angle of 7,4°. Vertical exaggeration of Fig. b is 6.

4.3.2 Interpretation

Both the randomly oriented and aligned linear to curvilinear depressions are interpreted as iceberg scours, formed by an iceberg keel scouring the sediments and creating a depression. Simultaneously, the sediments that the keel plows from the depression are deposited on the sides as berms (Belderson et al., 1973; Wellner et al., 2006). Iceberg scours are commonly observed on continental shelves, both in the Antarctic and Arctic, where iceberg keels have ploughed into soft substrate and reworked the surface sediments into iceberg turbate (Vorren et al., 1983a; Barnes and Lien, 1988; Dowdeswell et al., 1993). A result of this is that iceberg scours can obscure other preexisting geomorphological and sedimentological imprints of ice sheet presents and behavior. However, iceberg scours are not typically seen in areas consisting of bedrock or stiff till, due to the resistance of the substrate to scouring (e.g. Klages et al., 2015). The ridges inside the iceberg scours (Fig. 4.8d) could have been formed by tidal cycles as described by Jakobsson et al. (2011).

Parallel and aligned sets of iceberg scours are suggested to have been formed by two processes: either as several icebergs trapped in multiyear sea ice maintaining the icebergs in relative same positions to each other, or they were produced by multiple keels of a single huge iceberg (Jakobsson et al., 2011; Larter et al., 2012; Andreassen et al., 2014; Dowdeswell and Hogan, 2016). Since the aligned iceberg scours observed in the study area only are semi-parallel, and do not change direction simultaneously, they are suggested to have been formed by the keels of several icebergs trapped in a multiyear ice. Similar to the present conditions in the western part of the Brunt Ice Shelf System (Hulbe et al., 2005; section 2.2), but with icebergs large enough to ground on the seafloor. Since the direction of the iceberg scours is fairly similar to the direction of the set MSGL (Fig. 4.3d; section 4.2), it can be speculated that the mélange of icebergs has been pushed towards the shelf edge by an ice shelf extending from the formerly grounded ice that formed the MSGL and the icebergs. Similar to what Larter et al. (2012) suggest for parallel iceberg scours in the Filchner Trough. However, it is also possible that the transport of icebergs was driven by strong katabatic winds, or by ocean currents. The latter is less plausible, as the present coastal current and the Weddell Sea Gyre are flowing towards the southwest (Gladstone et al., 2001; Nicholls et al., 2009a; section 2.6.3), however the direction might have been different during the formation of the aligned iceberg scours.

The arch-shaped ridges and rimmed semi-circular depressions (Fig. 4.5b; Fig. 4.7c and d) are also suggested to be caused by grounded icebergs. These could have been formed when the icebergs encounter water depths where they were too big to float and ground on the seafloor, creating depressions and pushing sediments up to form ridges (Bass and Woodworth-Lynas, 1988). Examples of this are visible on Fig. 4.7c and d, where the arch-shaped ridges in association with the icebergs scours occur where the water depths decreases. The rimmed semi-circular depressions on the steeper slope are

interpreted to have been formed by floating icebergs bumping into the steep slope, scouring and/or grounding on the slope, similar to what Gales et al. (2014) observed on the steep slopes of the neighboring Halley Trough.

4.3.3 Distribution

The iceberg scours are dominating the seafloor in the outer part of the basin towards the shelf edge (Fig. 4.2), as well as the shallower middle part of the basin. The steeper slopes also contain iceberg scours. However, the iceberg scours are less abundant in the deeper part of the middle basin, in the inner basin, and on the shallower bank.

4.4 Hole and hill: Iceberg rolling

4.4.1 Description

Close to the shelf edge, there is a hill and a hole (Fig. 4.9), which both are mirroring each other in a cross-profile view (Fig. 4.9b). The hole is ~16 m at its deepest, whereas the hill is 15 m at its highest, the width and the length of both the hole and the hill is ~200 m and 160 m, respectively. The hill is located north of the corresponding hole, and a cross profile through both have a direction north-south (350°). There are no clear indications of any iceberg scours going into to the hole, and the feature appears to be very well preserved.

4.4.2 Interpretation

The feature described above closely resembles features describe by Klages et al., (2013) and Klages et al. (2015) from West Antarctica, where they interpreted the landform to be hill-hole pairs. Hill-hole pairs are believed to form by cold-based ice, where the ice freezes onto the bed beneath and rips up sediment rafts, forming a hole, and depositing the sediment raft downstream from the hole, forming a hill (Bluemle and Clayton, 1984; Hogan et al., 2010a). However, the distance between the hole and the hill observed in Fig. 4.9, is only minor, therefore, this feature could also be explained by tilting and rolling of an iceberg that pushes the sediments up from the hole to form a hill (Bass and Woodworth-Lynas, 1988). The latter is also supported by the preservation of the hill and the hole, as it appears to not have been reworked by iceberg scours, which you might expect if the feature was formed at the LGM or even before that, deposited when grounded ice would have reached the shelf edge. In addition the absence of similar features on the shelf edge supports the iceberg rolling formation of the hill and hole. The hill and the hole are therefore inferred to have been formed by an iceberg rolling over.
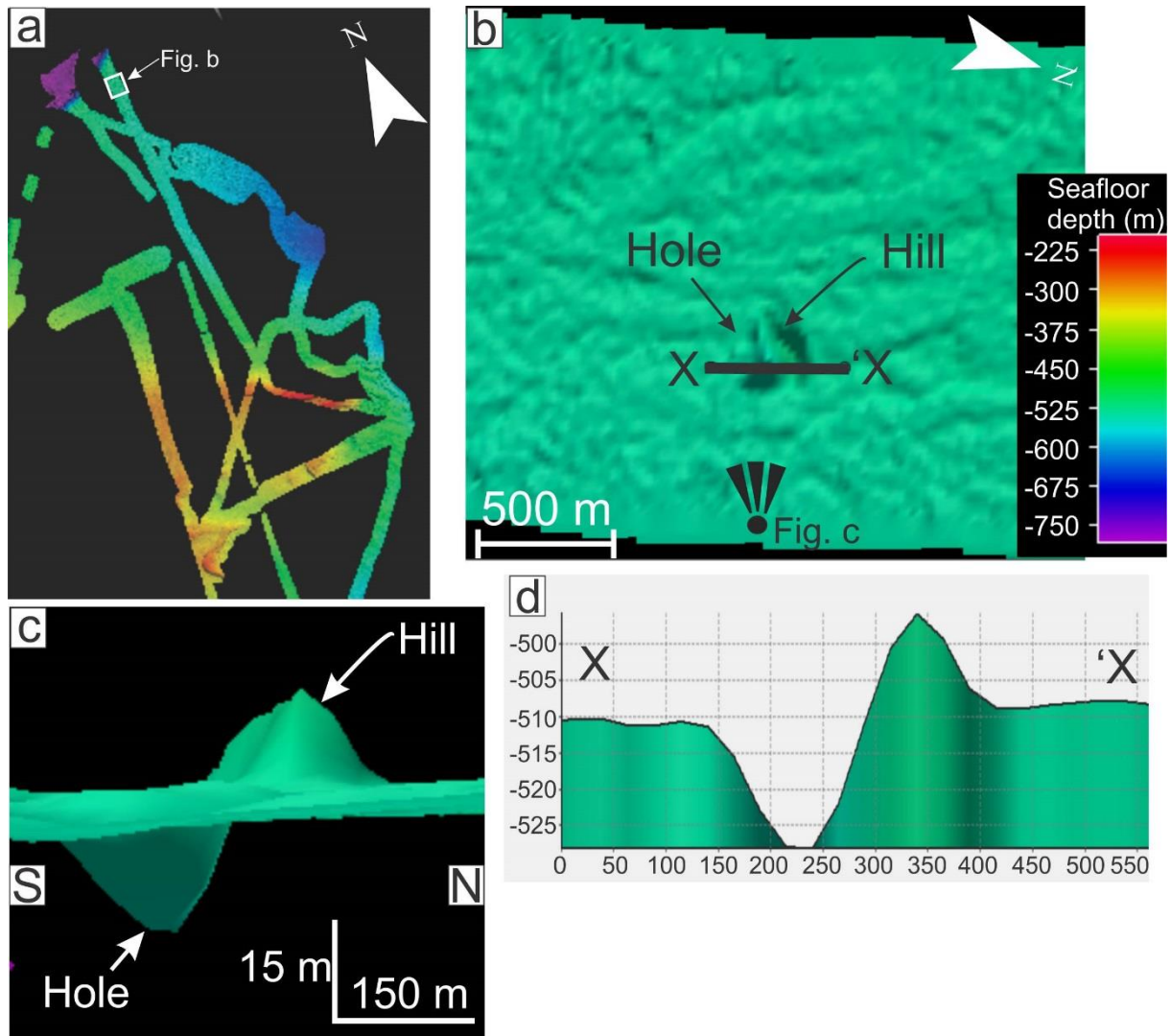
Fig. 4.9. (a) Indicates the location of Fig. b. (b) Hole and hill close to the shelf edge which are both mirroring each other. Note the abundant iceberg scours surrounding the hole and the hill. (c) 3D view of the hole and the hill, view direction is indicated in Fig. b. (d) Cross-sectional profile going through the hole and the hill. Fig. b and c are illuminated with an azimuth of 64,1º and a sun angle of 7,2º. Vertical exaggeration of Fig. c is 6.

4.5 Small curvilinear sets of ridges: Recessional moraines

4.5.1 Description

Two sets of small curvilinear ridges are located within the study area (Fig. 4.10 and Fig. 4.11). One set is located on the western side of the bank, on the slope down towards the Halley Trough with a northeast-southwest orientation of the ridges (Fig. 4.10). The other set is located in the inner basin, which has a less uniform orientation of ridges, but with a general direction of the crest line in a north-south direction (Fig. 4.11). In cross profile, the ridges are nearly symmetrical to asymmetrical, where the slope is generally steeper on the western side of both sets of ridges (land-distal). The ridges are relatively small, with heights and widths that vary between 2-15 m and 80-400 m, respectively. The spacing between the ridges varies between ~200-600 m for the ridges on the western side of the bank, and is less than 300 m

for the ridges in the inner part of the basin. The ridges in the inner part of the basin (Fig. 4.11), are partly overlapping each other, and are transverse to semi-parallel to the glacial lineation (described in section 4.2). Ten ridges were observed in the western part of the bank, but the data quality landwards from the westernmost ridge gets progressively poorer, which could prevent observation of more ridges. Four ridges were observed in the inner part of the basin.

4.5.2 Interpretation

These ridges are interpreted as recessional moraines, formed during minor still stands of the grounding line and/or by a small re-advances, where sediments are pushed into a ridge during an overall general retreat phase (e.g. Ottesen et al., 2005a; 2007; Dowdeswell et al., 2008). Their regular spacing, limited size, lack of linearity and asymmetric shape are all properties associated with small recessional moraines (Benn and Evans, 2010). Furthermore, the ridges resemble features interpreted as sets of recessional moraines from other formerly glaciated shelves (e.g. Ottesen et al., 2005a; 2007; 2009; Todd et al., 2007; Hogan et al., 2010a; Winsborrow et al., 2010; Klages et al., 2013; Rydningen et al., 2013). Some of these ridges have been suggested to be De Geer moraines (Hoppe, 1959), formed at or close to the grounding line during small still stands or re-advance during winter, when sea-ice covers suppressed iceberg calving. This could further indicate an annual cyclic deposition of these ridges, but long-term ice-front stability is also suggested to form the De Geer moraines (Lindén and Möller, 2005).
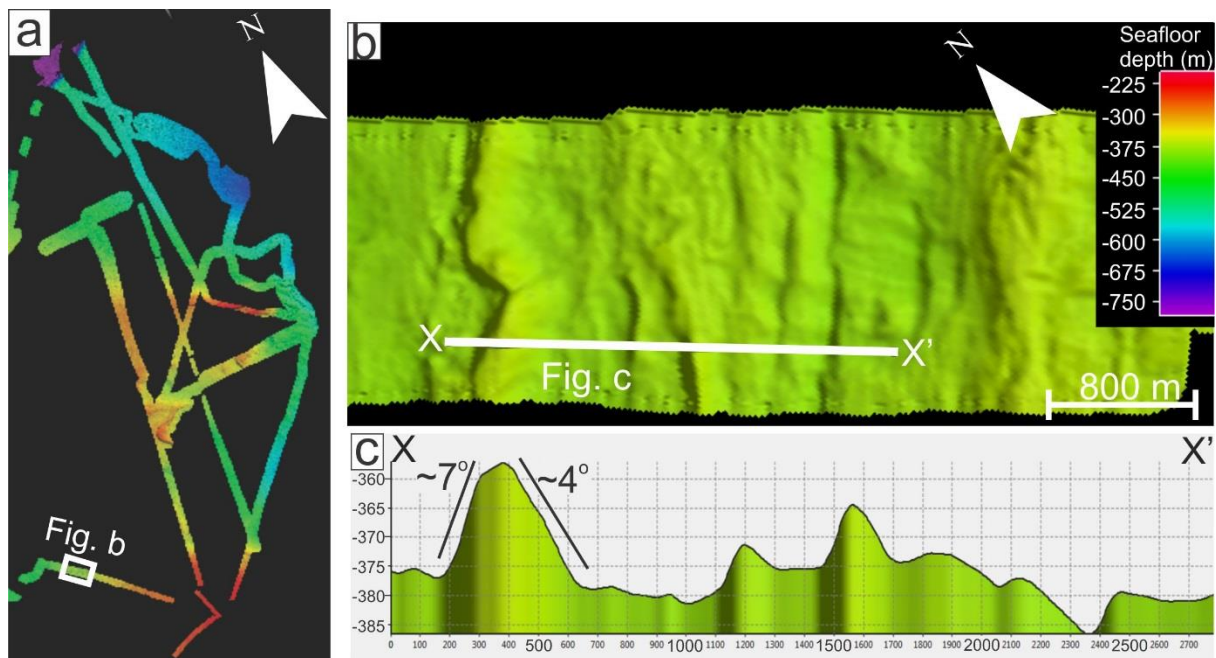
Fig. 4.10. Small curvilinear set of ridges: Recessional moraines. (a) White box indicates the location of Fig. b. (b) Small curvilinear set of ridges on the western side of the bank. (c) Profile line crossing several ridge fragments. The image in Fig. b is illuminated with an azimuth of 99,2º and a sun angle of 4,9º.

Fig. 4.11. Small curvilinear set of ridges: Recessional moraines. (a) White box indicates the location of Fig. b. (b) Small curvilinear set of ridges in the inner basin. (c) Interpretive image of Fig. b, black dotted lines indicate the location of the recessional moraines. (d) 3D view of the small curvilinear ridges, also note the glacial lineations (Type-II lineations) and the grounding zone wedge (GZW). 3D view angel is indicated in Fig. b. All images are illuminated with an azimuth of 99,2° and a sun angle of 6°, except Fig. a. The vertical exaggeration in Fig. d is 6.

Flink et al. (2015) provided compelling evidence that De Geer moraines can form on an annual basis as re-advance during wintertime, by comparing ice-front position and velocity data from satellite images with bathymetrical data in front of Tunabreen (a tidewater glacier in a fjord on Svalbard). Whether the recessional moraines observed in this study are formed annually by pushing or deposition is difficult to tell based on the bathymetry alone and the difference in size of these ridges may indicate a difference in the durations of halts or the distance in ice re-advancing (Ottesen et al., 2007). Nevertheless, the recessional moraines indicated a stepwise and slow retreat of the grounding line towards the east (e.g. Dowdeswell et al., 2008).

The westernmost ridge of the recessional moraines on the western side of the bank might in fact be a terminal moraine, marking the maximum extent of the grounded ice (Fig. 4.10). However, Gales et al. (2014) observed a large ridge, ~40 km further seaward from these ridges, which they interpreted to be a terminal moraine, marking the maximum extent of grounded ice in the Halley trough during the last LGM.

4.6 Sub-parallel bank basin ridges: Lateral shear-moraine

4.6.1 Description

At the lower part of the bank basin slope (Fig. 4.12), there are three fragments of ridges covered by four bathymetrical lines, going sub-parallel to the slope between the bank and the basin. The ridges are asymmetrical in cross profiles (Fig. 4.12), with a gentle slope (~1-2º) on their southern sides (towards the bank). The northern sides of the ridges (towards the basin) have a longer slope, which are generally steeper (~3-5º). The heights of the ridges relative to the adjacent seafloor vary between 5-15m on the southern side and between 15-40 m on the northern side. The widths of these ridges are between ~400-1200 m. To the south of the two westernmost ridge fragments, there is a sub-horizontal zone (Fig. 4.12c and e). The ridge fragments have relatively large amounts of iceberg scours (described in section 4.3) in their northern slope, whereas the southern slope of the ridge fragments have less iceberg scours.

4.6.2 Interpretation

These fragments of ridges have been interpreted to be one continuous ridge, based on their similar geometry, similar orientation, and their position along the slope (Fig. 4.12). They are further believed to be lateral shear-moraines, because they are oriented sub-parallel to the inferred ice-flow direction from the glacial lineations and MSGLs (described in section 4.2). This is also based on their position along the slope and that their geometry is resembles other lateral shear-moraines (Batchelor and Dowdeswell, 2016, named ice-stream lateral shear-moraine therein).
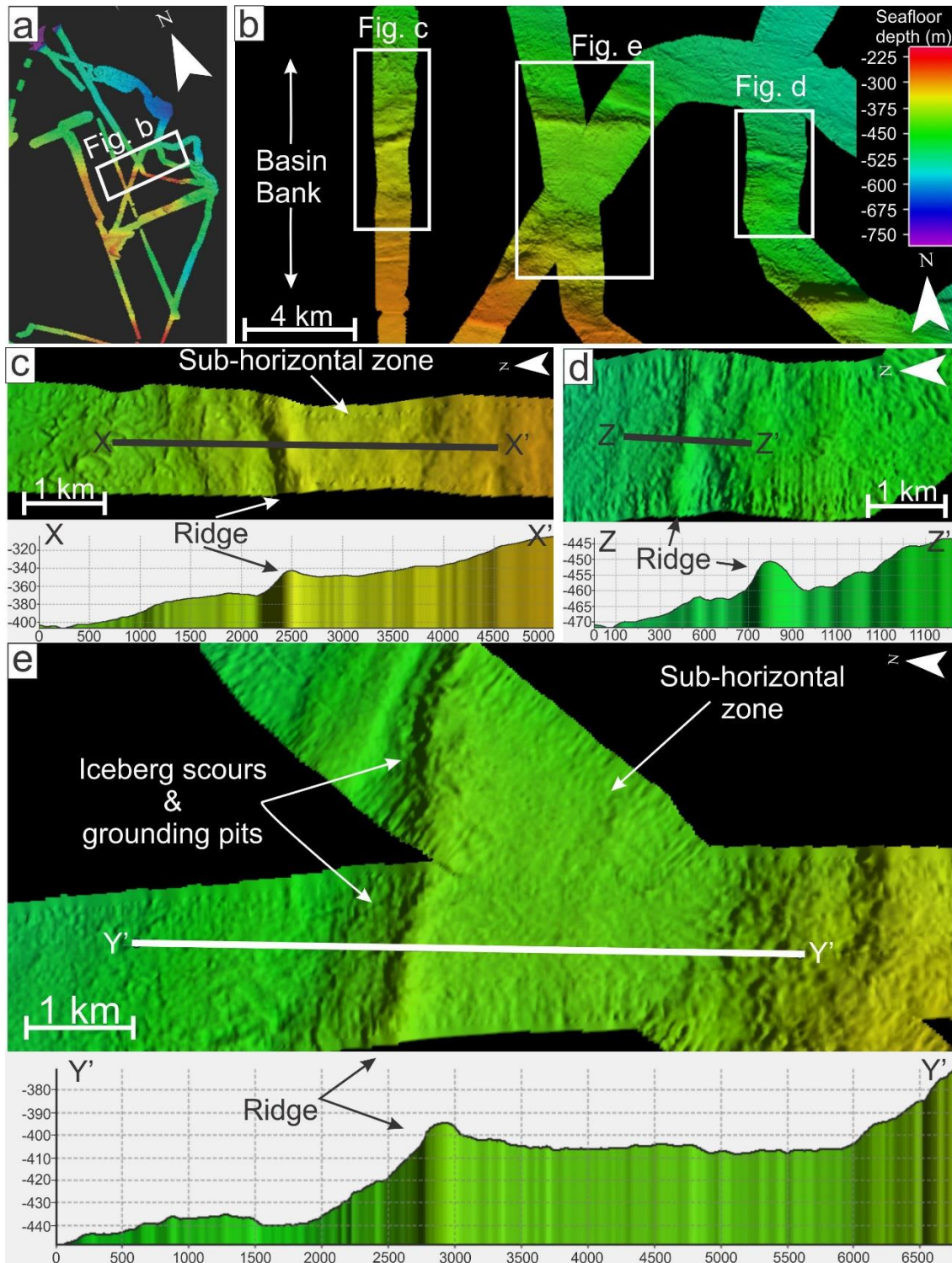
Fig. 4.12. Sub-parallel ridge fragments: Lateral shear-moraine (a) The white box indicates the location of Fig. b. (b) Location of the sub-parallel ridge fragments on the slope between the bank and the basin. White boxes indicate the location of the ridges and the location of Fig. c, d, and e. (c) The westernmost ridge fragment on the slope and a profile line across the ridge and parts of the slope, marked by the black line. Note the sub-horizontal zone above the ridge (south). (d) The easternmost ridge fragment on the slope and a profile line across the ridge, marked by the black line. Note that there is no sub-horizontal zone above the ridge (south). (e) Shows the ridge fragment in the center, with a profile line crossing the ridge and part of the slope. Note the large sub-horizontal zone above the ridge, and the marked change in the slope gradient towards the bank (south). All images are illuminated with an azimuth of 181,2° and a sun angle of 6,9°, except Fig. b.

Ice stream lateral shear-moraines, are suggested to form subglacially, at the transition between fast-flowing ice and slower flowing ice (e.g. Stokes and Clark, 2001, 2002a) and commonly have a steeper trough proximal side and a gentler trough distal side (Fig. 11 in Batchelor and Dowdeswell (2016)), which area similar to the geometry of the lateral moraine in this study (Fig. 4.12).

Ice stream lateral shear-moraines have been described from terrestrial environments in Canada (e.g. Stokes and Clark, 2002a; Cofaigh et al., 2010), from marine environments on Svalbard (Ottesen et al., 2005b) and on the Norwegian shelf (Ottesen et al., 2008; Rydningen et al., 2013), but have not been observed in Antarctica. Only a few lateral marginal-moraines have been observed on the Antarctic shelf, two in the Ross Sea (Ship et al., 1999), and one in East Antarctica, south of the Mertz Banks (e.g. Beaman and Harris, 2003). As the lateral marginal-moraines are deposited at the margin of an ice bordering ice-free ocean/terrain, their formation and shape differ from the ice-stream lateral shear-moraines. The lateral marginal-moraines are suggested to be formed by lateral accretion of sediments at the ice margin, prograding away from the ice, which creates an asymmetric ridge, with a steeper trough distal slope (Ship et al., 1999; Rydningen et al., 2013; Batchelor and Dowdeswell, 2016). This does not resemble the geometry of the lateral moraine in this study (Fig. 4.12), and further supports the interpretation of the ridges as lateral shear-moraine, rather than lateral marginal-moraine.

The sub-horizontal zone above the ridge (Fig. 4.12) is suggested to represent progradation of the ridge towards the basin, where the sediments are sourced from strain heating and basal melt-out from the shear zone between fast and slow flowing ice (Hindmarsh and Stokes, 2008). The steeper northern side of the ridge (Fig. 4.12) is interpreted to be caused by erosion of the faster flowing ice in the basin, similar to the suggestion of Batchelor and Dowdeswell (2016).

4.7 Arcuate Ridge: End moraine / Ice shelf moraine

4.7.1 Description

One prominent arcuate shaped ridge is located on the east side of the bank (Fig. 4.13). This ridge is asymmetric in cross profile, with a generally steeper distal slope (up to 17°) and a gentler proximal slope of ~2°-9°. The ridge stretches ~9 km in a northeast-southwest direction and reaches 55 m above the distal seafloor at its highest. The width of the ridge is difficult to measure, due to limited data, but it is ~800 m at its narrowest point in the north. The crest of the ridge has a very low gradient (Fig. 4.13), between less than 0,1° to 0,2°, and the width of the crest varies between 200-600m. The proximal slope is characterized by a hummocky terrain, with smaller ridges and depressions (Fig. 4.13c). One smaller continuous ridge segment is situated on the proximal side of the crest, on the northern part of the ridge. and is ~2m high. The small ridge segment has a gentle slope of ~2° towards the crest of the arcuate

ridge, and a steep slope (~9º) towards the proximal side of the arcuate ridge. The northern part of the arcuate ridge is lying on top of a undefined ridge.

4.7.2 Interpretation

The arcuate shape of the ridge resembles moraines deposited in front of valley or tidewater glaciers, either as moraines that are deposited inside the valley/fjords or moraines deposited just outside the valley/fjords. E.g., the arcuate moraine in front of Raudfjorden, in Northwestern Spitsbergen (Ottesen and Dowdeswell, 2009), the arcuate moraine inside the Royal Bay, South Georgia (Hodgson et al., 2014), and the moraines in the valley Bolterdalen (Sletten et al., 2001). Moraines in front of piedmont glaciers also resemble the arcuate shape (Barr and Clark, 2012), but are much more circular, with gentler slopes and lower reliefs. However, the ice depositions of the moraines mentioned above have been partly constricted by valleys and fjord topography and differ from the setting on the bank in the study area (Fig. 4.13).

A large arcuate moraine ridge named East Tromsøflaket Arcuate Moraine by Winsborrow et al. (2010), is described from a similar setting on the continental shelf offshore northern Norway, at ~170 m bellow the sea surface and deposited on a topographical high (Ottesen et al., 2008; Winsborrow et al., 2012). The ridge was suggested to have been formed during a re-advance, where grounded ice pushed sediments into the arcuate moraine (Winwsborrow et al., 2010).

The arcuate ridge (Fig. 4.13) is therefore interpreted to have been formed at the margin of grounded ice. Due to the morphology of the accurate ridge, it is suggested to have been formed by pushing sediments into the ridge, in a somewhat similar process as the East Tromsøflaket Arcuate Moraine (Winsborrow et al., 2010; Winsborrow et al., 2012). This is also supported by the hummocky terrain and the small continues ridge on the proximal side of the ridge (Fig. 4.13c), commonly observed together with push moraines, formed by thrusting of the sediments (Hambrey et al., 1997). Thus, the hummocky terrain can also partly have been formed by iceberg scours, but the resolution of the data makes it hard to tell. The steep slope on the distal side of the arcuate ridge may indicate that the ridge is highly compacted, which could be explained by compaction of the ridge from pushing, and even compaction by a partly grounded ice shelf floating up and down due to tidal cycles (Doake et al., 2002; Fricker and Padman, 2006).

The limited spatial extent of the ridge (Fig. 4.13) indicates a small and narrow ice forming the moraine. The arcuate ridge is therefore suggested to have been formed by either a narrow grounded ice (re-) advancing onto the bank, or by a small part of an ice shelf grounding onto the bank.
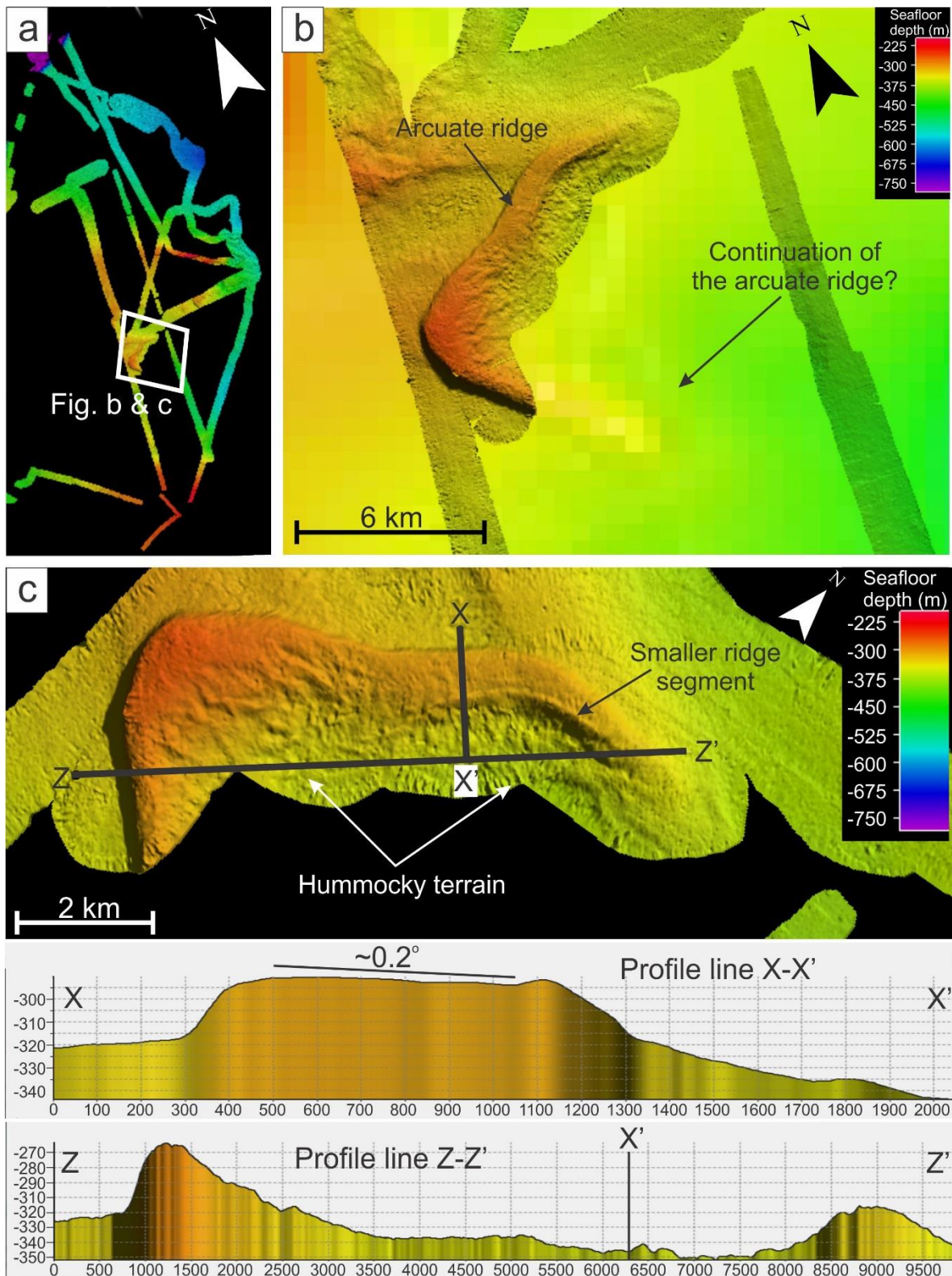
Fig. 4.13. Arcuate ridge: End moraine or ice shelf moraine. (a) White box indicates the location of Fig. b and c. (b) The arcuate ridge on the eastern side of the bank. Note its possible extent based on the IBCSO (Arndt et al., 2013). (c) The arcuate ridge and two profile line across the ridge, where the small ridge segment and the hummocky terrain are indicated. Note the low angeld crest of the ridge in profile line X-X'. Fig. b is illuminated with an azimuth of 57º, and a sun angle of 6,5º and Fig. c is illuminated with an azimuth of 57º and a sun angle of 5,3º.

In the scenario where a small part of the ice shelf grounded onto the bank, it most likely partly froze onto the seafloor (Vorren et al., 1983a), which would have provided friction, lower velocity and created an ice rumple on the surface of the ice shelf at the grounding point (e.g. Hulbe et al., 2005; Matsuoka et al., 2015). As the ice shelf landwards would have remained in floatation, with less friction and higher velocities, it would push the grounded part of the ice shelf in front of it. As the grounded part of the ice shelf was partly frozen to the seafloor, it would push the sediments up into the arcuate ridge. In a somewhat similar process to the formation of push moraines in front of polythermal glaciers, where the front of the glacier is cold based, and the main body is warm based (e.g. Hambrey et al., 1997; Glasser and Hambrey, 2003). In fact, parts of the modern Brunt Ice Shelf is grounded in an area called the McDonald Ice Rumples (Fig. 4.1), close to the ice shelf front (Hulbe et al., 2005), which might be a modern analog to the formation of the ridge. The low gradient crest of the ridge is also consistent with what is expected of ice shelf moraines, which reflect the low gradient of the base of an ice shelf (Benn and Evans, 2010). A similar theory of ice shelf grounding have been suggested for the Porcupine Bank, west of Ireland, where an ice shelf in front of the British-Irish Ice Sheet grounded onto the Porcupine Bank, pushing up sediments into moraine ridges (Peters et al., 2015).

In the scenario where the arcuate moraine (Fig. 4.13) was formed by a narrow grounded ice that re-advanced. The main body of ice must have been constantly retreating, as it has not been leaving any imprints, and only a small and narrow part of the ice would have re-advanced and pushed the sediments up into the arcuate moraine. Additionally, I suggest that there must have been an ice shelf in front of the grounded ice, that limited the vertical accommodation space and formed the low angled crest of the arcuate moraine (e.g. Powell and Alley, 1997; Dowdeswell and Fugelli, 2012; Batchelor and Dowdeswell, 2015). However, the spatial data coverage is rather limited and could be hiding critical information of the origin of the arcuate moraine.

4.8 Wedge-shaped ridges: Grounding zone wedges (GZW)

4.8.1 Description

Several fragments of wedge-shaped ridges are observed in the study area (Fig. 4.14). Their wedge shapes are caused by their asymmetrical morphology, with a steep slope on one side (7-12°), and a gentler slope on the other side (1-1,5°). The ridge fragments are located in two regions, in the inner part of the basin and at the edge of the bank (Fig. 4.14a). The height of these ridges varies between 15-50 m, where the smaller ridges are generally located in the basin. The length and width of these ridges are difficult to measure, but by measuring from where there is a marked change in slope gradient inferred to be the start of the ridge, to the steep slope, the width varies between ~1-3 km. The orientation of the ridges varies within the inner basin and on the bank (Fig. 4.14b and e), but the steeper slope of the ridges are generally

located on the western side. Glacial lineations and MSGL (described in section 4.2), are located in front of the gentle slope of some of these ridges (Fig. 4.4d), and one ridge has glacial lineations on top of it (Fig. 4.4a). Iceberg scours and grounding pits (described in section 4.3) are located on top of some of these ridges (Fig. 4.14d).

4.8.2 Interpretation

The asymmetric morphology of the ridges resembles landforms that have previously been interpreted as GZW, which are suggested to form predominantly by delivery of subglacial debris at the grounding line of marine-terminating ice sheets (e.g. Christoffersen et al., 2010; Dowdeswell and Fugelli, 2012; Batchelor and Dowdeswell, 2015). Due to their subdued relief and asymmetry, the GZWs are believed to form preferentially by grounded ice with ice shelves extending beyond the grounding line, where the vertical accommodation space is restricted (Dowdeswell and Fugelli, 2012; Batchelor and Dowdeswell, 2015). They differ from the classical marginal moraines, which have a clear positive relief, due to almost unlimited vertical accommodation space (Powell and Alley, 1997). As GZWs are usually related to ice-streams, and they are commonly found as transverse wedge-shaped ridges in palaeo-ice stream troughs, with a steeper ice distal side (e.g. Ó Cofaigh et al., 2005a; Graham et al., 2010; Larter et al., 2012; Rydningen et al., 2013; Hogan et al., 2016).

The ridge fragments located on the bank edge (Fig. 4.14) differ from this typical location of GZWs, but have a similar geometry and location as lateral GZWs described from the M'Clure Strait Trough in the Amundsen Gulf (Batchelor et al., 2014). They also show similarities to GZWs deposited on topographical highs that have acted as pinning points for the ice stability (Dowdeswell and Fugelli, 2012; Batchelor and Dowdeswell, 2015). The ridge fragments in the basin are more similar to the GZWs, in the way that they are located in the deeper areas, where one could expect a warm based and fast-flowing ice.

The ridge fragments are therefore interpreted as GZWs, where the use of GZW, refers to a non-generic term for sediment accumulation at or near the grounding line, where the deposition mechanisms are not specified at this point. The limited spatial coverage and the complex pattern of the ridges, especially on the edge of the bank (Fig. 4.14b and e), makes it very ambiguous to connect the ridges in a suitable manner, and hence subdividing them into lateral or frontal components. The asymmetrical shape is inferred to have been caused by an ice shelf extending beyond the grounded line, limiting the vertical accommodation space, where the steeper slope of the GZW fragments are interpreted as the ice distal side of the ridge (Powell and Alley, 1997; Dowdeswell and Fugelli, 2012; Batchelor and Dowdeswell, 2015). As it is not possible to connect all the ridge fragments into one continuous ridge, the ridge fragments must reflect at least more than one grounding line position, during different stages.
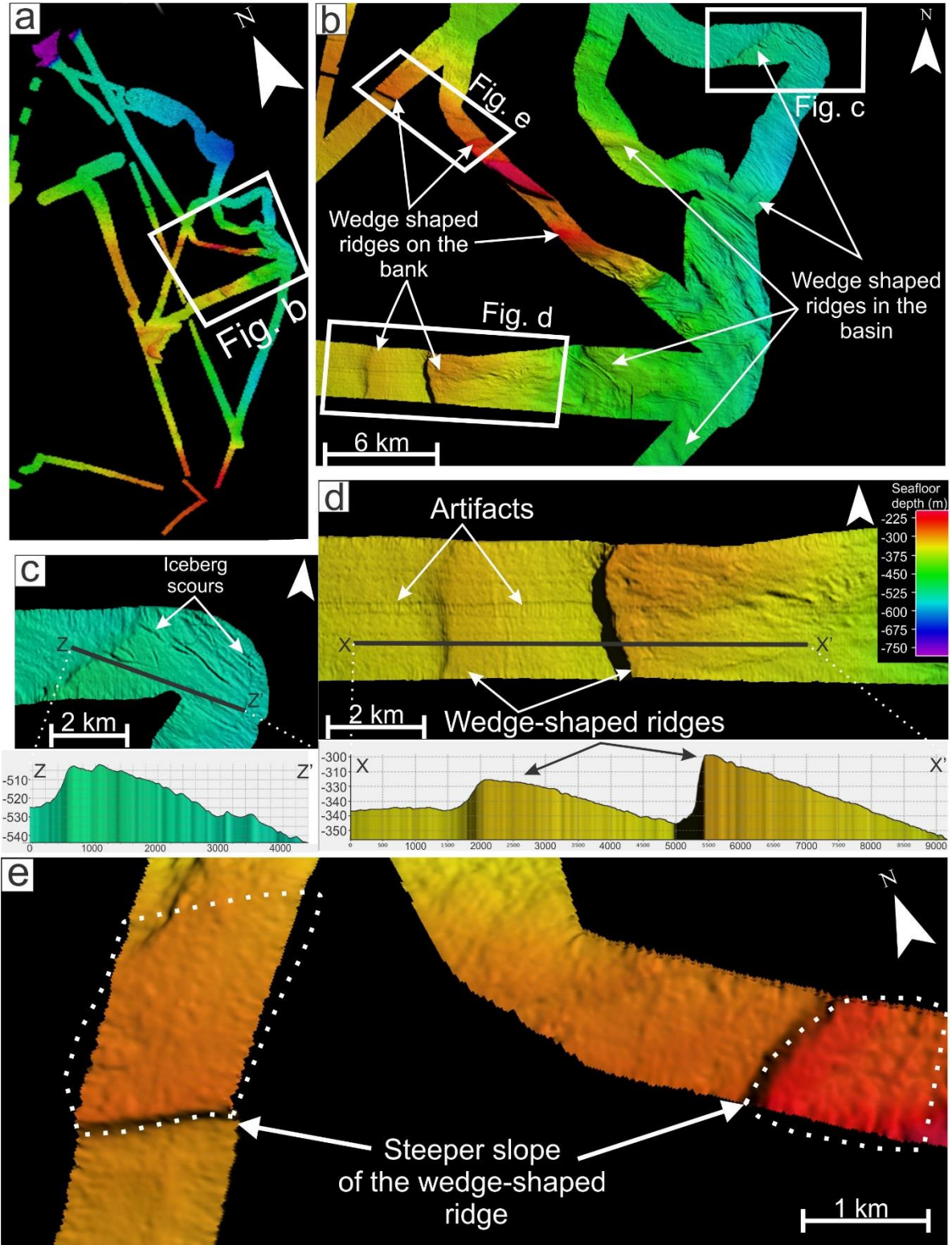
Fig. 4.14. Wedge-shaped ridges: Grounding zone wedges (GZW). (a) The white box indicates the location of Fig. b. (b) Location of the wedge-shaped ridges on the bank and in the inner basin. The white boxes indicate the location of Fig. c, d, and e. (c) Wedge-shaped ridge located in the inner basin and a profile line (Z-Z') going across the ridge. (d) Two wedge-shaped ridges on the eastern edge of the bank and a profile line (X-X') going across the two wedge-shaped ridges. (e) Two wedge-shaped ridges on the edge of the bank, with their steep slope facing in different directions. The wedge shaped ridges are outlined with white dotted lines. Fig. b, c, and e are illuminated with an azimuth of 90º, and a sun angle of 6º and Fig. d is illuminated with an azimuth of 51,5º and a sun angle of 6º.

The sizes of these GZWs fragments (Fig. 4.14d) indicate that the grounding lines remained relatively stable for a longer period, during a still-stand either in a retreat phase or related to a re-advance of the ice-margin (Batchelor and Dowdeswell, 2015). From Fig. 4.14d, we can see that the ridge fragments show a back stepping trend landwards, which might indicate an episodic retreat, with longer still stand in an overall retreat phase (cf. Dowdeswell et al., 2008).

4.9 Sediment scarp: Palaeo-grounding line

4.9.1 Description

At the transition between the middle and outer basin, there is a distinct sediment scarp, which is between 5-12 m high and has sinus shape in bird view (Fig. 4. 15). The MSGL on the northern, elevated side of the sediment scarp have a different orientation than the subtle glacial lineations on the southern side of the sediment scarp. The sediment scarp is parallel to semi parallel to the MSGL on the northern side.
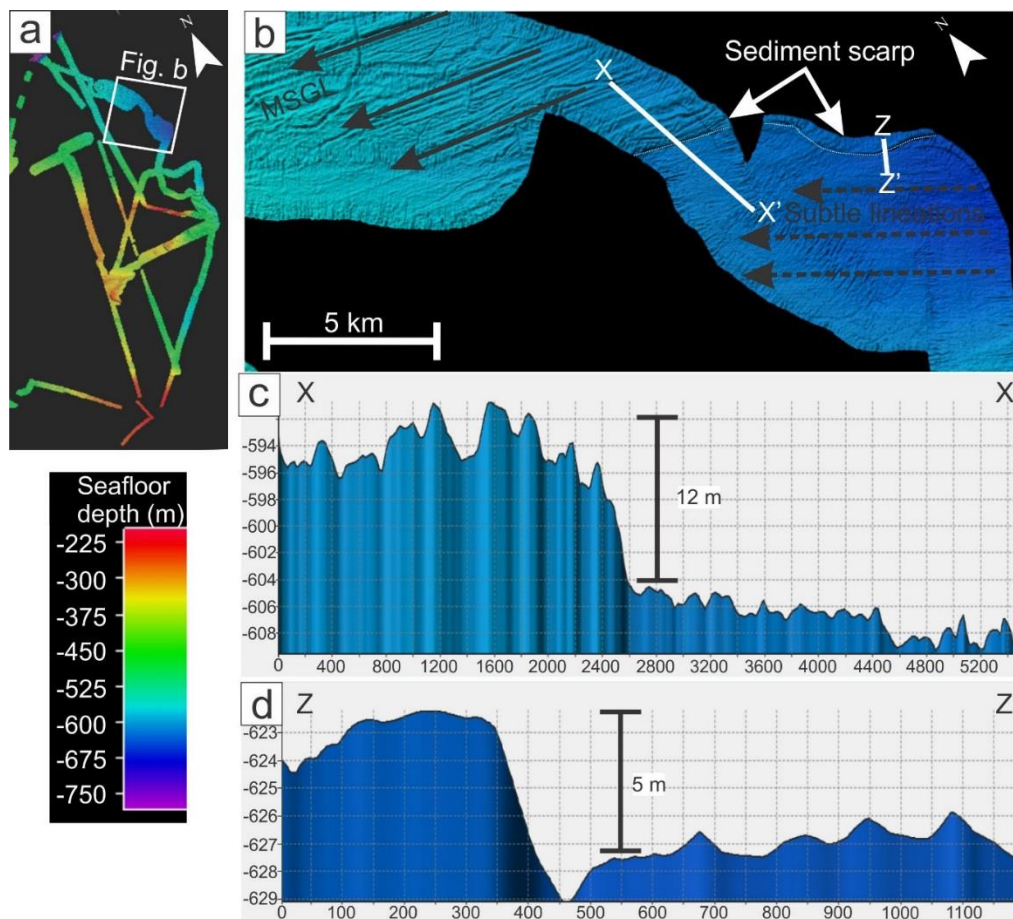
Fig. 4. 15 Sediment scarp: Palaeo-grounding line. (a) The white box indicates location of Fig. b. (b) Location of the sediment scarp at the transition from the middle to outer basin. Note the different directions of the MSGL and the subtle glacial lineation. The white lines indicates to location of profile line in Fig. c and d. (c and d) Profile line crossing the sediment scarp, vertical scale displays the height of the sediment scarp. Fig. b is illuminated with an azimuth of 29,7º, and a sun angle of 5,3º.

4.9.2 Interpretation

Based on the different orientations of the MSGL and the subtle glacial lineations, this sediment scarp has been interpreted to represent a palaeo-grounding line position. This is also supported by the fact that the MSGL and subtle glacial lineations are not cross cutting each other. The sediment scarp is similar to other sediment scarps described on the Antarctic continental shelf, where they have been interpreted to represent palaeo-grounding lines (Ó Cofaigh et al., 2005a; 2008; Graham et al., 2010). In those other cases, the sediment scarp has been linked to the distal part of a GZW, and it is plausible that the sediment scarp observed in the study area represents a distal part of a GZW. However, since the orientation of the MSGL are parallel to semi-parallel to the sediment scarp, it is presumably a lateral component of the palaeo-grounding line (Fig. 4. 15).

4.10 Undefined ridges

Several fragments of ridges are located within the study area, which are generally only covered by one or two bathymetrical lines. The limited spatial coverage of the data set, together with the low resolution from the IBCSO data set makes it difficult to assign any conclusive formation processes for the individual ridges. However, their character may suggest that they are formed or modified by glacial processes, but they might also be related to structural features. For now the ridges remain undefined.

5 Acoustic stratigraphy

The following chapter will assess the TOPAS sub-bottom profiler data collected during the JR2444 cruise to combines, surface, near-surface and deep sub-bottom profile information within the study area, to the landforms described in section 4, and to the sediment cores in section 6. The reflection patterns vary between the defined zones within the study area, and therefore, the description of the TOPAS data is divided into four subchapters, where the reflection patterns in each area will be described separately. The main seismic reflections and units are named accordingly to their location (bank-B, inner basin- I-B. middle basin, M-B, and outer basin, O-B).

The y-axis on the TOPAS profiles are shown in two-way travel time (TWT) in milliseconds (ms). Vertical scales in meters (m) shown in the profiles are converted from the TWT into meters using a sound velocity of 1500 m/s (e.g. Larter et al., 2012). In most of the TOPAS profiles, there is a "cloud-looking" feature above the seafloor reflection regarded as noise (e.g. Fig. 5.1e and g). Attempts to remove this during processing of the TOPAS data resulted in the disappearance of other features assumed real. In order to preserve real features, the "cloud" was not removed.

5.1 Description

5.1.1 Bank area

The TOPAS profiles from the bank (Fig. 5.1) show one acoustically strong reflection, defined as *Ref. B.* The *Ref. B.* are continues throughout the entire bank area, where it follows the seafloor, except for where the seafloor is locally intersected by features interpreted as iceberg scours (described in section 4.3; Fig. 5.1c). The reflection has a characteristically strong signal that is generally constant over the whole bank, both on the smooth featureless seafloor, as well as on the (moraine) ridges. However, it is weaker on the steeper slopes (Fig. 5.1c and d). In certain areas, there is a very subtle sub-bottom reflection (SBR), traceable for about 500-1000 m, and between ~2-7 ms in TWT below the seafloor reflection (~1-5 m; Fig. 5.1f and g).
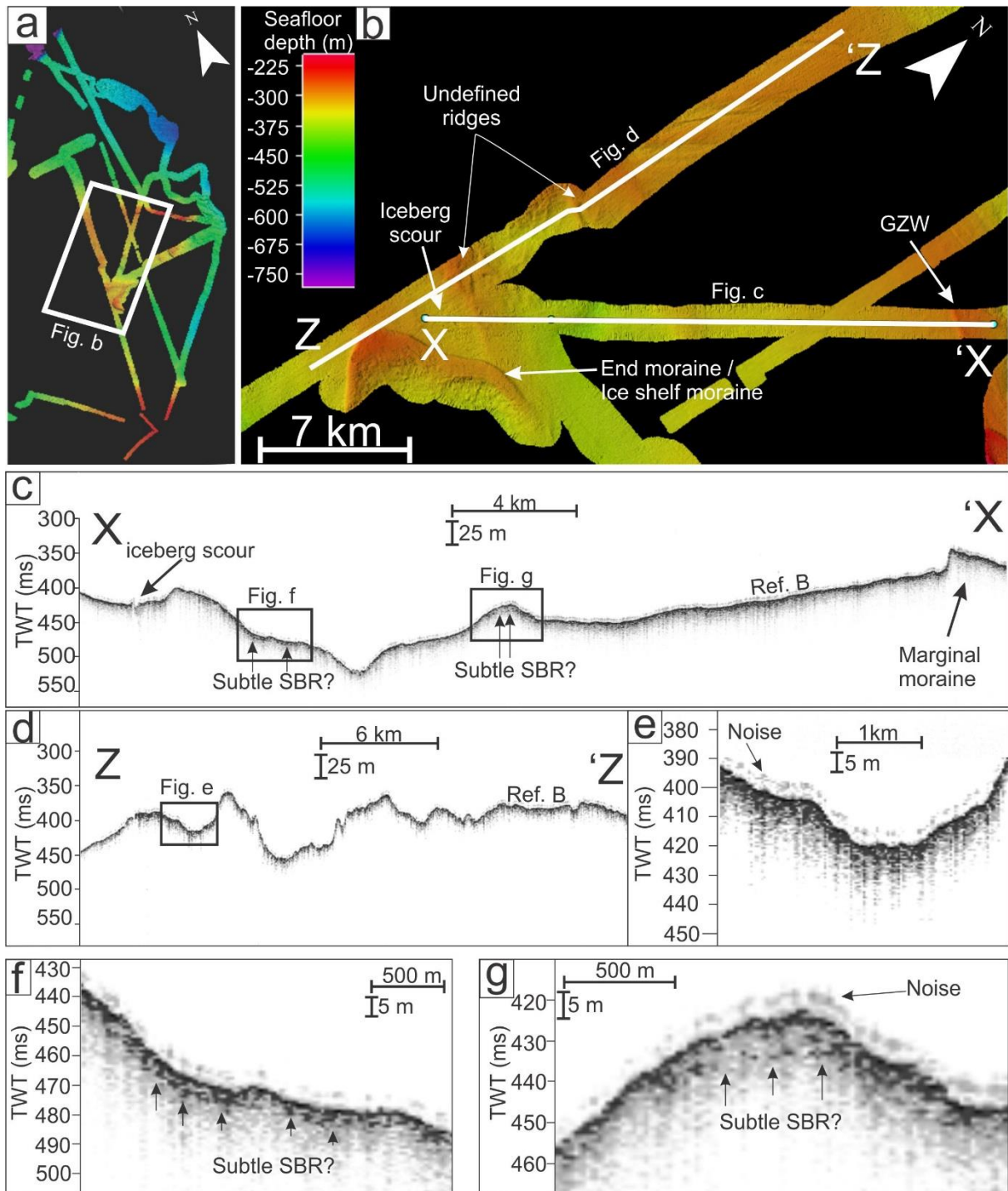
Fig. 5.1. TOPAS profiles from the Bank area. (a) The white box indicates the location of Fig. b. (b) Bathymetry of parts of the bank area, indicating the location of the TOPAS profiles in Fig. c and d. (c) TOPAS profiles from the bank area, displaying the Ref. B, and the location of Fig. f and g. Note that the Ref. B. is cut by an iceberg scour in the southwest part of the line. (d) TOPAS profile over a more uneven surface on the bank area, showing the Ref. B, and the location of Fig. e. (e) Close up of Ref. B, in a topographic depression, showing a chaotic and prolonged seafloor reflection. (f) Ref. B and a subtle continues SBR. (g) Ref. B over a topographical high, and a subtle SBR. Ref. B- Reflection bank area, SBR- sub-bottom reflection.

5.1.2 Inner basin

The TOPAS profiles from the inner basin are characterized by a strong reflection, defined *as Ref. I-B* (Fig. 5.2). Similar, to the *Ref. B* on the bank, the signal is weaker on the steeper slopes, and continues throughout most of the inner basin. However, patches of subtle SBRs occur occasionally below the *Ref. I-B* (Fig. 5.2c). Locally, acoustically transparent to semi-transparent ridges (ATR), with weak seafloor reflections, defined as *ATR I-B*, are located on top of the *Ref. I-B* (Fig. 5.2e and f). The ATRs are between ~2-7 ms TWT thick (~1-5 m) and 100-200 m wide (Fig. 5.1). At the southernmost part of the TOPAS line in Fig. 5.2c, there is a complex pattern of ATRs where the *Ref. I-B* disappears. This complex pattern is suggested to be caused by diffractions due to the oblique angle (~45º) of the TOPAS line above the MSGL. The seafloor in the inner basin are composed of glacial lineation and MSGL (Fig. 5.2b; see also section 4.2; page 56; Fig. 4.3) and the location of the lineations appears to correlate to the location of the ATR in the TOPAS profiles.

5.1.3 Middle basin

The TOPAS profile from the deeper area in the middle basin shows an acoustically transparent to semi-transparent layer, defined as *ATL 1 M-B* (Fig. 5.3), above a distinct and continuous SBR, and below a smooth seafloor reflection. The *ATL 1 M-B* varies in thickness between less than 2 ms in TWT (~1 m) to ~8 ms in TWT (~6 m). The configuration of the *ATL 1 M-B* appears to infill the deeper part of the middle basin. However, it terminates at the transition to the outer part of the basin (Fig. 5.4c and d), and pinches out on the slope towards the shallower area of the middle basin (Fig. 5.3c). Locally the *ATL 1 M-B* grades into ATRs towards the seafloor (Fig. 5.3d). The seafloor in this area is characterized by subtle glacial lineations (Fig. 5.3b; see also section 4.2; page 56; Fig. 4.6). Most of these lineations are too small to be resolved by the TOPAS system, but the ATR in Fig. 5.3d appears to correspond to a subtle lineation on the seafloor.

The TOPAS profile from the shallower part of the middle basin shows a chaotic acoustically transparent to semi-transparent layer, defined as *ATL 2 M-B,* between an irregular seafloor reflection, and a continuous SBR (Fig. 5.3e and f). The *ATL 2 M-B* is between ~2-4 ms in TWT thick (~1-3 m). It is thickest in the east, towards the feature interpreted as GZW (Fig. 5.3; see also section 4.8; page 75; Fig. 4.14c) However, it terminates abruptly on the steeper slope of the GZW. The *ATL 2 M-B* gets thinner towards the west, where it is less conform, and appears more as individual ATRs. Further to the west it pinches out towards the feature interpreted as a lateral shear-moraine (Fig. 5.3e; see also section 4.6; page 70; Fig. 4.12). Features interpreted as iceberg scours (see section 4.3; page 62) characterize the seafloor in this area (Fig. 5.3b).

Fig. 5.2. TOPAS profiles from the inner basin. (a) The white box indicates the location of Fig. b. (b) Bathymetry of the inner basin. White lines indicates the location of the TOPAS profiles in Fig. c and f. (c) TOPAS profile from the inner basin. (d) Interpretive line drawing of the TOPAS profile shown in Fig. c with Ref. I-B, ATR I-B, and subtle SBR. (e) Close-up of the TOPAS line in Fig. c, with a prominent ATR I-B located on top of the Ref. I-B. (f) TOPAS profile with ATR I-B located on top of the Ref. I-B. ATR I-B, - acoustic transparent ridges inner basin area, Ref. I-B. - reflection inner basin area. SBR –sub-bottom reflection.
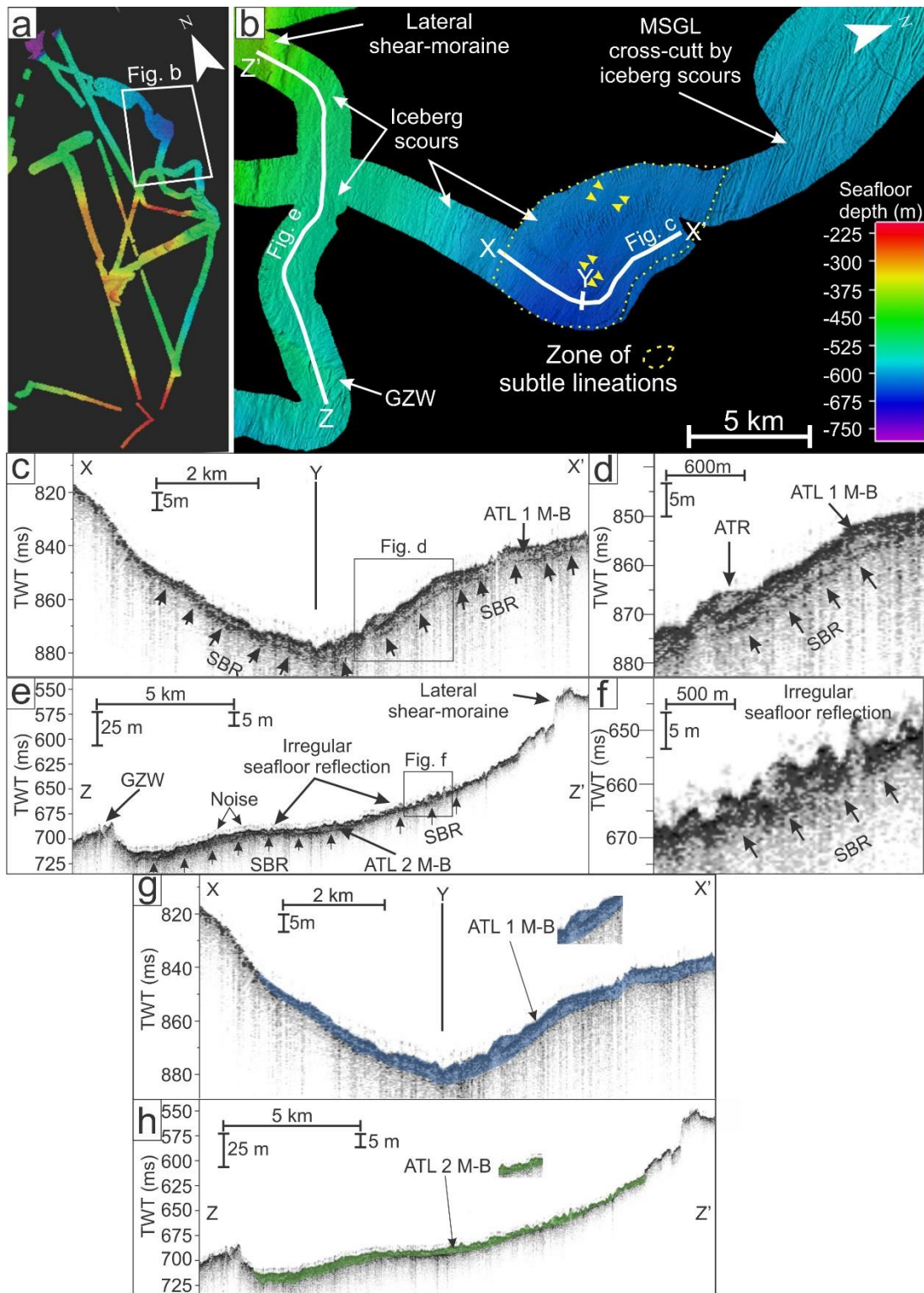
Fig. 5.3. TOPAS profiles from the middle basin. (a) The white box indicates location of Fig. b. (b) Bathymetry of the middle basin, with white lines indicating the location of TOPAS profiles in Fig. c and e. The short yellow arrows indicates the location of subtle glacial lineations. (c) TOPAS profile with ATL1 M-B, a distinct SBR and the location of Fig. d. (d) Close up of the ATL 1 M-B, the SBR, and an ATR. (e) TOPAS profile with the ATL 2 M-B, the SBR, an irregular seafloor reflection, and the location of Fig. f. (f) Close up of the irregular seafloor reflection above the ATL 2 M-B. (g) Interpretation of the TOPAS profile in Fig c. (h) Interpretation of the TOPAS profile in Fig e. ATL 1 M-B, - acoustic transparent layer 1 middle basin area, ATL 2 M-B, - acoustic transparent layer 2 middle basin area, SBR –sub-bottom reflection. ATR- acoustic transparent ridge, GZW- grounding zone wedge.

5.1.4 Outer basin

At the transition from the middle to the outer basin, there is a marked change in the TOPAS profile, where the sediment scarp is located (Fig. 5.4). A thick unit of acoustically transparent to semi-transparent layer is located on the northern side of the sediment scarp, defined as *ATL 1 O-B*. The *ATL 1 O-B* is located above a smooth SBR that is relatively subtle and discontinuous (Fig. 5.4c). The seafloor reflection, which marks the top of the *ATL 1 O-B*, displays a set of regularly spaced ridges at the surface of *ATL 1 O-B*. The unit is up to 20 ms thick in TWT (~15 m) at the south of the unit, and thins gradually in the northwesterly direction to a thickness of ~8 ms in twt (~6 m). Multiple MSGL occur in this area of the *ATL 1 O-B* (section 4.2; *p. 56*), which are partly cross-cut by iceberg scours (section 4.3; *p. 62*)
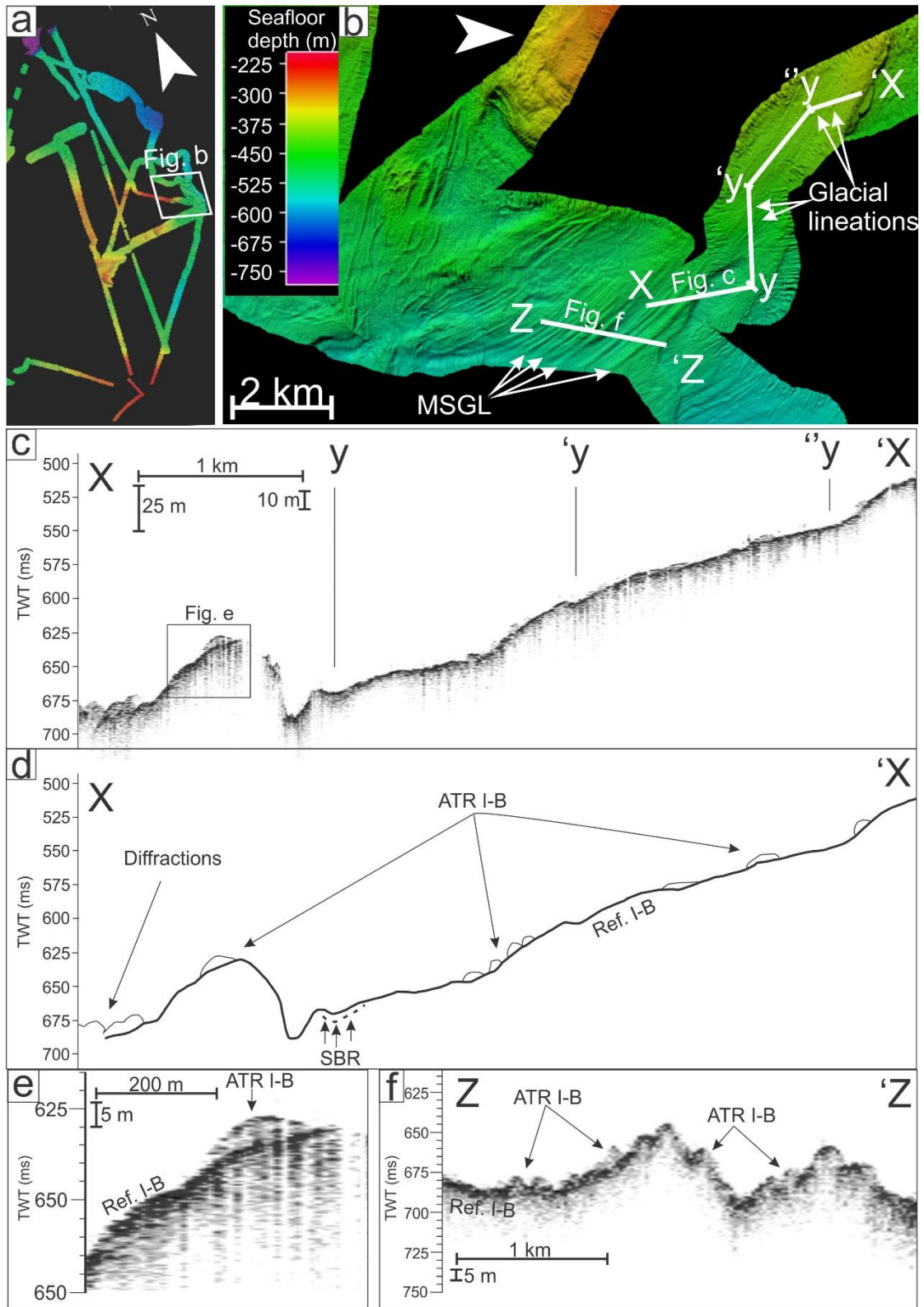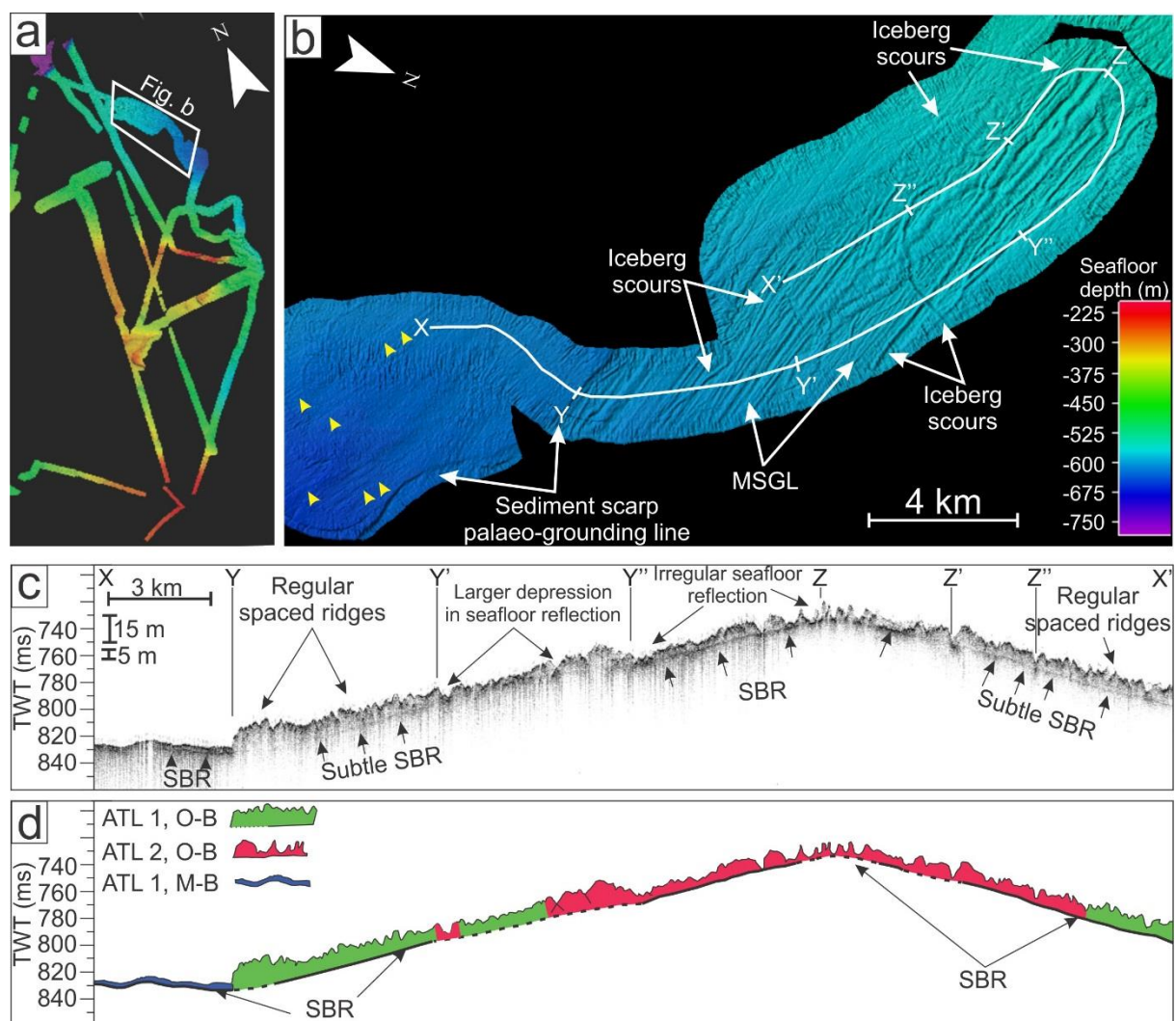

Fig. 5.4. TOPAS profile from the middle and outer basin. (a) The white box indicates the location of Fig. b (b) Bathymetry of the transition from the middle to the outer basin, marked by the sediment scarp. White line indicates the location of the TOPAS profile in Fig. c. The short yellow arrows indicates the location of subtle glacial lineations in the middle basin. (c) TOPAS profile with acoustically transparent to semi-transparent layer above a distinct to subtle sub bottom reflection (SBR). (d) Interpretation of the acoustic units on TOPAS profile shown in Fig. c. ATL 1 M-B- acoustic transparent layer 1 middle basin area, ATL 1 O-B- acoustic transparent layer 1 outer basin area, ATL 2 O-B- acoustic transparent layer 2 outer basin area.

There is a diffuse change in the character of the ATL towards the northwest (Fig. 5.4c). Where the seafloor reflection of the ATL, defined as *ATL 2 O-B*, gets much more irregular, with larger depressions, and more patchy continuation towards the northwest (Fig. 5.4c). A smooth SBR is located below the *ATL 2 O-B,* which is subtle to distinct and continuous to discontinuous. Further to the northwest, towards the shelf edge, the *ATL 2 O-B* becomes more patchy and thinner, and appears more as individual ATR, than an actual layer (similar to observations on other TOPAS profiles from the vicinity of the shelf edge, but not shown here). Multiple iceberg scours have been identifies in the area where ATL 2 O-B occurs (Fig. 5.4b; see also section 4.3; *p.* 62; Fig. 4.8b).

5.2 Interpretation

5.2.1 Reflections

Strong seafloor reflections with poor TOPAS penetration imply a hard substratum such as stiff till or/and bedrock (e.g. Batchelor et al., 2011; Reinardy et al., 2011a; Klages et al., 2014). Based on the character of the *Ref. B* (Fig. 5.1) and *Ref. I-B* (Fig. 5.2), which are similar on the smooth seafloor as well as on the moraine ridges, that the reflection is intersected by iceberg scours and the subtle SBR below *Ref. B* and *Ref. I-B,* they are interpreted to reflect the surface of stiff till. However, it is possible that the strong reflection might actually represent bedrock cropping out at certain areas. As one would expect similar reflection characteristics. However, given the smoothness of the seafloor (e.g. Fig. 5.1b) which do not resemble areas interpreted as bedrock (cf. Larter et al., 2009; Graham et al., 2010; Hogan et al., 2010b), it is likely that the reflections represents stiff till in most parts of the bank and inner basin. The subtle SBR bellow *Ref. B* and *Ref. I-B,* probably represents the top of bedrock and/or internal structures within the stiff till (Forwick and Vorren, 2010).

The SBR bellow the *ATL 1 M-B, ATL 2 M-B* (Fig. 5.3c and e), *ATL 1 O-B* and *ATL 2 O-B* (Fig. 5.4c) is suggested to represent the surface of stiff till of bedrock, based on the fact that the SBR appears to be acoustically impenetrable with the TOPAS system. Vibrocores recovered from troughs on the West Antarctic continental shelf, has demonstrated that such SBR below ATL often correspond to the surface of stiff till (e.g. Evans et al., 2005; Ó Cofaigh et al., 2005a; Reinardy et al., 2011a). However, with the current available data it is not possible to determine if the SBR correspond to the surface of stiff till or bedrock.
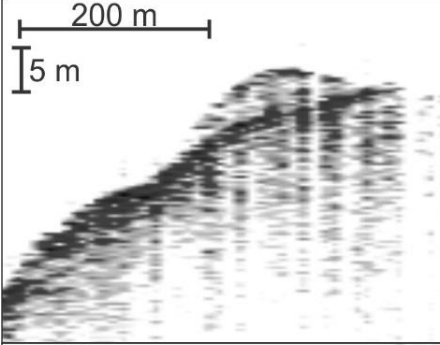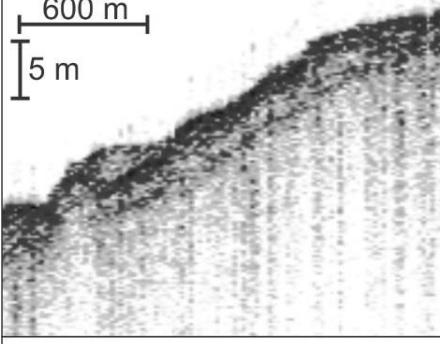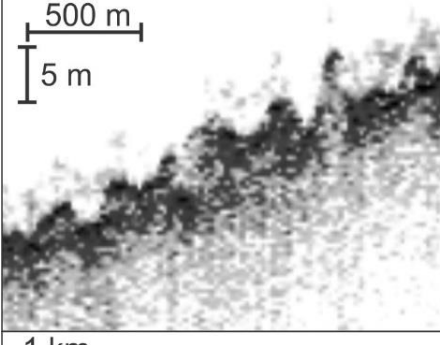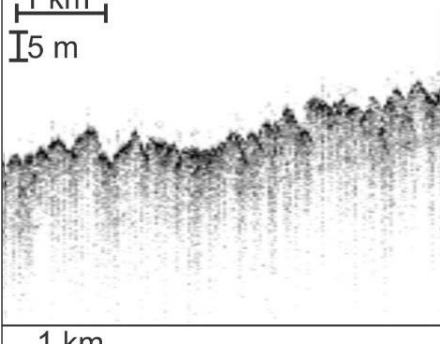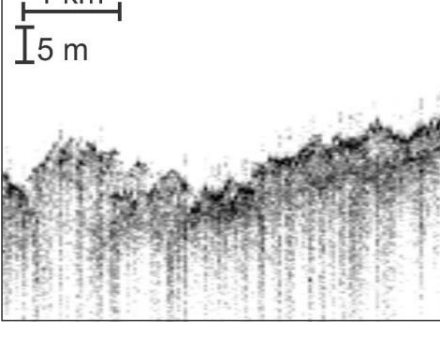
200 m ⊢————⊣ · 5 m	**ATR I-B = Soft deformation till** Acoustic transparent to semi-transparent ridges. Corresponds to MSGL and glacial lineation at the seafloor.
600 m ⊢———⊣ · 5 m	**ATL 1 M-B = Soft deformation till** Acoustic transparent to semi-transparent layer. Located in an area with subtle glacial lineations.
500 m ⊢——⊣ · 5 m	**ATL 2 M-B = Iceberg turbate** Acoustic transparent to semi-transparent layer and ridges. Located in an area dominated by iceberg scours.
1 km ⊢——⊣ · 5 m	**ATL 1 O-B = Soft deformation till** Acoustic transparent to semi-transparent layer. Located in an area dominated by MSGL.
1 km ⊢——⊣ · 5 m	**ATL 2 O-B = Iceberg turbate** Acoustic transparent to semi-transparent layer. Located in an area dominated by iceberg scours.

Fig. 5.5. Summary of acoustic units in the study area, together with interpretation of the units.

5.2.2 Acoustic units

5.2.2.1 ATR I-B, ATL 1 M-B, and ATL 1 O-B: Soft deformation till

The *ATR I-B*, which correspond to the MSGL and glacial lineations (Fig. 5.2c), the *ATL 1 M-B*, located in the area of subtle lineations, (Fig. 5.3c), and the *ATL 1 O-B,* located in the area of MSGL (Fig. 5.4c), are interpreted to be composed of predominantly soft deformation till, where the ridge represents soft deformation till moulded into glacial lineations and MSGL. Similar ATL and ATR bellow MSGL and glacial lineations have been observed in a several troughs on the Antarctic shelf, and cores recovered from these units have been inferred to be composed of soft deformable till (e.g. Ó Cofaigh et al., 2002; 2005a; 2005b; Dowdeswell et al., 2004; Evans et al., 2005; Reinardy et al., 2011a). Typically, ATL composed of soft deformation till, are more continuous than what is observed in the inner basin (Fig. 5.2c and f). However, it possible that any soft deformable till layer between the *ATR I-B* are too thin to be resolved by the TOPAS system, or that ice flow occurred by localized basal-sliding over bedrock or stiff till, rather than by deformation sliding (Engelhardt and Kamb, 1998; Evans et al., 2005; King et al., 2009; Reinardy et al., 2011a).

The *ATL1 M-B* (Fig. 5.3c) might also represent glaciomarine sediments, as it appears to infill the deeper part of the basin. However, as the glaciomarine sediment thickness elsewhere is thinner than the vertical resolution of the TOPAS system, it is rather unlikely that the *ATL 1 M-B* represent glaciomarine sediment with a thickness between ~2-8 ms twt (~2-6 m).

5.2.2.2 ATL 2 M-B and ATL 2 O-B: Iceberg turbate

The *ATL 2 M-B*, (Fig. 5.3e), and the *ATL 2 O-B* (Fig. 5.4c) located in the areas characterized by iceberg scours, is interpreted be composed of sediments heavily affected by iceberg scouring that have caused the highly irregular upper surface of the ATLs, and transformed most of the sediments into iceberg turbate (e.g. Vorren et al., 1983a; Dowdeswell et al., 1993; Batchelor et al., 2011).

6 Lithostratigraphy

6.1 Introduction

Four gravity cores (GC) were recovered from the Brunt Basin (Fig. 6.1). GC634 and GC635 were recovered from the inner basin, GC635 was recovered from the deeper part of the middle basin, and GC637 was recovered from the outer basin. This chapter presents a compilation of the results obtained from the different methods described in chapter 3 that was applied on the sediments in the cores
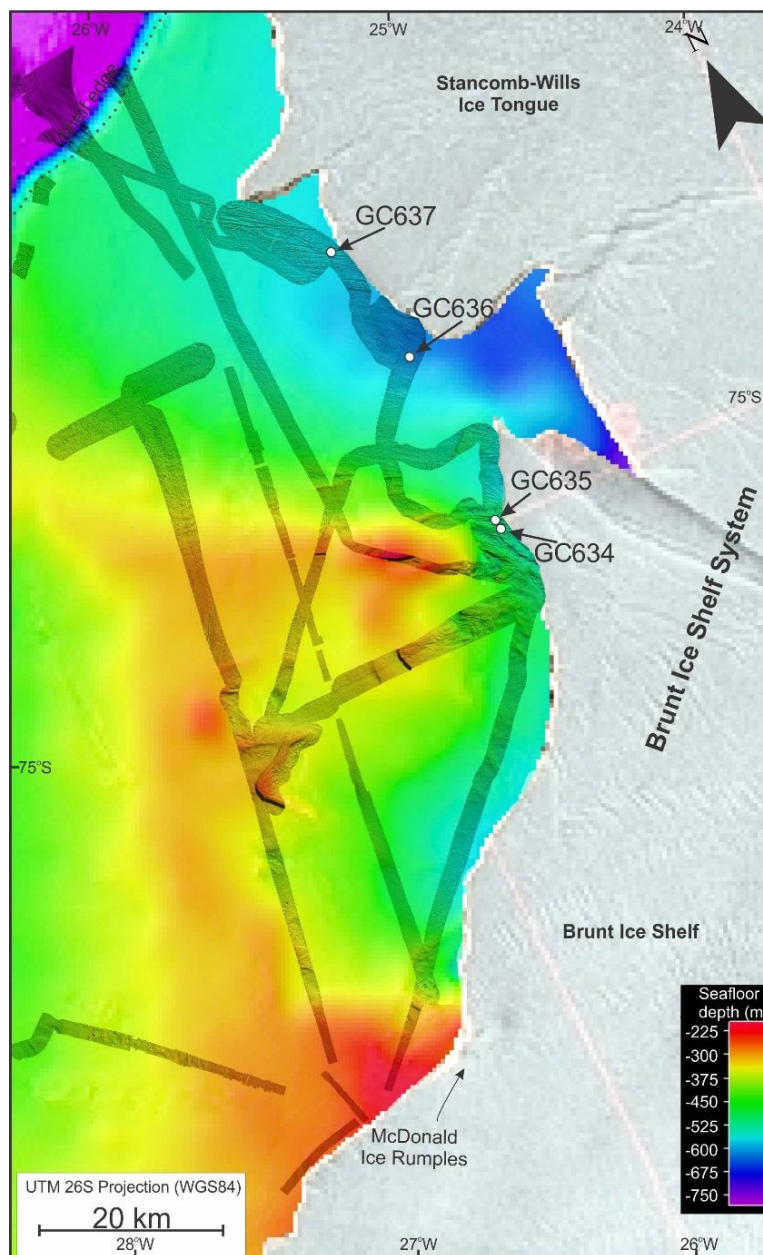
Fig. 6.1. Location of the cores (circles) used in this study. The swath bathymetrical data is draped on top the IBCSO bathymetry (Arndt et al., 2013), with an Envisat synthetic aperture radar image of the Brunt Ice Shelf System, taken the 4th March 2011.

6.1.1 Color code

The color and color codes of the sediments are based on the color of the core immediately after opening and can be compared to the color images in Fig. 6.6 (*p.* 96). The sediment colors changed between the opening of the cores and acquisition of line-scan images with the XRF core scanner. Images acquired with the XRF core scanner are used in figures showing physical properties, element compositions and sand fraction analyses, because they reveal the structures of the cores more clearly.

6.1.2 Lithological and structural logs

The lithological and structural logs presented in this chapter were created based on integration of visual core observation, X-radiographs, biogenic content in sand fraction and smear slides and grain-size data. The lithological key used from the lithology is displayed in Fig. 6.2. The key has been adapted from Melles and Kuhn (1993) and has been used by BAS for investigating sediments on the Antarctic shelf.

The sediment cores are composed of diamictons (see below). The definition used for diamicton are as followed: Unsorted to poorly sorted terrigenous sediment, consisting of mud, sand, and (more than 12.5%) gravel, (sub) angular gravel and/or cobbles is present throughout, and the sediment shows some consolidation. If the gravel and cobble grains are predominantly in contact with each other: *grain-supported diamicton*; if not: *matrix-supported diamicton*. If the sediment is dominated by a sandy matrix: *sandy diamicton*, if the sediment is dominated by a muddy matrix: *muddy diamicton*.

Fig. 6.2. Triangle diagram displaying the classification system for mud sand and gravel used. Modified from Melles and Kuhn (1993)

6.1.3 Smear-slide analysis

Several smear slides from different depths in the cores were taken to investigate the biogenic content in the mud fraction. Where the sediment had more than 15% biogenic content, it was named accordingly. The typical biogenic component was sponge spicules, diatoms and rare foraminiferas (Fig. 6.3).

6.1.4 AMS radiocarbon dating

The results from the AMS radiocarbon datings and the calibrated ages are displayed in Table 6.1. Three ^{14}C dates was obtained from GC634, and one ^{14}C date was obtained from GC635. The ages displayed in the figures and discussed further in the text are the calibrated ages. For GC634, at 12 cm, an ages of 2.8 cal. ka BP will be used. For GC635, at 50 cm, an age of 8.5 cal. ka BP will be used.
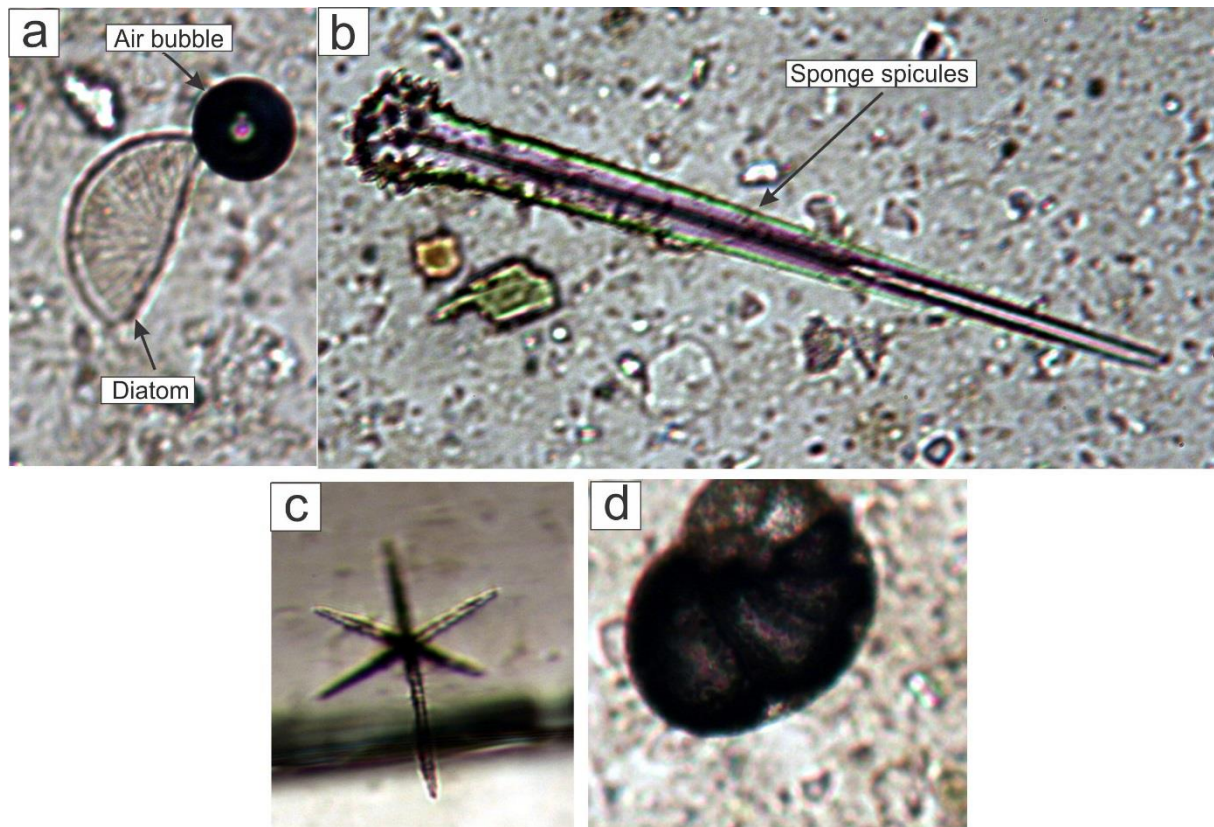
Fig. 6.3. Images of smear slides. (a) Fragment of a diatom. N.B.The black air bubble is from making the smear slide. (b) Example of a sponge spicules. (c) Well preserved sponge spicules. (d) Foraminifera. Note that there are no scale on the images, because of time constrains.

Table 6.1.
Uncorrected, corrected and calibrated AMS 14C dates from the Brunt Basin, together with sample depth and dated material. (AIO- acid insoluble organic matter) A marine reservoir effect correction of 1300 ± 70 years (Berkman and Forman, 1996) is used. Both the σ 1 and σ 2 range is plotted for each calibrated age (min-max), but the mean age are used trough out the text. AMS ^{14}C was carried out at the ETH laboratory in Zurich, using the MICADAS. The ^{14}C ages were calibrated using the Calib 7.1 software, with the Marine13 (Reimer et al., 2013). As the "pre-defined" marine reservoir effect in the Marine13 is 405, the delta R used to calibrate was set to 895.

Lab reference	Core	Sampling Depth (cm)	Species	^{14}C age BP	Cal. yr BP Calib 7.1 σ 1 range	Cal. yr BP Calib 7.1 2 σ range	Cal. yr BP Calib 7.1 1 σ mean
69711.1.1	GC634	12	*N. Pachyderma* sin.	5470 (±70)	2673-2948	2543-3097	2826
69710.1.1	GC634	12	*Cibicides* sp.	5490 (±70)	2705-2996	2559-3161	2857
70776.1.1	GC634	12	*AIO*	11550 (±220)	9676-10491	9303-10632	10010
69709.1.1	GC635	50	One shell valve	10475 (±90)	8340-8623	8240-8764	8499

6.1.5 Glauconite

During the investigation of the sand fraction from each core, green and orange grains were observed (Fig. 6.4). Some of these grains had a similar shape as foraminiferas, whereas others were elliptic to almost flat. These grains are suggested to be glauconite. Element composition and structures investigated with acquired with a SEM, correlated well with compositions of glauconite grains from other studies (Odin and Matter, 1981; Bornhold and Giresse, 1985; Lim et al., 2000).
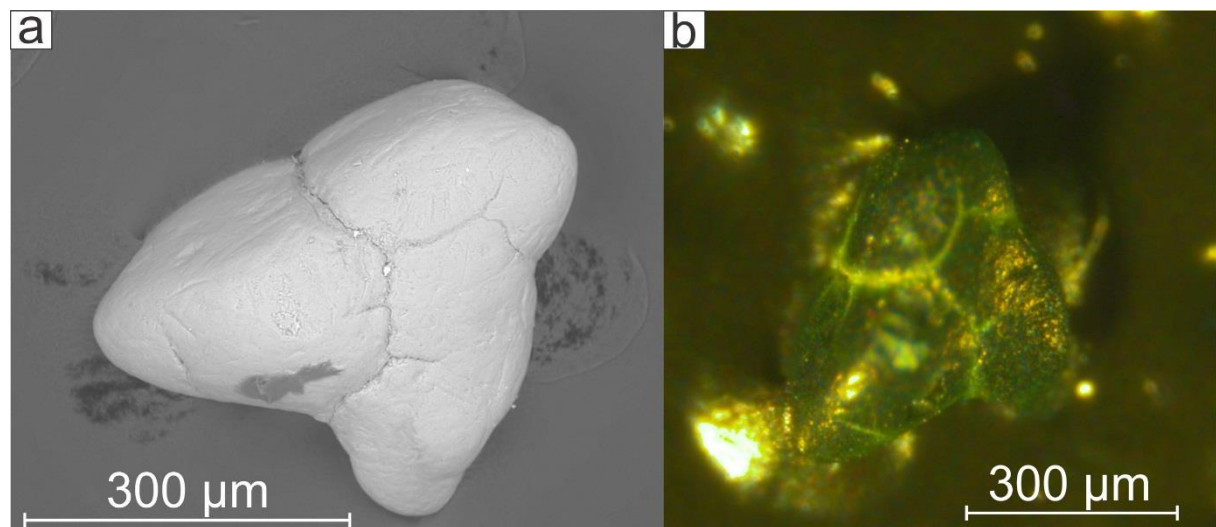
Fig. 6.4. (a) Image of glauconite grain acquired with a scanning election microscope (SEM). The white minerals in the middle of the glauconite crack are pyrites. (b) Color image of the same glauconite grain.

6.1.6 Subtle layer artifact

The X-radiographs of the cores show repeated subtle stratification that was ~1 cm thick, with "layers" of coarser sediments that appeared denser, and finer grained sediments that appeared less dense throughout all the core sections (Fig. 6.5). This subtle stratification were artifacts. This were proved by acquisition of new X-radiographs of one core section. By changing the settings to taking images every 1 cm, the "layers" became thinner (~1cm) and by taking images every 0.5 cm, the subtle stratification disappeared (Fig. 6.5).

6.1.7 Mottles

During the visual core observation immediately after opening of the cores, more grayish brown mottles were observed on the fresh surfaces. These were most probably caused by small variation in the matrix of the sediments and/or the ability of the sediment to keep the water, rather than by bioturbation, as the latter was absent. E.g. intervals with mottles in the lower part of GC635 (101-93 cm) observed strait after opening revealed a more sandy matrix when surface of the core dried.
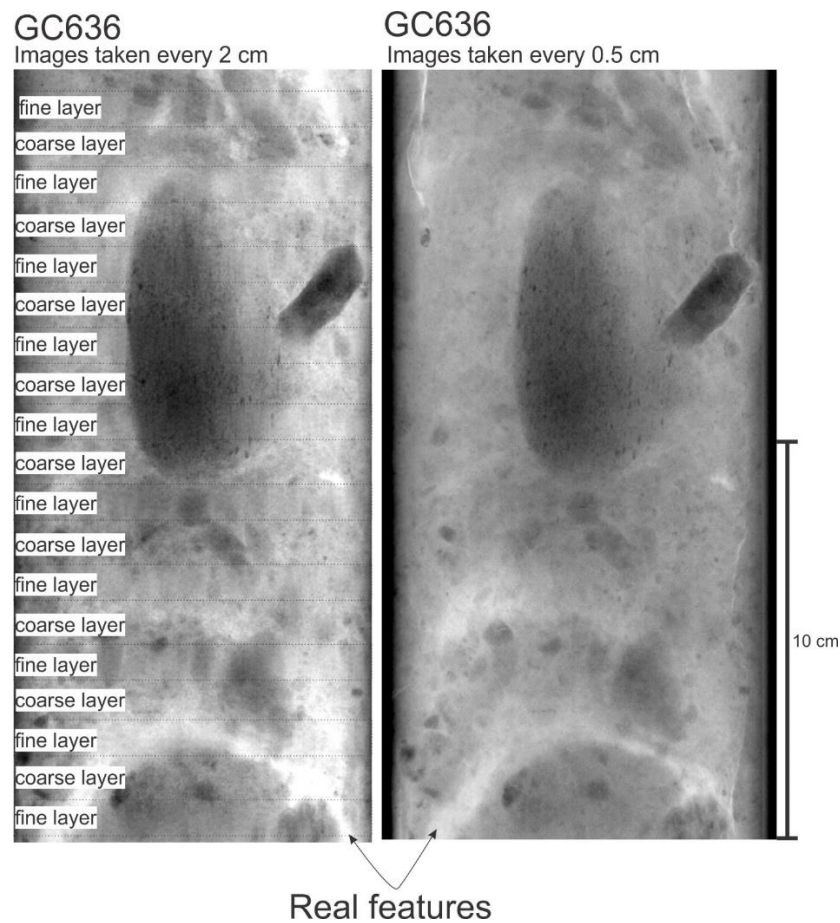
Fig. 6.5. The X-radiograph to the left is displaying the subtle stratification of finer and less dense layers, and the coarser and more dense layers. The X-radiograph to the right, is absent of subtle stratification, where images were taken every 0.5 cm.
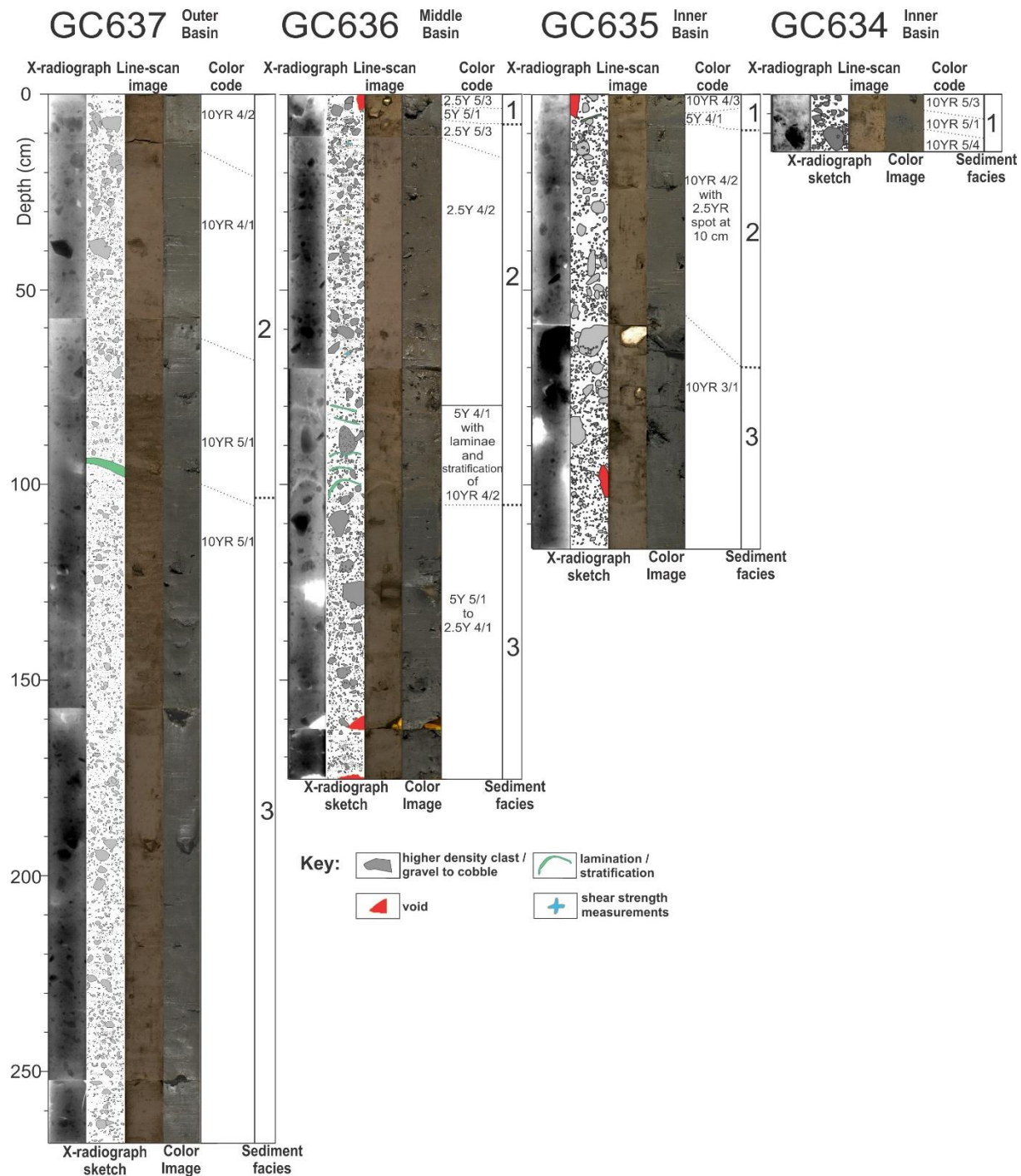
Fig. 6.6. X-radiographs, X-radiograph sketches, line-scan images, color codes and sediment facies from the different cores. Note: The color codes can be compared to the color images of the cores, and not the line-scan image of the core.

6.2 Sedimentary facies

Based on visual core observation and description, lithology, color, structures, grain-size, X-radiographs, physical parameters, sand fraction analysis, and the partly element composition of the cores, the sedimentary facies 1 to 3 have been defined. The main goal of this facies approach is to establish the major depositional environments for the sediments in the cores. The different facies will be described further in detail below, starting at the lowermost facies (facies 3), then the middle facies (facies 2), and then the uppermost facies (facies 1), and their representative sedimentary environments will be discussed in the next chapter (section 7, *p.* 115). GC635 and GC636 contain all three facies, GC637 contained facies 3 and 2, and GC634 contains exclusively facies 1 (Fig. 6.6-Fig. 6.19; Table 6.2).

6.2.1 Facies 3

6.2.1.1 Lithology and stratigraphy

Facies 3 consists of a massive matrix supported diamicton, with subangular to subrounded gravel and cobbles dispersed throughout in a muddy matrix (Fig. 6.6) of very dark gray (10YR 3/1) to gray (10YR 5/1 and 5Y 5/1) color (Fig. 6.6).

GC635 contains 44-50 % mud, 42 % sand and 8-14 % gravel, GC636 contain 52-54 % mud, 37-41 % sand and 7-10 % gravel, and GC637 contain 53-57 % mud, 34-38 % sand and 6-13 % gravel.

In GC637 there appears to be some weak fabric, where clasts are arranged in a sub-horizontal to incline angle and there are also some layers or bands of denser and less dense sediments sub-horizontal to slightly inclined visible on the X- radiographs (Fig. 6.10). In GC635, between 101-93 cm there are some patches of more sandy matrix. It appears to be some crude stratification in the upper part of GC637 (153-105 cm) in line-scan image (e.g. Fig. 6.6 and Fig. 6.7), but this is caused by reflection of water at the core surface.

Facies 3 was recovered in GC637 (269-106 cm), GC636 (168-105 cm), and GC635 (116-70 cm). The transition to the overlaying facies in GC635 is very diffuse, due to its location around where the core sections are split and where there is one large cobble, around 70 cm (e.g. Fig. 6.6). The transition to the overlying facies at GC636 and GC637 are gradational, where there is a transition from the massive diamicton to a stratified to laminated diamicton (Fig. 6.10b and c).
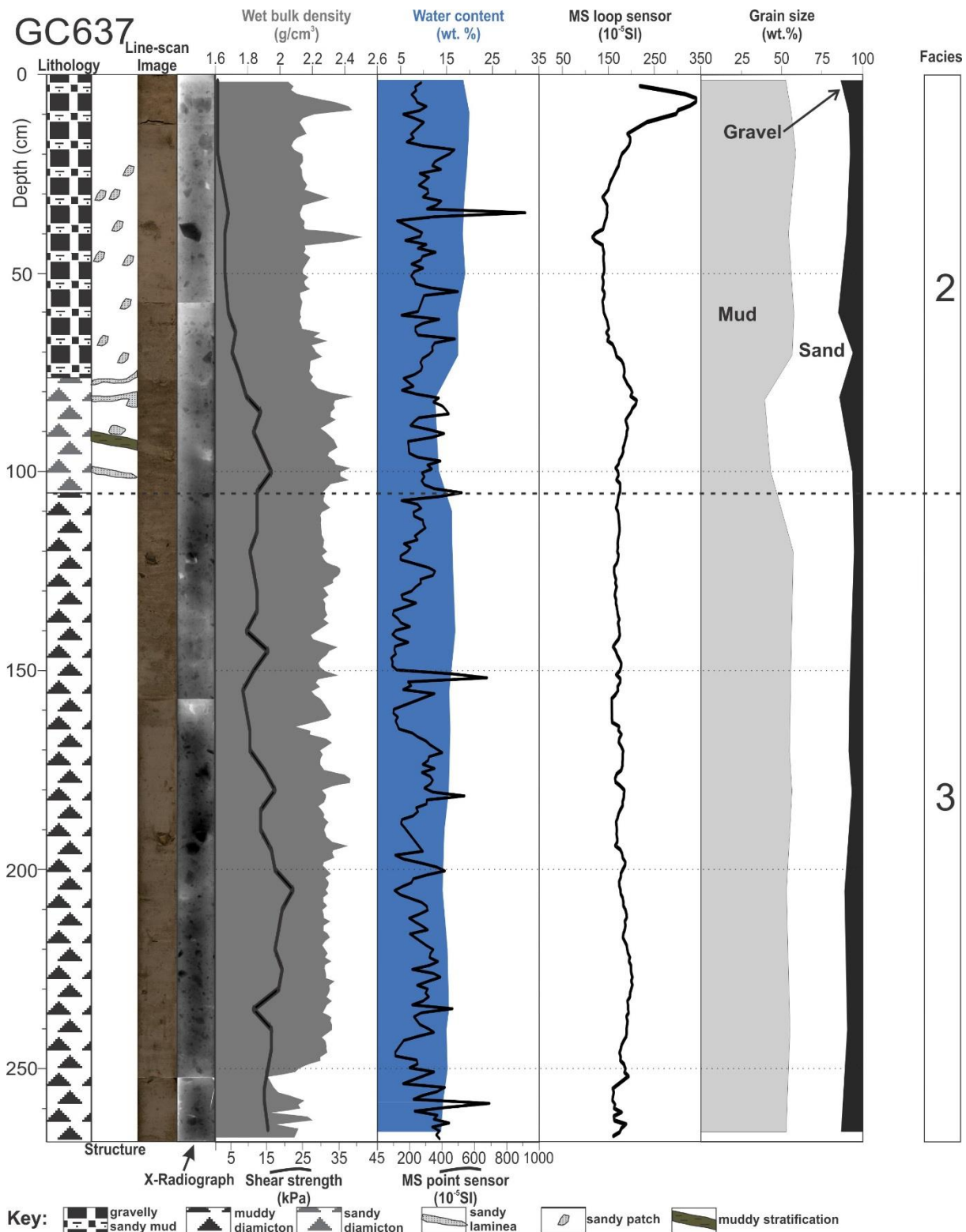
Fig. 6.7. Lithological composition, sedimentary structures, physical properties, grain size parameters, and facies interpretation of core GC637. MS- magnetic susceptibility. For facies description and interpretation see Table 7.1, p. 118.

Fig. 6.8. Lithological composition, sedimentary structures, element composition and facies interpretation of core GC637. The element composition is displayed as the ratio of the Sum of the 10 most abundant elements. For facies description and interpretation see Table 7.1, p. 118.
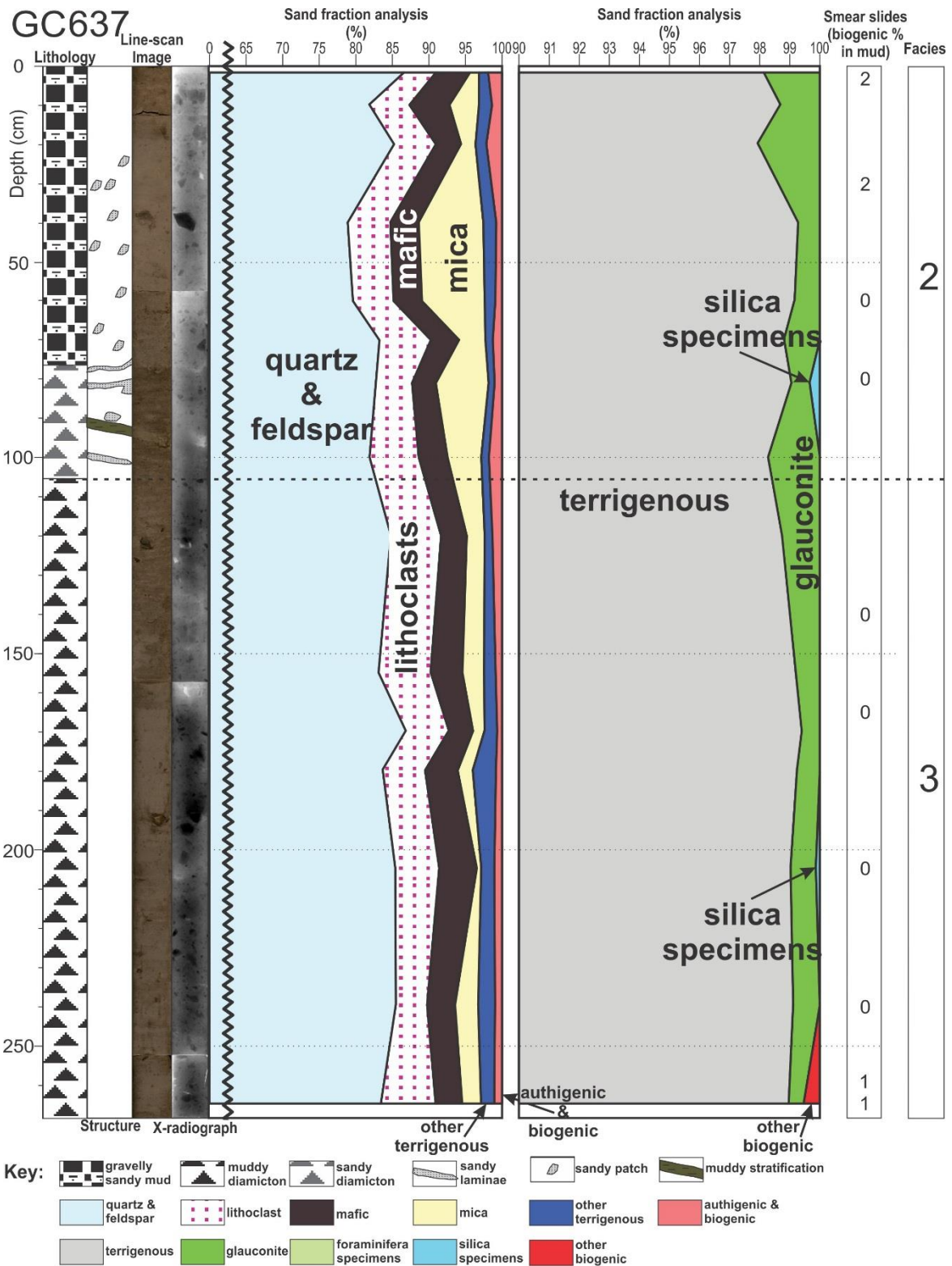
Fig. 6.9. Lithological composition, sedimentary structures, sand fraction analysis, smear slide analysis and facies interpretation of core GC637. The sand fraction analysis is displayed as % of the representative grains in the sub-samples. 'Lithoclasts' represent grains containing more than one mineral e.g., pyroxene and feldspar. 'Other terrigenous' represents grains not fitting to the other categories or unidentified grains. 'Silica specimens' represents diatoms, radiolarians and sponge spicules. 'Foraminifera specimens' represent agglutinated, benthic and planktonic foraminifera. 'Other biogenic' represents shell fragments and ostracods. For facies description and interpretation see Table 7.1, p. 118.
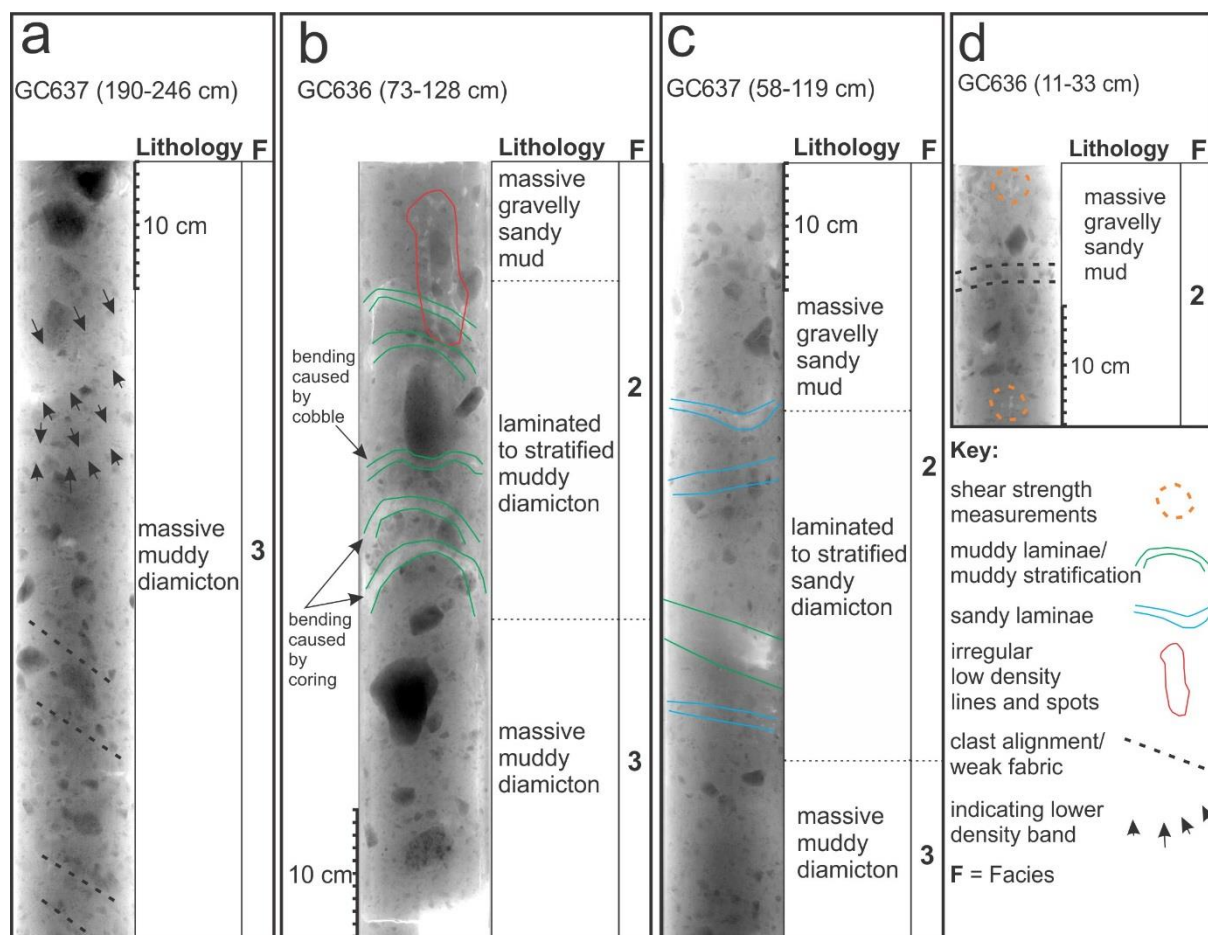
Fig. 6.10. X-radiographs of the cores. (a) Inclined weak fabric and bands of lower density in the massive muddy diamicton in facies 3. (b) GC636 showing an up-core transition from massive muddy diamicton (facies 3) to an overlying laminated to stratified muddy diamicton (facies 2), to a massive gravelly sandy mud (facies 2). Note the two lowermost laminae are bent downwards at the core side, which are caused by lateral friction drag of the core liner, during coring (cf. Skinner and McCave, 2003). Whereas, the middle laminae seem to be bent in the middle caused by the cobble above. Note also the irregular vertical lines and spots at the transition to a massive gravelly sandy mud. The red solid line highlights some. These irregular lines and spots are suggested to represent bioturbation. (c) GC637 showing an up-core transition from massive muddy diamicton (facies 3), to a overlying laminated to stratified sandy diamicton (facies 2), to a massive gravelly sandy mud (facies 2). Note the low amount of gravel and cobles around the mud stratification. (d) Clast alignment in GC636 which was observed both on the surface and in the X-radiograph. Shear strength measurements were taken in the archive half section of GC636, due to dewatering and compaction of this core section.

6.2.1.2 Physical properties

The wet-bulk density is moderate to high (mean 2,28 g/cm^3). It varies little in GC635 (Fig. 6.14) and GC637 (Fig. 6.7). However, at the base of GC637, the wet bulk density is lowest in the core catcher section, correlating to less sediment in the core catcher section. It decreases towards the top of the massive diamicton in GC636 (Fig. 6.11). Shear strengths are moderate to high, ranging from 2-21 kPa, and increases towards the base. (40 kPa was measured in the core catcher section of GC636, and are artificial high and should not be trusted, but it still indicates an increase in shear strength. (C-D. Hillenbrand, personal communication)).
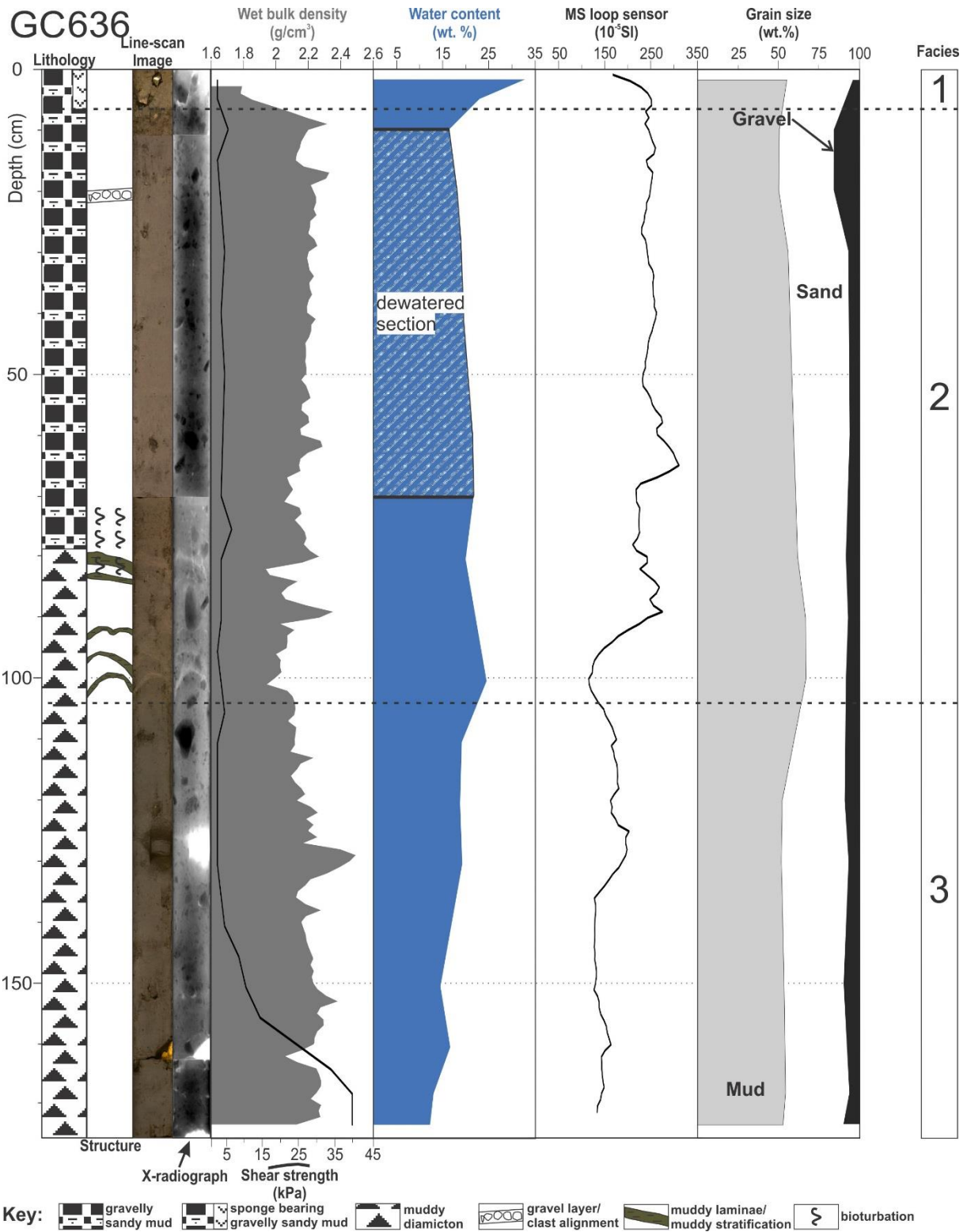
Fig. 6.11. Lithological composition, sedimentary structures, physical properties, grain size parameters, and facies interpretation of core GC636. MS- magnetic susceptibility. For facies description and interpretation see Table 7.1, p. 118.
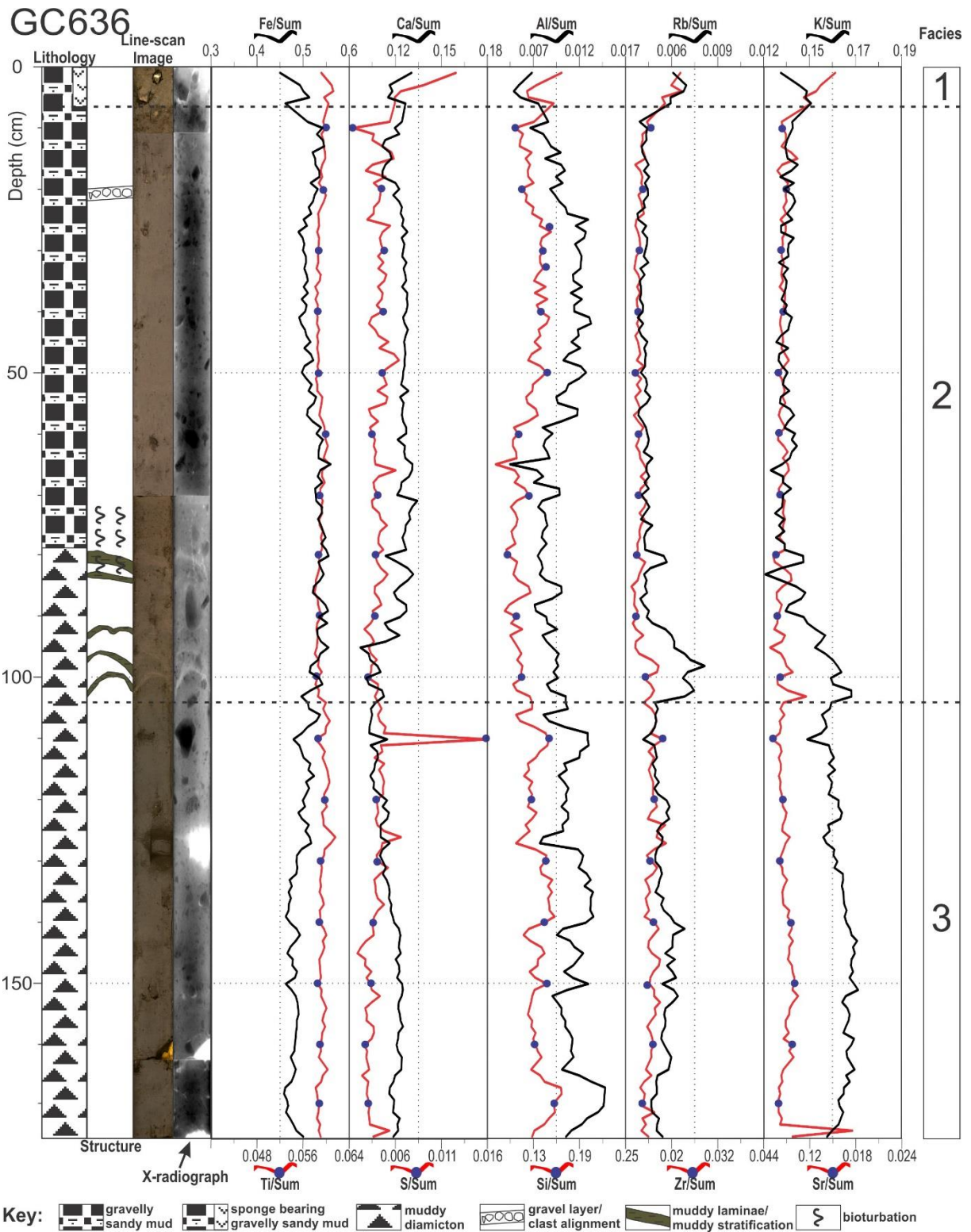
Fig. 6.12. Lithological composition, sedimentary structures, element composition and facies interpretation of core GC636. The element composition is displayed as the ratio of the Sum of the 10 most abundant elements. For facies description and interpretation see Table 7.1, p. 118.
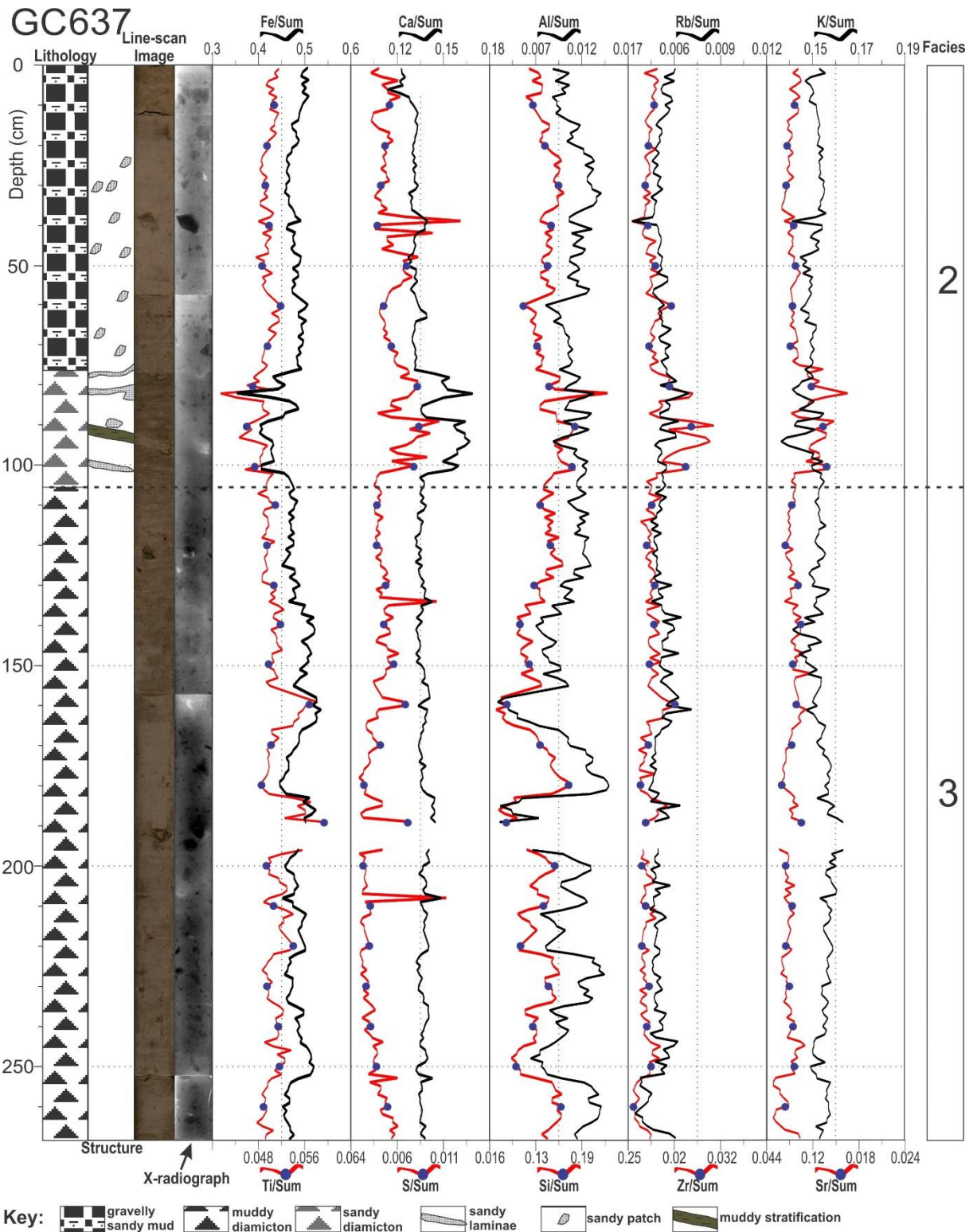
Fig. 6.13. Lithological composition, sedimentary structures, sand fraction analysis, smear slide analysis and facies interpretation of core GC636. The sand fraction analysis is displayed as % of the representative grains in the sub-samples. 'Lithoclasts' represent grains containing more than one mineral e.g., pyroxene and feldspar. 'Other terrigenous' represents grains not fitting to the other categories or unidentified grains. 'Silica specimens' represents diatoms, radiolarians and sponge spicules. 'Foraminifera specimens' represent agglutinated, benthic and planktonic foraminifera. 'Other biogenic' represents shell fragments and ostracods. For facies description and interpretation see Table 7.1, p. 118.

|	**Facies 1**	**Facies 2**	**Facies 3**
GC637	x	0-106 cm	106-269
GC636	0-6 cm	6-105 cm	105-170 cm
GC635	0-9 cm	9-70 cm	70-106 cm
GC634	0-14 cm	x	x
Wet bulk density (g/cm^3)			
Min	1.79	1.94	1.91
Max	2.26	2.69	2.50
Mean	2.01	2.21	2.28
Magnetic susceptibility (10^{-5}SI)			
Min	36	64	47
Max	244	339	203
Mean	83	180	150
Shear strength measurements (kPa)			
Min	0	0	2
Max	5	15	21 (40)
Mean	2	4	11
Water content (wt. %)			
Min	19.9	12.5	12.0
Max	32.8	24.6	19.3
Mean	26.7	17.9	15.1
Biogenic (% in sand fraction)			
Min	1	0	0
Max	17.05	0.7	1
Mean	4.01	0.08	0.2
Fe/Sum ratio (Mean)	0.468	0.487	0.477
Ti/Sum ratio (Mean)	0.053	0.051	0.052
Ca/Sum ratio (Mean)	0.121	0.127	0.130
S/Sum ratio (Mean)	0.007	0.005	0.004
Si/Sum ratio (Mean)	0.136	0.136	0.137
Al/Sum ratio (Mean)	0.008	0.011	0.011
Rb/Sum ratio (Mean)	0.008	0.006	0.005
Zr/Sum ratio (Mean)	0.024	0.015	0.015
Sr/Sum ratio (Mean)	0.014	0.010	0.009
K/Sum ratio (Mean)	0.160	0.153	0.160
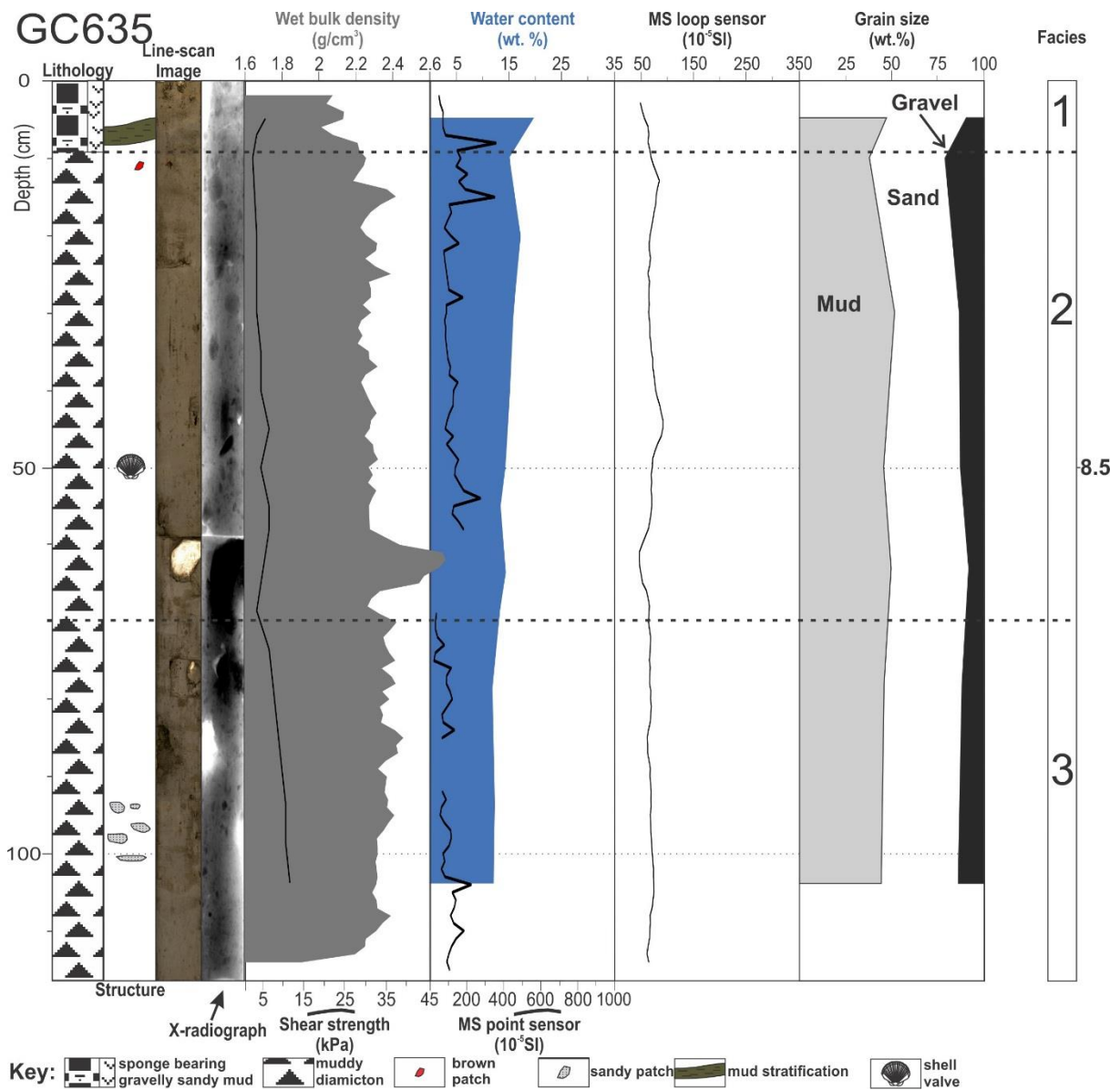
Fig. 6.14. Lithological composition, sedimentary structures, physical properties, grain size parameters, and facies interpretation of core GC635. MS- magnetic susceptibility. The number to the right show calibrated ^{14}C ages of calcareous material (in ka BP). For facies description and interpretation see Table 7.1, p. 118.

The mean water content is 15.1 wt. % with generally little variation. It increases towards the top of the facies, especially for GC636, which correlates to a decrease in the wet bulk density, shear strength and sand content (Fig. 6.11).

The MS loop sensor and point sensor values are on average around 150 *10⁻⁵ SI, with little fluctuation in the loop sensor values. However, in the upper part of the massive diamicton in GC636 (130-105 cm), some larger fluctuations result most likely from clasts (Fig. 6.11). There is more fluctuation in the point
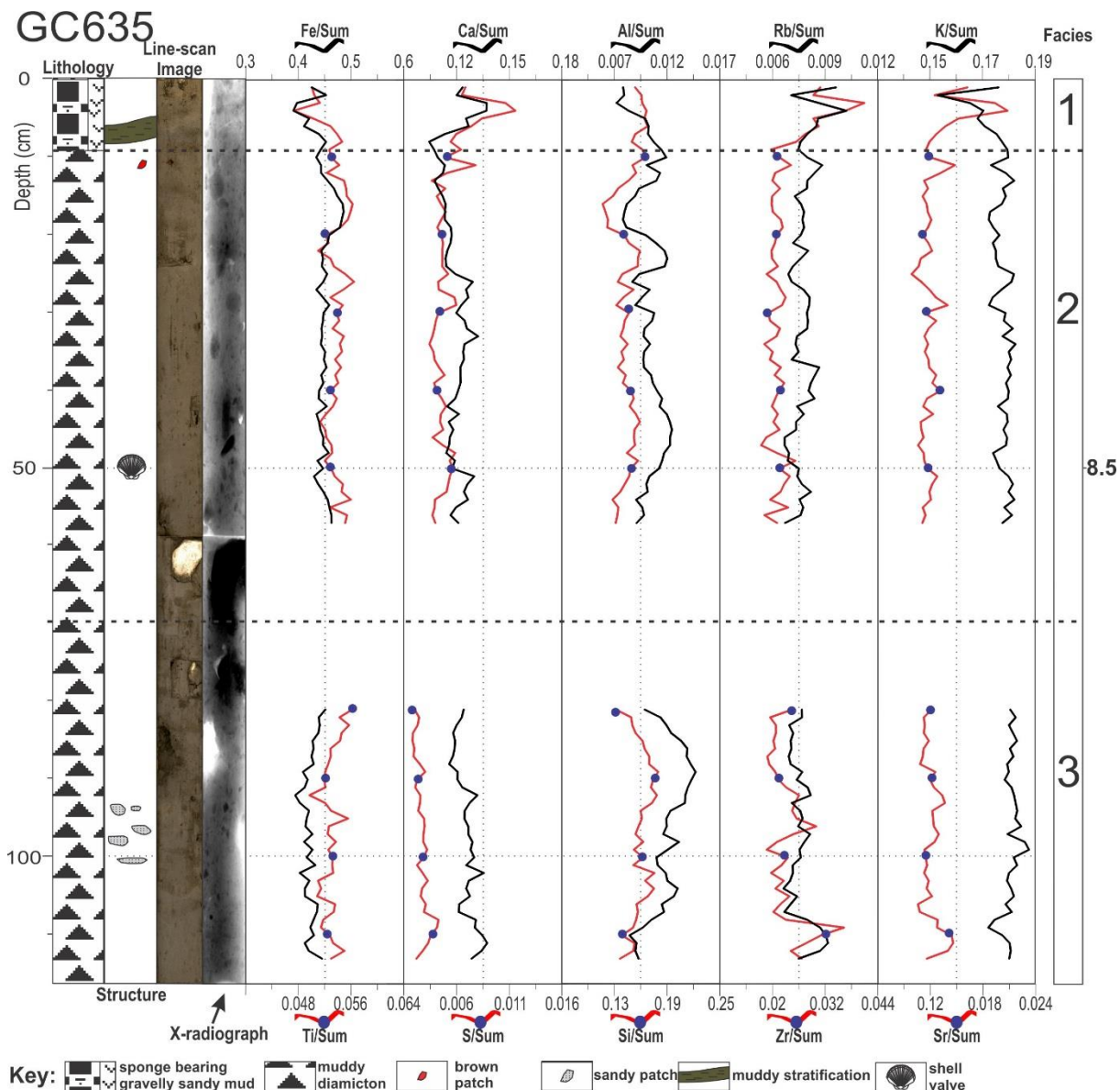
Fig. 6.15. Lithological composition, sedimentary structures, element composition and facies interpretation of core GC635. The element composition is displayed as the ratio of the Sum of the 10 most abundant elements. The number to the right show calibrated ^{14}C ages of calcareous material (in ka BP). For facies description and interpretation see Table 7.1, p. 118.

sensor values, but no distinct trends can be observed. Discrete peaks and troughs in the physical properties can typically be correlated to large cobbles and pebbles, and/or lack of sediment.

6.2.1.3 Element composition

The Ca/Sum and S/Sum ratios are low to moderate with generally little fluctuations, but distinct peaks in S/Sum in GC637 at 208 and 132 cm (Fig. 6.8) and GC636 at 110 cm (Fig. 6.12). These peaks are accompanied with a narrow smaller peak in Ca/sum ratio. At the same depth, both Fe/Sum and Ti/Sum
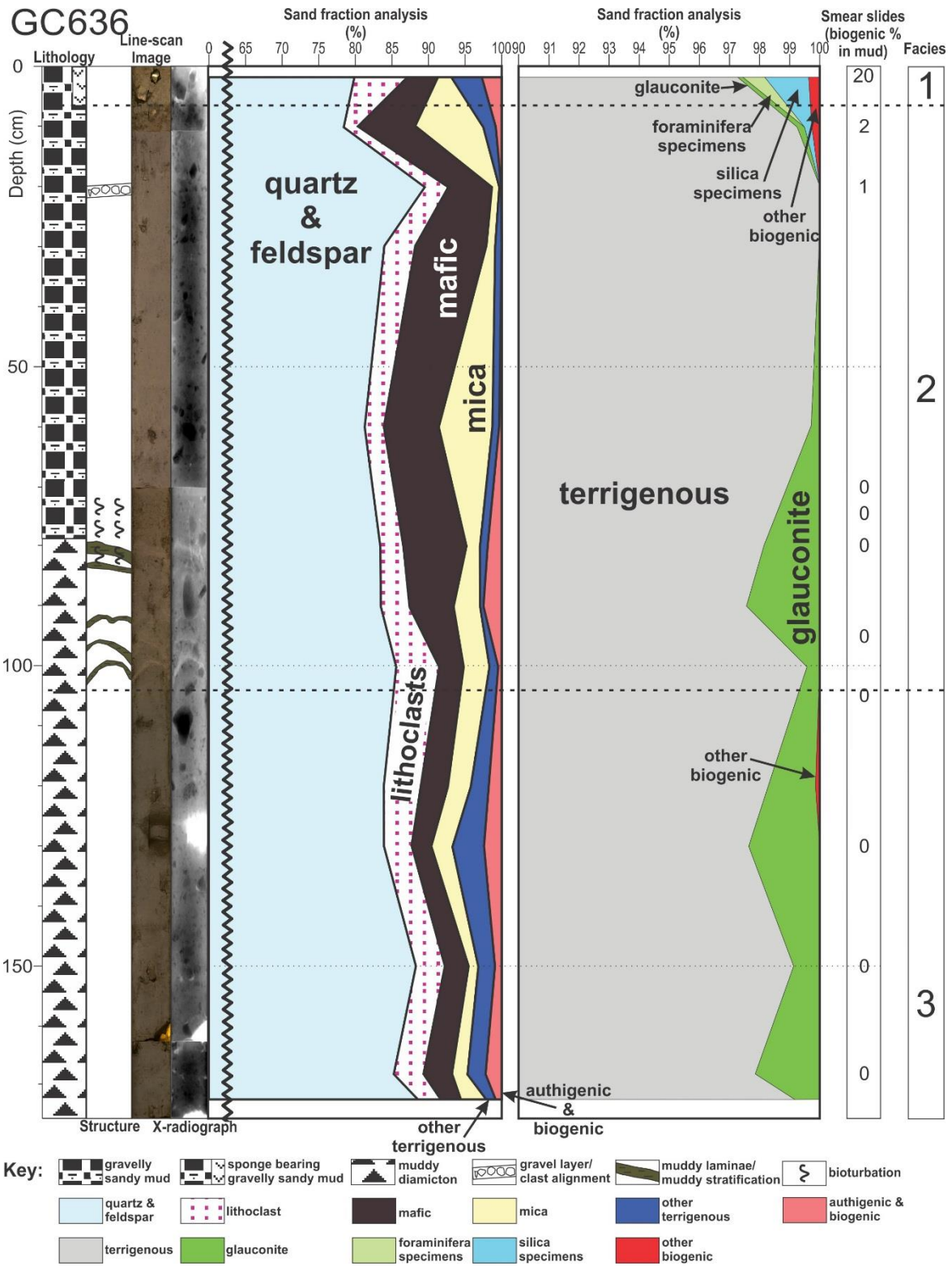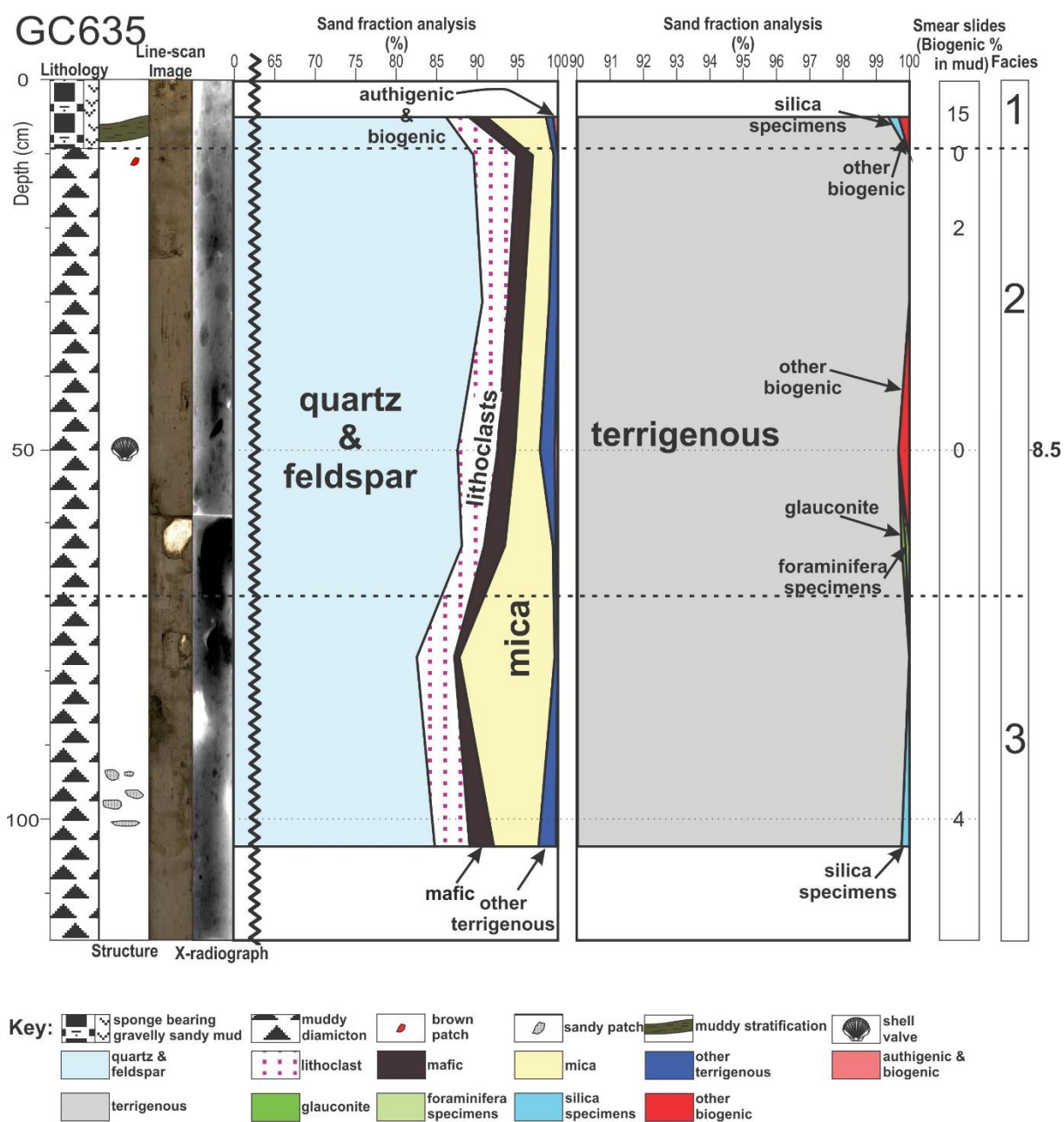
Fig. 6.16. Lithological composition, sedimentary structures, sand fraction analysis, smear slide analysis and facies interpretation of core GC635. The sand fraction analysis is displayed as % of the representative grains in the sub-samples. 'Lithoclasts' represent grains containing more than one mineral e.g., pyroxene and feldspar. 'Other terrigenous' represents grains not fitting to the other categories or unidentified grains. 'Silica specimens' represents diatoms, radiolarians and sponge spicules. 'Foraminifera specimens' represent agglutinated, benthic and planktonic foraminifera. 'Other biogenic' represents shell fragments and ostracods. The number to the right show calibrated ^{14}C ages of calcareous material (in ka BP). For facies description and interpretation see Table 7.1, p. 118.

ratios have small depressions, which are slightly wider than the peaks in S/Sum and Ca/sum ratio. Also at the same depth, the Al/Sum and Si/Sum ratios show peaks, but wider than the S/Sum and Ca/sum ratios.

Si/Sum and Al/Sum ratios are fluctuating, especially in GC637, below 155 cm (Fig. 6.8). Fe/Sum and Ti/Sum ratios appear be mirroring the fluctuation of the Si/Sum and Al/Sum ratios, but with a smaller amplitude of fluctuation. Zr/Sum and Rb/Sum ratios have the same trend as Fe/Sum and Ti/Sum ratio, but with minor fluctuations. The same is observed in GC635 and GC636, but with smaller amplitudes of fluctulation (Fig. 6.12; Fig. 6.15). The K/Sum ratio is generally higher in facies 3 than in facies 2.

6.2.1.4 Biogenic content and sand fraction analysis

The biogenic content in the sand fraction is low, i.e. less than 1% to absent. It consists of broken sponge spicules and broken shell fragments. The smear slides for this facies are also typically absent of biogenic material, however, traces (less than 5 %) of sponge spicules and diatoms occur at some depths, typically as small and broken fragments of the sponge spicules.

The quartz and feldspar grains within facies 3 in the three cores exceeds 80%; lithoclasts, mafic, mica and other terrigenous grains occur in lower abundances. There are generally very small variations, but the amount of mica grains in GC635 is relatively high compared to the two other cores. Both GC636 and GC637 are composed of 0.5-2.4 % glauconite grains in the sand fraction. No glauconite grains were observed in GC635.

6.2.2 Facies 2

6.2.2.1 Lithology and stratigraphy

Facies 2 consists of gray (10YR 5/1), dark gray (10YR 4/1 and 5Y 4/1) to dark grayish brown (10YR 4/2 and 2.5Y 4/2), laminated to stratified, muddy to sandy diamictons to massive gravelly sandy mud, with random to horizontal orientation of gravel and cobbles throughout the facies (Fig. 6.6). The sediments are poorly sorted, and the grain size data have slightly more variations than the underlying facies. The grain size data is generally showing a coarsening upwards trend.

GC635 contains 38-51 % mud, 36-41 % sand and 13-20 % gravel, GC636 contains 50-67 % mud, 24-37 % sand and 6-16 % gravel, and GC637 contains 38-57 % mud, 28-51 % sand and 6-15 % gravel.

The lower parts of this sedimentary facies consist of stratification and lamina of mud and sand in GC636 and GC637. At the lower part of facies 2 in GC636, between 104-74 cm, there is muddy stratification (thicker than 1 cm) and lamination (thinner than 1 cm) (Fig. 6.10b). At the same depth, the mud content is increasing and the sand content is decreasing. One of these laminae is bent in the middle, most probably due to deformation by a cobble up core of the laminae (Fig. 6.10b). Also in GC636 between ~84-70 cm (Fig. 6.10b), some irregular sub-vertical lines and spots can be observed in the X-photograph,

going through the laminated and stratified diamicton to the massive gravelly sandy mud, which are suggested to have been caused by bioturbation.

In the lower part of facies 2 in GC637 (between 102-78 cm) there are sandy laminas, but also one muddy stratification (Fig. 6.6c). At the same depth, the sand content is increasing, and the mud content is decreasing (Fig. 6.7). The X-radiograph shows that there are less gravel and cobble clasts around the muddy stratification (Fig. 6.10c).

The upper part of this facies is predominantly massive, with some patches of more sandy sediments in GC637 (Fig. 6.7). Some sub-horizontal zones of less dense and denser sediment, and occasionally sub-horizontal clast alignment can be observed on the X-radiographs. However, it is difficult to tell if all of these features are real due to the subtle layer artifact described in section 6.1.6. However, clast alignment at 21 cm in core GC636 is real, as it was also observed on the surface, in addition to the X-radiographs (Fig. 6.10d). A reddish brown patch (2.5YR 4/3), with sand and mud grains of similar color, was observed at ~11 cm in core GC635 (Fig. 6.6 and Fig. 6.14).

Facies 2 was recovered as the middle facies in both GC636 (105-6 cm) and GC635 (70-9 cm), and is the uppermost facies of GC637 (106-0 cm). The border to facies 1 in GC635 and GC636 is gradational and is defined by color changes and changes in biogenic content.

6.2.2.2 Physical properties

The wet-bulk density of facies 2 is moderate to high (mean 2.21 g/cm^3), but generally lower than in facies 3. The lower part of GC637 has the highest wet-bulk density, which is not related to discrete peaks that can be correlated to cobbles and pebbles (Fig. 6.7), which correlates to a increase in sand content. In contrast, GC636 has the lowest values of wet bulk density at the lower part of facies 2 (Fig. 6.11), which correlates to a decrease in sand content.

The shear strength is generally low to moderate (0-15kPa) and fluctuates little in cores GC635 and GC636. It decreases towards the top of GC637, which correlates to an increase in water content and a decreases sand content and wet bulk density.

The water content increases slightly towards the top of facies 2 in GC635 and GC637, but decreases in core GC636, before there is an abrupt increase towards facies 1. As shown in Fig. 6.11, and mentioned in the methods (section 3.4.8), this core section of GC636 had dewatered and compacted in one-half. However, it doesn't seem like the dewatering and compaction of the core section has a large influence

on the reliability of the data, as the decrease in water content seems to be correlating well with the wet bulk density increase towards the top of this facies.

The magnetic susceptibility (both MS loop sensor and point sensor) is generally moderate to high (mean 180 *10^{-5} SI). It varies more and is generally higher than in facies 1 and 3. Discrete peaks and minima in the physical properties can typically be correlated to large pebbles and cobbles, and/or lack of sediments in the end of the sections (Fig. 6.6).

6.2.2.3 Element composition

Al/Sum and Si/Sum ratios have a somewhat similar trend in all the cores, which increases up-core from transition from facies 3, but starts decreasing towards the top of facies 2, but increases again close to the transition to facies 1 in GC635 (Fig. 6.15).

The element composition is strongly fluctuating in the lower part of facies 2 in GC637 between 105-78 cm (Fig. 6.8), where Ca/Sum and S/Sum ratios are increasing and Fe/Sum and Ti/Sum ratios are decreasing up-core from the transition from facies 3, but "recovers" its mean values again at ~78 cm.

In GC636 (Fig. 6.12), the Ca/Sum ratios increases, whereas the Rb/Sum ratio decreases up-core from facies 3. In both GC636 and GC637, the K/Sum ratio is decreasing up-core from the transition from facies 3. The S/Sum ratio, has as "spiky" appearance at 35-42 cm in GC637.

6.2.2.4 Biogenic content and sand fraction analysis

Similar to facies 3 the biogenic content in facies 2 is low or nearly absent, and traces (less than 3%) of sponge spicules and diatoms occur at certain depths (Fig. 6.9, Fig. 6.13 and Fig. 6.16). One shell valve was observed at 50 cm in core GC636. This was sampled for dating purposes.

The lithology of the grains in the sand fraction is fairly similar to facies 3, but the quartz and feldspar content decreases slightly up-core from facies 3 in cores GC636 and GC637 before it increases again towards the top of the facies (Fig. 6.9 and Fig. 6.13). Simultaneously, the mafic content in GC636 increases and the mica content increases in GC637. Opposite to the other cores, the quartz and feldspar content increases up-core in GC635 (Fig. 6.16). The lithology of the reddish brown patch in GC635 differs a lot from the general lithology in the sand fraction and is dominated by lithoclasts, with a reddish brown color.

The glauconite content increases slightly up-core above facies 3 in GC636 and GC637 and then starts decreasing to where the glauconite grains are absent or very few in the upper part of facies 2 in GC636.
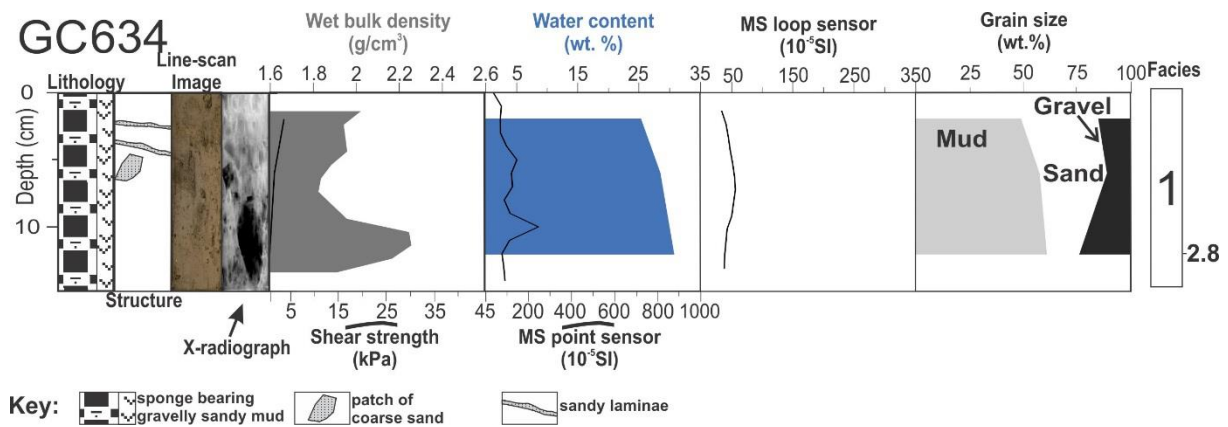
Fig. 6.17. Lithological composition, sedimentary structures, physical properties, grain size parameters, and facies interpretation of core GC634. MS- magnetic susceptibility. The number to the right show calibrated ^{14}C ages of calcareous material (in ka BP). For facies description and interpretation see Table 7.1, p. 118.

In GC637 the glauconite content increases again towards the top of facies 2, whereas no glauconite grains were observed in facies 2 in GC635, except for at 63 cm, where the lithological composition contained ~0.1 % glauconite grains.

6.2.2.5 AMS radiocarbon dates

One radiocarbon date was obtained from a shell valve in GC635, at 50 cm, that yielded an age of ~8.5 cal. ka BP.

6.2.3 Facies 1

6.2.3.1 Lithology and stratigraphy

Facies 1 is composed of a brown (10YR 5/3 and 10YR 4/3), gray (10YR 5/1 and 5Y 5/1), dark gray (5Y 4/1), yellowish brown (10YR 5/4), to light olive brown (2.5Y 5/3), massive and occasionally laminated to stratified, sponge bearing gravelly sandy mud.

The granulometric composition of core GC634 varies between 49-61 % mud, 15-35 % sand, and 10-24 % gravel. Only one sample from facies 1 was taken from GC635 and GC636, and thus there is no variation. GC635 contains 47 % mud, 43 % sand and 10 % gravel, and GC636 contains 55 % mud, 41 % sand and 4 % gravel.

Facies 1 overlies facies 2 in GC635 (9-0cm) and GC636 (6-0 cm) and it is the only facies in GC634 (14-0 cm).
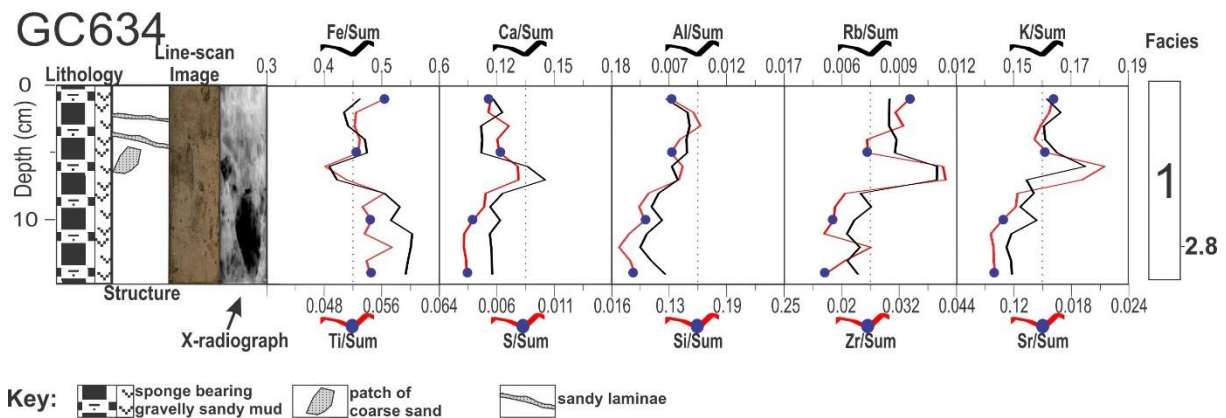
Fig. 6.18. Lithological composition, sedimentary structures, element composition and facies interpretation of core GC634. The element composition is displayed as the ratio of the Sum of the 10 most abundant elements. The number to the right show calibrated ^{14}C ages of calcareous material (in ka BP). For facies description and interpretation see Table 7.1, p. 118.

6.2.3.2 Physical properties

Wet bulk density (mean 2.01 g/cm^3) and shear strength (0-5 kPa) are generally low and the water content is typically higher than in the two other facies. MS point and loop sensor values (mean 83 *10^{-5}SI) are low for GC634 and GC635, and have little variation, whereas the MS loop sensor values are high in GC636 (Fig. 6.11). The discrete peak in wet bulk density and MS point sensor at 12 cm in GC634 is caused by a large cobble (Fig. 6.17).

6.2.3.3 Element composition

Sr/Sum, Rb/Sum, Zr/Sum, Ca/Sum and S/Sum ratios are generally increasing, and Fe/Sum, Ti/Sum ratio are generally decreasing up-core in facies 1. GC634 and GC635 have a similar trend in element composition, with positive peaks in both Ca/Sum, S/Sum, Rb/Sum, Zr/Sum, K/Sum and Sr/Sum ratios, and a minimum in Fe/Sum and Ti/Sum ratios in the middle of the facies at ~5 cm. Al/Sum and Si/sum ratios are decreasing in GC635 and increasing in GC634 and GC636 up-core in this facies. K/Sum ratio is decreasing up-core in GC635 and increasing in GC634 and GC636.

6.2.3.4 Biogenic content and sand fraction analysis

The biogenic content in facies 1 is relatively high compared to facies 2 and 3. Smear slides have between 15-30 % of biogenic content in facies 1, dominated by sponge spicules. The sand fraction also contains relatively high amounts of biogenic material, where sponge spicules also dominate the biogenic composition.

GC634 has a decreasing trend in the biogenic content towards the top of the facies, especially in terms of foraminifera specimen content. Only one sample was investigated in GC635 and GC636 and thus the biogenic content has no variation, but are increasing upwards from facies 2.
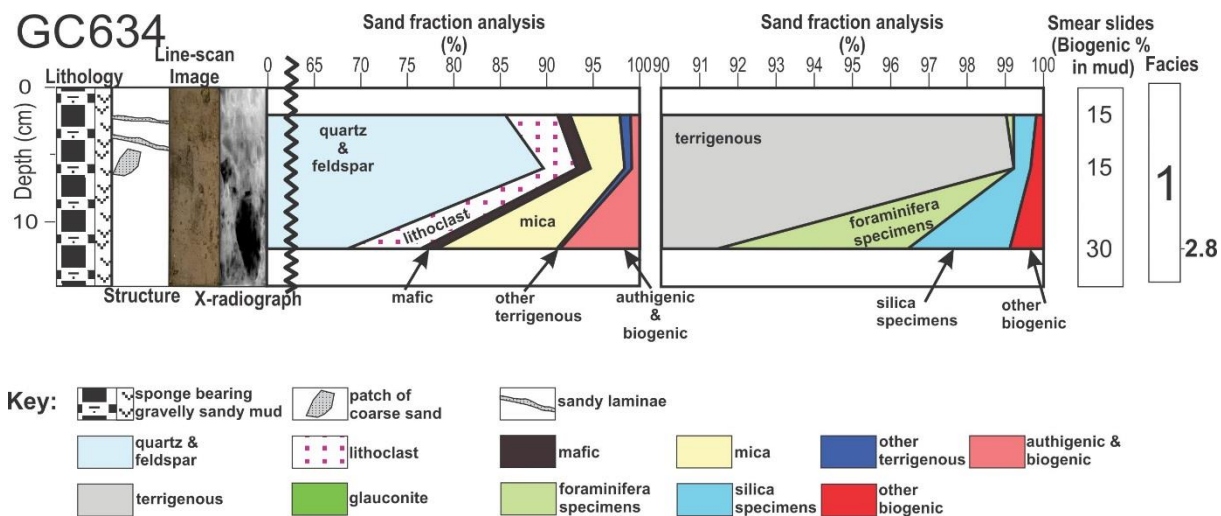
Fig. 6.19. Lithological composition, sedimentary structures, sand fraction analysis, smear slide analysis and facies interpretation of core GC634. The sand fraction analysis is displayed as % of the representative grains in the sub-samples. 'Lithoclasts' represent grains containing more than one mineral e.g., pyroxene and feldspar. 'Other terrigenous' represents grains not fitting to the other categories or unidentified grains. 'Silica specimens' represents diatoms, radiolarians and sponge spicules. 'Foraminifera specimens' represent agglutinated, benthic and planktonic foraminifera. 'Other biogenic' represents shell fragments and ostracods. The numbers to the right show calibrated ^{14}C ages of calcareous material (in ka BP). For facies description and interpretation see Table 7.1, p. 118.

The quartz and feldspar amount in GC634 increases, as the biogenic content decreases. Other lithologies only change slightly. The glauconite content in GC636 is low, less than 1%, and no glauconite was observed in GC635. Some less developed glauconite grains were observed at 12 cm in GC634, where they appeared to be coating or growing on mica grains.

6.2.3.5 AMS radiocarbon dates

Three radiocarbon dates were obtained from this facies in GC634, all at 12 cm. One sample from a planktic foraminifera (*N. pachyderma* sin.) with an age of 2826 cal. yr BP, one sample from a benthic foraminifera (*Cibicides* sp.) with an age of 2857 cal. yr BP, and one sample from AIO fraction with an age of 10010 cal. yr BP.

7 Discussion

7.1 Correlation of lithological and acoustic data

In this section, the sediment cores and acoustic data will be correlated to improve the interpretation of the depositional environments archived in the sediments in the cores.
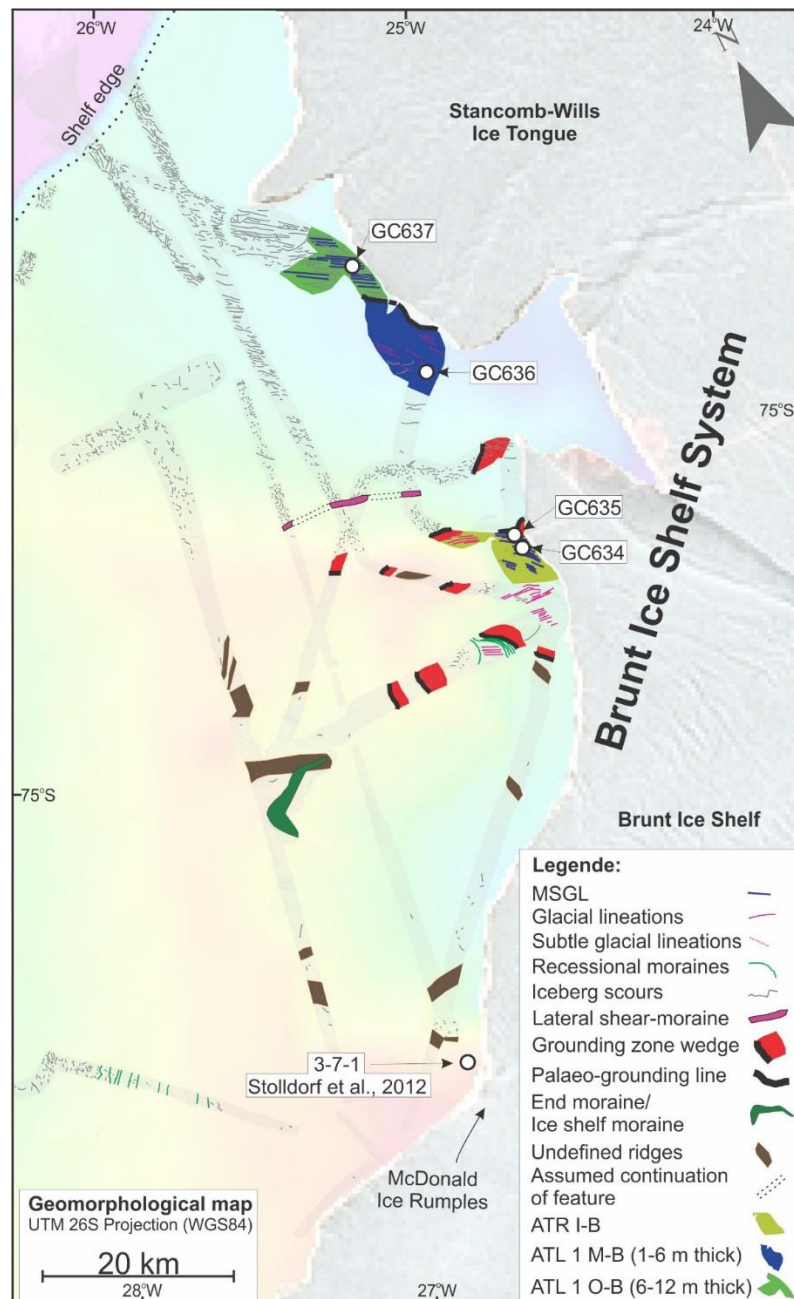
Fig. 7.1. Geomorphological map of the study area, including the extent of ART I-B, ATL1 M-B and ATL1 O-B, together with the location of the gravity cores (GC) from this study. A transparent version of the swath bathymetry data overlying the IBCSO map (Arndt et al., 2013), as well as an Envisat synthetic aperture radar image of the Brunt Ice Shelf System from 4th of March 2011 are underlying the geomorphological map. Note also the location of core 3-7-1 from Stolldorf et al., (2012) used in the discussion.

GG634 and GC635 were retrieved from the inner basin (Fig. 7.1; Fig. 7.2), where the seafloor is characterized by features interpreted as MSGL. The TOPAS profiles (Fig. 7.2c) show locally ATR (*ATR I-B*) on top of a strong reflection (*Ref. I-B*). The *ATR I-B* was interpreted to consist of soft deformation till, moulded into ridges, and the *Ref. I-B* was interpreted to possibly represent the surface of stiff till.

GC636 was retrieved in the deeper part of the middle basin (Fig. 7.1; Fig. 7.2). The seafloor in this region is characterized by subtle linear features interpreted as glacial lineations. The subtle appearance
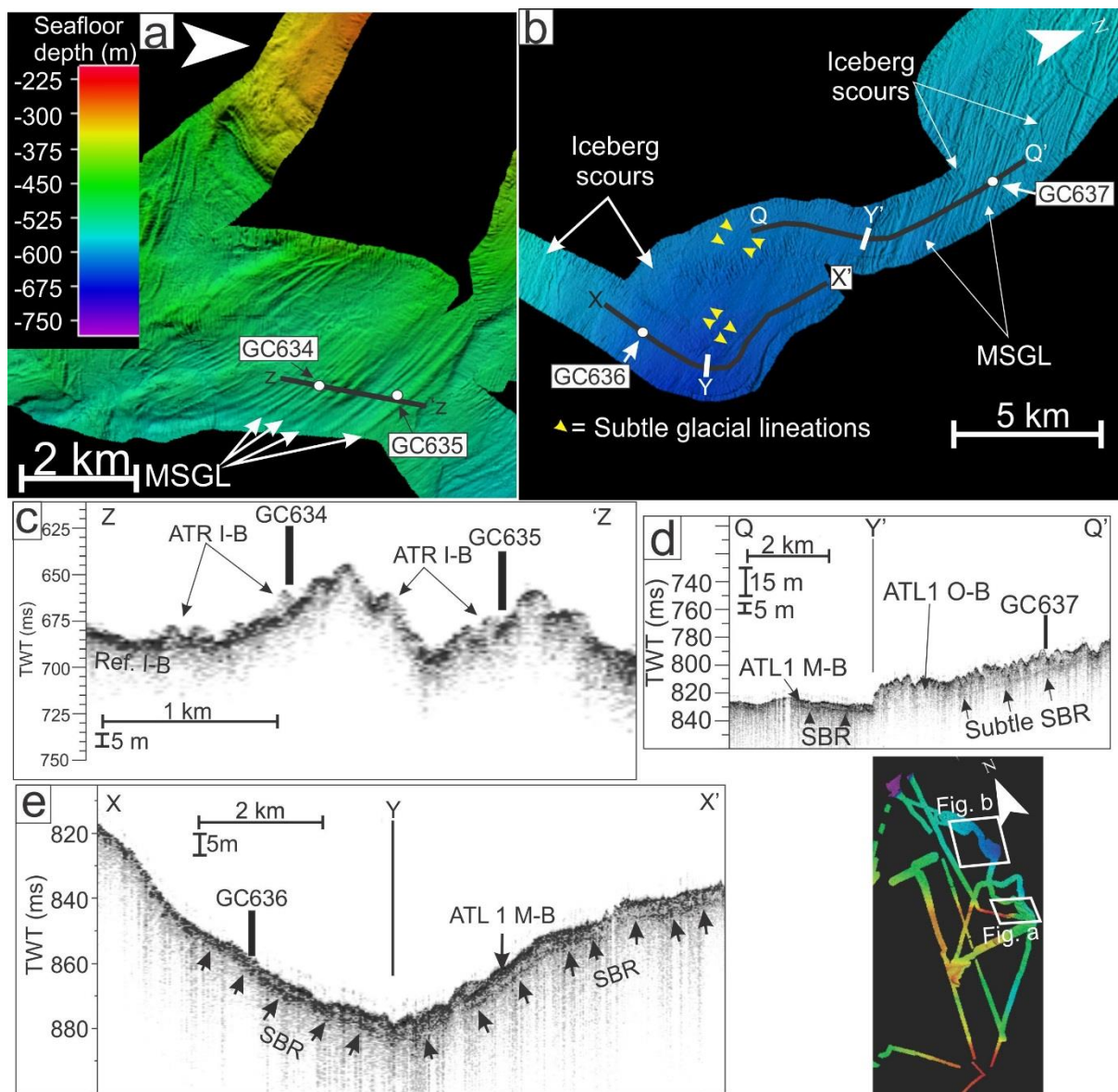
Fig. 7.2. (a) Bathymetry of the inner basin, with the location of GC634 and GC635 (b) Bathymetry of the middle and outer basin, with the location of GC636 and GC637. The black line indicates the location of TOPAS profiles in Fig.d and e. (c) TOPAS profile with the approximately location of GC634 and GC635. (d) TOPAS profile with the approximate location of GC637. (e) TOPAS profile with the approximate location of GC636.

of the glacial lineations was suggested to be caused by a thin ice, which was lightly or episodically grounded. The TOPAS profiles from the deeper part of the middle basin revealed an ATL (*ATL 1 M-B*), with a thickness between ~1-6 m, interpreted to consist of soft deformation till. A distinct SBR is located below the *ATL 1 M-B* (Fig. 7.2e).

GC637 was retrieved in the outer basin (Fig. 7.1; Fig. 7.2). The seafloor in this region is characterized by features interpreted as MSGL, which are locally crosscut by iceberg scours. The TOPAS profile from the outer basin reveals a thick ATL (*ATL 1 O-B*), with a thickness of ~6-15 m, interpreted to consist of soft deformation till. A subtle SBR is located below the ATL1 O-B (Fig. 7.2d).

7.2 Sedimentary facies and depositional environment

7.2.1 Facies 3: Subglacial facies

The massive muddy diamictons in facies 3 are similar to other massive diamictons reported from the Antarctic shelves, where they have been interpreted as soft deformation till, deposited subglacially beneath ice streams (e.g. Domack et al., 1999; Licht et al., 1999; Evans and Pudsey, 2002; Evans et al., 2005; Hillenbrand et al., 2005; 2010; Ó Cofaigh et al., 2005a; 2005b; 2007; Reinardy et al., 2011a; 2011b; Smith et al., 2011; 2014). However, similar lithologies, structures and physical properties have also been described from sediments such as glaciogenic debris flows, iceberg turbated sediments, and sub-ice shelf glaciomarine sediments proximal to the grounding line (e.g. Domack et al., 1999; Licht et al., 1999; Evans and Pudsey, 2002; Hillenbrand et al., 2005; 2009; 2010; 2012; Smith et al., 2011). The bathymetry and the TOPAS profiles do not reveal any features that could represent glaciogenic debris flow close to the cores that recovered the facies 3 diamictons (e.g. Fig. 7.2). Furthermore, features interpreted as iceberg scours occur exclusively in the vicinity of core GC637. Such iceberg-turbated sediments typically display more spikey shear strength values (e.g., VC430 and VC436 in Smith et al., 2011).

The swath bathymetry and TOPAS profiles reveal features interpreted as glacial lineations and MSGL together with ATR and ATL (section 4.2 and 5.2.2; Fig. 7.2), indicative of ice streaming and soft till deformation (Dowdeswell et al., 2004; Ó Cofaigh et al., 2007; King et al., 2009; Reinardy et al., 2011a) close to all coring sites. Therefore, it is suggested that the facies 3 diamicton is a soft deformation till, deposited beneath grounded ice in the Brunt Basin (Fig. 7.3). This is also supported by several other parameters, such as, lack of sediment structures (e.g. lamination and stratification) indicative of current activity, low to absent biogenic content in the smear slides and sand fraction, generally higher wet bulk density, and lower water content than facies 1 and 2. The shear strength values are also generally higher, and typically display an increase down-core, and that the grain size data and the MS values showing

little variations are also consistent with soft deformation tills (e.g. Domack et al., 1999; Hillenbrand et al., 2005; 2010; Smith et al., 2011; 2014). In addition, similar weak fabric and layers or bands of less dense sediments as observed in GC637 (Fig. 6.10a), have also been observed in sediments interpreted as soft deformation tills from the western and eastern Antarctic Peninsula shelves (Evans et al., 2005; Ó Cofaigh et al., 2005b; 2007).

The transition from facies 3 to facies 2 has in GC636 and GC637 been defined mainly on the basis of the onset of stratification and lamination in facies 2, but also partly because of fluctuations in the element composition (Fig. 6.8 and Fig. 6.12), as well as more pronounced variation in the physical properties. The transition in GC635 is more diffuse and, therefore, defined by more consolidated sediment in facies 3, with higher wet bulk density and shear strength, as well as decreasing water content down-core.

Table 7.1.
Diagram of facies interpretation of the different sediment types recovered in the cores from the Brunt Basin.

Lithology	Sedimentary structures	Key sedimentological properties	Facies Interpretation
Sponge bearing gravelly sandy mud	Massive, to stratified or laminated	Relatively high biogenic content and water content, moderat to high variability of parameters.	Glaciomarine deposition, with seasonal sea ice cover (1)
Muddy to sandy diamicton and gravelly sandy mud	Massive to laminated or stratified, (bioturbated in GC636)	Low to absent biogenic content, low to medium wet bulk density and shear strength, moderate water content and variation in grain size	Glaciomarine deposition, in an sub-ice shelf setting or with perennial sea ice cover (2)
Massive muddy diamicton	Massive (weak fabric in GC637)	Low to absent biogenic content, low to high shear strength and wet bulk density, moderate to low water content. Little variation in grain size and MS	Subglacial deposition (3)

However, it is possible that the upper parts of facies 3 may have been partly deposited in an glaciomarine sub-ice shelf environment, proximal to the grounding line. As sediments deposited close to the grounding line in sub-ice shelf cavities will mainly be composed of basal debris derived from the ice shelf, it can be similar to subglacial till (c.f. Licht et al., 1999; Domack et al., 1999; Hillenbrand et al., 2005). More proxies are therefore wanted to determine an accurate transition from subglacial to glaciomarine environment (cf. Hillenbrand et al., 2005; 2009 vs. Hillenbrand et al., 2010). Especially the low shear strength in the upper part of facies 3 in GC636 is suspicious, but similar low shear strength have been reported from soft deformation tills (Evans et al., 2005; Ó Cofaigh et al., 2005b). It is therefore suggested that the low shear strength in GC636 reflects less pressure ice-sediment interface, presumably caused by lightly grounded ice.
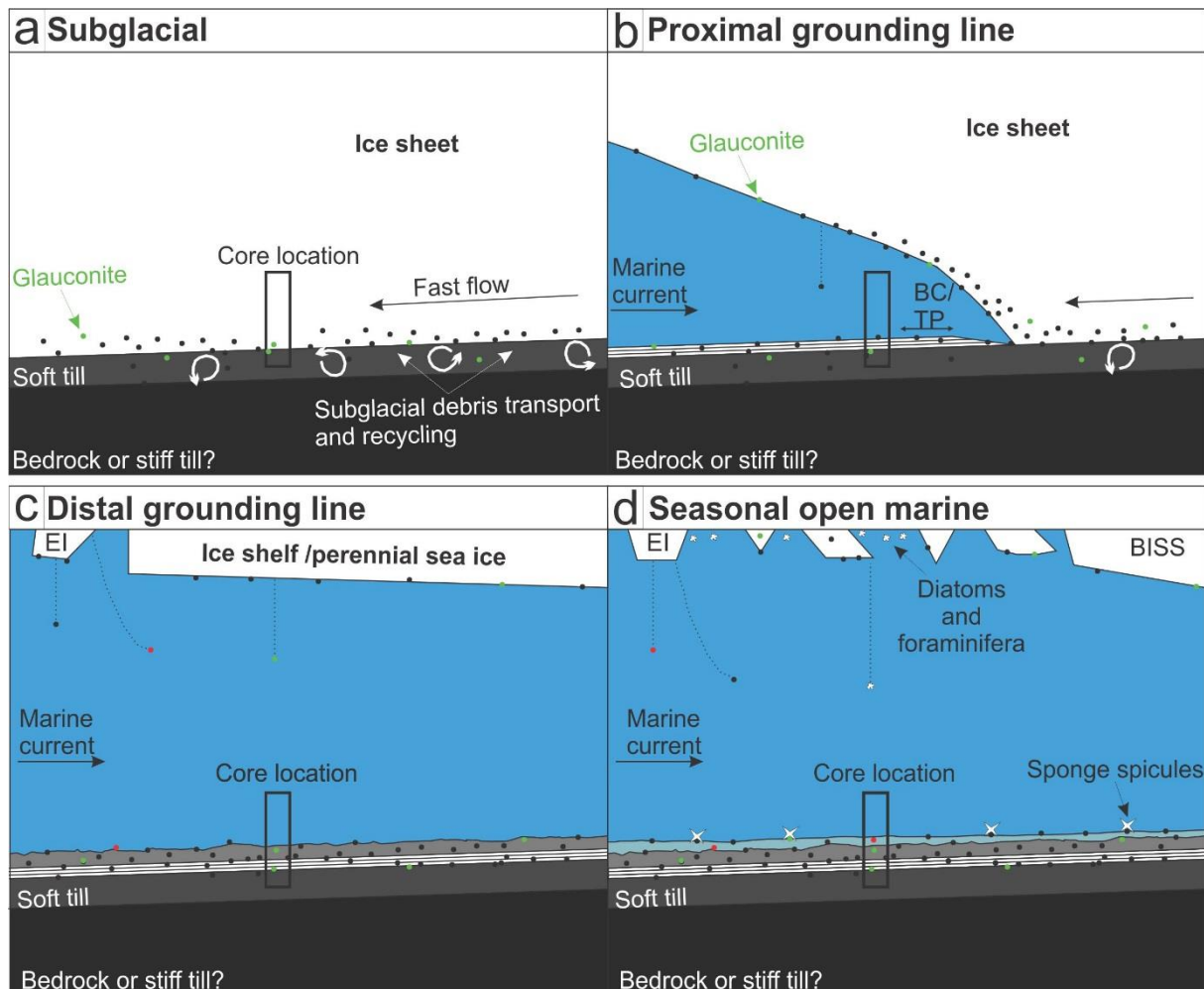
Fig. 7.3. Schematic model of the depositional environment for the sediments in the cores from the Brunt Basin. (a) Subglacial environment. (b) Proximal grounding line to (c) distal grounding line in a sub-ice shelf environment or perennial sea ice cover. (d) Seasonal open marine environment. EI- exotic iceberg, BISS-Brunt Ice Shelf System. Model is not to scale.

7.2.2 Facies 2: Glaciomarine sub-ice shelf /perennial sea ice cover facies

The coarse grained sandy to muddy diamictons and gravelly sandy muds in facies 2 are believed to be deposited in a transitional environment, from subglacial (facies 1), to an open marine (facies 3) environment as the grounded ice retreated from the core locations (Fig. 7.3b and c). The lamination and stratification in the lower part of facies 2 in GC637 and GC636, bioturbation in the lower part of GC636, and a shell valve of Holocene age in GC635, reflect a marine influence (e.g. Domack and Harris, 1998; Licht et al., 1999; Evans and Pudsey, 2002; Hillenbrand et al., 2010). However, the low biogenic content could indicate a sub-ice shelf environment or perennial sea ice cover at the core positons during the deposition of the facies 2. This is also supported by the similarities to sediments reported from Holocene ice shelf environments (Domack et al., 1999; Evans and Pudsey, 2002; Hillenbrand et al., 2009; 2010). In addition, the modern Brunt Ice Shelf System exists in close proximity to the core locations today and it is therefore likely that a palaeo version of the Brunt Ice Shelf System existed during the time when the facies 2 sediments were deposited. As climatic conditions would have been colder and more favorable for ice shelf and sea ice formation (e.g. Benn and Evans, 2010). The sand fraction of the facies 2 are also very similar to the soft deformation till in facies 3, which could indicate that the sediments predominantly are sourced by basal melt from sub-ice shelf cavities and iceberg rafted sediments source by the same ice (e.g. Domack et al., 1999). The depositional environment for the facies 2 sediments is therefore suggested to be glaciomarine environment under sub-ice shelf or perennial sea ice cover.

The sediments reflect a transition from a proximal grounding line position to a more distal positon, where it is suggested that the laminated and stratified diamictons in GC636 and GC637 are deposited close to the grounding line (e.g. Domack et al., 1999; Hillenbrand et al., 2010; Klages et al., 2013). The laminated and stratified diamictons may have formed from episodic plumes of sediment-laden water emitted from grounding line cavities with settling of fine-grained material, and/or sorting of fine grained material by bottom currents and tidal pumping, and/or gravity flows (e.g. Domack et al., 1999; Evans and Pudsey, 2002; Evans et al., 2005), rather than melt-water driven subaqueous outwash, which would not be expected due to the polar climatic conditions (Evans and Pudsey, 2002; Evans et al., 2005). The cobble causing the bending of the lamination in GC636 (Fig. 6.10) has most likely been ice rafted or melted out from the base of an ice shelf.

The differences in the grain-size and the various composition of the lamination and stratification possibly reflects differences in the proximity of the grounding line, the thickness of the basal debris layer in the ice shelf, and/or the strength of the bottom currents at the location of GC636 and GC637 (Domack et al., 1999). The lack of lamination and stratification of the lower part of facies 2 in GC635 does not exclude it being deposited close to the grounding line. The coarse sediment with the large cobble above the facies 3 transition in GC635 (Fig. 6.6; Fig. 6.14) might be what Domack et al. (1999)

refer to as the granulated facies, which they suggest is caused by ice shelf lift off from the seafloor and deposition of coarse-grained material. However, the lack of lamination and stratification indicates somewhat different conditions, than at the location of GC636 and GC637 after the grounding line retreated.

The structureless, upper part of facies 2 is suggested to reflect a gradual transition to a more distal grounding line position for the core locations (Fig. 7.3c). The increase in gravel content towards the top of facies 2 in GC635 and GC636 might reflect the landwards retreat of the ice shelf calving line over the core sites (cf. Domack et al., 1999). This is also supported by the reddish brown patch in GC635, where the grain composition differs from the typical composition and thus, most likely reflects deposition from an exotic iceberg (Fig. 7.3c). The random to horizontal orientation of gravel and pebbles in this facies indicates basal melt-out from the below an ice shelf, or iceberg rafting (Smith et al., 2011), and the sub horizontal clast alignment in GC636 at 21 cm might be formed during one event, either by ice shelf calving or tilting of an iceberg.

7.2.3 Facies 1: Seasonal open marine facies

The sponge bearing gravelly sandy mud overlying facies 2 in GC635 and GC636 and being the only facies in GC634, is interpreted to have been deposited primarily in a seasonal open marine environment with plankton production, similar to the present day conditions at the core sites (Fig. 7.3). This is primarily based on the relatively high biogenic content, contrasting the sub-ice shelf/perennial sea ice cover environment in facies 2. This interpretation is consistent with other deposits of seasonally open marine environment from the Antarctic continental shelf (e.g. Domack et al., 1999; Licht et al., 1999; Evans and Pudsey, 2002; Hillenbrand et al., 2009; 2010; Smith et al., 2011; 2014).

However, the typically seasonal open marine facies from other regions of the Antarctic shelf differ from the sponge bearing gravelly sandy mud in the seasonally open marine facies observed in the Brunt Basin. The seasonally open marine facies is generally composed of diatom bearing- to diatomaceous mud, foraminifera bearing- to foraminiferal mud to terrigenous mud in e.g., the Bellingshausen Sea (Hillenbrand et al., 2005; 2009; 2010), the Amundsen Sea (Smith et al., 2011; 2014) and the eastern Antarctic Peninsula (Evans and Pudsey, 2002; Evans et al., 2005). The seasonally open marine facies in the southern Weddell Sea is more similar in the way that it is composed of more coarse-grained sediments (cf. Hillenbrand et al., 2012 and reference therein). The texture of the sediments in the Brunt Basin indicates that terrigenous detritus from icebergs, but also partly from tidal currents and wind driven currents, dominates the seasonal open marine depositional environment. Whereas sedimentation from biogenic content is low, dominated by sponge spicules. Other studies have also found that the

eastern Weddell Sea shelf is composed of coarse-grained sediment, where they suggested ice rafting to be the most important depositional process (Elverhøi and Roaldset, 1983; Elverhøi, 1984).

Sponge spicules are typically related to zones of hard seafloor or coarse-grained sediments with gravels and pebbles, high productivity in overlying water masses and low sedimentation rates (Barthel and Gutt, 1992). The suitable substratum in the Brunt Basin is ice rafted and the ice shelf probably also acted as a sediment trap, keeping the sedimentation rates low (e.g. Elverhøi and Roaldset, 1983). Nutrition are possibly sourced by upwelling around the eastern margin of the Weddell Sea continental shelf, and transported along with the coastal current (Ryan et al., 2016). However, it is possible that the sponge spicules dominance partly is related to low concentration of diatoms and foraminifera, as a result of harsh conditions.

The absence of this facies in the top of GC637 does not necessary mean that the location of this core site has not been exposed to seasonal open marine environments. As mentioned in the methods (section 3.3, page 36), this core over penetrated during coring, which could have caused the uppermost sediments to be pushed out of the core liner. Furthermore, it is also not possible to exclude that winnowing by strong bottom currents has removed the biogenic content, which is the most important criteria for distinguishing open marine facies and sub-ice shelf/perennial sea ice cover facies (cf. Domack et al., 1999).

7.2.4 Element composition

This is the first time XRF-measurements of soft-sediment cores in cm resolution have been used on gravity cores recovering the transition from soft deformation till to open marine facies. This novel approach provides interesting results and has helped defining the sedimentary facies, but it is difficult to correlate the element composition data from the cores to other parameters of the cores. This may partly be due to the measured element compositions mostly are dependent on the fine-grained matrix, such as the clay mineralogy, which was not investigated in this study. Thus, some speculation on what the result from the element composition might indicate in relationship to the depositional environment and the difference between the environments is possible.

The large fluctuations observed in GC637, and the smaller amplitude fluctuations in GC636 and GC635 in the soft deformation till, are suggested to be reflecting changes in element composition in the matrix. Aluminum (Al) and silicon (Si) are abundant elements in clay minerals, and the fluctuation observed might reflect changes in clay mineral assemblages in the matrix. These changes in the clay minerals possibly reflect small changes in the basal regime of the grounded ice depositing them, and/or might

reflect different dynamics and minor changes in source area of the ice and the sediments (Monien et al., 2012).

The marked change in element composition from subglacial environment (facies 3) to marine environment (facies 2) in GC636 and GC637 is suggested to be caused by the influence of marine environment. The largest difference is observed the in K/Sum ratio.

The higher K/Sum ratio in the subglacial environment (facies 3), compared to the marine environment (facies 2), might reflect a different clay mineral composition. This is because potassium (K) is an important element in clay minerals such as illite (McKay et al., 2012). The difference in potassium content could be explained by enhanced current activity during deposition of facies 2, where other clay minerals with lower potassium (K) content have been supplied by marine currents, or that clay rich minerals are removed by current sorting. Whereas a subglacial environment is unaffected by current activities, which might lead to differences in the clay content and the potassium content between the different facies. The up-core decreases in potassium in GC636 could be related to increasing distance to the grounding line and the source of clay rich potassium. Such differences in clay mineral content and composition between subglacial facies and marine facies have been reported from several areas on the Antarctic shelf; e.g., the Bellingshausen Sea (Hillenbrand et al., 2010), the Ross Sea (Domack et al., 1999), and eastern Antarctic Peninsula (Evans and Pudsey, 2002).

The marked change in element composition in the seasonal open marine environment is suggested to be related to more productivity in the water masses, more supply from marine current and possibly ice rafting from exotic icebergs (Fig. 7.3).

There are also some differences in the element composition between the cores. The most obvious difference is the K/Sum ratio in GC635 vs. GC636 and GC637. This difference is suggested to be related to the core location and the source area. GC635 is located closer to the Brunt Ice Shelf, whereas GC636 and GC637 are located closer to the Stancomb-Wills Ice Tongue (Fig. 6.1; Fig. 7.1). These two ice shelves are fed by different source areas (Hulbe et al., 2005), which could be, at least partly, the reason for the difference in element composition. However, differences in current regime in the different locations could also affect the element composition, as GC636 and GC637 are located closer to the shelf edge and are possibly supplied more by marine currents than GC635, which is more "sheltered" in the inner basin.

The spikes in the S/Sum ratio, are not fully understood, but are believed to be artifacts. An explanation is presented in the appendix.

7.2.5 Glauconite

Glauconite grains in subglacial tills have also been reported from the Ross Sea (Anderson et al., 1980), despite the conditions below ice sheets and glaciers are not favorable for the formation of glauconite (e.g. Odin and Matter, 1981; Bornhold and Giresse, 1985; Lim et al., 2000). The glauconite in facies 3 must therefore be reworked from bedrock or glaciomarine sediments deposited prior to grounding line advance. The traces of broken diatoms and sponge spicules in the subglacial environment might indicate that it is composed of partly recycled glaciomarine sediments (Fig. 7.3).

The glauconite in GC636 and GC637 in the facies 2 might also be reworked glauconite, sourced from basal melt-out from under the ice shelf. Based the ^{14}C age obtained in GC635, the sediment rates are probably too high for the formation of glauconites, at least mature glauconites (cf. Odin and Matter 1981). The decreases in glauconite in GC636 towards the top of the core could be related to a more distal ice shelf position and less basal melt-out from below the ice shelf. However, I can't exclude that some glauconite also were formed in facies 2.

The glauconite in facies 1 could also have been ice rafted, possibly from icebergs calved from the same ice shelf. However, the observed coating of glauconites in GC634 could indicate that glauconite formation occurred in the facies 1.

The (almost) absence of glauconite grains in GC634 and GC635 might be caused by their location is closer to the Brunt Ice Shelf, whereas GC636 and GC637 are closer to the Stancomb-Wills Ice Tongue (Fig. 7.1; Fig. 6.1). This could further indicate that the glauconites are transported by the Stancomb-Wills Ice Tongue.

7.2.6 AMS radiocarbon ages

The shell valve at 50 cm in GC635 yields an age of 8499 cal. yr. BP. This can be used as a minimum age of deglaciation from the inner basin, as it was recovered 20 cm above the transition from subglacial to glaciomarine sub-ice shelf /perennial sea ice environment.

The ^{14}C dates from the planktonic, N. pachyderma sin. (2826 cal. yr. BP) and the benthic, Cibicides sp. (2857 cal. yr BP) from GC634 at 12 cm, are in good agreement with each other, giving confidence in the ages. These ages can be used as a minimum age from the onset of seasonal open marine environment. This could indicate that the Brunt Ice Shelf System front had reached close to its modern position or further southeast of it, and possibly the grounding line as well, which marks the completion of the deglaciation.

As these ^{14}C ages were obtained from cores located less than 2 km apart (Fig. 7.1), similar age for the retreat of the grounding ice, as well as the onset of seasonal open marine environment can be assumed. This implies that the onset of deglaciation in the inner part of the Brunt Basin occurred prior to ~8.5 cal ka BP, and a possible retreat of the ice shelf front further south of the inner basin ~2.8 cal. ka BP.

The ^{14}C date of the AIO fraction is 10,010 cal. yr. BP. From this, the local contamination offset from the AIO fraction can be calculated by using the C[14] age from the calcareous microfossils at the same depth. This gives a local contamination offset of ~7160 cal. yr. BP (10,010 - ~2850). This local contamination offset, can be used to correct the local contamination offset in future AIO dates obtained from the cores in the vicinity of GC634.

7.3 Reconstruction the ice sheet history in the Brunt Basin region

7.3.1 Timing and extent of grounded ice

The knowledge of maximum extent and subsequent retreat of the Antarctic Ice Sheet is important in order to understand its contribution to sea level rise (e.g. Bentley et al., 2014) and Hillenbrand et al. (2014) stressed the need of more constrains on the glacial extent in the Weddell Sea during the LGM and the subsequent deglaciation.

The swath bathymetry documents a widespread distribution of glacial landforms on the continental shelf off the Brunt Ice Shelf System, both in the Brunt Basin and on the unnamed bank, separating the Brunt Basin and the Halley Trough, providing evidence of ice sheet advance on to the shelf in the past (Fig. 7.1). Gravity cores recovered from the seafloor with MSGL and glacial lineations, recovered soft deformation till interpreted to be deposited beneath fast flowing ice (except for GC634).

One ^{14}C date obtained from glaciomarine sediments overlaying the soft deformation till in the inner basin, gives an age of ~8.9 cal. ka BP, indicating that the soft deformation till in GC635, and the MSGL in the inner basin was formed during the last glaciation. The timing of the formation of the glacial lineations and the MSGL in the middle and outer basin remains unconstrained in terms of ^{14}C dating. However, I suggest that these landforms were formed during the last glaciation as well. This is based on the pristineness of the MSGL, and the fact that the TOAPS system is not able to resolve any overlying sediments above the ATLs, interpreted as soft deformation till, indicating that less than 1 m of sediment has accumulated after the grounded ice retreated. This is also consistent with the glaciomarine sediments overlaying the soft deformation till recovered in the gravity cores, which are typically less than 1 m thick.

Deposition of the undated glacial landforms and the soft deformation till during previous glaciations is also possible, as sedimentation rates reported from some sub-ice shelf settings on the Antarctic shelf are as low as 2-3 cm/ka (Hemer et al., 2007). More ^{14}C dates from the sediment cores in the middle and outer basin are needed to verify if the deposition of the MSGL, glacial lineations, and the soft deformation till occurred during the last glaciation. However, the ~50 cm of sediments that has accumulated in the location of GC635 since 8.9 cal. ka BP, further supports the interpretation that the MSGL and glacial lineation in the middle and outer basin also were formed by grounded ice in the Brunt Basin close to the last glaciation.

By assuming a constant sedimentation rate for the deeper part of the transition from subglacial to glaciomarine sub-ice shelf/perennial sea ice cover environment in GC635 (70-50 cm) that is similar to the average sediment rate after ~8.5 cal. yr BP in GC635 (50-0 cm). The transition from subglacial to glaciomarine sub-ice shelf/perennial sea ice cover environment would have occurred ~11.9 cal. ka BP, which also puts a date on the deglaciation of the inner basin.

MSGL occur 24 km from the shelf edge in the Brunt Basin, and GC637 recovered subglacial soft deformation till below glaciomarine sediments in the location of the MSGL. As these features are formed subglacially (Fig. 7.4; King et al., 2009), they provide direct evidence that grounded ice extended close to shelf edge (e.g. Clark, 1999; Evans et al., 2005; Reinardy et al., 2011a). Unfortunately, iceberg scouring has eradicated the seafloor and any evidence of MSGL, with in 24 km of the shelf edge that might have formed during full glacial conditions. Ice contact features within 24 km of the shelf edge, such as GZW or marginal moraine, which would have marked the extent of grounded ice, might also have been removed by iceberg scouring and are limiting an accurate reconstruction of the ice extent in the Brunt Basin during the last glaciation. However, the lack of ice contact features could also be explained by grounded ice reaching all the way to the shelf edge. If so, ice contact features did not necessary need to form in front of the MSGL in the outer basin. However, with the current available data it remains uncertain if the ice extended all the way to the shelf edge.

The landform assemblage on the bank also indicate the presence of grounded ice in the past (Fig. 7.1). Recessional moraines on the western side of the bank show that grounded ice extended across the bank (e.g. Todd et al., 2007; Benn and Evans, 2010). Several grounding line features are located on the eastern side of the bank, indicating episodic retreat or repeated advance of grounded ice onto the bank (cf. Dowdeswell et al., 2008). The lateral shear-moraine also points towards grounded ice located on the bank (e.g. Stokes and Clark, 2002a; Batchelor and Dowdeswell, 2016), and the extent of the lateral shear-moraine might indicate the extent of ground ice on the bank. However, as no cores were recovered from the bank and thus no ^{14}C dates, it is not possible to constrain when grounded ice advance and
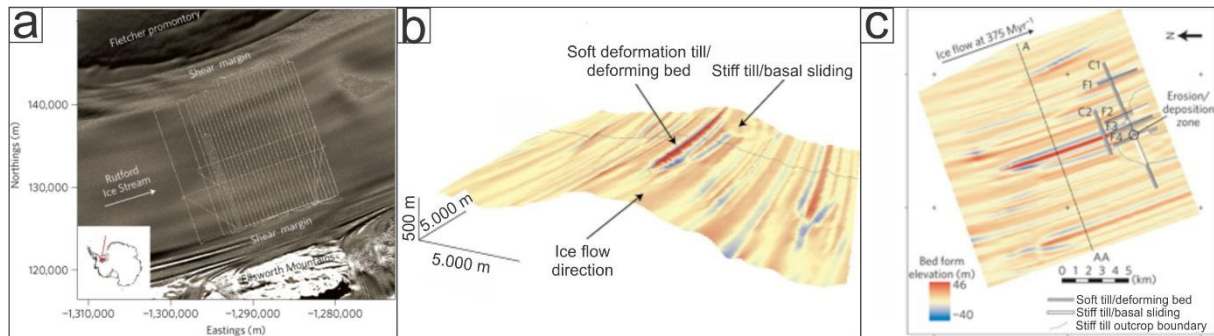
Fig. 7.4. Formation of mega-scale glacial lineations (MSGL) beneath the Rutford Ice Stream. (a) Location of the radar survey on the Rutford Ice Stream, and the location of Fig. b and c. Inset map indicates the location of the Rutford ice stream within Antarctica. (b) Three dimensional image of the bed of Rutford Ice Stream, with MSGL dominating the topography. (c) Map view of MSGL beneath Rutford Ice Stream. Slightly modified from King et al., 2009.

retreated from the bank. However, the pristineness of the glacial landforms, and the lack of a sediment cover thicker than 1 m on top of the glacial landforms, indicate that ice retreated relatively recently.

These results are in conflict with interpretations of Stolldorf et al. (2012) who suggested that the grounded ice had retreated from the eastern Weddell Sea shelf, and that the grounding line was located close to its present day location before ~33 cal. ka BP (section 1.3.2, page 12). This includes the continental shelf in front of the Brunt Ice Shelf System (Stolldorf et al., 2012). The interpretation was based on ^{14}C dates obtained from benthic foraminifera assemblages, that spanned the last ~33 cal. ka BP in core 3-7-1 (for location see: Fig. 7.1). However, the ^{14}C ages showed inverted ages (Table 1.1, page 12). Whereas the lowermost ^{14}C agesobtained was the youngest, ~14 cal. ka BP, and the uppermost ^{14}C age obtained exceeded the dating range (older than 52.8 cal. ka BP). The inverted down core dates of the core were attributed to iceberg scouring (Stolldorf et al., 2012). It could, of course, be that grounded ice on the bank, in fact, had retreated before ~33 cal. ka BP, and that the ice in the Brunt Basin was more sustainable. Another solution could be that the ^{14}C ages that pre-dates the LGM, where preserved beneath cold-based ice (cf. Kleman, 1994) and later reworked into the core location of core 3-7-1. Nevertheless, I suggest that the deglaciation age obtained from the GC635 (8.9 cal. ka BP / 11.9 cal. ka BP) is more reliable for the onset of deglaciation in the inner part of Brunt Basin, than the ages obtained from core 3-7-1. Based on the fact that core 3-7-1 is clearly composed of reworked material and was retrieved from the bank, whereas GC635 was retrieved from the Brunt Basin, and is less prone to reworking by current winnowing and iceberg scouring (e.g. Vorren et al., 1984).

The results from this study are also in conflict with terrestrial data, which show limited thickening of the ice sheet in the EAIS region during the LGM (Hein et al., 2011; Thor and Low, 2011). In addition to ice core data from the EPICA core in Dronning Maud Land (Fig. 1.3, page 6), which showed that accumulation rates during the LGM was 1.5-2 times lower than after c.15 ka (Huybrechts et al., 2009).

However, the limited observed thickening could also be explained by cold-based ice covering the sample locations used for reconstructing the ice-sheet thickening during the LMG (cf. Clark, 2011), which simply did not remove the bedrock used for surface exposure dating (Hein et al., 2011) and the mumiyo samples used for ^{14}C dating (Thor and Low, 2011).

However, the mismatch between the terrestrial data could also be explained by the fact that there was no significant thickening in the EAIS region and that the ice sheet could advance due to LGM sea-level low-stand, which was ~130 m lower than present-day sea level (e.g. Weber et al., 2011; Hillenbrand et al., 2012). If the LGM sea-level low-stand was taken into account for the seafloor depths in the study area, most of the bank would be at ~120 m-, the shelf edge would be at ~370 m-, and the deepest part of the middle basin would be at ~510 m below the sea surface during the LGM. Presently, the ice shelf thickness of the Stancomb-Wills Ice Tounge is more than 450 m close to the grounding line and thins to 200 m at the ice shelf front, and the Brunt Ice Shelf is presently between 100- 250 m thick (Humbert et al., 2009). During the LGM, climatic conditions would be colder and more favorable for ice-shelf formation (e.g. Benn and Evans, 2010). This would presumably lead to a thickening of both the Stancomb-Wills Ice Tongue and the Brunt Ice Shelf during the last glacial, and ice-shelf grounding would almost be unavoidable. Ice-sheet surface elevation required for such a grounding event would not have to be much higher than the present ice-sheet surface. A similar scenario has been proposed for ice sheet grounding in the Flichner Trough (cf. Hillenbrand et al., 2012; Larter et al., 2012; section 1.3.1, page 5). This supports my suggestion of ice-shelf grounding scenario in the study area. However, such a grounding event in the Brunt Basin could have resulted in ice-sheet thickening in the drainage basin due to increased basal friction, unless the basal conditions were very "slippery" and fast flow occurred (Hillenbrand et al., 2012; Larter et al., 2012). MSGL and glacial lineations in the Brunt Basin indicate that the ice flow was fast (Stokes and Clark, 2002b), which would allow for more ice to be drained from the interior of the EAIS, effectively lowering the ice sheet profile, and could explain why there was little thickening in the interior of the EAIS. Additionally, the subtle glacial lineations in the deeper part of the middle basin and the low shear strength and wet bulk density values in the top of the soft deformation till in GC636, could point to a relatively thin ice, with a low surface gradient, similar to an ice plain in front of ice streams (Bindschadler et al., 2005). This could also explain why the ice sheet could advance close to the shelf edge without a major thickening in the drainage basins.

The results from this study are consistent with the results obtained by Weber et al. (2011), who suggested that the EAIS advanced onto the continental shelf during the LGM. These authors based their conclusions on ^{14}C ages obtained by *N.pachyderma sin.* and sedimentological changes on the continental slope and rise. The sedimentological changes were related to deposition of siliciclastic varves, which the authors suggested was caused by formation of polynyas over the continental slope and rise, which

they again argued was formed because the EAIS was located at the shelf edge during the LGM (Weber et al., 2011).

Nevertheless, the results from this study help improve significantly on the recent ice-sheet reconstruction in the Weddell Sea (Hillenbrand et al., 2014). It provides important information about the ice-sheet extent in a previously unmapped area, where reconstructions so far were based on spare data along the eastern Weddell Sea (section 1.3.1), and where the chronology was only constrained in the Brunt Basin region by the suspiciously inverted down core ^{14}C ages in core 3-7-1 (Stolldorf et al., 2012).

7.3.2 Basal regime and dynamics

The distribution of glacial landforms on the seafloor and information obtained from the TOPAS sub-bottom profilers and the sediments in the cores have been used to infer former basal regime and dynamics of the grounded ice in the Brunt Basin and on the shallower bank prior to the deglaciation. A schematic model of the basal regime and dynamics is presented in Fig. 7.5 (*p.* 131).

MSGL and glacial lineations are confined within the Brunt Basin, but are absent on the bank and in the southern part of the inner basin (Fig. 7.1). The absence of these landforms, together with the general smoothness of the seafloor, indicates slow flowing ice (e.g. Evans et al., 2005; Klages et al., 2013; 2015; Rydningen et al., 2013). In addition, the TOPAS profiles from the bank show a strong seafloor reflector, interpreted as the surface of stiff till (section 5.2, page 87), which is typically associated with regions of slow flowing ice (e.g. Evans et al., 2005; Klages et al., 2013). Both the seafloor on the bank and the southern part of the inner basin contain comparatively iceberg scours (Fig. 7.1) and it is, therefore, unlikely that any indications of fast flowing ice have been removed. The occurrence of iceberg scours indicates that the seafloor surface is not completely composed of solid bedrock (e.g. Klages et al., 2013).

Ice contact features such as recessional moraines and GZW on the bank (e.g. Fig. 7.1) could indicate that ice was not completely cold based (frozen to the ground), as sediment was available to form the moraine ridges (e.g. Benn and Evans, 2010; Christoffersen et al., 2010; Hogan et al., 2010a). However, formation of the ice contact features could also be explained by a (re-) advancing ice, pushing sediment up into moraine ridges. This could certainly be the case for the recessional moraines on the western side bank, but based on the size and shape of the GZW (up to 50 m high) on the eastern side of the bank, I find it unlikely that they were formed by an ice push alone. Therefore, I suggest that basal melt-out and delivery of subglacial debris was an important factor for their formation, which implies warm based conditions (cf. Christoffersen et al., 2010; Batchelor and Dowdeswell, 2015). However, it is possible

that basal conditions change during the deglaciation, and that warm based conditions occurred as the ice started to retreat from the bank.

The presence of MSGL and glacial lineations, together with ATL and ATR corresponding to soft deformation till in the Brunt Basin is inferred to represent a zone of fast flowing, warm based ice (Stokes and Clark, 2002b; Clark et al., 2003a; King et al., 2009; Klages et al., 2015). Modern and former fast-flowing ice streams in Antarctica are commonly associated with soft deformation till at the base of the ice stream, which are typically linked to fast flow by deformation of the water saturated soft tills (Smith, 1997; Engelhardt and Kamb, 1998; Dowdeswell et al., 2004; King et al., 2009). Additionally, MSGL observed on the Norwegian and Svalbard-Barents Sea shelf have been used to reconstruct the presence of fast ice streams during the last glaciation (Ottesen et al., 2005b; 2007; Rydningen et al., 2013), representing warm based zones within the ice sheet. The observed contrast with slow flowing ice in the southern part of the inner basin and the bank, and fast flowing ice in the middle and outer basin, are also consistent with the lateral shear marginal-moraine observed along the bank basin slope (Fig. 7.1). However, the subglacial conditions during the last glaciation within the fast flowing zones varied spatially from the inner to the outer basin in the Brunt Basin (Fig. 7.5).

In the inner basin (Fig. 7.5), a strong reflection (*Ref. I-B*) is locally overlain by soft deformation till moulded into ridge, corresponding to *ATR I-B* and MSGL at the sea floor, indicating that ice flow occurred by localized basal sliding over hard substratum, presumably stiff till (cf. King et al., 2009; Fig. 7.4).

In the deeper part of the middle basin (Fig. 7.5), a continuous ATL (*ATL 1 M-B*) of soft deformation till and subtle glacial lineations, indicates that ice flow occurred by basal deformation of soft deformation till (cf. Reinardy et al., 2011a). However, the subtle nature of the lineations and the low shear strength and wet bulk density values are inferred to reflect less pressure at the sediment ice interface, and possibly a thin ice, just thick enough to remain grounded or periodically ground in the deeper part of the middle basin (cf. VC 324 and VC337 and Fig. 16 in Evans et al., (2005)).

In the outer basin (Fig. 4a), well defined MSGL above a relative thick layer of soft deformation till (ATL1 O-B), indicates that widespread deformation sliding at the base of a fast flowing ice that was properly grounded during the formation of these features (e.g. Evans et al., 2005).
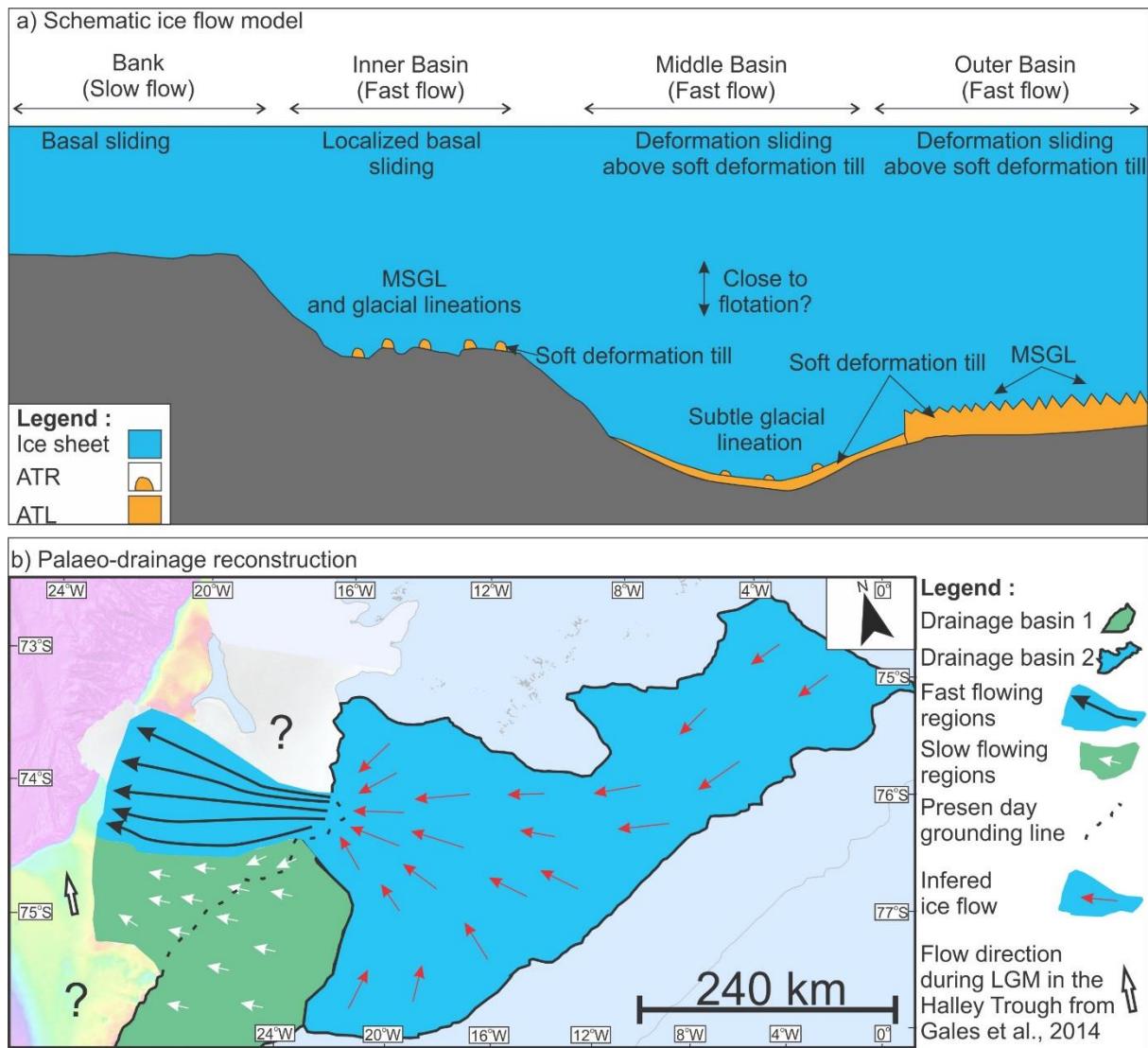
Fig. 7.5. (a) Schematic ice flow model of the study area, indicating basal conditions and regions of fast flow and slow flow (not to scale). (b) Palaeo-drainage reconstruction of the study area. The drainage basins are basin on the present day ice divides according to Fredwell et al., (2013). Flow direction in the Halley Trough are from Gales et al., (2014). The transparent version of the IBCSO (Arndt et al., 2013) data set is underlain the palaeo-drainage reconstruction. For reference seafloor depth color scale see (Fig. 6.1, p. 91). ATR-acoustical transparent ridge, ATL- acoustical transparent layer.

The difference in thickness of the soft deformation till in ATL1 M-B and ATL1 O-B (e.g. Fig 2d; Fig. 4a) is likely to represent a difference in the subglacial conditions and/or possibly duration of ice flow in the middle and outer basin. However, the detailed origin of this process remains unclear, but a tentative suggestion of the difference has been made:

If the ice in the deeper part of the middle basin only was slightly grounded, less pressure would be applied to the base of the ice, which would lead to less basal friction and less heat generated, which

again would lead to less englacial and basal melt-out and less deposition of soft deformation till. Whereas in the outer basin, ice was properly grounded on the seafloor, leading to more pressure at the base of the ice and more deposition of soft deformation till. However, as the transition between the middle and outer basin, also represent a palaeo grounding line (Fig. 7.1), it is possible that the difference in thickness of the ATL1 M-B and ATL1 O-B also reflects that ice remained grounded in the outer basin for a longer time than in the deeper part of the middle basin.

This spatial pattern of ice flow dynamics with localized basal sliding in the inner basin and deformation of soft deformation till in the middle and outer part of the basin resembles the pattern inferred from seismic surveys beneath the modern Rutford Ice stream (Smith, 1997; Smith and Murray, 2009). Similar patterns are also reported from former palaeo-ice stream on the Antarctic continental shelf, where soft deformation till layers are either absent or patchy on the inner shelf, but increases in thickness towards the outer shelf (e.g. Ó Cofaigh et al., 2002; Wellner et al., 2001; Evans et al., 2005; Reinardy et al., 2011a). This transition has been suggested to reflect a transition from crystalline to sedimentary bedrock, but also reflects an increase in down flow velocity, that evolve to rapid ice-streaming in the middle and outer shelf (Wellner et al., 2001; Ó Cofaigh et al., 2002; 2005a; Evans et al., 2004).

If this transition in the Brunt Basin is related to bedrock boundaries or acceleration in down flow velocities, remains unclear. However, based on the similarities to modern and former ice streams, I suggest that the ice draining through the Brunt Basin must have been in the form of fast flowing ice, and presumably ice streaming in the middle and outer basin. This is further supported by the elongation ratio of some of the MSGL in the outer basin, which generally excides 1:10 (Stokes and Clark, 2002b; Clark and Stokes, 2003b), together with the presence of the lateral shear-moraine which is suggested to be closely related to ice streams (Stokes and Clark, 2001; Batchelor and Dowdeswell, 2016)

The distribution of fast flowing and slower flowing regions within the study area is believed to be predominantly linked to the palaeo-drainage area of the ice in the different regions. To illustrate this, a palaeo-drainage reconstruction has been made (Fig. 7.1). The slower flowing regions are suggested to have been occupied by slower flowing ice from the same drainage area that are currently feeding the Brunt Ice Shelf (Drainage area 1 in Fig. 7.5). Whereas the fast flow regions are suggested to have been occupied by fast flowing ice from the same area that is feeding the Stancomb-Wills Ice Tongue (Drainage area 2 in Fig. 7.5).

This is supported by the orientation of the MSGL and subtle glacial lineations in the outer and middle basin, which are very similar to the current flow of the Stancomb-Wills Ice Tongue. Additionally, parts of the ice shelf is actually located above some of the MSGL in the outer basin. This supports that the

middle and outer part of the basin was drained by ice with a similar drainage basin as the Stancomb-Wills Ice Tongue is today (drainage basin 1). The glacial lineations in the inner basin show a complex pattern of flow directions, assumed to have been formed during different stages. Even though, the MSGL and glacial lineations observed in the inner basin might have been formed during different stages, it is possible that they represent the ice flow during full glacial conditions. I therefore suggest that during full glacial conditions, fast flowing ice from drainage basin 1 also moved around the bank, towards the middle and outer basin. Whereas the slower flowing ice, flowed towards the bank and on top of it.

The current difference in velocities of the ice feeding the ice shelves also supports this (e.g. Hulbe et al., 2005; Humbert et al., 2009; Wuite and Jezek, 2009). The present flow velocity of the ice feeding the Brunt Ice shelf is ~170 m/a, whereas the present velocity of the ice feeding the Stancomb-Wills reaches up to ~900 m/a near the grounding line (Hulbe et al., 2005). The drainage areas are based on the present day ice divides suggested by Fretwell et al. (2013), by assuming that the drainage area would be fairly similar during the last glaciation, as there was no major thickening in the EAIS (Hein et al., 2011; Thor and Low, 2011). This is also consistent with observations done by Hein et al. (2016) who suggest that the ice sheet divides in the WAIS have been stable for 1.4 million years. I therefore assume that this suggestion also can be applied for the EAIS, which is regarded as a more stable ice sheet. The palaeo-drainage reconstruction (Fig. 4b), suggests that drainage area 2 is much larger than drainage area 1, which could explain why ice flow in the region fed by the drainage area 2 was much faster (Livingstone et al., 2012).

The slower flowing regions and the faster flowing regions are suggested to have moved as two independent ice masses, where the slower flowing regions presumably prevent the ice flow in area 2 from diverging, and therefore partly channelized the faster flowing ice. In the same way, the faster flowing region prevented the slower flowing region to flow northwards and forced it to flow over the bank (Fig. 7.5).

7.3.3 Deglaciation history

Ice contact landforms formed at the retreating margin of ice sheets provide insight in the retreat rate and dynamics during the deglaciation (Fig. 7.6; Dowdeswell et al., 2008; Cofaigh et al., 2008). Closely spaced moraine ridges, such as recessional moraines, indicates a slowly retreating grounded ice margin (Todd et al., 2007), whereas more spatially spaced GZW indicates episodic retreats, with longer still stand during the retreat phase (Dowdeswell et al., 2008). The absence of such ice contact landforms superimposed on well preserved subglacial sedimentary landforms on the continental shelf is typically associated with fast retreat, caused by flotation of the ice margin and ice loss due to rapid iceberg calving (Dowdeswell et al., 2008).
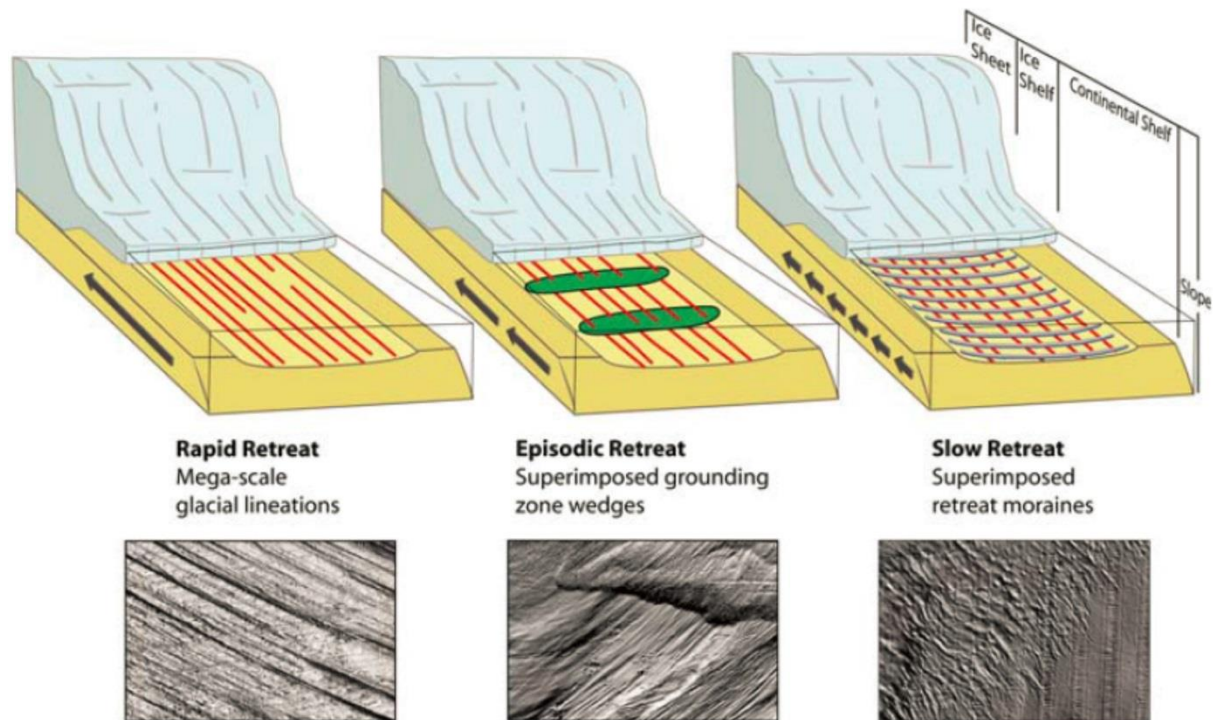
Fig. 7.6. Schematic diagram of submarine landform sets indicating rapid, episodic and slower retreat of ice streams across high-latitude continental shelves, with examples of swath bathymetry data (scale across swath images: rapid retreat, 15 km; episodic retreat, 40 km, slow retreat, 10 km). Floating ice shelves are included beyond the ice-sheet grounding zone in the diagram, because they are a pervasive part of modern Antarctic ice-sheet systems. From Dowdeswell et al. (2008).

The landform assemblage within the study area points towards a complex deglaciation history, including rapid retreat by floatation interrupted by punctuated still stands, as well as slower retreat of grounded ice.

On the western side of the bank (zone A in Fig. 7.7.), a set of closely spaced recessional moraines indicates a slow retreat of grounded ice towards east (Dowdeswell et al., 2008), which produced the recessional moraines during minor still stands or small re-advances during the retreat phase (Todd et al., 2007).

The deglaciation in the middle and outer basin (Zone b in Fig. 7.7) is suggested to have been episodically, but rapid caused by flotation of the ice margin, as recessional moraines or other prominent moraine ridges cross cutting the subtle glacial lineation and the MSGL are absent (Dowdeswell et al., 2008). Grounded ice lost its "foothold" first in the deeper part of the middle basin, possibly due to thinning of the ice sheet, and/or rising sea level, which lead to floatation of the ice located in the deeper part of the middle basin. The deglaciation of the outer basin occurred sometime later, and is also suggested to have occurred due to flotation (Zone b in Fig. 7.7). This rapid retreat of the ice margin

might also have been provoked by the inclined seafloor slope towards land, which is suggested be prone to rapid retreat and detachment from the seafloor (cf. Katz and Worster, 2010).

The complex pattern of ice contact landforms on the eastern side of the bank, and in the inner basin (Zone C Fig. 7.7), indicates a slow retreat, punctuated by several longer still stands or re-advances of the ice margin during the deglaciation.

The size of the GZW on the edge of the bank, (up to 50 m high) indicates that grounded ice remained stable for a relatively long period (cf. Howat and Domack, 2003). The bank might have acted as a pinning point and stabilized the ice (Batchelor and Dowdeswell, 2015), before the ice retreated further towards the inner basin. One set of recessional moraines indicates a slow retreat of grounded ice in the inner basin, punctuated by a longer still stand, forming the southeastern most GZW, before it eventually retreated from the inner basin prior to ~8.5 cal. ka BP. The final retreat from the inner basin is inferred to have occurred rapid due to flotation, as there are no superimposed ice contact features on top of well-preserved MSGL in the inner basin.

The origin of the end moraine / ice shelf moraine remains unclear, but it is possible that it was formed during the deglaciation, either by ice shelf grounding or by a narrow ice tongue re-advancing onto the bank. The absence of similar features observed on the Antarctic continental shelf can at least partly be explained by the preferential surveying in troughs, where the ice is expected to have been warm based and the seafloor depth is much greater, which differs from the conditions on the banks (e.g. Ó Cofaigh et al., 2002; 2005a; Evans et al., 2005; Jakobsson et al., 2012; Larter et al., 2012). The lack of information from the banks can hide important clues of ice shelves grounding features and their contribution to stabilizing ice shelves. As grounding features also provide buttressing for the ice shelves, it also plays a key role in buttressing discharge of ice from the interior of the Antarctic Ice Sheet, which is an important factor in its contribution to sea level rise (Matsuoka et al., 2015).
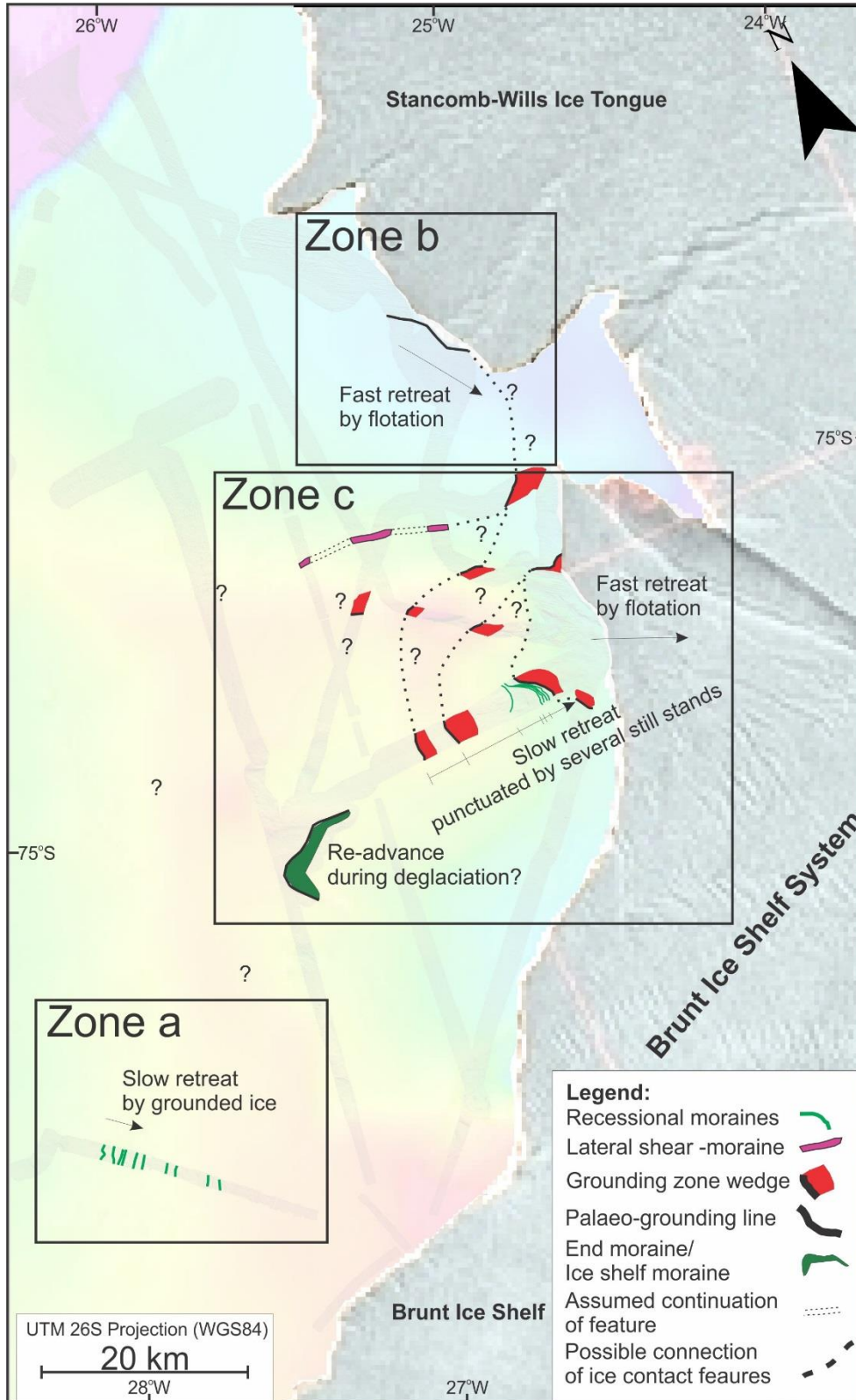
Fig. 7.7. Map of the interpreted ice contact landforms within the Brunt Basin region, including possible connections between the landforms, overlying a transparent version of the swath bathymetry data, the IBCSO map (Arndt et al., 2013), and a Envisat synthetic aperture radar image of the Brunt Ice Shelf System from 4th of March 2011. Three zones are marked out to display the different retreat patterns.

8 Conclusions

Swath-bathymetry data, TOPAS sub-bottom profiles and multi-proxy analyses of four gravity cores were performed with the purpose of reconstructing the glacial history the Brunt Basin since the last glacial. The main findings of this study are:

- Mega-scale glacial lineations located 24 km from the shelf edge indicate that the ice sheet advanced to the outer parts of the continental shelf in the Brunt Basin region during the last glaciation. Recessional moraines on the western side of the bank imply that grounded ice extended across the bank as well. However, intense iceberg scouring close to the shelf edge does not allow to constrain the accurate extent of the advance.

- Whereas the ice occupying the southern part of the inner basin and the shallower bank was relatively slowly flowing, fast-flowing ice occupied the northern part of the inner basin to the outer shelf prior to the deglaciation. This contrast between slow and fast flowing ice is inferred to be related to the different drainage basins of the ice in the two regions.

- The flow dynamics within the fast flowing regions vary spatially, from localized basal sliding in the inner basin where soft deformation till was moulded into glacial lineation and MSGL, to widespread deformation sliding above soft deformation till in the middle and outer basin.

- The fast flowing ice is inferred to have been in the form of an ice stream, draining the interior of the East Antarctic Ice Sheet, and is suggested to have efficiently lowered or maintained the ice sheet elevation in the drainage area. The ice-stream was presumably relatively thin, just thick enough to remain grounded or periodically grounded in the deeper part of the Brunt Basin prior to the deglaciation.

- Recessional moraines on the western side of the bank are inferred to reflect slow retreat of the grounding line during the deglaciation.

- The deglaciation of the middle and outer basin appears to have been episodically, but fast, facilitated by flotation in response to inclined landwards sloping seafloor and ice sheet thinning and/or rising sea level.

- The assemblage of ice contact landforms, such as GZW and recessional moraines points to a complex deglaciation history on the eastern side of the bank towards the inner basin. The ice contact landforms indicate a slow retreat that was punctuated by longer still stands of the ice margin on the edge of the bank, resulting in the formation of larger GZW. Ice retreat from the inner basin was initiated with slow retreat by grounded ice resulting in recessional moraines, and a GZW. The final retreat from the inner basin is inferred to have occurred rapid due to flotation.

- A ^{14}C date obtained from a shell valve 20 cm above the transition from subglacial sediments suggests that deglaciation of the inner basin occurred prior to 8.5 cal. ka BP. Assuming a constant sedimentation rate after the onset of marine sedimentation, ice retreated from the inner basin occurred around 11.9 cal. ka BP.

- After the major deglaciation, extensive ice shelves, or perennial sea ice cover occurred above the location of the retrieved sediment cores, resulting in deposition of coarse grained terrigenous debris and low to absent biogenic content in the sediment.

- Seasonally open marine environment occurred from ~2.8 cal. ka BP, resulting in increased productivity in the water masses. However, the coarse grained terrigenous sediments deposited in the open marine environment, indicates that ice rafting remained the dominant depositional process in the study area.

References

AN, Z., KUKLA, G. J., PORTER, S. C. & XIAO, J. 1991. Magnetic susceptibility evidence of monsoon variation on the Loess Plateau of central China during the last 130,000 years. *Quaternary Research,* 36**,** 29-36.

ANDERSON, J. B. 1972. Nearshore glacial-marine deposition from modern sediments of the Weddell Sea. *Nature,* 240**,** 189-192.

ANDERSON, J. B., KURTZ, D., DOMACK, E. & BALSHAW, K. 1980. Glacial and glacial marine sediments of the Antarctic continental shelf. *The Journal of Geology***,** 399-414.

ANDERSON, J. B., ANDREWS, B., BARTEK, L. & TRUSWELL, E. 1991. Petrology and palynology of Weddell Sea glacial sediments: implications for subglacial geology. *Geological Evolution of Antarctica. Cambridge University Press, New York***,** 231-235.

ANDERSON, J. B. 1999. *Antarctic marine geology*, Cambridge University Press.

ANDERSON, J. B. & ANDREWS, J. T. 1999. Radiocarbon constraints on ice sheet advance and retreat in the Weddell Sea, Antarctica. *Geology,* 27**,** 179-182.

ANDERSON, J. B., SHIPP, S. S., LOWE, A. L., WELLNER, J. S. & MOSOLA, A. B. 2002. The Antarctic Ice Sheet during the Last Glacial Maximum and its subsequent retreat history: a review. *Quaternary Science Reviews,* 21**,** 49-70.

ANDERSON, J. B., CONWAY, H., BART, P. J., WITUS, A. E., GREENWOOD, S. L., MCKAY, R. M., HALL, B. L., ACKERT, R. P., LICHT, K., JAKOBSSON, M. & STONE, J. O. 2014a. Ross Sea paleo-ice sheet drainage and deglacial history during and since the LGM. *Quaternary Science Reviews,* 100**,** 31-54.

ANDERSON, P. 1993. Evidence for an Antarctic winter coastal polynya. *Antarctic science,* 5**,** 221-226.

ANDERSON, R., JONES, D. & GUDMUNDSSON, G. 2014b. Halley Research Station, Antarctica: calving risks and monitoring strategies. *Natural Hazards and Earth System Sciences,* 14**,** 917-927.

ANDREASSEN, K., WINSBORROW, M. C., BJARNADÓTTIR, L. R. & RÜTHER, D. C. 2014. Ice stream retreat dynamics inferred from an assemblage of landforms in the northern Barents Sea. *Quaternary Science Reviews,* 92**,** 246-257.

ANDREWS, J. T., DOMACK, E. W., CUNNINGHAM, W. L., LEVENTER, A., LICHT, K. J., JULL, A. T., DEMASTER, D. J. & JENNINGS, A. E. 1999. Problems and possible solutions concerning radiocarbon dating of surface marine sediments, Ross Sea, Antarctica. *Quaternary Research,* 52**,** 206-216.

ARNDT, J. E., SCHENKE, H. W., JAKOBSSON, M., NITSCHE, F. O., BUYS, G., GOLEBY, B., REBESCO, M., BOHOYO, F., HONG, J. & BLACK, J. 2013. The International Bathymetric Chart of the Southern Ocean (IBCSO) Version 1.0−A new bathymetric compilation covering circum‐Antarctic waters. *Geophysical Research Letters,* 40**,** 3111-3117.

AVAATECH. *Specifications: Avaatech XRF Scanner* [Online]. Available: http://www.avaatech.com/specifications_1.htm [Accessed 28.10 2016].

BAETEN, N. J., FORWICK, M., VOGT, C. & VORREN, T. O. 2010. Late Weichselian and Holocene sedimentary environments and glacial activity in Billefjorden, Svalbard. *Geological Society, London, Special Publications,* 344**,** 207-223.

BAMBER, J., GOMEZ-DANS, J. & GRIGGS, J. 2009. A new 1 km digital elevation model of the Antarctic derived from combined satellite radar and laser data–Part 1: Data and methods. *The Cryosphere,* 3**,** 101-111.

BARKER, P. & THOMAS, E. 2004. Origin, signature and palaeoclimatic influence of the Antarctic Circumpolar Current. *Earth-Science Reviews,* 66**,** 143-162.

BARKER, P. F., FILIPPELLI, G. M., FLORINDO, F., MARTIN, E. E. & SCHER, H. D. 2007. Onset and role of the Antarctic Circumpolar Current. *Deep Sea Research Part II: Topical Studies in Oceanography,* 54**,** 2388-2398.

BARNES, P. W. & LIEN, R. 1988. Icebergs rework shelf sediments to 500 m off Antarctica. *Geology,* 16**,** 1130-1133.

BARR, I. D. & CLARK, C. D. 2012. An updated moraine map of Far NE Russia. *Journal of Maps,* 8**,** 431-436.

BARTHEL, D. & GUTT, J. 1992. Sponge associations in the eastern Weddell Sea. *Antarctic Science,* 4**,** 137-150.

BARTINGTON 2002. Operation Manual for MS2 Magnetic Susceptibility System. Barington. *Instruments Limited, Witney, Oxford*.

BASS, D. & WOODWORTH-LYNAS, C. 1988. Iceberg crater marks on the sea floor, Labrador Shelf. *Marine Geology,* 79**,** 243-260.

BATCHELOR, C., DOWDESWELL, J. & HOGAN, K. 2011. Late Quaternary ice flow and sediment delivery through Hinlopen Trough, Northern Svalbard margin: submarine landforms and depositional fan. *Marine Geology,* 284**,** 13-27.

BATCHELOR, C., DOWDESWELL, J. & PIETRAS, J. 2014. Evidence for multiple Quaternary ice advances and fan development from the Amundsen Gulf cross-shelf trough and slope, Canadian Beaufort Sea margin. *Marine and Petroleum Geology,* 52**,** 125-143.

BATCHELOR, C. & DOWDESWELL, J. 2015. Ice-sheet grounding-zone wedges (GZWs) on high-latitude continental margins. *Marine Geology,* 363**,** 65-92.

BATCHELOR, C. & DOWDESWELL, J. 2016. Lateral shear-moraines and lateral marginal-moraines of palaeo-ice streams. *Quaternary Science Reviews,* 151**,** 1-26.

BEAMAN, R. J. & HARRIS, P. T. 2003. Seafloor morphology and acoustic facies of the George V Land shelf. *Deep Sea Research Part II: Topical Studies in Oceanography,* 50**,** 1343-1355.

BELDERSON, R., KENYON, N. & WILSON, J. 1973. Iceberg plough marks in the northeast Atlantic. *Palaeogeography, Palaeoclimatology, Palaeoecology,* 13**,** 215-224.

BENN, D. & EVANS, D. 2010. Glaciers and Glaciation, 2nd Ed. London: Hodder Education.

BENTLEY, M. J. & ANDERSON, J. B. 1998. Glacial and marine geological evidence for the ice sheet configuration in the Weddell Sea–Antarctic Peninsula region during the Last Glacial Maximum. *Antarctic Science,* 10**,** 309-325.

BENTLEY, M. J. 1999. Volume of Antarctic Ice at the Last Glacial Maximum, and its impact on global sea level change. *Quaternary Science Reviews,* 18**,** 1569-1595.

BENTLEY, M. J., FOGWILL, C. J., LE BROCQ, A. M., HUBBARD, A. L., SUGDEN, D. E., DUNAI, T. J. & FREEMAN, S. P. 2010. Deglacial history of the West Antarctic Ice Sheet in the Weddell Sea embayment: Constraints on past ice volume change. *Geology,* 38**,** 411-414.

BENTLEY, M. J., Ó COFAIGH, C., ANDERSON, J. B., CONWAY, H., DAVIES, B., GRAHAM, A. G. C., HILLENBRAND, C.-D., HODGSON, D. A., JAMIESON, S. S. R., LARTER, R. D., MACKINTOSH, A., SMITH, J. A., VERLEYEN, E., ACKERT, R. P., BART, P. J., BERG, S., BRUNSTEIN, D., CANALS, M., COLHOUN, E. A., CROSTA, X., DICKENS, W. A., DOMACK, E., DOWDESWELL, J. A., DUNBAR, R., EHRMANN, W., EVANS, J., FAVIER, V., FINK, D., FOGWILL, C. J., GLASSER, N. F., GOHL, K., GOLLEDGE, N. R., GOODWIN, I., GORE, D. B., GREENWOOD, S. L., HALL, B. L., HALL, K., HEDDING, D. W., HEIN, A. S., HOCKING, E. P., JAKOBSSON, M., JOHNSON, J. S., JOMELLI, V.,

JONES, R. S., KLAGES, J. P., KRISTOFFERSEN, Y., KUHN, G., LEVENTER, A., LICHT, K., LILLY, K., LINDOW, J., LIVINGSTONE, S. J., MASSÉ, G., MCGLONE, M. S., MCKAY, R. M., MELLES, M., MIURA, H., MULVANEY, R., NEL, W., NITSCHE, F. O., O'BRIEN, P. E., POST, A. L., ROBERTS, S. J., SAUNDERS, K. M., SELKIRK, P. M., SIMMS, A. R., SPIEGEL, C., STOLLDORF, T. D., SUGDEN, D. E., VAN DER PUTTEN, N., VAN OMMEN, T., VERFAILLIE, D., VYVERMAN, W., WAGNER, B., WHITE, D. A., WITUS, A. E. & ZWARTZ, D. 2014. A community-based geological reconstruction of Antarctic Ice Sheet deglaciation since the Last Glacial Maximum. *Quaternary Science Reviews,* 100**,** 1-9.

BERKMAN, P. A. & FORMAN, S. L. 1996. calcareous marine species in the Southern Ocean. *Geophysical Research Letters,* 23**,** 363-366.

BINDSCHADLER, R., VORNBERGER, P. & GRAY, L. 2005. Changes in the ice plain of Whillans Ice Stream, West Antarctica. *Journal of Glaciology,* 51**,** 620-636.

BINTANJA, R., VAN OLDENBORGH, G., DRIJFHOUT, S., WOUTERS, B. & KATSMAN, C. 2013. Important role for ocean warming and increased ice-shelf melt in Antarctic sea-ice expansion. *Nature Geoscience,* 6**,** 376-379.

BLOEMENDAL, J., LIU, X. & ROLPH, T. 1995. Correlation of the magnetic susceptibility stratigraphy of Chinese loess and the marine oxygen isotope record: chronological and palaeoclimatic implications. *Earth and Planetary Science Letters,* 131**,** 371-380.

BLUEMLE, J. P. & CLAYTON, L. 1984. Large‐scale glacial thrusting and related processes in North Dakota. *Boreas,* 13**,** 279-299.

BOHATY, S. M., ZACHOS, J. C. & DELANEY, M. L. 2012. Foraminiferal Mg/Ca evidence for Southern Ocean cooling across the Eocene–Oligocene transition. *Earth and Planetary Science Letters,* 317**,** 251-261.

BOLTUNOV, V. 1970. Certain earmarks distinguishing glacial and moraine-like glacial-marine sediments, as in Spitsbergen. *International Geology Review,* 12**,** 204-211.

BORNHOLD, B. D. & GIRESSE, P. 1985. Glauconitic sediments on the continental shelf off Vancouver Island, British Columbia, Canada. *Journal of Sedimentary Research,* 55.

BOWMAN, S. 1990. *Radiocarbon dating*, Univ of California Press.

BRITISH ANTARCTIC SURVEY. *Multibeam echosounder* [Online]. British Antarctic Survey. Available: https://www.bas.ac.uk/polar-operations/sites-and-facilities/facility/rrs-james-clark-ross/multibeam-echosounder-2/#about [Accessed 27.10.2016 2016].

BROUWER, P. 2006. Theory of XRF. *Almelo, Netherlands: PANalytical BV*.

BURGER, H. R. 1992. Exploration geophysics of the shallow subsurface.

BUTT, F., ELVERHØI, A., SOLHEIM, A. & FORSBERG, C. 2000. Deciphering Late Cenozoic development of the western Svalbard Margin from ODP Site 986 results. *Marine Geology,* 169**,** 373-390.

CAMERLENGHI, A., DOMACK, E., REBESCO, M., GILBERT, R., ISHMAN, S., LEVENTER, A., BRACHFELD, S. & DRAKE, A. 2001. Glacial morphology and post-glacial contourites in northern Prince Gustav Channel (NW Weddell Sea, Antarctica). *Marine Geophysical Researches,* 22**,** 417-443.

CARTER, L. 2006. *Charting the sea floor - Multibeam echo sounding* [Online]. Available: http://www.TeAra.govt.nz/en/charting-the-sea-floor/page-4 [Accessed 27.10.2016 2016].

CARTER, L., MCCAVE, I. & WILLIAMS, M. J. 2008. Circulation and water masses of the Southern Ocean: a review. *Developments in earth and environmental sciences,* 8**,** 85-114.

CARTER, L., CORTESE, G., BRIGHAM-GRETTE, J., POWELL, R., NEWMAN, L. & KIEFER, T. 2009. Change in the Southern Ocean: responding to Antarctica. *PAGES News,* 17, 1-3.

CHRISTOFFERSEN, P., TULACZYK, S. & BEHAR, A. 2010. Basal ice sequences in Antarctic ice stream: exposure of past hydrologic conditions and a principal mode of sediment transfer. *Journal of Geophysical Research: Earth Surface,* 115.

CLARK, C. D. 1993. Mega‐scale glacial lineations and cross‐cutting ice‐flow landforms. *Earth surface processes and landforms,* 18**,** 1-29.

CLARK, C. D. 1999. Glaciodynamic context of subglacial bedform generation and preservation. *Annals of Glaciology,* 28**,** 23-32.

CLARK, C. D., TULACZYK, S. M., STOKES, C. R. & CANALS, M. 2003a. A groove-ploughing theory for the production of mega-scale glacial lineations, and implications for ice-stream mechanics. *Journal of Glaciology,* 49**,** 240-256.

CLARK, C. D. & STOKES, C. R. 2003b. Palaeo-ice stream landsystem. *Glacial Landsystems. Arnold, London***,** 204-227.

CLARK, P. U. 2011. Deglacial history of the West Antarctic Ice Sheet in the Weddell Sea embayment: Constraints on past ice volume change: COMMENT. *Geology,* 39**,** e239-e239.

COFAIGH, C. Ó., DOWDESWELL, J. A., EVANS, J. & LARTER, R. D. 2008. Geological constraints on Antarctic palaeo‐ice‐stream retreat. *Earth Surface Processes and Landforms,* 33**,** 513-525.

COFAIGH, C. Ó., EVANS, D. J. & SMITH, I. R. 2010. Large-scale reorganization and sedimentation of terrestrial ice streams during late Wisconsinan Laurentide Ice Sheet deglaciation. *Geological Society of America Bulletin,* 122**,** 743-756.

COOK, A., FOX, A., VAUGHAN, D. & FERRIGNO, J. 2005. Retreating glacier fronts on the Antarctic Peninsula over the past half-century. *Science,* 308**,** 541-544.

COXALL, H. K., WILSON, P. A., PÄLIKE, H., LEAR, C. H. & BACKMAN, J. 2005. Rapid stepwise onset of Antarctic glaciation and deeper calcite compensation in the Pacific Ocean. *Nature,* 433**,** 53-57.

CUNNINGHAM, S., ALDERSON, S., KING, B. & BRANDON, M. 2003. Transport and variability of the Antarctic circumpolar current in drake passage. *Journal of Geophysical Research: Oceans,* 108.

DAHLGREN, K. T. & VORREN, T. O. 2003. Sedimentary environment and glacial history during the last 40 ka of the Vøring continental margin, mid-Norway. *Marine Geology,* 193**,** 93-127.

DAVIS, C. H., LI, Y., MCCONNELL, J. R., FREY, M. M. & HANNA, E. 2005. Snowfall-driven growth in East Antarctic ice sheet mitigates recent sea-level rise. *Science,* 308**,** 1898-1901.

DEARING, J. 1999. Magnetic susceptibility. *Environmental magnetism: A practical guide,* 6**,** 35-62.

DENBIGH, P. N. 1989. Swath bathymetry: Principles of operation and an analysis of errors. *IEEE Journal of Oceanic Engineering,* 14**,** 289-298.

DENTON, G. H. & HUGHES, T. J. 1981. *The last great ice sheets*, Wiley.

DEPOORTER, M., BAMBER, J., GRIGGS, J., LENAERTS, J., LIGTENBERG, S., VAN DEN BROEKE, M. & MOHOLDT, G. 2013. Calving fluxes and basal melt rates of Antarctic ice shelves. *Nature,* 502**,** 89-92.

DIEKMANN, B. & KUHN, G. 1999. Provenance and dispersal of glacial–marine surface sediments in the Weddell Sea and adjoining areas, Antarctica: ice-rafting versus current transport. *Marine Geology,* 158**,** 209-231.

DOAKE, C., CORR, H., NICHOLLS, K., GAFFIKIN, A., JENKINS, A., BERTIGER, W. & KING, M. 2002. Tide‑induced lateral movement of Brunt Ice Shelf, Antarctica. *Geophysical research letters,* 29.

DOMACK, E. W. & HARRIS, P. T. 1998. A new depositional model for ice shelves, based upon sediment cores from the Ross Sea and the Mac. Robertson shelf, Antarctica. *Annals of Glaciology,* 27, 281-284.

DOMACK, E. W., JACOBSON, E. A., SHIPP, S. & ANDERSON, J. B. 1999. Late Pleistocene– Holocene retreat of the West Antarctic Ice-Sheet system in the Ross Sea: Part 2— sedimentologic and stratigraphic signature. *Geological Society of America Bulletin,* 111, 1517- 1536.

DOWDESWELL, J., OTTESEN, D., EVANS, J., COFAIGH, C. Ó. & ANDERSON, J. 2008. Submarine glacial landforms and rates of ice-stream collapse. *Geology,* 36, 819-822.

DOWDESWELL, J., JAKOBSSON, M., HOGAN, K., O'REGAN, M., BACKMAN, J., EVANS, J., HELL, B., LÖWEMARK, L., MARCUSSEN, C. & NOORMETS, R. 2010. High-resolution geophysical observations of the Yermak Plateau and northern Svalbard margin: implications for ice-sheet grounding and deep-keeled icebergs. *Quaternary Science Reviews,* 29, 3518-3531.

DOWDESWELL, J. & FUGELLI, E. 2012. The seismic architecture and geometry of grounding-zone wedges formed at the marine margins of past ice sheets. *Geological Society of America Bulletin,* 124, 1750-1761.

DOWDESWELL, J. & HOGAN, K. Huge iceberg ploughmarks and associated corrugation ridges on the northern Svalbard shelf. 2016. Geological Society of London.

DOWDESWELL, J. A. & DOWDESWELL, E. K. 1989. Debris in icebergs and rates of glaci-marine sedimentation: observations from Spitsbergen and a simple model. *The Journal of Geology,* 221-231.

DOWDESWELL, J. A. & SCOURSE, J. D. 1990. On the description and modelling of glacimarine sediments and sedimentation. *Geological Society, London, Special Publications,* 53, 1-13.

DOWDESWELL, J. A., VILLINGER, H., WHITTINGTON, R. J. & MARIENFELD, P. 1993. Iceberg scouring in Scoresby Sund and on the East Greenland continental shelf. *Marine Geology,* 111, 37-53.

DOWDESWELL, J. A., COFAIGH, C. Ó. & PUDSEY, C. J. 2004. Thickness and extent of the subglacial till layer beneath an Antarctic paleo–ice stream. *Geology,* 32, 13-16.

DOWDESWELL, J. A., HOGAN, K., COFAIGH, C. Ó., FUGELLI, E., EVANS, J. & NOORMETS, R. 2014. Late Quaternary ice flow in a West Greenland fjord and cross-shelf trough system: submarine landforms from Rink Isbrae to Uummannaq shelf and slope. *Quaternary Science Reviews,* 92, 292-309.

ELVERHØI, A. 1981. Evidence for a late Wisconsin glaciation of the Weddell Sea. *Nature,* 293, 641- 642.

ELVERHØI, A., LØNNE, Ø. & SELAND, R. 1983. Glaciomarine sedimentation in a modern fjord environment, Spitsbergen. *Polar Research,* 1, 127-150.

ELVERHØI, A. & ROALDSET, E. 1983. Glaciomarine sediments and suspended particulate matter, Weddell Sea Shelf, Antarctica. *Polar Res,* 1, 1-21.

ELVERHØI, A. 1984. Glacigenic and associated marine sediments in the Weddell Sea, fjords of Spitsbergen and the Barents Sea: a review. *Marine Geology,* 57, 53-88.

ENGELHARDT, H. & KAMB, B. 1998. Basal sliding of ice stream B, West Antarctica. *Journal of Glaciology,* 44, 223-230.

EPICA COMMUNITY MEMBERS 2006. One-to-one coupling of glacial climate variability in Greenland and Antarctica. *Nature,* 444**,** 195-198.

ETH. 2013. *0.2 MV radiocarbon dating facility (MICADAS)* [Online]. Eidgenössische Technische Hochschule Zurich, Swiss Federal Institute of Technology Zurich. Available: https://www1.ethz.ch/ams/instruments/micadas [Accessed 05.11 2016].

EVANS, H. B. GRAPE*-A Device For Continuous Determination Of Material Density And Porosity. SPWLA 6th Annual Logging Symposium (Volume II), 1965. Society of Petrophysicists and Well-Log Analysts.

EVANS, J. & PUDSEY, C. 2002. Sedimentation associated with Antarctic Peninsula ice shelves: implications for palaeoenvironmental reconstructions of glacimarine sediments. *Journal of the Geological Society,* 159**,** 233-237.

EVANS, J., DOWDESWELL, J. A. & COFAIGH, C. Ó. 2004. Late Quaternary submarine bedforms and ice‑sheet flow in Gerlache Strait and on the adjacent continental shelf, Antarctic Peninsula. *Journal of Quaternary Science,* 19**,** 397-407.

EVANS, J., PUDSEY, C. J., ÓCOFAIGH, C., MORRIS, P. & DOMACK, E. 2005. Late Quaternary glacial history, flow dynamics and sedimentation along the eastern margin of the Antarctic Peninsula Ice Sheet. *Quaternary Science Reviews,* 24**,** 741-774.

FAHRBACH, E., PETERSON, R., ROHARDT, G., SCHLOSSER, P. & BAYER, R. 1994. Suppression of bottom water formation in the southeastern Weddell Sea. *Deep Sea Research Part I: Oceanographic Research Papers,* 41**,** 389-411.

FAVIER, L., DURAND, G., CORNFORD, S., GUDMUNDSSON, G., GAGLIARDINI, O., GILLET-CHAULET, F., ZWINGER, T., PAYNE, A. & LE BROCQ, A. 2014. Retreat of Pine Island Glacier controlled by marine ice-sheet instability. *Nature Climate Change,* 4**,** 117-121.

FER, I., MAKINSON, K. & NICHOLLS, K. W. 2012. Observations of thermohaline convection adjacent to Brunt Ice Shelf. *Journal of Physical Oceanography,* 42**,** 502-508.

FIELDING, C. R., NAISH, T., WOOLFE, K. & LAVELLE, M. 2000. Facies analysis and sequence stratigraphy of CRP-2/2A, Victoria Land Basin, Antarctica. *Terra Antartica,* 7**,** 323-338.

FLINK, A. E., NOORMETS, R., KIRCHNER, N., BENN, D. I., LUCKMAN, A. & LOVELL, H. 2015. The evolution of a submarine landform record following recent and multiple surges of Tunabreen glacier, Svalbard. *Quaternary Science Reviews,* 108**,** 37-50.

FOGWILL, C., BENTLEY, M., SUGDEN, D., KERR, A. & KUBIK, P. 2004. Cosmogenic nuclides 10Be and 26Al imply limited Antarctic Ice Sheet thickening and low erosion in the Shackleton Range for> 1 my. *Geology,* 32**,** 265-268.

FOLDVIK, A. & KVINGE, T. Conditional instability of sea water at the freezing point. Deep Sea Research and Oceanographic Abstracts, 1974. Elsevier, 169-174.

FOLDVIK, A., GAMMELSRØD, T. & TØRRESEN, T. 1985. Circulation and water masses on the southern Weddell Sea shelf. *Oceanology of the Antarctic continental shelf***,** 5-20.

FOLDVIK, A., GAMMELSRØD, T., ØSTERHUS, S., FAHRBACH, E., ROHARDT, G., SCHRÖDER, M., NICHOLLS, K. W., PADMAN, L. & WOODGATE, R. 2004. Ice shelf water overflow and bottom water formation in the southern Weddell Sea. *Journal of Geophysical Research: Oceans,* 109.

FOOTE, K. G., PATEL, R. & TENNINGEN, E. Target-tracking in a parametric sonar beam, with applications to calibration. OCEANS 2010 MTS/IEEE SEATTLE, 2010. IEEE, 1-7.

FORWICK, M. & VORREN, T. O. 2009. Late Weichselian and Holocene sedimentary environments and ice rafting in Isfjorden, Spitsbergen. *Palaeogeography, Palaeoclimatology, Palaeoecology,* 280**,** 258-274.

FORWICK, M. & VORREN, T. O. 2010. Stratigraphy and deglaciation of the Isfjorden area, Spitsbergen. *Norwegian Journal of Geology/Norsk Geologisk Forening,* 90.

FRETWELL, P., PRITCHARD, H. D., VAUGHAN, D. G., BAMBER, J. L., BARRAND, N. E., BELL, R., BIANCHI, C., BINGHAM, R. G., BLANKENSHIP, D. D., CASASSA, G., CATANIA, G., CALLENS, D., CONWAY, H., COOK, A. J., CORR, H. F. J., DAMASKE, D., DAMM, V., FERRACCIOLI, F., FORSBERG, R., FUJITA, S., GIM, Y., GOGINENI, P., GRIGGS, J. A., HINDMARSH, R. C. A., HOLMLUND, P., HOLT, J. W., JACOBEL, R. W., JENKINS, A., JOKAT, W., JORDAN, T., KING, E. C., KOHLER, J., KRABILL, W., RIGER-KUSK, M., LANGLEY, K. A., LEITCHENKOV, G., LEUSCHEN, C., LUYENDYK, B. P., MATSUOKA, K., MOUGINOT, J., NITSCHE, F. O., NOGI, Y., NOST, O. A., POPOV, S. V., RIGNOT, E., RIPPIN, D. M., RIVERA, A., ROBERTS, J., ROSS, N., SIEGERT, M. J., SMITH, A. M., STEINHAGE, D., STUDINGER, M., SUN, B., TINTO, B. K., WELCH, B. C., WILSON, D., YOUNG, D. A., XIANGBIN, C. & ZIRIZZOTTI, A. 2013. Bedmap2: improved ice bed, surface and thickness datasets for Antarctica. *The Cryosphere,* 7**,** 375-393.

FRICKER, H. A. & PADMAN, L. 2006. Ice shelf grounding zone structure from ICESat laser altimetry. *Geophysical Research Letters,* 33.

FÜTTERER, D. & MELLES, M. 1990. Sediment patterns in the southern Weddell Sea: Filchner shelf and Filchner depression. *Geological history of the polar oceans: Arctic versus Antarctic.* Springer.

GALES, J., LEAT, P., LARTER, R., KUHN, G., HILLENBRAND, C.-D., GRAHAM, A., MITCHELL, N., TATE, A., BUYS, G. & JOKAT, W. 2014. Large-scale submarine landslides, channel and gully systems on the southern Weddell Sea margin, Antarctica. *Marine Geology,* 348**,** 73-87.

GEOTEK 2000. Multi-Sensor Core Logger Manual 1-127.

GEOTEK 2014. Multi-Sensor Core Logger, Manual.

GILLETT, N. P. & THOMPSON, D. W. 2003. Simulation of recent Southern Hemisphere climate change. *Science,* 302**,** 273-275.

GLADSTONE, R. M., BIGG, G. R. & NICHOLLS, K. W. 2001. Iceberg trajectory modeling and meltwater injection in the Southern Ocean. *Journal of Geophysical Research: Oceans,* 106**,** 19903-19915.

GLADSTONE, R. M., LEE, V., ROUGIER, J., PAYNE, A. J., HELLMER, H., LE BROCQ, A., SHEPHERD, A., EDWARDS, T. L., GREGORY, J. & CORNFORD, S. L. 2012. Calibrated prediction of Pine Island Glacier retreat during the 21st and 22nd centuries with a coupled flowline model. *Earth and Planetary Science Letters,* 333**,** 191-199.

GLASSER, N. & HAMBREY, M. 2003. Ice-marginal terrestrial landsystems: Svalbard polythermal glaciers. *Glacial Landsystems. Arnold, London***,** 65-88.

GRAHAM, A. G., LARTER, R. D., GOHL, K., DOWDESWELL, J. A., HILLENBRAND, C. D., SMITH, J. A., EVANS, J., KUHN, G. & DEEN, T. 2010. Flow and retreat of the Late Quaternary Pine Island‐Thwaites palaeo‐ice stream, West Antarctica. *Journal of Geophysical Research: Earth Surface,* 115.

GUNN, D. & BEST, A. 1998. A new automated nondestructive system for high resolution multi-sensor core logging of open sediment cores. *Geo-Marine Letters,* 18**,** 70-77.

GUTOWSKI, M., BULL, J., HENSTOCK, T., DIX, J., HOGARTH, P., LEIGHTON, T. & WHITE, P. 2002. Chirp sub-bottom profiler source signature design and field testing. *Marine Geophysical Researches,* 23**,** 481-492.

HAASE, G. M. 1986. Glaciomarine sediments along the Filchner/Rønne Ice Shelf, southern Weddell Sea—First results of the 1983/84 Antarktis-II/4 expedition. *Marine geology,* 72**,** 241-258.

HAMBREY, M. J., HUDDART, D., BENNETT, M. R. & GLASSER, N. F. 1997. Genesis of 'hummocky moraines' by thrusting in glacier ice: evidence from Svalbard and Britain. *Journal of the Geological Society,* 154**,** 623-632.

HAMILTON, E. L. 1971. Prediction of in-situ acoustic and elastic properties of marine sediments. *Geophysics,* 36**,** 266-284.

HEIN, A. S., FOGWILL, C. J., SUGDEN, D. E. & XU, S. 2011. Glacial/interglacial ice-stream stability in the Weddell Sea embayment, Antarctica. *Earth and Planetary Science Letters,* 307**,** 211-221.

HEIN, A. S., FOGWILL, C. J., SUGDEN, D. E. & XU, S. 2014. Geological scatter of cosmogenic-nuclide exposure ages in the Shackleton Range, Antarctica: Implications for glacial history. *Quaternary Geochronology,* 19**,** 52-66.

HEIN, A. S., WOODWARD, J., MARRERO, S. M., DUNNING, S. A., STEIG, E. J., FREEMAN, S. P., STUART, F. M., WINTER, K., WESTOBY, M. J. & SUGDEN, D. E. 2016. Evidence for the stability of the West Antarctic Ice Sheet divide for 1.4 million years. *Nature communications,* 7.

HELLMER, H. H., KAUKER, F., TIMMERMANN, R., DETERMANN, J. & RAE, J. 2012. Twenty-first-century warming of a large Antarctic ice-shelf cavity by a redirected coastal current. *Nature,* 485**,** 225-228.

HEMER, M., POST, A., O'BRIEN, P. E., CRAVEN, M., TRUSWELL, E., ROBERTS, D. & HARRIS, P. 2007. Sedimentological signatures of the sub-Amery Ice Shelf circulation. *Antarctic Science,* 19**,** 497-506.

HEROY, D. C. & ANDERSON, J. B. 2007. Radiocarbon constraints on Antarctic Peninsula ice sheet retreat following the Last Glacial Maximum (LGM). *Quaternary Science Reviews,* 26**,** 3286-3297.

HILLENBRAND, C.-D. & FÜTTERER, D. 2001. Neogene to Quaternary deposition of opal on the continental rise west of the Antarctic Peninsula, ODP Leg 178, Sites 1095, 1096, and 1101. *Barker, PF, Camerlenghi, A., Acton, GD, and Ramsay, ATS (Eds.), Proc. ODP, Sci. Results, 178 [Online]. Available from World Wide Web: http://www-odp.tamu.edu/publications/178_SR/VOLUME/CHAPTERS/SR178_23. PDF,* 1.

HILLENBRAND, C.-D., BAESLER, A. & GROBE, H. 2005. The sedimentary record of the last glaciation in the western Bellingshausen Sea (West Antarctica): implications for the interpretation of diamictons in a polar-marine setting. *Marine Geology,* 216**,** 191-204.

HILLENBRAND, C.-D., EHRMANN, W., LARTER, R. D., BENETTI, S., DOWDESWELL, J., COFAIGH, C. Ó., GRAHAM, A. G. & GROBE, H. 2009. Clay mineral provenance of sediments in the southern Bellingshausen Sea reveals drainage changes of the West Antarctic Ice Sheet during the Late Quaternary. *Marine Geology,* 265**,** 1-18.

HILLENBRAND, C.-D., MELLES, M., KUHN, G. & LARTER, R. D. 2012. Marine geological constraints for the grounding-line position of the Antarctic Ice Sheet on the southern Weddell Sea shelf at the Last Glacial Maximum. *Quaternary Science Reviews,* 32**,** 25-47.

HILLENBRAND, C.-D., BENTLEY, M. J., STOLLDORF, T. D., HEIN, A. S., KUHN, G., GRAHAM, A. G. C., FOGWILL, C. J., KRISTOFFERSEN, Y., SMITH, J. A., ANDERSON, J. B., LARTER, R. D., MELLES, M., HODGSON, D. A., MULVANEY, R. & SUGDEN, D. E. 2014. Reconstruction of changes in the Weddell Sea sector of the Antarctic Ice Sheet since the Last Glacial Maximum. *Quaternary Science Reviews,* 100**,** 111-136.

HILLENBRAND, C. D., LARTER, R. D., DOWDESWELL, J. A., EHRMANN, W., Ó COFAIGH, C., BENETTI, S., GRAHAM, A. G. C. & GROBE, H. 2010. The sedimentary legacy of a palaeo-ice stream on the shelf of the southern Bellingshausen Sea: Clues to West Antarctic glacial history during the Late Quaternary. *Quaternary Science Reviews,* 29**,** 2741-2763.

HINDMARSH, R. C. & STOKES, C. R. 2008. Formation mechanisms for ice‑stream lateral shear margin moraines. *Earth Surface Processes and Landforms,* 33**,** 610-626.

HITACHI 2011. Tabletop Microscope TM3000. 1-20.

HOBBS, H. C. 1998. Use of 1-2 millimeter sand-grain composition in Minnesota Quaternary studies. *Contributions to Quaternary studies in Minnesota: Minnesota Geological Survey Report of Investigations,* 49**,** 193-208.

HODGSON, D. A., BENTLEY, M. J., SCHNABEL, C., CZIFERSZKY, A., FRETWELL, P., CONVEY, P. & XU, S. 2012. Glacial geomorphology and cosmogenic 10 Be and 26 Al exposure ages in the northern Dufek Massif, Weddell Sea embayment, Antarctica. *Antarctic Science,* 24**,** 377-394.

HODGSON, D. A., GRAHAM, A. G. C., ROBERTS, S. J., BENTLEY, M. J., COFAIGH, C. Ó., VERLEYEN, E., VYVERMAN, W., JOMELLI, V., FAVIER, V., BRUNSTEIN, D., VERFAILLIE, D., COLHOUN, E. A., SAUNDERS, K. M., SELKIRK, P. M., MACKINTOSH, A., HEDDING, D. W., NEL, W., HALL, K., MCGLONE, M. S., VAN DER PUTTEN, N., DICKENS, W. A. & SMITH, J. A. 2014. Terrestrial and submarine evidence for the extent and timing of the Last Glacial Maximum and the onset of deglaciation on the maritime-Antarctic and sub-Antarctic islands. *Quaternary Science Reviews,* 100**,** 137-158.

HOGAN, K., DOWDESWELL, J., NOORMETS, R., EVANS, J., COFAIGH, C. Ó. & JAKOBSSON, M. 2010b. Submarine landforms and ice-sheet flow in the Kvitøya Trough, northwestern Barents Sea. *Quaternary Science Reviews,* 29**,** 3545-3562.

HOGAN, K. A., DOWDESWELL, J. A., NOORMETS, R., EVANS, J. & COFAIGH, C. Ó. 2010a. Evidence for full-glacial flow and retreat of the Late Weichselian Ice Sheet from the waters around Kong Karls Land, eastern Svalbard. *Quaternary Science Reviews,* 29**,** 3563-3582.

HOGAN, K. A., COFAIGH, C. Ó., JENNINGS, A. E., DOWDESWELL, J. A. & HIEMSTRA, J. F. 2016. Deglaciation of a major palaeo-ice stream in Disko Trough, West Greenland. *Quaternary Science Reviews*.

HOPPE, G. 1959. Glacial morphology and inland ice recession in northern Sweden. *Geografiska Annaler,* 41**,** 193-212.

HOWAT, I. M. & DOMACK, E. W. 2003. Reconstructions of western Ross Sea palaeo‑ice‑stream grounding zones from high‑resolution acoustic stratigraphy. *Boreas,* 32**,** 56-75.

HTTP://CHEM.LIBRETEXTS.ORG/. *Implementing the Sampling Plan* [Online]. Chemistry, LibreTexts. Available: http://chem.libretexts.org/Textbook_Maps/Analytical_Chemistry_Textbook_Maps/Map%3A_Analytical_Chemistry_2.0_(Harvey)/07%3A_Collecting_and_Preparing_Samples/7.3%3A_Implementing_the_Sampling_Plan [Accessed 27.10. 2016].

HTTP://WWW.TIMESATLAS.COM/. 2014. *Ernest Shackleton and the Endurance* [Online]. Available: http://www.timesatlas.com/category/Ernest+Shackleton+and+the+Endurance [Accessed 15.11 2016].

HUGHEN, K., LEHMAN, S., SOUTHON, J., OVERPECK, J., MARCHAL, O., HERRING, C. & TURNBULL, J. 2004. 14C activity and global carbon cycle changes over the past 50,000 years. *Science,* 303**,** 202-207.

HULBE, C. L., JOHNSTON, R., JOUGHIN, I. & SCAMBOS, T. 2005. Marine ice modification of fringing ice shelf flow. *Arctic, Antarctic, and Alpine Research,* 37**,** 323-330.

HUMBERT, A., KLEINER, T., MOHRHOLZ, C.-O., OELKE, C., GREVE, R. & LANGE, M. A. 2009. A comparative modeling study of the Brunt Ice Shelf/Stancomb-Wills Ice Tongue system, East Antarctica. *Journal of Glaciology,* 55**,** 53-65.

HUYBRECHTS, P., RYBAK, O., STEINHAGE, D. & PATTYN, F. 2009. Past and present accumulation rate reconstruction along the Dome Fuji–Kohnen radio-echo sounding profile, Dronning Maud Land, East Antarctica. *Annals of glaciology,* 50**,** 112-120.

HÄTTESTRAND, C. & JOHANSEN, N. 2005. Supraglacial moraines in Scharffenbergbotnen, Heimefrontfjella, Dronning Maud Land, Antarctica–significance for reconstructing former blue ice areas. *Antarctic Science,* 17**,** 225-236.

JAKOBSSON, M., ANDERSON, J. B., NITSCHE, F. O., DOWDESWELL, J. A., GYLLENCREUTZ, R., KIRCHNER, N., MOHAMMAD, R., O'REGAN, M., ALLEY, R. B. & ANANDAKRISHNAN, S. 2011. Geological record of ice shelf break-up and grounding line retreat, Pine Island Bay, West Antarctica. *Geology,* 39**,** 691-694.

JAKOBSSON, M., ANDERSON, J. B., NITSCHE, F. O., GYLLENCREUTZ, R., KIRSHNER, A. E., KIRCHNER, N., O'REGAN, M., MOHAMMAD, R. & ERIKSSON, B. 2012. Ice sheet retreat dynamics inferred from glacial morphology of the central Pine Island Bay Trough, West Antarctica. *Quaternary Science Reviews,* 38**,** 1-10.

JANSEN, J., VAN DER GAAST, S., KOSTER, B. & VAARS, A. 1998. CORTEX, a shipboard XRF-scanner for element analyses in split sediment cores. *Marine Geology,* 151**,** 143-153.

JESSEN, S. P., RASMUSSEN, T. L., NIELSEN, T. & SOLHEIM, A. 2010. A new Late Weichselian and Holocene marine chronology for the western Svalbard slope 30,000–0 cal years BP. *Quaternary Science Reviews,* 29**,** 1301-1312.

JOUGHIN, I., BAMBER, J. L., SCAMBOS, T., TULACZYK, S., FAHNESTOCK, M. & MACAYEAL, D. R. 2006. Integrating satellite observations with modelling: basal shear stress of the Filcher-Ronne ice streams, Antarctica. *Philosophical Transactions of the Royal Society of London A: Mathematical, Physical and Engineering Sciences,* 364**,** 1795-1814.

JOUGHIN, I., SMITH, B. E. & HOLLAND, D. M. 2010. Sensitivity of 21st century sea level to ocean‐induced thinning of Pine Island Glacier, Antarctica. *Geophysical Research Letters,* 37.

JOUGHIN, I., SMITH, B. E. & MEDLEY, B. 2014. Marine ice sheet collapse potentially under way for the Thwaites Glacier Basin, West Antarctica. *Science,* 344**,** 735-738.

KANEMARU, T., HIRATA, K., TAKASU, S.-I., ISOBE, S.-I., MIZUKI, K., MATAKA, S. & NAKAMURA, K.-I. 2009. A fluorescence scanning electron microscope. *Ultramicroscopy,* 109**,** 344-349.

KATZ, R. F. & WORSTER, M. G. Stability of ice-sheet grounding lines. Proceedings of the Royal Society of London A: Mathematical, Physical and Engineering Sciences, 2010. The Royal Society, rspa20090434.

KENNETT, J. P. 1977. Cenozoic evolution of Antarctic glaciation, the circum‐Antarctic Ocean, and their impact on global paleoceanography. *Journal of geophysical research,* 82**,** 3843-3860.

KETCHAM, R. A. & CARLSON, W. D. 2001. Acquisition, optimization and interpretation of X-ray computed tomographic imagery: applications to the geosciences. *Computers & Geosciences,* 27**,** 381-400.

KHAZENDAR, A., RIGNOT, E. & LAROUR, E. 2009. Roles of marine ice, rheology, and fracture in the flow and stability of the Brunt/Stancomb‐Wills Ice Shelf. *Journal of Geophysical Research: Earth Surface,* 114.

KIHL, R. 1975. Physical preparation of organic matter samples for 14C dating. *Arctic and Alpine Research,* 7**,** 90-91.

KING, E. C., HINDMARSH, R. C. & STOKES, C. 2009. Formation of mega-scale glacial lineations observed beneath a West Antarctic ice stream. *Nature Geoscience,* 2**,** 585-588.

KING, J., ANDERSON, P., SMITH, M. & MOBBS, S. 1996. The surface energy and mass balance at Halley, Antarctica during winter. *Journal of Geophysical Research: Atmospheres,* 101**,** 19119-19128.

KLAGES, J. P., KUHN, G., HILLENBRAND, C.-D., GRAHAM, A., SMITH, J., LARTER, R. & GOHL, K. 2013. First geomorphological record and glacial history of an inter-ice stream ridge on the West Antarctic continental shelf. *Quaternary Science Reviews,* 61**,** 47-61.

KLAGES, J. P., KUHN, G., HILLENBRAND, C.-D., GRAHAM, A. G., SMITH, J. A., LARTER, R. D., GOHL, K. & WACKER, L. 2014. Retreat of the West Antarctic Ice Sheet from the western Amundsen Sea shelf at a pre-or early LGM stage. *Quaternary Science Reviews,* 91**,** 1-15.

KLAGES, J. P., KUHN, G., GRAHAM, A., HILLENBRAND, C.-D., SMITH, J., NITSCHE, F., LARTER, R. & GOHL, K. 2015. Palaeo-ice stream pathways and retreat style in the easternmost Amundsen Sea Embayment, West Antarctica, revealed by combined multibeam bathymetric and seismic data. *Geomorphology,* 245**,** 207-222.

KLEMAN, J. 1994. Preservation of landforms under ice sheets and ice caps. *Geomorphology,* 9**,** 19-32.

KONGSBERG MARITIME 2005. EM 120, 21 kHz multibeam echo sounder, Seabed mapping to full ocean depth. 1-4.

KONGSBERG MARITIME 2012. TOPAS PS 18, Parametric sub-bottom profiler, Sysem specification. 1-2.

KONGSBERG MARITIME 2013. Kongsberg EM 122, 12 kHz Multibeam echo sounder. 1-2.

KRISTOFFERSEN, Y., STRAND, K., VORREN, T., HARWOOD, D. & WEBB, P. 2000a. Pilot shallow drilling on the continental shelf, Dronning Maud Land, Antarctica. *Antarctic Science,* 12**,** 463-470.

KRISTOFFERSEN, Y., WINTERHALTER, B. & SOLHEIM, A. 2000b. Shelf progradation on a glaciated continental margin, Queen Maud Land, Antarctica. *Marine Geology,* 165**,** 109-122.

KUHLMANN, H. 2013. *Penetration / shear strength* [Online]. Marum, Center for Marine Environmental Sciences. Available: https://www.marum.de/en/Penetration__shear_strength.html [Accessed 28.10 2016].

LARTER, R. D., GRAHAM, A. G., GOHL, K., KUHN, G., HILLENBRAND, C.-D., SMITH, J. A., DEEN, T. J., LIVERMORE, R. A. & SCHENKE, H.-W. 2009. Subglacial bedforms reveal complex basal regime in a zone of paleo–ice stream convergence, Amundsen Sea embayment, West Antarctica. *Geology,* 37**,** 411-414.

LARTER, R. D., GRAHAM, A. G., HILLENBRAND, C.-D., SMITH, J. A. & GALES, J. A. 2012. Late Quaternary grounded ice extent in the Filchner Trough, Weddell Sea, Antarctica: new marine geophysical evidence. *Quaternary Science Reviews,* 53**,** 111-122.

LARTER, R. D., ANDERSON, J. B., GRAHAM, A. G. C., GOHL, K., HILLENBRAND, C.-D., JAKOBSSON, M., JOHNSON, J. S., KUHN, G., NITSCHE, F. O., SMITH, J. A., WITUS, A. E., BENTLEY, M. J., DOWDESWELL, J. A., EHRMANN, W., KLAGES, J. P., LINDOW, J., COFAIGH, C. Ó. & SPIEGEL, C. 2014. Reconstruction of changes in the Amundsen Sea and Bellingshausen Sea sector of the West Antarctic Ice Sheet since the Last Glacial Maximum. *Quaternary Science Reviews,* 100**,** 55-86.

LAWVER, L. A., GAHAGAN, L. M. & COFFIN, M. F. 1992. The development of paleoseaways around Antarctica. *The Antarctic Paleoenvironment: A Perspective on Global Change: Part One***,** 7-30.

LE BROCQ, A., BENTLEY, M., HUBBARD, A., FOGWILL, C., SUGDEN, D. & WHITEHOUSE, P. 2011. Reconstructing the Last Glacial Maximum ice sheet in the Weddell Sea embayment, Antarctica, using numerical modelling constrained by field evidence. *Quaternary Science Reviews,* 30**,** 2422-2432.

LI, F., VIKHLIAEV, Y. V., NEWMAN, P. A., PAWSON, S., PERLWITZ, J., WAUGH, D. W. & DOUGLASS, A. R. 2016. Impacts of Interactive Stratospheric Chemistry on Antarctic and Southern Ocean Climate Change in the Goddard Earth Observing System, Version 5 (GEOS-5). *Journal of Climate,* 29**,** 3199-3218.

LICHT, K., DUNBAR, N., ANDREWS, J. & JENNINGS, A. 1999. Distinguishing subglacial till and glacial marine diamictons in the western Ross Sea, Antarctica: Implications for a last glacial maximum grounding line. *Geological Society of America Bulletin,* 111**,** 91-103.

LICHT, K. J., JENNINGS, A. E., ANDREWS, J. T. & WILLIAMS, K. M. 1996. Chronology of late Wisconsin ice retreat from the western Ross Sea, Antarctica. *Geology,* 24**,** 223-226.

LIM, D., PARK, Y., CHOI, J., CHO, J. & KHIM, B. 2000. Glauconite grains in continental shelf sediments around the Korean Peninsula and their depositional implications. *Geo-Marine Letters,* 20**,** 80-86.

LINDÉN, M. & MÖLLER, P. 2005. Marginal formation of De Geer moraines and their implications to the dynamics of grounding‐line recession. *Journal of Quaternary Science,* 20**,** 113-133.

LIVINGSTONE, S. J., Ó COFAIGH, C., STOKES, C. R., HILLENBRAND, C.-D., VIELI, A. & JAMIESON, S. S. R. 2012. Antarctic palaeo-ice streams. *Earth-Science Reviews,* 111**,** 90-128.

LOFI, J. & WEBER, O. 2001. SCOPIX–digital processing of X-ray images for the enhancement of sedimentary structures in undisturbed core slabs. *Geo-Marine Letters,* 20**,** 182-186.

MACKIEWICZ, N. E., POWELL, R. D., CARLSON, P. R. & MOLNIA, B. F. 1984. Interlaminated ice-proximal glacimarine sediments in Muir Inlet, Alaska. *Marine Geology,* 57**,** 113-147.

MACKINTOSH, A. N., VERLEYEN, E., O'BRIEN, P. E., WHITE, D. A., JONES, R. S., MCKAY, R., DUNBAR, R., GORE, D. B., FINK, D., POST, A. L., MIURA, H., LEVENTER, A., GOODWIN, I., HODGSON, D. A., LILLY, K., CROSTA, X., GOLLEDGE, N. R., WAGNER, B., BERG, S., VAN OMMEN, T., ZWARTZ, D., ROBERTS, S. J., VYVERMAN, W. & MASSE, G. 2014. Retreat history of the East Antarctic Ice Sheet since the Last Glacial Maximum. *Quaternary Science Reviews,* 100**,** 10-30.

MATSUOKA, K., HINDMARSH, R. C., MOHOLDT, G., BENTLEY, M. J., PRITCHARD, H. D., BROWN, J., CONWAY, H., DREWS, R., DURAND, G. & GOLDBERG, D. 2015. Antarctic ice rises and rumples: Their properties and significance for ice-sheet dynamics and evolution. *Earth-science reviews,* 150**,** 724-745.

MCKAY, R., BROWNE, G., CARTER, L., COWAN, E., DUNBAR, G., KRISSEK, L., NAISH, T., POWELL, R., REED, J. & TALARICO, F. 2009. The stratigraphic signature of the late Cenozoic Antarctic Ice Sheets in the Ross Embayment. *Geological Society of America Bulletin,* 121**,** 1537-1561.

MCKAY, R., NAISH, T., POWELL, R., BARRETT, P., SCHERER, R., TALARICO, F., KYLE, P., MONIEN, D., KUHN, G. & JACKOLSKI, C. 2012. Pleistocene variability of Antarctic ice sheet extent in the Ross embayment. *Quaternary Science Reviews,* 34**,** 93-112.

MEIER, M. F., DYURGEROV, M. B., RICK, U. K., O'NEEL, S., PFEFFER, W. T., ANDERSON, R. S., ANDERSON, S. P. & GLAZOVSKY, A. F. 2007. Glaciers dominate eustatic sea-level rise in the 21st century. *Science,* 317**,** 1064-1067.

MELLES, M. & KUHN, G. 1993. Sub-bottom profiling and sedimentological studies in the southern Weddell Sea, Antarctica: evidence for large-scale erosional/depositional processes. *Deep Sea Research Part I: Oceanographic Research Papers,* 40**,** 739-760.

MERCER, J. H. 1978. West Antarctic ice sheet and CO 2 greenhouse effect- A threat of disaster. *Nature,* 271**,** 321-325.

MONIEN, D., KUHN, G., VON EYNATTEN, H. & TALARICO, F. M. 2012. Geochemical provenance analysis of fine-grained sediment revealing Late Miocene to recent Paleo-Environmental changes in the Western Ross Sea, Antarctica. *Global and Planetary Change,* 96**,** 41-58.

MOSOLA, A. B. & ANDERSON, J. B. 2006. Expansion and rapid retreat of the West Antarctic Ice Sheet in eastern Ross Sea: possible consequence of over-extended ice streams? *Quaternary Science Reviews,* 25**,** 2177-2196.

MULVANEY, R., ALEMANY, O. & POSSENTI, P. 2007. The Berkner Island (Antarctica) ice-core drilling project. *Annals of glaciology,* 47**,** 115-124.

MUNSELL, M. S. C. C. Available: http://www.vcsu.edu/cmsfiles/327/b2fc4f5ebb.pdf [Accessed 28.10 2016].

NATIONAL SNOW AND ICE DATA CENTER. 2014. *Sea Ice maximum in Antarctica* [Online]. University of Colorado, Boulder. Available: http://nsidc.org/arcticseaicenews/2014/10/2014-melt-season-in-review/ [Accessed 16.10.2016 2016].

NATIONAL SNOW AND ICE DATA CENTER. 2016. *Sea Ice* [Online]. University of Colorado, Boulder. Available: https://nsidc.org/cryosphere/sotc/sea_ice.html [Accessed 26 September 2016].

NICHOLLS, K. W., PADMAN, L., SCHRÖDER, M., WOODGATE, R., JENKINS, A. & ØSTERHUS, S. 2003. Water mass modification over the continental shelf north of Ronne Ice Shelf, Antarctica. *Journal of Geophysical Research: Oceans,* 108.

NICHOLLS, K. W., ØSTERHUS, S., MAKINSON, K., GAMMELSRØD, T. & FAHRBACH, E. 2009a. Ice‐ocean processes over the continental shelf of the southern Weddell Sea, Antarctica: A review. *Reviews of Geophysics,* 47.

NICHOLS, G. 2009b. *Sedimentology and stratigraphy*, John Wiley & Sons.

Ó COFAIGH, C., PUDSEY, C. J., DOWDESWELL, J. A. & MORRIS, P. 2002. Evolution of subglacial bedforms along a paleo‐ice stream, Antarctic Peninsula continental shelf. *Geophysical Research Letters,* 29.

Ó COFAIGH, C., LARTER, R. D., DOWDESWELL, J. A., HILLENBRAND, C. D., PUDSEY, C. J., EVANS, J. & MORRIS, P. 2005a. Flow of the West Antarctic Ice Sheet on the continental margin of the Bellingshausen Sea at the Last Glacial Maximum. *Journal of Geophysical Research: Solid Earth,* 110.

Ó COFAIGH, C., DOWDESWELL, J. A., ALLEN, C. S., HIEMSTRA, J. F., PUDSEY, C. J., EVANS, J. & EVANS, D. J. 2005b. Flow dynamics and till genesis associated with a marine-based Antarctic palaeo-ice stream. *Quaternary Science Reviews,* 24**,** 709-740.

Ó COFAIGH, C., EVANS, J., DOWDESWELL, J. A. & LARTER, R. D. 2007. Till characteristics, genesis and transport beneath Antarctic paleo‐ice streams. *Journal of Geophysical Research: Earth Surface,* 112.

Ó COFAIGH, C., DAVIES, B. J., LIVINGSTONE, S. J., SMITH, J. A., JOHNSON, J. S., HOCKING, E. P., HODGSON, D. A., ANDERSON, J. B., BENTLEY, M. J., CANALS, M., DOMACK, E., DOWDESWELL, J. A., EVANS, J., GLASSER, N. F., HILLENBRAND, C.-D., LARTER, R. D., ROBERTS, S. J. & SIMMS, A. R. 2014. Reconstruction of ice-sheet changes in the Antarctic Peninsula since the Last Glacial Maximum. *Quaternary Science Reviews,* 100**,** 87-110.

ODIN, G. S. & MATTER, A. 1981. De glauconiarum origine. *Sedimentology,* 28**,** 611-641.

OLBERS, D., BOROWSKI, D., VÖLKER, C. & WOELFF, J.-O. 2004. The dynamical balance, transport and circulation of the Antarctic Circumpolar Current. *Antarctic science,* 16**,** 439-470.

OPPENHEIMER, M. 1998. Global warming and the stability of the West Antarctic Ice Sheet. *Nature,* 393**,** 325-332.

ORSI, A., JOHNSON, G. & BULLISTER, J. 1999. Circulation, mixing, and production of Antarctic Bottom Water. *Progress in Oceanography,* 43**,** 55-109.

ORSI, A. H., NOWLIN, W. D. & WHITWORTH, T. 1993. On the circulation and stratification of the Weddell Gyre. *Deep Sea Research Part I: Oceanographic Research Papers,* 40**,** 169-203.

ORSI, A. H., WHITWORTH, T. & NOWLIN, W. D. 1995. On the meridional extent and fronts of the Antarctic Circumpolar Current. *Deep Sea Research Part I: Oceanographic Research Papers,* 42**,** 641-673.

OTTESEN, D., RISE, L., KNIES, J., OLSEN, L. & HENRIKSEN, S. 2005a. The Vestfjorden-Trænadjupet palaeo-ice stream drainage system, mid-Norwegian continental shelf. *Marine Geology,* 218**,** 175-189.

OTTESEN, D., DOWDESWELL, J. & RISE, L. 2005b. Submarine landforms and the reconstruction of fast-flowing ice streams within a large Quaternary ice sheet: The 2500-km-long Norwegian-Svalbard margin (57–80 N). *Geological Society of America Bulletin,* 117**,** 1033-1050.

OTTESEN, D., DOWDESWELL, J. A., LANDVIK, J. Y. & MIENERT, J. 2007. Dynamics of the Late Weichselian ice sheet on Svalbard inferred from high‐resolution sea‐floor morphology. *Boreas,* 36**,** 286-306.

OTTESEN, D., STOKES, C. R., RISE, L. & OLSEN, L. 2008. Ice-sheet dynamics and ice streaming along the coastal parts of northern Norway. *Quaternary Science Reviews,* 27**,** 922-940.

OTTESEN, D. & DOWDESWELL, J. A. 2009. An inter–ice-stream glaciated margin: Submarine landforms and a geomorphic model based on marine-geophysical data from Svalbard. *Geological Society of America Bulletin,* 121**,** 1647-1665.

PARKINSON, C. & CAVALIERI, D. 2012. Antarctic sea ice variability and trends, 1979–2010. *The Cryosphere,* 6**,** 871-880.

PETERS, J. L., BENETTI, S., DUNLOP, P. & COFAIGH, C. Ó. 2015. Maximum extent and dynamic behaviour of the last British–Irish Ice Sheet west of Ireland. *Quaternary Science Reviews,* 128**,** 48-68.

PFUHL, H. A. & MCCAVE, I. N. 2005. Evidence for late Oligocene establishment of the Antarctic Circumpolar Current. *Earth and Planetary Science Letters,* 235**,** 715-728.

POWELL, R. D. & ALLEY, R. B. 1997. Grounding‐Line Systems: Processes, Glaciological Inferences and the Stratigraphic Record. *Geology and seismic stratigraphy of the Antarctic Margin, 2***,** 169-187.

RAHMSTORF, S. 2002. Ocean circulation and climate during the past 120,000 years. *Nature,* 419**,** 207-214.

REBESCO, M., ÖZMARAL, A., URGELES, R., ACCETTELLA, D., LUCCHI, R. G., RÜTHER, D., WINSBORROW, M., LLOPART, J., CABURLOTTO, A. & LANTZSCH, H. 2016. Evolution of a high-latitude sediment drift inside a glacially-carved trough based on high-resolution seismic stratigraphy (Kveithola, NW Barents Sea). *Quaternary Science Reviews*.

REIMER, P. J., BARD, E., BAYLISS, A., BECK, J. W., BLACKWELL, P. G., BRONK RAMSEY, C., BUCK, C. E., CHENG, H., EDWARDS, R. L. & FRIEDRICH, M. 2013. IntCal13 and Marine13 radiocarbon age calibration curves 0-50,000 years cal BP.

REINARDY, B. T., LARTER, R. D., HILLENBRAND, C.-D., MURRAY, T., HIEMSTRA, J. F. & BOOTH, A. D. 2011a. Streaming flow of an Antarctic Peninsula palaeo-ice stream, both by basal sliding and deformation of substrate. *Journal of Glaciology,* 57**,** 596-608.

REINARDY, B. T., HIEMSTRA, J. F., MURRAY, T., HILLENBRAND, C. D. & LARTER, R. D. 2011b. Till genesis at the bed of an Antarctic Peninsula palaeo‑ice stream as indicated by micromorphological analysis. *Boreas,* 40**,** 498-517.

RICHTER, T. O., VAN DER GAAST, S., KOSTER, B., VAARS, A., GIELES, R., DE STIGTER, H. C., DE HAAS, H. & VAN WEERING, T. C. 2006. The Avaatech XRF Core Scanner: technical description and applications to NE Atlantic sediments. *Geological Society, London, Special Publications,* 267**,** 39-50.

RIGNOT, E. 2002. Mass balance of East Antarctic glaciers and ice shelves from satellite data. *Annals of Glaciology,* 34**,** 217-227.

RIGNOT, E., CASASSA, G., GOGINENI, P., KRABILL, W., RIVERA, A. U. & THOMAS, R. 2004. Accelerated ice discharge from the Antarctic Peninsula following the collapse of Larsen B ice shelf. *Geophysical Research Letters,* 31.

RIGNOT, E., BAMBER, J. L., VAN DEN BROEKE, M. R., DAVIS, C., LI, Y., VAN DE BERG, W. J. & VAN MEIJGAARD, E. 2008. Recent Antarctic ice mass loss from radar interferometry and regional climate modelling. *Nature geoscience,* 1**,** 106-110.

RIGNOT, E., MOUGINOT, J. & SCHEUCHL, B. 2011. Ice Flow of the Antarctic Ice Sheet. *Science,* 333**,** 1427-1430.

RIGNOT, E., MOUGINOT, J., MORLIGHEM, M., SEROUSSI, H. & SCHEUCHL, B. 2014. Widespread, rapid grounding line retreat of Pine Island, Thwaites, Smith, and Kohler glaciers, West Antarctica, from 1992 to 2011. *Geophysical Research Letters,* 41**,** 3502-3509.

ROSENBERG, M. 2016. *The New Fifth Ocean* [Online]. Available: http://geography.about.com/od/learnabouttheearth/a/fifthocean.htm [Accessed 26.10.2016 2016].

ROSS, N., BINGHAM, R. G., CORR, H. F., FERRACCIOLI, F., JORDAN, T. A., LE BROCQ, A., RIPPIN, D. M., YOUNG, D., BLANKENSHIP, D. D. & SIEGERT, M. J. 2012. Steep reverse bed slope at the grounding line of the Weddell Sea sector in West Antarctica. *Nature Geoscience,* 5**,** 393-396.

RYAN, S., SCHRÖDER, M., HUHN, O. & TIMMERMANN, R. 2016. On the warm inflow at the eastern boundary of the Weddell Gyre. *Deep Sea Research Part I: Oceanographic Research Papers,* 107**,** 70-81.

RYDNINGEN, T. A., VORREN, T. O., LABERG, J. S. & KOLSTAD, V. 2013. The marine-based NW Fennoscandian ice sheet: glacial and deglacial dynamics as reconstructed from submarine landforms. *Quaternary Science Reviews,* 68**,** 126-141.

RYDNINGEN, T. A. 2014. *Sedimentary processes, late Cenozoic evolution and sediment yield on the continental margin offshore Troms, northern Norway.* Philosophiae Doctor, University of Tromsø – the Arctic University of Norway.

SCAMBOS, T., HULBE, C. & FAHNESTOCK, M. 2003. Climate‑induced ice shelf disintegration in the Antarctic peninsula. *Antarctic Peninsula Climate Variability: Historical and Paleoenvironmental Perspectives***,** 79-92.

SCAMBOS, T. A., BOHLANDER, J., SHUMAN, C. U. & SKVARCA, P. 2004. Glacier acceleration and thinning after ice shelf collapse in the Larsen B embayment, Antarctica. *Geophysical Research Letters,* 31.

SHEPHERD, A., IVINS, E. R., GERUO, A., BARLETTA, V. R., BENTLEY, M. J., BETTADPUR, S., BRIGGS, K. H., BROMWICH, D. H., FORSBERG, R. & GALIN, N. 2012. A reconciled estimate of ice-sheet mass balance. *Science,* 338**,** 1183-1189.

SHINDELL, D. T. & SCHMIDT, G. A. 2004. Southern Hemisphere climate response to ozone changes and greenhouse gas increases. *Geophysical Research Letters,* 31.

SHIP, S., ANDERSON, J. & DOMACK, E. 1999. Late Pleistocene–Holocene retreat of the West Antarctic Ice-Sheet system in the Ross Sea: part 1—geophysical results. *Geological Society of America Bulletin,* 111**,** 1486-1516.

SIGMOND, M. & FYFE, J. 2010. Has the ozone hole contributed to increased Antarctic sea ice extent? *Geophysical Research Letters,* 37.

SIMMONS, D. & ROUSE, J. 1984. Accelerating flow of the Brunt ice shelf, Antarctica. *Journal of Glaciology,* 30**,** 377-380.

SKINNER, L. & MCCAVE, I. 2003. Analysis and modelling of gravity-and piston coring based on soil mechanics. *Marine Geology,* 199**,** 181-204.

SLETTEN, K., LYSÅ, A. & LØNNE, I. 2001. Formation and disintegration of a high‐arctic ice‐cored moraine complex, Scott Turnerbreen, Svalbard. *Boreas,* 30**,** 272-284.

SMITH, A. 1997. Basal conditions on Rutford ice stream, West Antarctica, from seismic observations. *Journal of Geophysical Research: Solid Earth,* 102**,** 543-552.

SMITH, A. M. & MURRAY, T. 2009. Bedform topography and basal conditions beneath a fast-flowing West Antarctic ice stream. *Quaternary Science Reviews,* 28**,** 584-596.

SMITH, J. A., HILLENBRAND, C.-D., KUHN, G., LARTER, R. D., GRAHAM, A. G., EHRMANN, W., MORETON, S. G. & FORWICK, M. 2011. Deglacial history of the West Antarctic Ice Sheet in the western Amundsen Sea embayment. *Quaternary Science Reviews,* 30**,** 488-505.

SMITH, J. A., HILLENBRAND, C.-D., KUHN, G., KLAGES, J. P., GRAHAM, A. G., LARTER, R. D., EHRMANN, W., MORETON, S. G., WIERS, S. & FREDERICHS, T. 2014. New constraints on the timing of West Antarctic Ice Sheet retreat in the eastern Amundsen Sea since the Last Glacial Maximum. *Global and Planetary Change,* 122**,** 224-237.

SMITH, L. M. & LICHT, K. J. 2000. *Radiocarbon Date List IX, Antarctica, Arctic Ocean, and the Northern North Atlantic Region,* Institute of Arctic and Alpine Research, University of Colorado.

SOUNDING, E. 2003. High-resolution sub-bottom profiling using parametric acoustics. *International Ocean Systems,* 7**,** 6-11.

SPAGNOLO, M., CLARK, C. D., ELY, J. C., STOKES, C. R., ANDERSON, J. B., ANDREASSEN, K., GRAHAM, A. G. & KING, E. C. 2014. Size, shape and spatial arrangement of mega‐scale glacial lineations from a large and diverse dataset. *Earth Surface Processes and Landforms,* 39**,** 1432-1448.

STOKES, C. R. & CLARK, C. D. 2001. Palaeo-ice streams. *Quaternary Science Reviews,* 20**,** 1437-1457.

STOKES, C. R. & CLARK, C. D. 2002a. Ice stream shear margin moraines. *Earth Surface Processes and Landforms,* 27**,** 547-558.

STOKES, C. R. & CLARK, C. D. 2002b. Are long subglacial bedforms indicative of fast ice flow? *Boreas,* 31**,** 239-249.

STOKES, C. R., CLARK, C. D., LIAN, O. B. & TULACZYK, S. 2007. Ice stream sticky spots: a review of their identification and influence beneath contemporary and palaeo-ice streams. *Earth-Science Reviews,* 81**,** 217-249.

STOLLDORF, T., SCHENKE, H.-W. & ANDERSON, J. B. 2012. LGM ice sheet extent in the Weddell Sea: evidence for diachronous behavior of Antarctic Ice Sheets. *Quaternary Science Reviews,* 48**,** 20-31.

STUVIER, M. & REIMER, J. 1993. Extended 14 C data base and revised CALIB 3.0 14 C age calibration program. *Radiocarbon,* 35**,** 215-30.

SYNAL, H.-A., STOCKER, M. & SUTER, M. 2007. MICADAS: a new compact radiocarbon AMS system. *Nuclear Instruments and Methods in Physics Research Section B: Beam Interactions with Materials and Atoms,* 259**,** 7-13.

SYVITSKI, J. P. 1991. Towards an understanding of sediment deposition on glaciated continental shelves. *Continental Shelf Research,* 11**,** 897-937.

TEN BRINK, U. S., SCHNEIDER, C. & JOHNSON, A. H. 1995. Morphology and stratal geometry of the Antarctic continental shelf: insights from models. *Geology and seismic stratigraphy of the Antarctic margin***,** 1-24.

THE OPEN UNIVERSITY 2002. *Ocean Circulation,* Walton Hall, Milton Keynes, UK, Butterworth-Heinemann.

THE WORLD FACTBOOK. 2014. *Southern Ocean* [Online]. Central Inteligence Agency. Available: https://www.cia.gov/library/publications/the-world-factbook/geos/oo.html [Accessed 26.10.2016 2016].

THOMAS, R. H. 1973. *The dynamics of the Brunt Ice Shelf, Coats Land, Antarctica*, British Antarctic Survey.

THOR, G. & LOW, M. 2011. The persistence of the snow petrel (Pagodroma nivea) in Dronning Maud Land (Antarctica) for over 37,000 years. *Polar biology,* 34**,** 609-613.

TINTO, K. & BELL, R. 2011. Progressive unpinning of Thwaites Glacier from newly identified offshore ridge: Constraints from aerogravity. *Geophysical Research Letters,* 38.

TJALLINGII, R., RÖHL, U., KÖLLING, M. & BICKERT, T. 2007. Influence of the water content on X‐ray fluorescence core‐scanning measurements in soft marine sediments. *Geochemistry, Geophysics, Geosystems,* 8.

TODD, B. J., VALENTINE, P. C., LONGVA, O. & SHAW, J. 2007. Glacial landforms on German Bank, Scotian Shelf: evidence for Late Wisconsinan ice‐sheet dynamics and implications for the formation of De Geer moraines. *Boreas,* 36**,** 148-169.

TODOKORO, H. & EZUMI, M. 1999. Scanning electron microscope. Google Patents.

TURNER, J., COMISO, J. C., MARSHALL, G. J., LACHLAN‐COPE, T. A., BRACEGIRDLE, T., MAKSYM, T., MEREDITH, M. P., WANG, Z. & ORR, A. 2009. Non‐annular atmospheric circulation change induced by stratospheric ozone depletion and its role in the recent increase of Antarctic sea ice extent. *Geophysical Research Letters,* 36.

TURNER, J. & OVERLAND, J. 2009. Contrasting climate change in the two polar regions. *Polar Research,* 28**,** 146-164.

TURNER, J., BARRAND, N. E., BRACEGIRDLE, T. J., CONVEY, P., HODGSON, D. A., JARVIS, M., JENKINS, A., MARSHALL, G., MEREDITH, M. P. & ROSCOE, H. 2014. Antarctic climate change and the environment: an update. *Polar Record,* 50**,** 237-259.

UDDEN, J. A. 1914. Mechanical composition of clastic sediments. *Geological Society of America Bulletin,* 25**,** 655-744.

URI, S. & SCHNEIDER, C. 1995. Glacial morphology and depositional sequences of the Antarctic continental shelf. *Geology,* 23**,** 580-584.

VAN DER VEEN, C. Backstress: what it is and how it affects glacier flow. Calving glaciers: report of a workshop, 1997. 173-180.

VAN GEET, M., SWENNEN, R. & WEVERS, M. 2000. Quantitative analysis of reservoir rocks by microfocus X-ray computerised tomography. *Sedimentary Geology,* 132**,** 25-36.

VAUGHAN, D. & DOAKE, C. 1996. Recent atmospheric warming and retreat of ice shelves on the Antarctic Peninsula.

VAUGHAN, D. G. 2008. West Antarctic Ice Sheet collapse–the fall and rise of a paradigm. *Climatic Change,* 91**,** 65-79.

VORREN, T., HALD, M., EDVARDSEN, M. & LIND-HANSEN, O. 1983a. Glacigenic sediments and sedimentary environments on continental shelves: general principles with a case study from the Norwegian shelf. *Glacial Deposits in North-West Europe. Balkema, Rotterdam***,** 61-73.

VORREN, T., LEBESBYE, E., ANDREASSEN, K. & LARSEN, K.-B. 1989. Glacigenic sediments on a passive continental margin as exemplified by the Barents Sea. *Marine Geology,* 85**,** 251-272.

VORREN, T. 2003. Subaquatic landsystems: continental margins. *Glacial Landsystems: London, Arnold Publishers***,** 289-312.

VORREN, T. O., EDVARDSEN, M., HALD, M. & THOMSEN, E. 1983b. Deglaciation of the continental shelf off southern Troms, North Norway. *Norges geologiske undersøkelse,* 380**,** 173-187.

VORREN, T. O., HALD, M. & THOMSEN, E. 1984. Quaternary sediments and environments on the continental shelf off northern Norway. *Marine geology,* 57**,** 229-257.

VORREN, T. O. & LABERG, J. S. 1997. Trough mouth fans—palaeoclimate and ice-sheet monitors. *Quaternary Science Reviews,* 16**,** 865-881.

WACKER, L., BONANI, G., FRIEDRICH, M., HAJDAS, I., KROMER, B., NEMEC, M., RUFF, M., SUTER, M., SYNAL, H. & VOCKENHUBER, C. 2010. MICADAS: routine and high-precision radiocarbon dating. *Radiocarbon,* 52**,** 252.

WEBER, M. E., NIESSEN, F., KUHN, G. & WIEDICKE, M. 1997. Calibration and application of marine sedimentary physical properties using a multi-sensor core logger. *Marine Geology,* 136**,** 151-172.

WEBER, M. E., CLARK, P. U., RICKEN, W., MITROVICA, J. X., HOSTETLER, S. W. & KUHN, G. 2011. Interhemispheric ice-sheet synchronicity during the Last Glacial Maximum. *Science,* 334**,** 1265-1269.

WELLNER, J., LOWE, A., SHIPP, S. & ANDERSON, J. 2001. Distribution of glacial geomorphic features on the Antarctic continental shelf and correlation with substrate: implications for ice behavior. *Journal of Glaciology,* 47**,** 397-411.

WELLNER, J., HEROY, D. & ANDERSON, J. 2006. The death mask of the Antarctic ice sheet: comparison of glacial geomorphic features across the continental shelf. *Geomorphology,* 75**,** 157-171.

WELTJE, G. J. & TJALLINGII, R. 2008. Calibration of XRF core scanners for quantitative geochemical logging of sediment cores: theory and application. *Earth and Planetary Science Letters,* 274**,** 423-438.

WENTWORTH, C. K. 1922. A scale of grade and class terms for clastic sediments. *The Journal of Geology,* 30**,** 377-392.

WHITEHOUSE, P. L., BENTLEY, M. J. & LE BROCQ, A. M. 2012. A deglacial model for Antarctica: geological constraints and glaciological modelling as a basis for a new model of Antarctic glacial isostatic adjustment. *Quaternary Science Reviews,* 32**,** 1-24.

WHITWORTH, T., ORSI, A., KIM, S. J., NOWLIN, W. & LOCARNINI, R. 1998. Water masses and mixing near the Antarctic Slope Front. *Ocean, ice, and atmosphere: interactions at the Antarctic continental margin***,** 1-27.

WINSBORROW, M. C., ANDREASSEN, K., CORNER, G. D. & LABERG, J. S. 2010. Deglaciation of a marine-based ice sheet: Late Weichselian palaeo-ice dynamics and retreat in the southern

Barents Sea reconstructed from onshore and offshore glacial geomorphology. *Quaternary Science Reviews,* 29**,** 424-442.

WINSBORROW, M. C., STOKES, C. R. & ANDREASSEN, K. 2012. Ice-stream flow switching during deglaciation of the southwestern Barents Sea. *Geological Society of America Bulletin,* 124**,** 275-290.

WRIGHT, A. P., WHITE, D. A., GORE, D. B. & SIEGERT, M. J. 2008. Antarctica at the Last Glacial Maximum, Deglaciation and the Holocene. *In:* FABIO, F. & MARTIN, S. (eds.) *Developments in Earth and Environmental Sciences.* Elsevier.

WUITE, J. & JEZEK, K. 2009. Evidence of past fluctuations on Stancomb-Wills Ice Tongue, Antarctica, preserved by relict flow stripes. *Journal of Glaciology,* 55**,** 239-244.

ZACHOS, J. C., QUINN, T. M. & SALAMY, K. A. 1996. High‑resolution (104 years) deep‑sea foraminiferal stable isotope records of the Eocene‑Oligocene climate transition. *Paleoceanography,* 11**,** 251-266.

ZECCHIN, M., CATUNEANU, O. & REBESCO, M. 2015. High-resolution sequence stratigraphy of clastic shelves IV: High-latitude settings. *Marine and Petroleum Geology,* 68**,** 427-437.

ZHANG, J. 2007. Increasing Antarctic sea ice under warming atmospheric and oceanic conditions. *Journal of Climate,* 20**,** 2515-2529.

ZWALLY, H. J., GIOVINETTO, M. B., BECKLEY, M. A. & SABA, J. L. 2012. Antarctic and Greenland drainage systems. *GSFC Cryospheric Sciences Laboratory*.

Appendix

Curiosity chapter

The Brunt Ice Shelf was discovered and surveyed during the Imperial Trans-Antarctic Expedition in January 1915 led by Ernst Shackleton. As the ship, Endurance, was attempting to reach the Antarctic continent, at Vahsel Bay, the ship entered pack ice and was forced to follow the coast southwestward along the coast of Coats Land. Shackleton named that part of the Coats Land for Caird Coast, after the biggest sponsor of the expedition Sir James Caird. A reconstruction of the Brunt Ice Shelf ice front position in 1915 was done by Anderson et al. (2014b)based on the Endurance survey map.
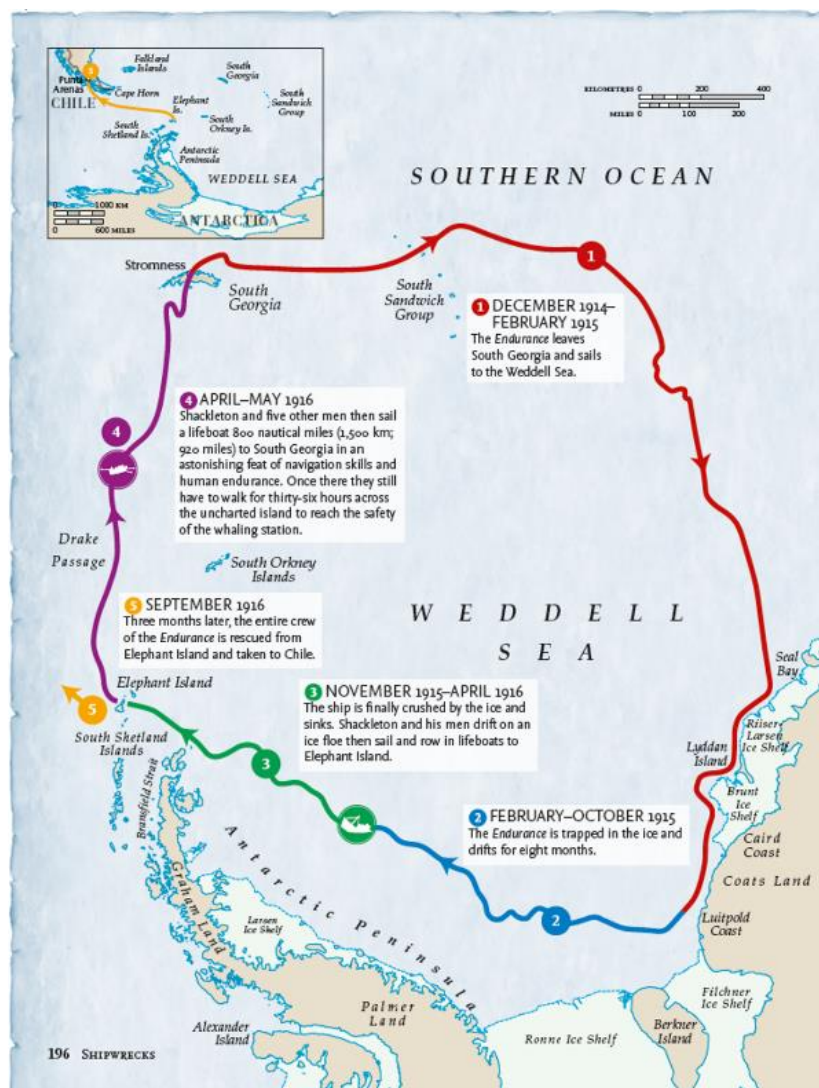

Fig. A. 1. From http://www.timesatlas.com/, 2014

S/Sum ratio spikes

The distinct peaks in the S/Sum ratio and the smaller peaks in Ca/Sum ratio in GC636 at 110 cm and GC637 at 132, 159 and 208 cm, and the "spiky" appearance of S/Sum ratio between 35-42 cm in GC637, might be related to the present of organic material. As organic material that decompose produces Sulphur (S). However, there was no black spots was observed when opening the core. During processing of the element composition data it was noted that the S/Sum ratio had large distinct peaks at the end and start of each core section, where the measurements was affected by air measurments. This was probably not caused by an increase of Sulphur at the core section ends, but rather a larger decrease in the measured amount of the other elements, compared to the Shulphur. A result of this was that the Sum values dropped more than the Sulphur amount, which are generally low, leading to discreet peaks in the graphs. Close inspection of the line-scan images, which where taken the same day as the XRF-measurements and the X-radiographs at the depth of the S/Sum ratio peaks, shows small holes in the line-scan images and less dense areas in the X-radiographs. The correlation of less sediment and poor measurements are therefore suggested to be causing these discreet peaks in the S/Sum ratio. However, it might be worth it to sample the depth of these discreet peaks to investigate the sediment for any biogenic material.
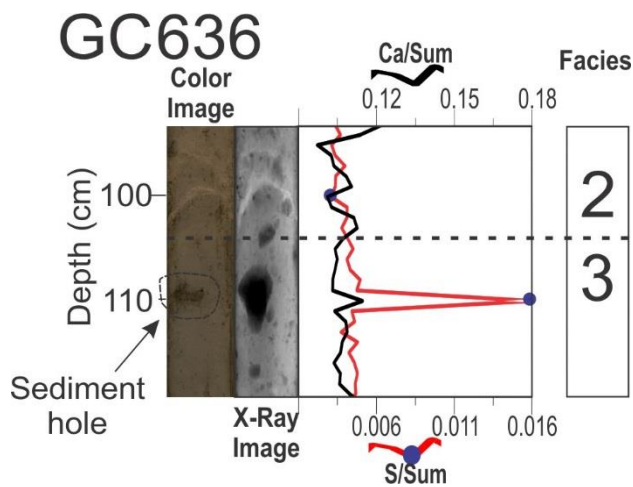

Fig. A. 2 Zoom in of GC636, at the distinct peak of S/Sum ratio, and the smaller peak in Ca/Sum ratio. The line scane color image, show a hole in the sediment surface of the core at the same depth as the peaks of S/Sum and Ca/Sum ratio.